JG|U

Max Planck Graduate Center
mit der Johannes Gutenberg-Universität

Strain control of magnetization for magnetoresistive sensors

Dissertation for Attaining the Academic Degree of "Doctor rerum naturalium" (Dr. rer. nat.) of the Departments

08 – Physics, Mathematics, and Computer Science,
09 – Chemistry, Pharmaceutics, and Geoscience,
10 – Biology,
University Medicine

of the Johannes Gutenberg University

Giovanni Masciocchi

geb. in Como (Italien)

Mainz, 2023

Reviewers:
Prof. Mathias Kläui[1], Prof. Jeffrey McCord[2]

[1]Department of Physics
Johannes Gutenberg University
Mainz, Germany

[2]Institute for Materials Science
Kiel University
Kiel, Germany

Examination date: October, 13^{th} 2023

Strain control of magnetization for magnetoresistive sensors

Short abstract:

Magnetoresistive (MR) sensors consist of magnetic thin films and micro- to nanostructures. It is important to understand the behavior of magnetic domain walls in these structures, to be able to optimize the performance of the sensors. Strain or mechanical stress is, up to now, always seen as a negative impact on MR sensors. In this project, the influence of strain on MR sensor is studied with two aspects. On the one hand, the conventional approach of minimizing the sensitivity of the sensor to strain by means of design and choice of materials will be pursued. On the other hand, the utilization of strain to realize new or improved functionalities allowed the realization and demonstration of a new sensor for discrete magnetic field detection.

Keywords: Strain, MR sensors, Spintronics, Magnetostriction

Contents

Abstract

This thesis focuses on the magneto-elastic interactions in thin films and their significance in technological applications with particular focus on sensors. The magnetostriction, constant which determines the strength of these interactions, plays a crucial role in various applications. For instance, strain immunity is essential for magnetic sensors to reduce strain cross-sensitivity, particularly in the case of flexible substrates. On the other hand, to sense strain materials require giant strain effects. The optimization of the magnetic sensing layer, including strain anisotropy, is crucial for magnetic sensors performance, depending on their specific application requirements. The first part of this thesis discusses the characterization and the engineering of the strain-dependent material properties for the development of the free layer of magnetic sensors. The focus is on two material platforms: a Ni/Fe multilayer and Permalloy. The use of He^+ ion irradiation as a post-deposition technique is explored to control magnetostriction and enhance magnetic softness. The strain dependence of anisotropy and magnetization compensation is explored in another material platform, Co/Gd synthetic ferrimagnets, that has the unique ability to switch their magnetic state using a laser pulse.

In the second part of this thesis, the control of domain walls using strain is extensively studied for their applications in memory devices and magnetic sensors. Domain walls offer non-volatile positioning and energy efficiency in various applications. However, the influence of mechanical strain or stress on these sensing components has been overlooked. In our studies, we highlight the importance of considering mechanical strain in actual devices, exploring the effects of different types of strain on a sensor-type device. Uniform strain and its compensation through material preparation are discussed, along with the conceptualization and realization of a new magnetic sensor based on spatially variant strain. Furthermore, the impact of time-dependent strain on domain wall devices in the presence of surface acoustic waves is investigated. By considering these factors, a comprehensive understanding of the behavior and optimization of free layer of magnetic sensors under different strain conditions is achieved.

Zusammenfassung

Diese Arbeit befasst sich mit den magnetoelastischen Wechselwirkungen in Materialien und ihrer Bedeutung für technologische Anwendungen mit besonderem Schwerpunkt auf Sensoren. Die Magnetostriktionskonstante, welche die Stärke dieser Wechselwirkungen bestimmt, spielt bei verschiedenen Anwendungen eine entscheidende Rolle. So ist beispielsweise die Unempfindlichkeit gegenüber Dehnungen für magnetische Sensoren wichtig, um die Querempfindlichkeit gegenüber mechanischem Stress zu verringern, insbesondere bei flexiblen Substraten. Andererseits sind für die Erfassung von Dehnungen Materialien mit großen Dehnungseffekten erforderlich. Die Optimierung der magnetischen Sensorschicht, einschließlich der Dehnungsanisotropie, ist entscheidend für die Leistung der magnetischen Sensoren, je nach ihren spezifischen Anwendungsanforderungen. Der erste Teil dieser Arbeit befasst sich mit der Materialvorbereitung für die Entwicklung magnetischer Sensoren, wobei der Schwerpunkt auf zwei Materialplattformen liegt: einem Ni/Fe-Multischicht-System und reinem Permalloy. Der Einsatz von He^+ -Ionenbestrahlung als Post-Depositions-Technik wird erforscht, um die Magnetostriktion zu kontrollieren und die magnetische Weichheit zu verbessern. Die Fleckenabhängigkeit der Anisotropie und der Magnetisierungskompensation wurde in einer anderen Materialplattform, den synthetischen Co/Gd-Ferrimagneten, erforscht, welche die einzigartige Fähigkeit haben, ihren magnetischen Zustand mittels Laserpuls zu wechseln.

Im zweiten Teil dieser Arbeit wurde die Kontrolle von Domänenwänden durch mechanische Deformation speziell für ihre Anwendung in Speichergeräten und magnetischen Sensoren eingehend untersucht. Domänenwände ermöglichen eine nichtflüchtige Positionierung und Energieeffizienz in verschiedenen Anwendungen. Der Einfluss mechanischer Dehnungen oder Spannungen auf diese Sensorkomponenten wurde jedoch bisher übersehen. In unseren Studien betonen wir die Bedeutung der Berücksichtigung mechanischer Dehnungen in tatsächlichen Geräten und untersuchen die Auswirkungen verschiedener Arten von Dehnungen auf ein sensorartiges Gerät. Gleichmäßige Dehnungen und ihre Kompensation durch Materialpräparation werden ebenso diskutiert wie die Konzeption und Realisierung eines neuen magnetischen Sensors, der auf räumlich variierenden Dehnungen basiert. Darüber hinaus werden die Auswirkungen zeitabhängiger Dehnungen auf diesen Bauteile in Gegenwart akustischer Oberflächenwellen untersucht. Durch die Berücksichtigung dieser Faktoren kann ein umfassendes Verständnis des Verhaltens und der Optimierung der freien Schicht von magnetischen Sensoren unter verschiedenen Dehnungsbedingungen erreicht werden.

List of acronyms

AOS - all-optical switching

AMR - anisotropic magneto resistance

CMOS - complementary metal-oxide semiconductor

CVD - chemical vapor deposition

DW - domain wall

DOS - density of states

EA - easy axis

EBL - electron-beam lithography

EDX - energy dispersive X-ray spectroscopy

ESD - electrostatic discharge

EELS - electron energy-loss spectroscopy

FEM - finite element method

FM - ferromagnetic

FFT - fast Fourier transform

FWHM - full-width at half-maximum

GMR - giant magneto resistance

IDT - interdigitated transducer

LLG - Landau-Lifshitz-Gilbert

ME - magnetoelastic

MO - magneto-optical

MOKE - magneto-optical Kerr effect

MOSFET - metal oxide semiconductor field effect transistor

MR - magneto resistance

OOP - out-of-plane

PDE - partial differential equations

PECVD - plasma-enhanced chemical vapor deposition

PEM - photo-elastic modulator

PMA - perpendicular magnetic anisotropy

PVD - physical vapor deposition

RE-TM - rare earth transition metal

RF - radio-frequency

RIE - reactive ion etching

SAW - surface acoustic wave

SOC - spin-orbit coupling

SRT - spin reorientation transition

SSAW - standing surface acoustic wave

STEM - scanning transmission electron microscope

TMR - tunnel magneto resistance

TOF-SIMS - time-of-flight secondary ion mass spectrometer

UV - ultra-violet

VNA - vector network analyzer

VSM - vibrating sample magnetometer

XRD - X-ray diffraction

XRR - X-ray reflectivity

Declaration of Authorship

I, Giovanni Masciocchi, declare that this thesis titled, "Strain control of magnetization for magnetoresistive sensors" and the work presented in it are my own. I confirm that:

- This work was done wholly while in candidature for a research degree at this University.
- Where any part of this thesis has previously been submitted for a degree or any other qualification at this University or any other institution, this has been clearly stated.
- Where I have consulted the published work of others, this is always clearly attributed.
- Where I have quoted from the work of others, the source is always given. With the exception of such quotations, this thesis is entirely my own work.
- I have acknowledged all main sources of help. Where the thesis is based on work done by myself jointly with others, I have made clear exactly what was done by others and what I have contributed myself.

I hereby declare that I wrote the dissertation submitted without any unauthorized external assistance and used only sources acknowledged in the work. All textual passages which are appropriated verbatim or paraphrased from published and unpublished texts as well as all information obtained from oral sources are duly indicated and listed in accordance with bibliographical rules. In carrying out this research, I complied with the rules of standard scientific practice as formulated in the statutes of Johannes Gutenberg University Mainz to insure standard scientific practice.

Signature: _____

Giovanni Masciocchi
Mainz, August 2023

Alla mia famiglia:

Loretta, Giorgio, Evelina ed Eleonora.

1

Background and motivation

The first chapter introduces magnetoresistive sensors and highlights the motivation of the research conducted in the thesis.

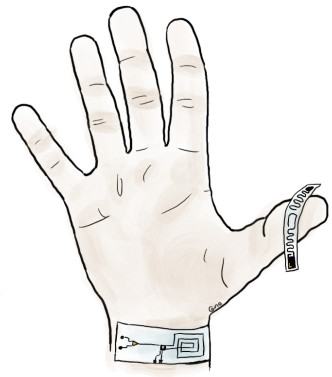

Contents

1.1 Spintronics for magnetoresistive sensors

A variety of sensors - able to measure pressure, proximity, position, fluid flow, and more - have become nowadays an essential component of the internet of things, consumer electronics, healthcare, wearable technology, navigation in automotive and beyond. Many of these sensors can be realized using the measurement of magnetic field and belong accordingly to the group of magnetic sensors. Only one part of magnetic sensors relies on the direct measurement of magnetic fields (magnetometers for compass applications), while for probing other quantities e.g. position or rotation, the movement of a permanent magnet can be translated to magnetic field changes (indirect measurement). The magnetic sensor market, and therefore the interest in research and development, is expected to generate over 6.2 billion dollars in revenue worldwide by 2025,[1] driven by growth in the automotive, industrial, and biomedical sectors. In this thesis, an interdisciplinary approach to the development of magnetic sensors involving material science, electrical engineering and modeling is used with the focus on the effects of stress on the sensor device. In this chapter, a brief overview of magnetic sensors that motivates our research efforts is presented.

1.1.1 Applications of MR sensors

Various physical phenomena such as Electromagnetic Induction, Hall Effect, Tunnel Magnetoresistance (TMR), Giant Magnetoresistance (GMR), and Anisotropic Magnetoresistance (AMR) are utilized to develop magnetic sensors.[2] Depending on the application and use, each of these technologies can be advantageous. As magnetoresistance is the focus of this thesis, we will present here a brief description of the AMR, GMR and TMR effect. For a review we refer the reader as an example to the work of Lenz et al.[3]

Anisotropic magnetoresistance

In some materials (e.g. Fe and Ni) the resistance is dependent on the angle between the magnetization and the current flow. Magnetization direction dependent scattering of conducting electrons with uncompensated spins leads to the presence of a high resistance state if magnetization and current are parallel while a low resistance state is be measured if they are perpendicular to each other.[4]

Typically, the current is passed in the plane of a magnetic strip, whose easy axis of magnetization is set by the strip geometry and defines the sensitivity direction. The magnetization will follow the applied field direction, therefore the magnetic layer is also called "free-layer" and is typically made by an alloy of $Ni_{81}Fe_{19}$. A schematic representation of an AMR strip is shown in Fig. 1.1 (a) where the contacts define the current direction. The great advantage of the AMR technology is the easy fabrication process (therefore low cost) and flexibility in device shape and base resistance. One of the key differences between the three MR technologies discussed here, is the sensitivity S [V/T] defined in a sensor as the slope of the output characteristic curve (see Fig. 1.1 (d)) which is ideally linear between the two saturation resistance values (linear range).[5] The low fabrication cost of AMR technology comes at the expenses of the sensitivity as the AMR effect (relative changes to the stripe resistance) is in the order of 2-5%.

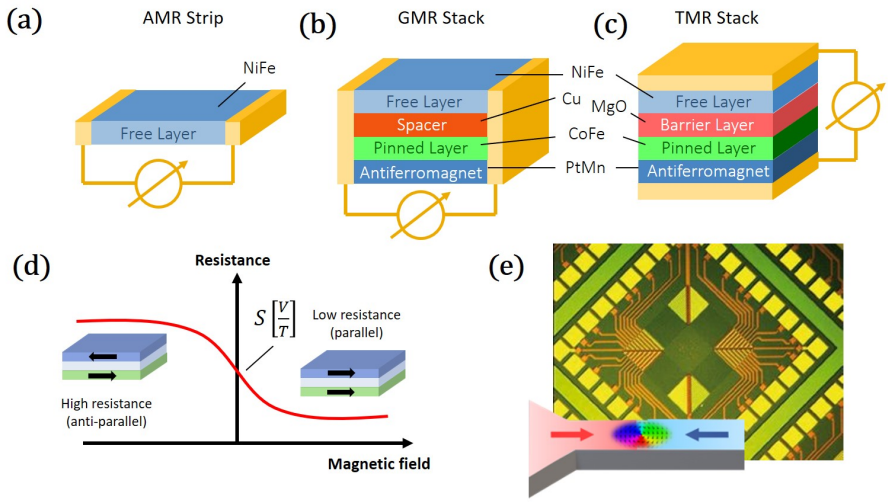

Figure 1.1: Schematic of the three magnetoresistive effects used in magnetoresistive (MR) sensors: (a) anisotropic magnetoresistance (AMR), (b) giant magnetoresistance (GMR) and (c) tunnel magnetoresistance (TMR). (d) resistance changes in a spin valve, at the base of magnetic field detection using resistance changes. (e) One example of rotation counter based on domain walls. Source: novotechnik.de.

Giant magnetoresistance

The resistance of a thin film structure, which consists of a non-magnetic metal layer sandwiched between two magnetic layers (Fig. 1.1 (b)), varies depending on the alignment of the magnetization of the two magnetic layers. This phenomenon arises from the spin-dependent scattering of electrons.[6,7] As shown in Fig. 1.1 (d), when the magnetization of the two layers is parallel, only electrons with a particular spin polarization are significantly scattered,

leading to a lower resistance of this composite structure. Conversely, when the magnetization of the layers is anti-parallel, both up and down spin polarized electrons experience strong scattering, resulting in a higher resistance. This discovery (which yielded the Nobel prize in 2007 to A. Fert and P. Grunberg) was heavily used in the reading heads of hard disks memories starting form the 1990s and is still used now.

The device in Fig. 1.1 (b) is called "spin-valve" and is composed by a free layer (soft magnetic) whose magnetization follows the applied field and a pinned layer that has a constant magnetization - set by an antiferromagnetic layer (e.g. IrMn). Sensor realized with GMR technology will have significant sensitivity (GMR effect in the order of 20-50%) and are capable of sensing the Earth's magnetic field,[8] which makes them attractive for orientation and navigation applications. However, this comes at the expenses of a increase complexity in the fabrication of the multilayer design. Moreover, the realization of a pinned layer direction, requires additional production step (e.g. annealing).

-	**AMR**	**GMR spin-valve**	**TMR**
MR effect	$< 4\%$	$< 50\%$	$< 500\%$
Current direction	in plane	in plane	out of the plane
Geometry	meander	meander	circular/dot

Table 1.1: Summary of the main characteristics of the three magnetoresistive effects discussed in the present section.

Tunnel magnetoresistance

If at a first glance the layer structure of GMR and TMR technology might look similar in Figs. 1.1 (b) and (c), a closer look shows that the spacing layer (in red) is an insulator (AlO or MgO) in the case of TMR technology. This insulating layer is called tunneling barrier throughout electrons can "tunnel". If two ferromagnets are magnetized in the same direction, the likelihood of electrons tunneling through the insulating layer is greater than if the magnetizations were in opposite directions. This results in a lower resistance for the parallel configuration and a higher resistance for the anti-parallel configuration.[9] To obtain a linear sensor transfer curve (typically [V/T]), perpendicular orientation between the easy axis of free layer and pinned layer are imperative. This gives some freedom in the design of the device geometry and on the layers preferential direction of magnetization. As shown in Fig. 1.2, multiple strategies for linearization of TMR sensors are possible (also applicable to GMR). For more details we refer the reader to the work of Silva et al.[5] where Fig. 1.2 is taken from.

In comparison to GMR sensors, TMR sensors exhibit extremely high sensitivity (TMR effect can be several hundreds of %,[10] see Table 1.1) but have typically

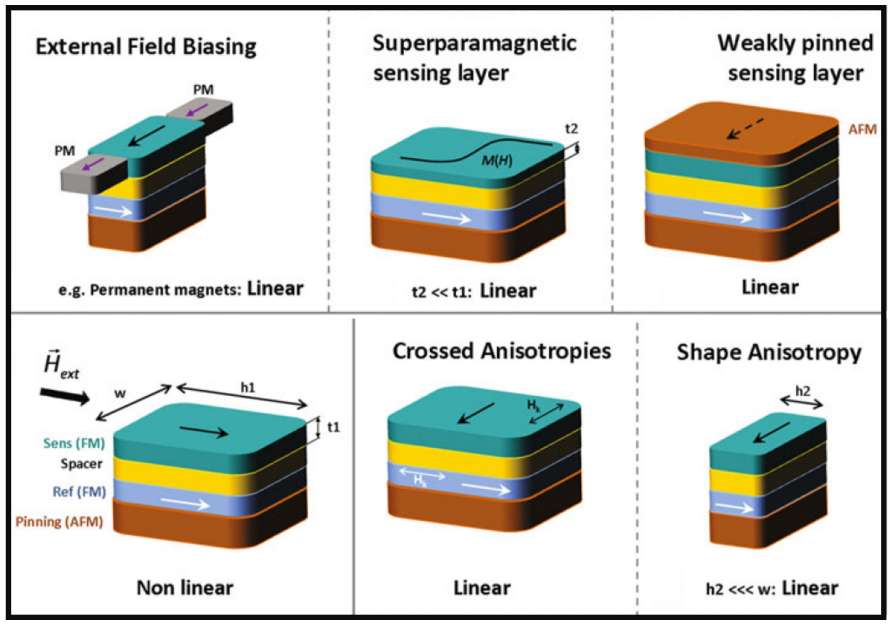

Figure 1.2: Summary of the most common linearization strategies for MR sensors. The non-linear case, in the bottom left corner, serves as a comparison for the other linearized designs. The proposed strategies can be used both for GMR and for TMR sensors. Source: Silva et al.[5]

larger noise.[11] This comes from the smaller required area and usually higher resistance, that conversely, as a benefit, allows them to consume less power than GMR sensors operating under identical voltage conditions. The major noise sources in TMR sensors are the electrical thermal noise - a white noise source proportional to the sensor resistance - and the magnetic noise. The latter has typically a thermal-magnetic noise contribution and magnetic 1/f noise. These noises are associated with the sensing layer volume and they can be reduced up to some extent by increasing the sensing area or the thickness of the sensing layer. Another drawback for TMR sensors is the realization. TMR elements are more expensive and challenging to manufacture due to the necessity of a high-quality, defect-free ultra-thin tunnel barrier. The layer thickness required can be lower than 1 nm and needs to be homogeneous over a whole wafer below fraction of an atom. In addition to that, a TMR stack requires a vertical flow of the current, that makes the sensors more fragile due to electrostatic discharge (ESD). They are therefore used for applications where the high sensitivity justifies the elevated cost.

Magnetic DW-based sensors

The possibility of driving magnetic domain walls (DWs) - magnetic quasi-

particles discussed in Chap. 2 - in nanowires has been exploited for diverse sensor concepts.[12–14] The idea at the base of these sensors, is that magnetic domains grow or shrink propagating the domain walls between them with a quasi-particle nature when external magnetic fields are applied. These magnetic domains can therefore be used as nonvolatile information carrier. Fig. 1.3 shows a micromagnetic simulation of a DW device comprising of a round nucleation pad and a spiral channel for DW propagation. Magnetic domains in Fig. 1.3 (b) are separated by DWs, that are created in the nucleation pad each 180° rotation of the external magnetic field. The first of this type of device to be commercialized was a rotation counter designed by Novotechnick (novotechnik.de) and produced by Sensitec GmbH (sensitec.com) and more recently by Analog Devices (analog.com).

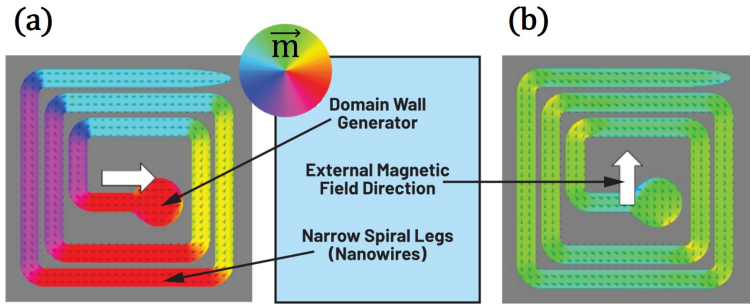

Figure 1.3: Micromagnetic simulation of a rotation counter based on magnetic DWs able to count up to three full rotations. (a) shows the initial sensor state, without any DWs inside while (b) shows the magnetic state after several rotations of the external magnetic field. DWs are located at the corners of the spiral structure. Source: Analog Devices.

An image of this "Multiturn sensor" can be seen in Fig. 1.1 (e) and it relies on the GMR effect. The number and the position of DWs (sketched in the inset of Fig. 1.1 (e)) can be read out electrically by multiple contacts and it encodes the absolute angular position of an object. This type of sensors enables nonvolatile measurements, that allow for non stop sensing even when electrical power is lost. This can be an advantage in some applications e.g. position sensing in embedded systems or harsh environments.

1.2 Novel frontiers in magnetoresistive sensors

The three MR technologies discussed in Sec. 1.1.1 enabled reliable sensing in the most diverse application. Starting from industrial applications[15] to

magnetic biosensors[16] MR devices can reach noise level of few nT/$\sqrt{Hz}$ and sensitivity larger than 100 mV/Oe.[2] A fundamental aspect in the development of MR sensors, which can be a limitation to the device sensitivity or working window, is the dependence of the magnetic response of the active layer to mechanical stress, which can result in measurement errors or failure of the sensor. As is discussed in more detail in Chap. 2 and Chap. 3, the stress acting on the sensor is induced during fabrication mainly during packaging[17] (Fig. 1.4 (a)) and layer deposition[18] (Fig. 1.4 (b)). Both these production steps can involve large temperature changes.

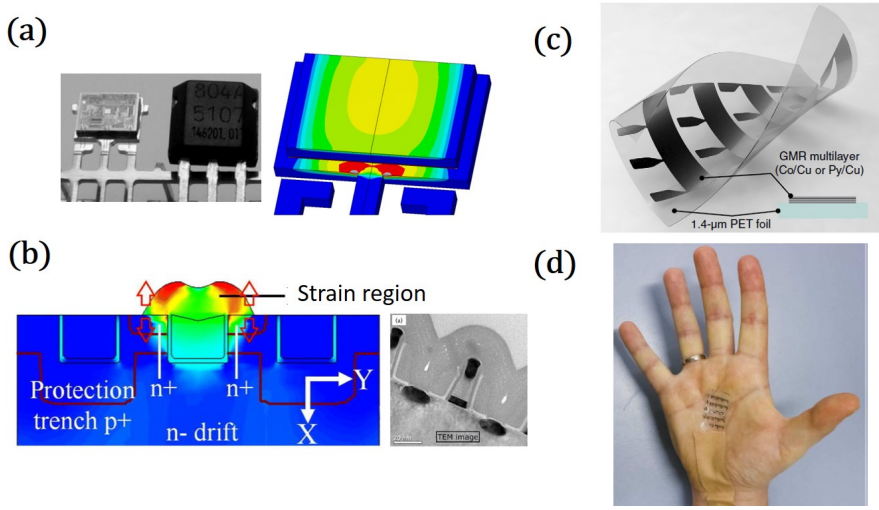

Figure 1.4: (a) The stress acting on a sensor dice after packaging is shown with a simulation. Source:[17] Fischer, PhD Thesis Univ. Freiburg (2006). (b) stress induced in the channel of a MOSFET transistor with layer deposition. Source (adapted): Yao et al.,(2021).[18] (c) and (d) GMR sensor on a flexible substrate for on-skin applications. Source:[19] Melzer et. al., (2015).

Stress and magnetization are coupled by a bidirectional energy exchange between magnetic and elastic states, which is called magnetostriction (discussed in more details in Chap. 2). In most sensing applications, the material choice and the device design want to minimize the stress response of the free layer (zero magnetostriction), to reach a pure magnetic sensing. Part of the work of presented in this thesis is devoted to the minimization of magnetostriction of magnetic materials for sensing.

If on the one hand stress effects minimization is desirable to maintain the sensitivity direction, on the other hand strain effects on magnetization can be exploited for the realization of innovative sensor concepts.[20] Some results where strain was intentionally used in MR to realize a new sensor concept are presented in Chap. 5 of this thesis.

1.2.1 Sensors on flexible substrates

If intrinsic stress in the active layer of a MR sensor can arise during the fabrication process, substrate bending and mechanical force applied to the package (extrinsic stress) can also influence the device. Stress originating by substrate bending is particularly significant in applications that involve flexible substrates that attracted attentions in the last years.

Deformable magnetic materials offer a distinct benefit as they can be utilized in applications requiring flexibility or stretchability, a characteristic that conventional rigid sensors lack.[21,22] This advantage is particularly useful in the realm of flexible electronics, where the aim is to develop electronic circuits and devices that can be bent or folded during usage. The close relationship between the underlying principles and practical applications of curved magnetic thin films arises from the fact that magnetic domain walls can be pinned at bends. This fundamental discovery has significant implications for magnetic field sensors that utilize geometrically curved magnetic thin films.[19] In fact, the curvature of the structure can cause an additional source of magnetoelastic anisotropy, which can increase the coercive field and consequently increase error in magnetic field sensors for angle measurements. Furthermore, the sensitive elements typically posses a high degree of shape anisotropy to ensure a steady state of magnetic domains and defined the sensitivity direction. Thin films applied onto rather rough and flexible substrates can have significant impact of the magnetoelastic anisotropy which would hinder the sensitivity direction.[15] For this reason, magnetostriction needs to be minimized.

With this technology as a foundation, numerous potential applications in e-Mobility, healthcare,[23] and interactive electronics[24] can be envisioned. Some examples of flexible MR sensors are presented in Figs. 1.4 (c) and (d). The GMR sensor can be placed on skin and is able to detect magnetic fields for touch-less control. A complete review about this topic can be found in the recent book from Makarov et al.[21]

If the prototypes of these devices are promising regarding stability of output signal, MR ration and mechanical integrity upon stretching,[25] still some efforts need to be made in the development of flexible sensors that should work upon thousand of bending cycles.

2

Theory notions

This chapter contains fundamental notions of spintronics and magnetism, useful for understanding the content of this thesis. Furthermore, the chapter introduces the important principles of strain and mechanical deformation in solids.

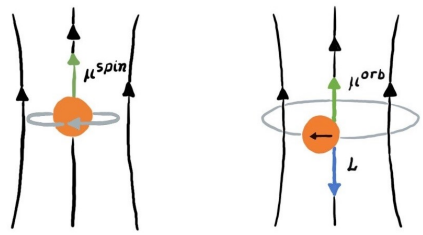

Contents

In this Chapter, we start from the atomic level and work our way up to the phenomenological description of magnetism in the micromagnetic description in condensed matter. The different phenomenological thermodynamic contributions to the magnetic free energy are considered, which determine the magnetic state at the system's equilibrium. Particular emphasis is put in the description of the interactions between the elastic state and the magnetic state of a solid. The derivation is done in the framework of magnetic domain wall theory, which is the focus of this thesis. Furthermore, the dynamical behavior of the magnetization and its theoretical description by the classical Landau-Lifshitz-Gilbert (LLG) equation is introduced. Finally, several means for application of strain are proposed as a promising approach to control magnetism.

2.1 Magnetism at the nanoscale

The magnetism of solids arises from the magnetism of their electrons, as electrons themselves possess intrinsic magnetism. However, the *Bohr–Van Leeuwen* theorem asserts that if statistical mechanics and classical mechanics are employed, the average magnetization will invariably be zero.[26] Consequently, the presence of magnetism in solids is attributed to quantum mechanics, rendering classical physics inadequate to explain paramagnetism, diamagnetism, and ferromagnetism. A quantum mechanical explanation is needed to comprehend the source of magnetism. In order to do so, we refer to the derivation outlined in the books of Blundell[27] and Skomski.[28]

2.1.1 Atomic origin of magnetism

A very simple model ascribes the magnetic moment to a circular motion of electrons around atomic nuclei. An electron's angular momentum arises from two distinct sources as shown in Fig. 2.1. The first is its intrinsic angular momentum, also known as spin, while the second is its orbital momentum, which results from the electron's current generated by motion around the nucleus.

The amount of orbital angular momentum that an electron possesses in an actual atom varies depending on the electronic state it occupies. Both the orbital angular momentum **L** and the spin angular momentum **S** result in a

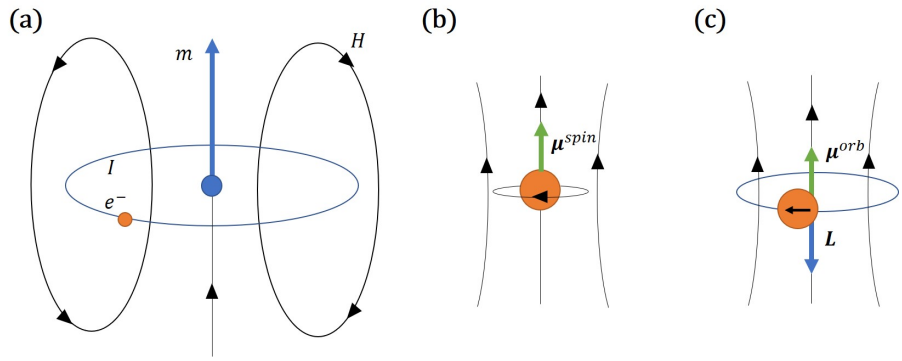

Figure 2.1: (a) The orbital moment of an atom is created by the circular motion of electrons, similar to the magnetic field created by a solenoidal coil. Magnetic moments associated with (b) spin angular momentum, $\boldsymbol{\mu}^{spin}$, of an electron and (c) the electron's orbital motion, $\boldsymbol{\mu}^{orb}$.

magnetic moment, so that the expression for the total magnetic moment is given by the sum of the orbital and the spin contributions:

$$\boldsymbol{\mu}^{total} = \boldsymbol{\mu}^{spin} + \boldsymbol{\mu}^{orb} = -\frac{\mu_B}{\hbar}(\mathbf{L} + 2\mathbf{S}), \tag{2.1}$$

where μ_B is the Bohr magneton. The interaction between spin and orbital angular momenta is known as spin-orbit coupling (SOC), which has significant implications in magnetism. It gives rise to a variety of fascinating effects, including magnetocrystalline anisotropy and the magnetoelastic (ME) effect, which we explore in more details later. One way to conceptually understand the SOC is by considering the interaction between the spin magnetic moment of an electron and the magnetic field in its rest frame, which is generated by the electron's orbital motion within the electric field of the atomic nucleus. The SOC energy can be computed using the formula for the energy of an electron with magnetic moment in a magnetic field $\mathbf{B}$. Accordingly, the SOC energy has a the expression

$$E_{SO} = -\boldsymbol{\mu}^{spin} \cdot \mathbf{B}_{SO} = -\lambda_{SO}\mathbf{S} \cdot \mathbf{L}, \tag{2.2}$$

where λ_{SO} is the SOC constant, that reflects the strength of the SOC.

Let us now consider an atom with many electrons, where the atomic minimum energy state is obtained filling the energy levels. According to Eq. 2.1, those occupying unfilled shells can combine to give rise to a non-zero net angular momentum, while the electrons in filled shells do not contribute at all. As a consequence, there are elements, such as Fe, Co and Ni (known as itinerant

ferromagnets), with not completely filled 3d sub-shells. This results in a non-zero atomic magnetic moment, which is one of the requirements for obtaining conventional ferromagnetism in condensed matter.

2.1.2 From single atom to solid matter

Magnetic ordering is present in condensed matter. This suggests that there is a means of long-distance communication (interaction) between magnetic moments, enabling them to align themselves in a particular manner. The magnetic dipolar interaction is the initial interaction to consider, but it is insufficient (about 1K in terms of energy) to explain the ordering of the majority of magnetic materials. Hence, there must be an alternative mechanism for coupling individual magnetic moments in a solid. This interaction is called Heisenberg exchange interaction and is derived from the innate nature of electrons as Fermi-particles.

Let us consider, for simplicity, a system of two electrons. The total wave function $\mathbf{\Psi}(\mathbf{r}_1, \mathbf{r}_2)$ can be written as the overlap of the tow single electron wave functions $\mathbf{\Psi}_1(\mathbf{r}_1)$ and $\mathbf{\Psi}_2(\mathbf{r}_2)$. Obeying quantum mechanical rules stating that the elections are indistinguishable fermions, the following forms for the total wave function are possible:

$$\mathbf{\Psi}(\mathbf{r}_1, \mathbf{r}_2) = \frac{1}{\sqrt{2}} \left[\mathbf{\Psi}_1(\mathbf{r}_1)\mathbf{\Psi}_2(\mathbf{r}_2) + \mathbf{\Psi}_1(\mathbf{r}_2)\mathbf{\Psi}_2(\mathbf{r}_1)\right] \chi_s, \tag{2.3}$$

$$\mathbf{\Psi}(\mathbf{r}_1, \mathbf{r}_2) = \frac{1}{\sqrt{2}} \left[\mathbf{\Psi}_1(\mathbf{r}_1)\mathbf{\Psi}_2(\mathbf{r}_2) - \mathbf{\Psi}_1(\mathbf{r}_2)\mathbf{\Psi}_2(\mathbf{r}_1)\right] \chi_t, \tag{2.4}$$

where the χ_s, being antisymmetric relative to the exchange of the electrons for a singlet state, and χ_t, symmetric for a triplet state, are the spin parts of the wave function. Knowing the energies of the singlet and triplet states we can re-write the Hamiltonian in the form of an effective Hamiltonian. The spin dependent part is in the form of

$$\hat{H}^{spin} = -2J\boldsymbol{S}_1 \cdot \boldsymbol{S}_2, \tag{2.5}$$

where J is the exchange integral or exchange constant, associated to the energy difference between the triplet and the singlet states. This representation of the effective Hamiltonian is particularly convenient since it allows to see which is the favorable energy state, according to the sign of the exchange constant. If $J > 0$, the triplet state is more energetically favorable, so that the spins couple

ferromagnetically, like in Ni, Co and Fe. In the case, when $J < 0$, the singlet state is more favorable, and the spins are aligned antiferromagnetically.

A simple way to extend this to a many-body system, is to write the Hamiltonian considering exchange interactions of the nearest neighbors i and j only, resulting in

$$\hat{H} = -\sum_{i,j}^{n.n.} J_{ij} \boldsymbol{S}_i \cdot \boldsymbol{S}_j, \tag{2.6}$$

which is the Heisenberg model. Phenomenologically, ferromagnetic materials maintain this ordering below a threshold temperature, called Curie temperature T_C. The strength of the exchange interaction defines the temperature $T_C \propto \frac{J}{K_B}$, above which a material is no longer ferromagnetic, but is in a paramagnetic phase. For Co and Fe T_C is above 1000 K, while for Ni is around 600 K.

In different systems like some oxide and environments with low symmetry, so-called indirect exchange interaction[29] or asymmetric exchange[30,31] interaction come into play. As these materials are not used in the current work, they are not described in the current chapter.

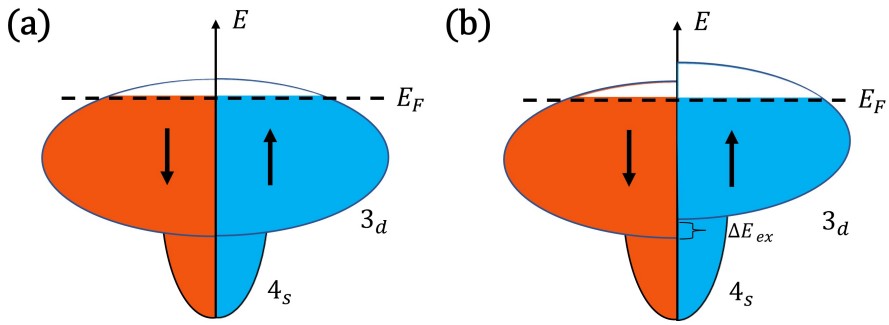

Figure 2.2: (a) The band structure of a non-magnetic metal is shown, where both spin sub-bands are equally filled. (b) The band structure of a ferromagnetic metal is displayed, which displays split spin sub-bands with different electronic populations for each spin sub-band, resulting in a net magnetic moment. The spin-up (↑) and spin-down (↓) sub-bands are presented on separate panels for clarity.

The exchange interaction in metallic systems occurs through itinerant electrons, making the use of the Heisenberg Hamiltonian unsuitable. The electrons in the broad s-bands, which are responsible for most of the current, interact with the more localized electrons in the d-orbitals to mediate the exchange interaction. The itinerant electrons also acquire polarization through hybridization with the spin-split d-states induced by the exchange field. In non-magnetic materials, the spin sub-bands are equally populated (Fig. 2.2 (a)), but an imbalance

of spin-up and spin-down electrons (Fig. 2.2 (b)) results in spin polarization. Stoner proposed a simple model to explain ferromagnetism in metals, known as itinerant magnetism. According to Stoner's model,[32] the two spin-polarized bands spontaneously split when the Stoner criterion is met[27]

$$I \cdot N_{\uparrow,\downarrow}(E_F) > 1, \tag{2.7}$$

where I is the Stoner exchange parameter and $N_{\uparrow,\downarrow}(E_F)$ is the density of states (DOS) per atom for spin-up and spin-down states, defined as $N_{\uparrow,\downarrow}(E_F) = \frac{D(E_F)}{2n}$. Here $D(E_F)$ is the total DOS at the Fermi level and n is the number of atoms per unit volume. Materials such as Fe, Ni and Co fulfill the Stoner criterion and, thus, exhibit a ferromagnetic ground state. For the materials that fulfill the Stoner criterion, the number of spin-up $N_\uparrow$ and spin-down $N_\downarrow$ electrons in two d sub-bands determines the magnetic moment $m = \mu_B(N_\uparrow - N_\downarrow)$ at a temperature below T_C.

Spin-dependent transport in Ferromagnetic metals

The presence of spin splitting in ferromagnetic materials also accounts for spin-dependent electronic transport,[33] which gives rise to the magnetoresistive effects discussed in Chap. 1. Electrical conductivity can be described in the simplest formula by the Drude model[34]

$$\sigma = \frac{e^2 n \tau}{m}, \tag{2.8}$$

where e, n, τ and m are the electrical charge, carrier density, lifetime and effective mass, respectively. The lifetime is related to the mean free path of electron, $\lambda = v_F \tau$, which is dependent on the density of states at the Fermi level $1/\tau \propto D_s(E_F)$. In the case of good conductors like gold or copper, the Fermi level resides within the *sp* band (*s* and *d* bands hybridized to form complicated electronic states), with the *d* band fully occupied (refer to Fig. 2.2 (a)). In ferromagnets, the scattering of electrons by atoms is influenced by the alignment of their magnetic moments, which is connected to the filling of the band responsible for the metal's magnetic properties, such as the 3*d* band in iron, nickel, or cobalt. The *d* band of ferromagnets undergoes splitting due to the presence of differing numbers of electrons with up and down spins. Consequently, the density of electronic states at the Fermi level differs depending on the direction of spin. Majority-spin electrons have their Fermi level situated within the *sp* band, resulting in similar transport characteristics in ferromagnets and non-magnetic metals. Conversely, minority-spin electrons experience hybridization of the *sp* and *d* bands, with their Fermi level residing within the *d* band (see Figure 2.2 (b)). The hybridized *spd* band possesses

a higher density of states, leading to stronger scattering and consequently a shorter mean free path (λ) for minority-spin electrons compared to majority-spin electrons. According to Eq. 2.8, that links λ to the conductivity, spin dependence of the electrical resistivity can be understood.

2.2 Micromagnetic approximation

In order to describe macroscopic magnetic systems it is convenient to substitute the atomistic description based on the Heisenberg Hamiltonian by a continuum description based on the micromagnetic approximation.[35,36] According to this principle, the vector field of magnetization directions $\boldsymbol{m}(\boldsymbol{r}) = \boldsymbol{M}(\boldsymbol{r})/M_s$ is chosen so that the total (free) energy reaches an absolute or relative minimum under the constraint $\boldsymbol{m}^2 = 1$. Micromagnetics allows one to simulate the macroscopic properties of a material including the best approximations to the fundamental atomic behavior. This approach is required to model spintronic phenomena happening at the micrometer scale and to capture functionalities of spintronic devices, such as magnetic domain motion. Micromagnetics, if compared to its alternative method covers larger length scales than atomistic spin dynamics simulations, limited to only several tens of nanometers of lateral size. Another possible approach, the Stoner–Wohlfarth macrospin model (see Sec. 2.23), in spite of its simplicity fails at describing magnetic textures, such as domain walls.

In the following sections, the different energy terms that contribute to the expression of the total free energy are reported as they describe the different magnetic interactions. All terms besides the stray field energy are local magnetic terms. The stray field energy depends on all other vector moments in the systems and it is the most onerous to be computed with numerical methods. A convenient way to describe the interaction with magnetization in the micromagnetic approximation is the use of an effective field acting on the magnetization. This is derived from the functional variation of the energy of the system with respect to the magnetization:

$$\boldsymbol{H}_{eff} = -\frac{1}{\mu_0 M_s}\frac{\delta E}{\delta \boldsymbol{m}}. \tag{2.9}$$

2.2.1 Zeeman energy

When an external magnetic field $\boldsymbol{H}_{ext}$ is applied, typically by a coil or magnet in a lab setting, the energy is minimized in a ferromagnet when the magnetization ($\mathbf{m}$) is aligned parallel to $\boldsymbol{H}_{ext}$. This is referred to as the Zeeman energy density given by

$$E_Z = -\mu_0 M_s \boldsymbol{m} \cdot \boldsymbol{H}_{ext}. \tag{2.10}$$

It is evident that the effective field associated with this phenomenon is $\boldsymbol{H}_{ext}$. The description of this basic energy term, resulting from an external interaction with the material, can be advantageous in explaining the complex dipolar interaction. The dipolar interaction is the energy term that arises from the reciprocal interaction between the magnetic moments of a magnetic system.

2.2.2 Exchange energy

A ferromagnet prefers a constant equilibrium magnetization direction . Deviations from this ideal case (constant magnetization, corresponding $(\nabla \boldsymbol{m})^2 = 0$) invoke an energy cost, which can be described by the exchange energy expression

$$E_{ex} = A_{ex} \int (\nabla \boldsymbol{m})^2 \, dV, \tag{2.11}$$

where A_{ex} is a material constant, the so-called exchange stiffness constant (dimension J/m or erg/cm), which is in general temperature dependent and V is the total volume. The origin of parallel alignment of spins in a ferromagnet is the exchange interaction, a quantum mechanical effect whose description and complete treatment can be found in Ref.[27] Here we limit to say that the quantum mechanical exchange forces arise from the overlapping orbital wave functions of the two nearest neighbor electron magnetic moments. The Pauli exclusion principle allows anti-parallel spins to occupy the same orbital, however Coulomb repulsion takes place if magnetic moments are too close. Exchange of such indistinguishable identical spins is subject to the exchange symmetry, given by the exchange integral. The exchange constant is linked to the exchange stiffness via $A_{ex} = 2JS^2 z/a$ Jm^{-1}, where we assume a uniform

exchange integral J, a is the first neighbor distance and z is a lattice constant that depends on the crystalline structure. J is negative for the anti-parallel, or - antiferromagnetic, arrangement of the spins in while it is positive for the ferromagnetic, or parallel spin arrangement.

Using Eq. 2.9 the effective field associated to the exchange is:

$$\boldsymbol{H}_{ex} = \frac{2A_{ex}}{\mu_0 M_s}\nabla^2 \boldsymbol{m}. \tag{2.12}$$

2.2.3 Magnetostatic energy

The magnetostatic energy, also called demagnetizing or stray field interaction, has its origin in the dipolar interaction. This potential energy of two magnetic moments $\boldsymbol{m}_1$ and $\boldsymbol{m}_2$ separated by a distance $\boldsymbol{r}$ is expressed as[28]

$$E_{dipole} = -\frac{1}{4\pi\mu_0}\frac{3(\boldsymbol{m}_1 \cdot \boldsymbol{r})(\boldsymbol{m}_2 \cdot \boldsymbol{r}) - \boldsymbol{m}_1 \cdot \boldsymbol{m}_2|\boldsymbol{r}|^2}{|\boldsymbol{r}|^5}, \tag{2.13}$$

and shows a long-range interaction. The dipolar interaction is connected to the energy of the shape anisotropy. The stray field of a structure refers to the magnetic field lines that emerge from the sample and re-enter it. The stray field can be defined using Maxwell's equation when no currents j are present ($\frac{\partial E}{\partial t} = 0$):

$$\nabla \times \boldsymbol{H}_{stray} = 0 \tag{2.14}$$

$$\nabla \cdot \boldsymbol{B} = \mu_0 \nabla \cdot (\boldsymbol{H}_{stray} + \boldsymbol{M}) = 0. \tag{2.15}$$

As the field $\boldsymbol{H}$ is conservative $\boldsymbol{H}_{stray} = -\nabla U$ which can be substitute into Eq. 2.15 to obtain

$$\nabla^2 U = \nabla \boldsymbol{M} \tag{2.16}$$

that by analogy with the Poisson's equation in electrostatics, Eq. 2.16 leads the definition of magnetic charge density

$$\rho_M = \nabla \boldsymbol{M}. \tag{2.17}$$

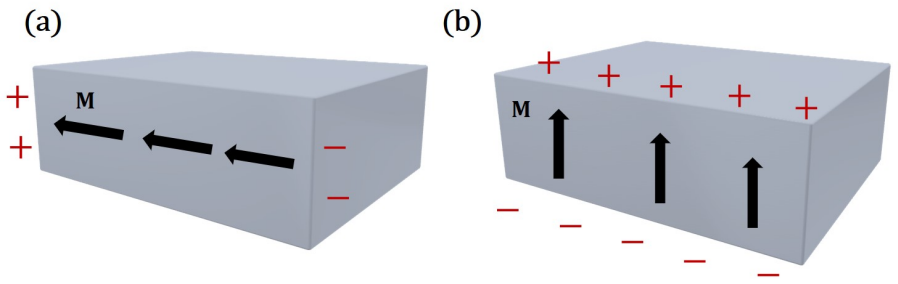

Figure 2.3: (a) Energetically favorable and (b) unfavorable magnetic configurations in terms of the magnetostatic energy given by Eq. 2.18. The magnetic moments in (a) aligned with the stray field created by the neighboring moments produce fewer effective magnetic surface charges than in (b).

Thus, the stray field can be thought of as generated by these magnetic charges. When interacting with other magnetic dipoles in the system, the stray field gives rise to the following contribution to the total energy

$$E_{stray} = \frac{\mu_0}{2} \int |\boldsymbol{H}_{stray}|^2 dV. \tag{2.18}$$

The result of the magnetostatic interactions between magnetic dipoles is the shape anisotropy. When the magnetization in a material is uniformly aligned on a macroscopic level, magnetic charges manifest at the surfaces as shown in Fig. 2.3. These surface charges, known as magnetostatic charges, create a demagnetizing field, $H_{demag} = -N\boldsymbol{M}$, that acts in the opposite direction of the magnetization. The value of N, is a shape-dependent parameter that is usually difficult to be computed for complex geometries. The magnetostatic energy resulting from the demagnetizing field can be calculated using a similar equation to Eq. 2.18, as $E_{stray} = \frac{1}{2}\mu_0 \int \boldsymbol{M}(\boldsymbol{r}) \cdot \boldsymbol{H}_{demag}(\boldsymbol{r}) dV$.

In the case of an ellipse (as described, for example in Ref.[28]), this magnetostatic energy term has the form of a uniaxial anisotropy along the major axis of the sample. For this reason it is called shape anisotropy.

2.2.4 Magnetic anisotropy

The exchange energy term is often isotropic, this means that the energy of a ferromagnet is independent on the orientation of the magnetization $\boldsymbol{M}$. However, in a real system this is not true. For example, the magnetic response

of a ferromagnet to an external magnetic field is found to be dependent on the direction of the applied field in experiment. Some directions are found to require less energy to saturate the magnetization, and are therefore called easy axis direction, while the directions that require more energy i.e. larger external fields to be saturated, are called magnetic hard axis of magnetization.

This phenomenological observation, which adds to the "shape" anisotropy, arises form the crystalline structure, as typically the atoms and their magnetic moments are located at the vertices of the lattice. The symmetry of the isotropic exchange interaction is broken due to spin-orbital interactions, resulting in certain crystallographic axes being preferred over others for magnetization orientations[37] which reflects the symmetry of the crystal. This phenomenon is known as magnetocrystalline anisotropy.

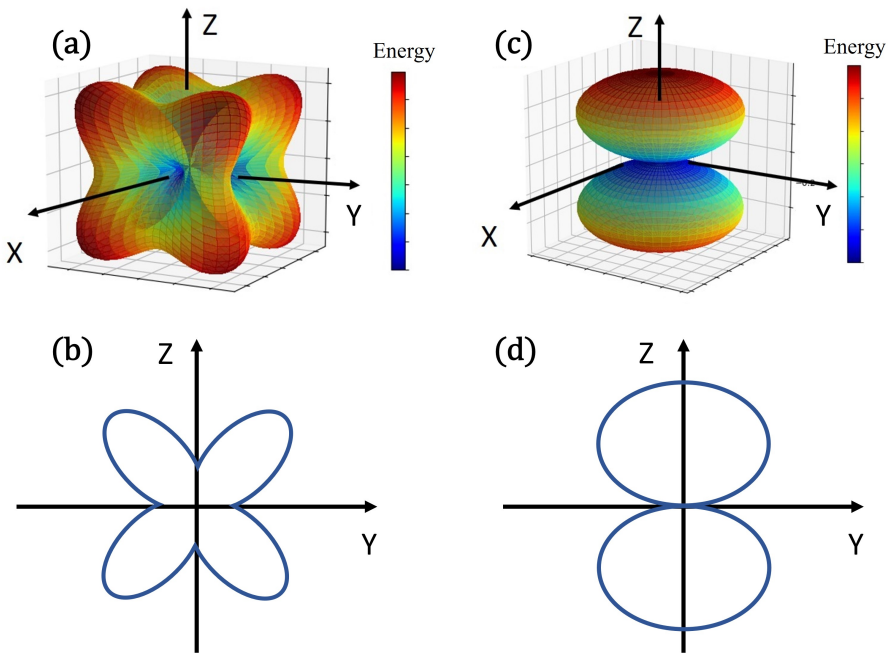

Figure 2.4: Isometric surfaces of the energy density of magnetic anisotropy for cubic (a) - (b) (case of K_{c1}>0) and uniaxial (c) - (d) types of magnetic anisotropy where "energy surfaces" are plotted. A minimum of energy represent the "easy" direction of magnetization. Adapted from Ref.[38]

The expression for the anisotropy energy density of a cubic crystal can be written to the lowest order in polar coordinates as

$$E_{cub} = \left(K_{c1} + K_{c2} sin^2\theta\right) cos^4\theta \sin^2\phi \cos^2\phi + K_{c1} \sin^2\theta \cos^2\theta, \qquad (2.19)$$

where K_{c1} and K_{c2} are material constants. The sign of K_{c1} determines the easy direction for magnetization along the <100> or <111> directions. A visual representation of the energy contribution of a cubic anisotropy is given in Figs. 2.4 (a) and (b) and gives an impression of the local energetic environment of the magnetization in a ferromagnet.

In the simplest case, the anisotropy is uniaxial (valid for hexagonal and tetragonal crystals, with a single easy axis[36]) and for this case the energy density term is

$$E_{anis} = K_1 sin^2\theta + K_2 sin^4\theta + ..., \tag{2.20}$$

where K_i are the anisotropy constants (J/m^{-3}) and θ is the angle between the volume magnetization and the anisotropy axis. A visual representation of uniaxial magnetic anisotropy energy can be seen in Figs. 2.4 (c) and (d).

Let us consider the first order term only in Eq. 2.20. When K_1 has a negative value, it indicates an easy-plane anisotropy where all magnetization orientations lying in the plane perpendicular to the easy axis are equally favored. Conversely, a positive K_1 value leads to an easy-axis anisotropy where lower energy configurations of magnetization are parallel to the easy axis. At times, it is necessary to take into account a generalized second-order anisotropy. This is applicable when dealing with crystals that have symmetry lower than tetragonal or hexagonal, or in situations where multiple uniaxial anisotropies overlap. One example of this is the occurrence of induced anisotropy in a cubic crystal, which can manifest as what is known as orthorhombic anisotropy. Similarly, in polycrystalline or amorphous materials, orthorhombic anisotropy leads to a uniaxial anisotropy with an "effective" easy axis, which may not necessarily align with the annealing direction.

Interface anisotropy

In the case of thin films, the coupling of a few atomic layers of ferromagnetic metals with an oxide creates a uniaxial anisotropy perpendicular to the interface between the two materials. This effect is attributed to the reduced symmetry of the atomic environment of surface atoms. This anisotropy's strength scales inversely with the ferromagnet's thickness, as seen for example in Pt/Co interfaces.[39] This happens because, in ordinary bulk samples, the surface magnetization is coupled to the bulk magnetization by exchange forces and becomes therefore negligible. Here, a surface anisotropy constant, K_s, exists that contributes to the bulk constant as

$$K_1 = K_{bulk} + \frac{K_s}{t}, \tag{2.21}$$

where t is the ferromagnet's thickness. The effective field associated with the anisotropy, obtained by Eq. 2.9 is

$$H_{anis} = \frac{2K_1}{\mu_0 M_s} cos\theta. \tag{2.22}$$

In general, the easy axis of magnetization in magnetic films is influenced by the interplay between interface and shape anisotropies, as explained in Eq. 2.21. The surface anisotropy term in this equation is independent of the ferromagnetic (FM) layer's thickness. Thus, at a particular thickness, K_1 becomes positive (negative), which favors perpendicular (in-plane) magnetic anisotropy. When the two contributions become comparable, a spin-reorientation transition (SRT) occurs,[40] and the magnetization tilts towards an intermediate canted state. This is investigated in Chap. 4 for a Co/Gd system.

Stoner-Wohlfarth model

The Stoner-Wohlfarth model provides a straightforward explanation of the energy angular dependence of a magnetic particle, where the magnetization rotates in unison as if it were a single macroscopic spin.[41] Although this model offers a limited description of hysteresis loops, it can be employed for magnetic anisotropy analysis. The magnetic free energy density, for only Zeeman and anisotropy energy considered, is given by

$$E = K_{eff} sin^2\phi_h - \mu_0 M_s H_{ext} cos(\phi_h - \theta) \tag{2.23}$$

where $K_{eff} = K_1 - \frac{1}{2}\mu_0 M_s$ is the effective anisotropy constant, which is the sum of the first-order anisotropy constant and the magnetostatic energy, the second term describes the interaction of the magnetization with the applied field H_{ext}. Here, θ and ϕ_h are the angles of the magnetization and the applied field with the easy axis of the sample defined by the longest length, and M_s is the saturation magnetization. The Stoner-Wohlfarth model[32] allows for the determination of the magnetic hysteresis loop shape, and the anisotropy field, which can be obtained by saturating the magnetization along the easy axis and then applying a field along the hard axis. In a film with dominating uniaxial magnetic anisotropy, the anisotropy field H_k can be measured by utilizing the Stoner-Wohlfarth model as long as the magnetization rotates coherently

$$H_k = \frac{2K_{eff}}{\mu_0 M_s}. \tag{2.24}$$

In the present configuration, the total energy exhibits 2 minima (Fig. 2.5 (b)) in both orientations of the easy axis, which are separated by an energy barrier

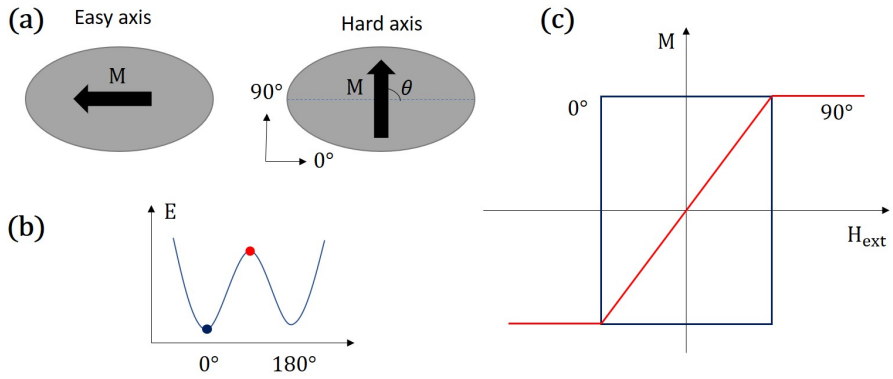

Figure 2.5: (a) Schematic representation of the configuration for the Stoner Wohlfarth model problem. The angle θ is defined between the easy axis and the magnetization vector. The angle ϕ_h is defined between the easy axis and the applied field direction. (b) energy diagram for magnetic configuration of an ellipse and (c) corresponding hysteresis loops along the easy and hard axis of magnetization.

defined by the hard axis formed by the shape anisotropy. The hysteresis loops obtained for a system described by Eq. 2.23 with a magnetic field applied along the easy and hard axis are shown in Fig. 2.5 (c).

2.2.4.1 Magnetoelastic anisotropy

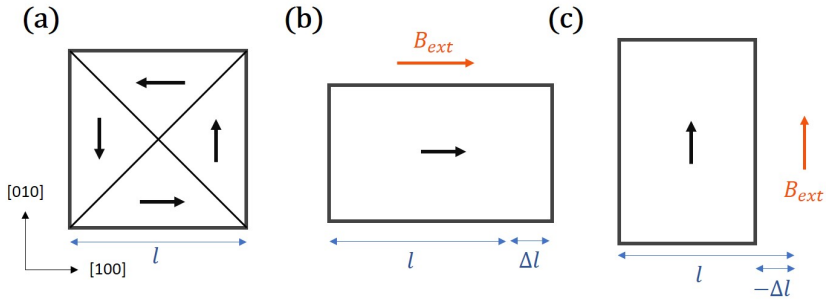

Figure 2.6: Macroscopic description of the direct magnetostriction of a ferromagnet. The sketch considers the change of length in a positive magnetostrictive material with cubic symmetry. With respect to the demagnetized state (a) a strain $\Delta l/l$ is induced in the sample magnetized to saturation by an external field (b) along the [100] or (c) [010] direction. Black arrows indicate the direction of magnetization of a single domain.

Magnetostriction describes changes in the sample dimensions with respect to

the demagnetized state when the magnetization direction is altered (shown in Fig. 2.6). In the same way, the effective magnetic anisotropy can be altered by strain in a ferromagnet, which can then affect the magnetization direction. This phenomenon is the inverse magnetostriction (Villari effect). As presented in Sec. 2.4, strain can be induced either intentionally, by mechanically bending the material or applying strain to a piezoelectric substrate, or naturally imposed during material growth and layer deposition. The relationship of the linear coupling between stress and strain is presented in Sec. 2.4 and in a more complete way in the book of Balluffi.[42] In this section we consider strain of non magnetic origin. We neglect moreover third order terms which means linear elasticity is considered. This is justified by the relatively small magnetoelastic effects in ferromagnets, if materials are not extremely stressed.[36] We are thus left with just one important mechanism in magneto-elastics: the anisotropic magnetostriction. This phenomenon stems from the magneto-crystalline anisotropy and exhibits a quadratic relationship with the magnetization's components.

At a microscopic level, the magnetoelastic (ME) anisotropy mainly arises from the spin-orbit coupling (SOC).[28,29] The SOC, which determines the crystal anisotropy, is modified by the sign of the lattice stress. Magnetoelastic interactions affect therefore the magnetic behavior strongly for alloys containing rare earth elements, which have a strong orbital moment.

Micro-magnetic description of magnetostriction

If we ignore third-order terms in the elastic strain components, we obtain linear elasticity that obeys Hooke's law. Ignoring higher order terms is usually accurate for magnetostrictive effects as the typical magnetostriction constants are in the order of 10^{-6} and typical strains are in the order of 10^{-3}. However, this energy contribution can become predominant together with the energy contributions of domain walls.

In general, the expression for the phenomenological ME energy can be obtained by expanding the crystal's free energy in terms of the strain tensor $\boldsymbol{\varepsilon}$ components.[43] Let us consider here the case of a cubic crystal, that we use as a starting point to derive the expression for a polycrystalline system. From this symmetry we obtain the following expression for the magneto-elastic interaction energy

$$e_{ME} = -3C_2\lambda_{100}\sum_{i=1}^{3}\varepsilon_{ii}(m_i^2 - \frac{1}{3}) - 6C_3\lambda_{111}\sum_{i>k}\varepsilon_{ik}m_i m_k \tag{2.25}$$

where C_2 and C_3 are abbreviations for the two shear moduli of the cubic crystal. The spontaneous magnetostriction values λ_{100} and λ_{111} are dimensionless and

independent of each other, and they represent the strength of the magneto-elastic interaction. The magneto-elastic energy is balanced by the elastic energy e_{el}. A full derivation can be found in Ref.,[36] here we limit ourselves to say that for a uniformly magnetized body with free surfaces, the spontaneous magnetostrictive deformation $\Delta l/l$ is computed by minimizing the sum of the energy contributions e_{ME} and e_{el} with respect to the components of the strain. This leads to a spontaneous magnetostrictive deformation (field-induced strain relative to the demagnetized state when the material is brought into saturation) and to a total energy - e^0 - of the system in the form:

$$e^0 = -\frac{3}{2}C_2\lambda_{100}^2 - \frac{9}{2}\left(C_3\lambda_{111}^2 - C_2\lambda_{100}^2\right)\left(m_1^2m_1^2 + m_3^2m_2^2 + m_2^2m_3^2\right). \quad (2.26)$$

Eq. 2.26 is obtained inserting the spontaneous magnetostrictive deformation into Eq. 2.25 and has the same symmetry as the first-order cubic anisotropy. For elastic and magnetostrictive anisotropy (amorphous or polycrystalline materials) the equations simplify by using the isotropic shear modulus $C_2 = C_3$ and the isotropic magnetostriction constant $\lambda_s = \lambda_{100} = \lambda_{111}$.[44]

The magneto-elastic interaction energy in Eq. 2.25 assumes a different meaning if the elastic strain tensor $\boldsymbol{\varepsilon}$ is replaced by the corresponding stress tensor $\boldsymbol{\sigma}$. In this stress formulation the magneto-elastic energy describes the interaction of magnetization with a stress $\boldsymbol{\sigma}$ of non-magnetic origin:

$$e_{ME} = -\frac{3}{2}\lambda_{100}\sum_i \sigma_{ii}(m_i^2 - \frac{1}{3}) - 3\lambda_{111}\sum_{i>k}\sigma_{ik}m_im_k \quad (2.27)$$

for a cubic system or

$$e_{ME} = -\frac{3}{2}\lambda_s\sum_{i,k}\sigma_{ik}(m_im_k - \frac{1}{3}\delta_{ik}) \quad (2.28)$$

for an isotropic system, where δ_{ik} is the Kronecker delta.

The stress can be caused by non-magnetic internal stress, which can result from dislocations, temperature, structure, or composition inhomogeneities, or an external stress. This coupling energy is similar to the interaction between magnetization and an external magnetic field, and it has the form of an orthorhombic anisotropy (Eq. 2.20). In the case of isotropic material and a uniaxial stress applied, the magneto-elastic coupling energy is the one of a uniaxial anisotropy. If the stress vector is **a**, the magneto elastic coupling simplifies to

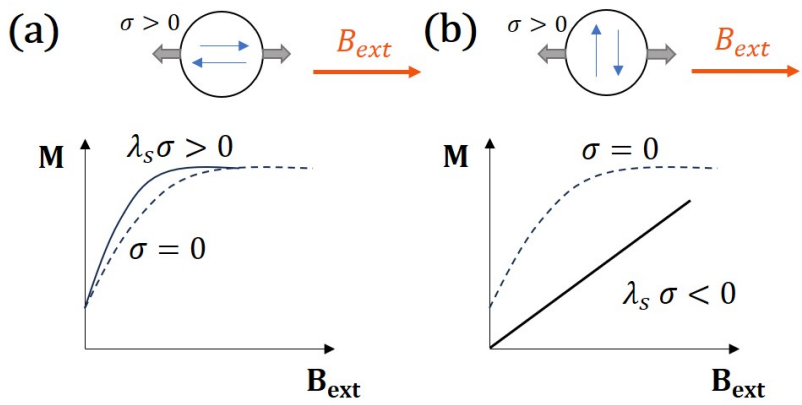

Figure 2.7: Schematic of the influence of mechanical stress on the magnetic anisotropy and thus on the magnetization curves for an isotropic material. (a) refers to a positive magnetostrictive material while (b) to a negative magnetostrictive one.

$$e_{ME} = -\frac{3}{2}\lambda_s \sigma \left[(\mathbf{m} \cdot \mathbf{a})^2 - \frac{1}{3} \right] \tag{2.29}$$

where the uniaxial anisotropy constant can be defined as $K_u = \frac{3}{2}\lambda_s \sigma$. This expression is widely used during the course of this thesis. The effect of this stress-anisotropy on the magnetization curves of an isotropic material can be see in Fig. 2.7 where the induced easy axis is opposite for a positive Fig. 2.7 (a) or negative Fig. 2.7 (b) magnetostrictive material.

Simple case - a polycrystalline system

For the sake of simplicity, we present here also an alternative derivation for the expression for the uniaxial magneto-elastic energy of a polycrystalline system ($C_2 = C_3$ and isotropic magnetostriction $\lambda_s = \lambda_{100} = \lambda_{111}$) - the most relevant for the systems used in this thesis. In this case the ME energy is given as[43]

$$E_{ME} = -\frac{\lambda_s Y}{2}(3cos^2\theta - 1)\varepsilon + \frac{Y}{2}\varepsilon^2 \tag{2.30}$$

The elongation along the stress axis is represented by the strain $\varepsilon = \Delta l/L$, while the ME coupling's strength is described by the saturation magnetostriction constant λ_s. Y represents Young's modulus, and θ represents the angle between the magnetization and strain axis. We can compare the angular-dependent term in Eq. 2.30 with the standard expression for the energy density of uniaxial anisotropy, which is given by $E_{anis} = K_1 sin^2\theta$, resulting in:

$$K_{ME} = \frac{3}{2}\lambda_s Y \varepsilon \tag{2.31}$$

Eq. 2.31 is the extra contribution to the magnetic anisotropy caused by strain. Hence, when a material with a negative magnetostriction coefficient, such as Ni, is subjected to tensile strain, the magnetic anisotropy decreases along the direction of the applied strain. Conversely, for a material with a positive λ_s, such as CoFeB, the magnetic anisotropy increases.[28]

Energy term	Coefficient	Definition	Typical value
Exchange energy	A [J/m]	Material constant	10^{-12} J/m
Anisotropy energy	K_u,K_s [J/m^3]	Material constants	$\pm(10^2$-$10^7)$ J/m^3
External field energy	$H_{ext}M_s$	External field, Saturation Magnet.	Depends on field magnitude
Stray field energy	K_d [J/m^3]	$K_d = M_s^2/2\mu_0$	0-3 $\cdot$ 10^6 J/m^3
External stress energy	$\sigma_{ext}\lambda$ [J/m^3]	External stress, magnetostriction	$5 \cdot 10^3$ J/m^3 in this thesis

Table 2.1: Different energy terms in a Ferromagnet discussed in Sec. 2.2. The definitions and the order of magnitude of these interactions are also reported for common materials. Note that the stray field energy depends on the value of M_s chosen. Table adapted form Ref.[36] p. 115.

2.3 Magnetic domain walls

The exchange interaction favors aligning a spin parallel to its neighbors, irrespective of their direction, while uniaxial anisotropy favors alignment with the easy axis of anisotropy. Applying an external field tends to align magnetization with the external field. These energy terms are short-range and depend on the orientation of a single spin or its direct neighbors at most. The existence

of domains in extended ferromagnets is mainly due to the minimization of magnetostatic energy, which is a long-range interaction.

While it is difficult to schematically represent the minimization of magnetostatic energy in a general way due to its complex nature, it is possible to analyze Eq. 2.17 for the magnetic charges. Doing so reveals that the two necessary conditions for minimizing magnetostatic energy are the absence of volume magnetic charges ($\nabla \cdot \boldsymbol{m} = 0$) and surface charges ($\boldsymbol{m} \cdot \boldsymbol{n} = 0$). This indicates that magnetostatic energy is minimized when the magnetization configuration within the magnetic specimen realizes a flux closure inside its volume and is tangential to the surface of the sample. Achieving this requires the magnetization to change direction within the sample, which results in an energy cost for anisotropy and exchange. However, the exchange interaction depends on the angle between neighboring spins, so the magnetization can change direction in space while keeping a low gradient, resulting in a low exchange energy cost.

This means that the system, instead of aligning itself in a mono-domain (uniformly magnetized state), spontaneously breaks into domains that are separated by domain walls (DWs). Within the domains, magnetization still follows the easy axis, while the reduced size of the domains, minimizes the stray field energy.[29] The different energy terms, discussed in Sec. 2.2 and summarized in Table 2.1 will in principle contribute to the final domain state.

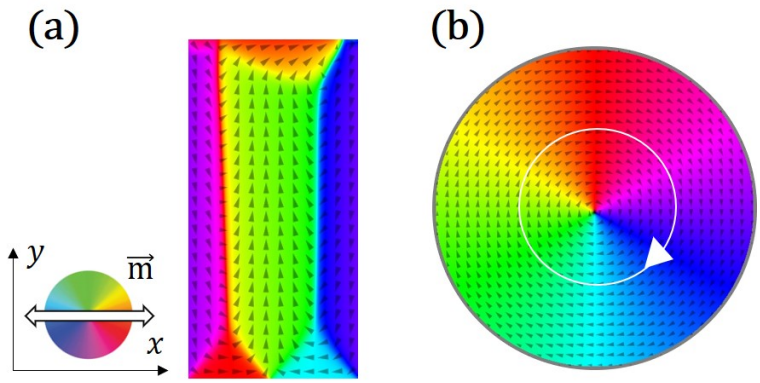

Figure 2.8: Different magnetic configurations obtained with micromagnetic simulations in the absence of external magnetic field (relaxed state). (a) multi-domain state with several domain walls. (b) vortex state, minimum energy configuration for a disk-shaped geometry. Material parameters are the one of a soft ferromagnet (Permalloy).

In this thesis, we explore different stable magnetic structures that result from the competition of energy terms, as shown in Fig. 2.8. One such structure is the Landau state, which is favored due to the flux closure it generates and the

curling of magnetization at the edges to avoid magnetic charges. This state, shown in Fig. 2.8 (a), mostly consists of 90° domain walls and a 180° domain wall at the center and is obtained when there is no applied field and the stray field is minimized.

Another possible structure is the magnetic vortex state, depicted in Fig. 2.8 (b), which arises in confined lateral structures where the magnetization curls in-plane along the edges. The vortex core, located at the center of the structure where the magnetization points out of the plane, is typically small, ranging from tens of microns to nanometers depending on the material.[45] Some of those structures, in particular the vortex state, are used in magnetoresistive sensors.[46] This is mainly due to the linear and hysteresis-free motion of the vortex core in the presence of in-plane field.

2.3.1 In-plane domain walls and Topology

The focus of this thesis are materials magnetized in-plane. In the case of in-plane nanowires, two types of domain walls exist: head-to-head domain walls, where the magnetization points in the direction of the domain wall, and tail-to-tail domain walls. For in-plane materials, the two most basic types of domain walls are 'transverse' and 'vortex' domain walls. Vortex walls are found in wider and thicker wires, while transverse walls can be found for smaller cross-sections. Those magnetic structures can be seen in Figs. 2.9 and 2.10 .

Domain walls can be regarded as composite objects consisting of magnetic topological charges, which arise due to magnetostatic considerations of the magnetization vector field's discontinuities. These discontinuities, known as topological defects, are crucial for comprehending the latest topics such as Domain Walls and Skyrmions.[47] In a mathematical sense, topology refers to the geometric study of an object that maintains its topological properties under continuous transformations (continuous map). This implies that objects can be gradually modified into one another through continuous alterations. A classic example of this is that the surface of a doughnut can be continuously transformed into the surface of a mug, rendering them homotopic surfaces. More details can be found in chapter 2 of Ref.[48] In this section we limit ourselves to the practical relevance of chirality and topology when it comes to magnetic sensors and devices.

Let us consider a magnetic strip in-plane magnetized with a transverse wall in its center, as shown in Figs. 2.9 (a)-(d). In this case, the chirality of the

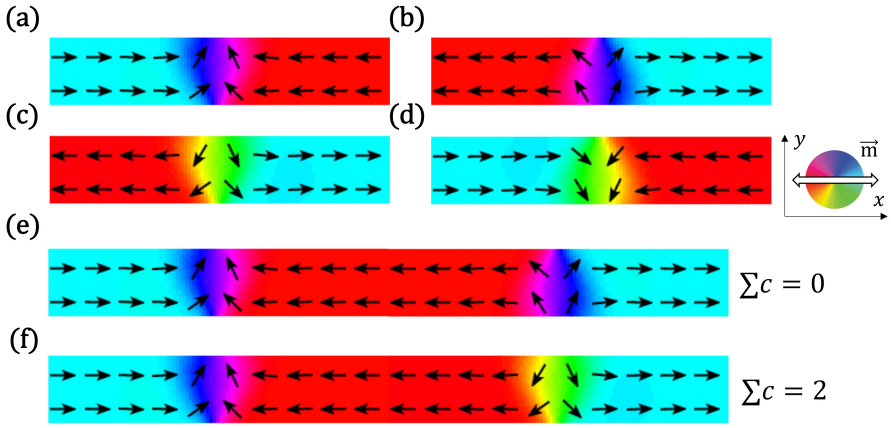

Figure 2.9: (a) - (d) micromagnetic simulations of a Py wire showing transverse domain walls of 180°. (a) and (d) are head to head type while (b) and (c) are tail-to-tail type. The topological winding number c is +1 for the DW in (a) and (c) while it is −1 for the DWs in (b) and (d). Two DWs in a nanowire without (e) and with (f) topological protection. Source: courtesy of M. Kläui, *MagnEFi tutorial spin orbitronics, 15.12.2020.*

spin structure is defined by the topological winding number, according (in the ground state) to the expression:

$$c = \frac{1}{\pi} \int_{-\infty}^{\infty} \left(\boldsymbol{m} \times \frac{\delta \boldsymbol{m}}{\delta x} \right) \hat{\boldsymbol{e}}_z dx = \pm 1. \tag{2.32}$$

The chirality c defines whether the magnetization rotates counter-clockwise (c= -1) or clockwise (c = 1) when passing from left to right through the DW. A texture is termed topologically stable if it cannot be in a continuum fashion erased, i.e. transformed into the ground state texture which is a uniform magnetization in most of the cases.

Figs. 2.9 (a) - (d) show four possible and energetically equivalent magnetic configurations for a transverse wall. Figs. 2.9 (a) and (b) show a DW pointing up with $c = +1$ (head-to-head) and $c = -1$ (tail-to-tail), respectively. Instead in Figs. 2.9 (c) and (d) DW pointing down with $c = +1$ (tail-to-tail) and $c = -1$ (head-to-head) are shown, respectively.

If we now consider the case of two domain walls in a magnetic strip, two possible scenarios can occur. In case the sum of the total topological charge is zero - Fig. 2.9 (e) - the structure has no topological protection. This means no energy cost is needed to reach the uniformly magnetized state and the two walls annihilate. If instead the total topological charge is nonzero[49,50] - Fig.

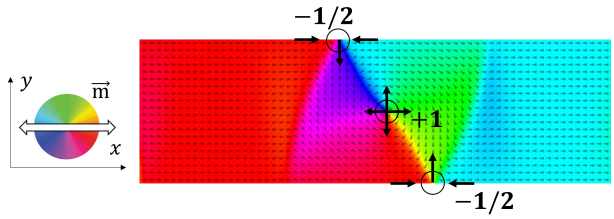

Figure 2.10: Topological defects of a vortex domain wall. The geometry simulated is a nanowire of Permalloy, 30 nm thick and 300 nm wide.

2.9 (f) - a finite energy barrier is present and the two transverse walls are stable in the magnetic strip. This is extremely relevant in devices that use a DW as a carrier of information for sensing, memory or logic applications as the energy barrier provided by the topological charge prevents information loss.

Also vortex walls can be characterized by their topological charges,[51] and vortex walls with the same chirality exhibit topological repulsion and form bound states in the same way as described for transverse walls. In Fig. 2.10 a vortex DW with a center defect of winding number +1 and two edge defects of number -1/2 is shown. As compared with a transverse DW, this configuration is more stable in thick and wide wires (in the case of Permalloy, above 100 nm width and 10 nm thickness[52]), since the center core reduces the stray field generated by the edge defects.

The use of winding numbers to define vortex domain walls offers a straightforward terminology for describing the structure and chirality and can classify the behavior of domain walls, their interactions with both other walls and geometric constrains in nanowires. DW chirality has also been used functionally to manipulate DW trajectory,[53] and formed the foundation for applications such as memory cells[54] and logic gates[55] based on chirality.

2.3.2 Dynamics of magnetization - LLG equation

In a medium exhibiting ferromagnetism, the magnetic moments precess around the direction of the local field known as the effective field $\boldsymbol{H}_{eff}$. This precessional motion is damped and aligns M to $\boldsymbol{H}_{eff}$ to minimize the overall energy of the system. $\boldsymbol{H}_{eff}$ acting on the magnetization comprises external fields, anisotropy fields etc. The expression that is used to describe this time-dependent phenomena is[56]

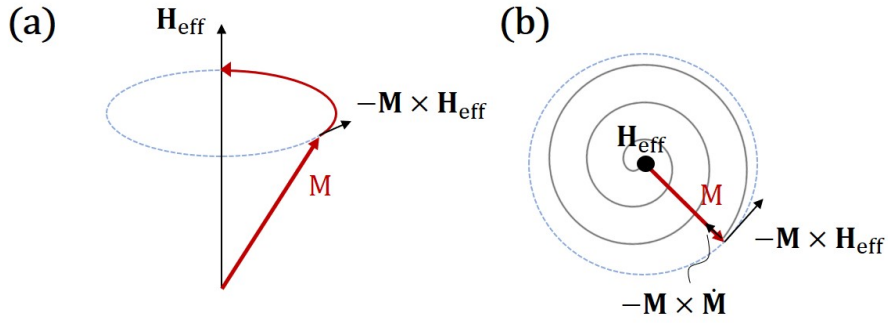

Figure 2.11: Schematic illustration of the magnetization dynamics in an effective magnetic field H_{eff}. The precession only leads to a continuous rotation (a), the damping slowly aligns the magnetization with the field, resulting in a spiraling motion (b).

$$\frac{d\boldsymbol{M}}{dt} = -\mu_0 \boldsymbol{M} \times \boldsymbol{H}_{eff} + \frac{\alpha}{M_s} \boldsymbol{M} \times \frac{d\boldsymbol{M}}{dt} \tag{2.33}$$

called Landau-Lifshitz-Gilbert equation (LLG), where γ is the gyromagnetic ratio and α is the Gilbert damping constant. $\boldsymbol{H_{eff}}$ is calculated from the derivative of the system energy with changes in $\boldsymbol{M}$, which includes any applied external field, as well as other energy contributions, e.g. magnetostatic, magnetocrystalline, and exchange energy terms. Eq. 2.33 can be written explicitly as

$$\frac{d\boldsymbol{M}}{dt} = -\mu_0 \boldsymbol{M} \times \boldsymbol{H}_{eff} + \frac{\alpha}{M_s} \boldsymbol{M} \times (\boldsymbol{M} \times \boldsymbol{H_{eff}}) \tag{2.34}$$

and is central in micromagnetic simulations as its numerical solution determines the time-dependent state of magnetization and is most accurate when solved at a scale up to the exchange length of a material, i.e. the length over which magnetization remains approximately uniform.

As shown in Fig. 2.11 (a), it can be observed that the magnetic moments precess continuously due to the term $\mu_0 \boldsymbol{M} \times \boldsymbol{H}_{eff}$. In nanowires and in a 1-D approximation, this means that a magnetic field applied parallel to the long axis of the nanowire (the longitudinal field component) causes DW magnetization, which is orthogonal to the field, to start to precess out of plane. This, in turn, creates an out-of-plane demagnetization field that acts upon the DW's remaining in- plane component of magnetization and causes it to precess towards alignment with the applied field direction, expanding the magnetic domain in this process.[57]

However, empirical evidence indicates that when samples are subjected to an external field, magnetization tends to align itself parallel to it. In order to explain the dynamics of this energy minimization process, a term that accounts for various local dissipative phenomena $\frac{\alpha}{M_s}\boldsymbol{M} \times \frac{d\boldsymbol{M}}{dt}$ is included. This contribution takes the form of an addition to the effective field leading to a spiral trajectory towards equilibrium as depicted in Fig. 2.11 (b).

Field induced dynamics of DWs and Walker breakdown

This section presents an introduction to domain wall dynamics, starting with the basic scenario of a domain wall moving parallel to an external field due to the expansion of a domain. Energy dissipation arguments derived directly from the LLG equation are employed for this purpose. 180° domain walls can be moved also by different means (e.g. electrical currents[58]) and their dynamics under an effective field is described by Eq. 2.33. Numerical integration can be used to solve the equations of motion governing a 180° domain wall in an infinitely large uniaxially anisotropic medium (i.e. a magnetic wire) subjected to a uniform DC magnetic field. A solution for this problem, using a 1D model for DWs can be found in Ref.[59] Here we limit ourselves to a phenomenological description.

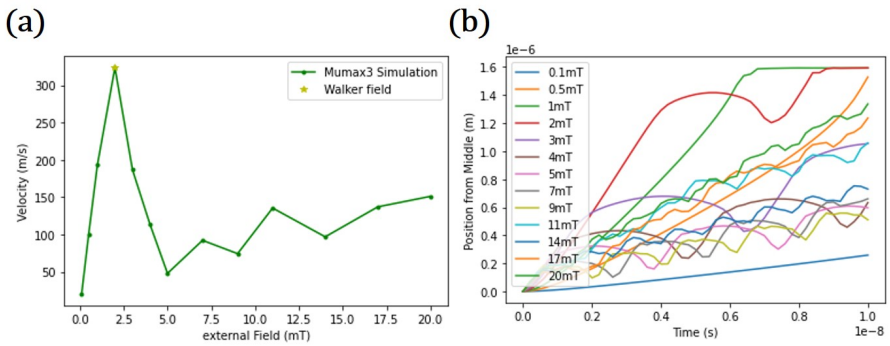

Figure 2.12: (a) transverse DW velocity as a function of the driving external magnetic field in a nanowire. (b) DW position as a function of time, different traces indicate the trajectory under different applied eternal magnetic fields. The values are obtained with micromagnetic simulations. The parameters used are the ones of Permalloy and the "ideal" system geometry considers a wire 10 nm thick and 100nm wide. The DW velocity was computed using the average magnetization component along x for a fixed computation time.

It is demonstrated that for low applied fields (yet larger than the pinning potential coming from defects in the system), the wall motion gradually converges to a steady-state solution, where the wall is only moving in the field direction and the velocity is constant[59]

$$v_0 = \frac{\gamma\Delta}{\alpha}\boldsymbol{H}_{ext} \tag{2.35}$$

where γ is the gyromagnetic ration and Δ is the domain wall width. In this linear regime, velocity is proportional to the applied field $\boldsymbol{H}_{ext}$. Let us considered a Permalloy wire, 10 nm thick and 100 nm wide simulated in Fig. 2.12. This linear regime is present in Fig. 2.12 (a) for an external field up to 2 mT. However, as can be seen from Fig. 2.12 (a), Eq. 2.35 is valid only for applied fields lower than a critical field $H_w = 2\pi\alpha M_s$ at which the DW velocity drops. This field is called Walker field and the sudden velocity decrease is called Walker breakdown. For fields above $\boldsymbol{H}_w \simeq 2.5$ mT, the magnetization processes around the field, leading to the emergence of a periodic component in the wall's forward motion. This oscillatory behavior can be seen in the plot of Fig. 2.12 (b) where the DW position is plotted as a function of time for different values of the applied field. In the condition where $\boldsymbol{H}_{ext} >> \boldsymbol{H}_w$, after the reduction of velocity, the velocity is followed, again, by a linear increase.

The vortex DW similarly possesses a velocity vs. field dependence that is comparable with the one of the transverse domain wall. Also for vortex walls large magnetic fields continuously transform the wall structure, causing an annihilation of the vortex at the edge that represent the expulsion of the vortex core from the geometric constrain.[60] This constitutes the limiting factors in the DW velocity above Walker breakdown and then the propagation at crossing of nanowires.[61,62]

In order to have fast field-driven DW motion and stabilize the wall spin structure, different approaches have been used such as geometry modulation[63,64] temperature[65] and strain gradients.[66]

2.3.3 Micromagnetic energy for domain walls - 1D model

The one dimensional model to describe a DW has proven to be a valuable technique for explaining the micromagnetic findings and interpreting experimental results. After its introduction by Walker and Slonczewski[67] numerous authors have made contributions to incorporate various factors such as pinning of various origins and thermal effects.[68,69] In this thesis, 1D model calculations are performed to extract the domain wall energy in the strain profile created by the etched areas in the SiN (see Sec. 5.2). The 1D strain profile, ε_{xx} and ε_{yy} is calculated form COMSOL simulations. Considering that the magnetoelastic energy is given by

$$u_{ME} = B_1 \left(\varepsilon_{xx} m_x^2 + \varepsilon_{yy} m_y^2\right) \tag{2.36}$$

the DW energy (per unit area) as a function of the DW position, x_0, can be calculated by convolution with the DW profile in the nanowire

$$U_{DW}(x_0) = B_1 \int \left[\varepsilon_{xx} m_x^2 (x - x_0) + \varepsilon_{yy} m_y^2 (x - x_0)\right] dx, \tag{2.37}$$

where B_1 is the magnetoelastic constant, and m_x, m_y are the x and y component of the magnetization, respectively. The magneto-elastic field is then trivially the first derivative of the magneto-elastic energy according to[70]

$$B_{ME} = -\frac{1}{M_s} \frac{du_{ME}}{dx}. \tag{2.38}$$

Between two uniformly magnetized domains, the analytical profile of the wall considered is

$$m_x(x - x_0) = \cos\left[\tan^{-1}\left[exp\left(-\frac{x - x_0}{w/2}\right)\right]\right] \tag{2.39}$$

for the x and

$$m_y(x - x_0) = \sin\left[\tan^{-1}\left[exp\left(-\frac{x - x_0}{w/2}\right)\right]\right] \tag{2.40}$$

for the y component of magnetization, respectively. Here w is the wire width.

The analytical profile for the DW used is that of a 1D domain wall of width $\delta = w/2$. The crude approximation is well justified by the following assumptions: firstly, a vortex DW extends over an area $\simeq w^2$ (Figs. 2.13 (a) and (b)), so the effective width is $\simeq w$. Secondly, the magnetoelastic energy is only sensitive to the net m_x and m_y components of magnetization. Consequently, except for the vortex core (which occupies a very small area) a vortex wall and a (triangular) transverse wall of the same width (Fig. 2.13 (c)) have the same net m_x and m_y. Eventually, following the same argument, a triangular transverse wall of width w and a 1D transverse wall of width $w/2$ (Fig. 2.13 (d)) have the same net m_x and m_y. In this model, it is assumed that exchange and magnetostatic energies do not change as a function of the DW position. In other words, we are assuming that the DW is not deformed as it moves through the strain profile.

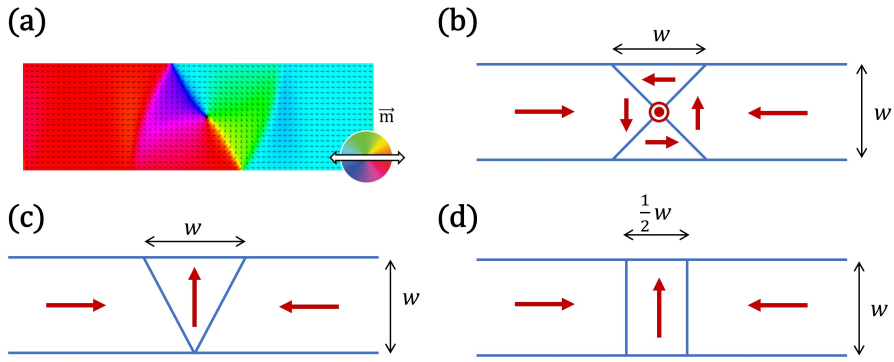

Figure 2.13: Simulated profile of an in-plane vortex wall in a wire whose width is w (a) and schematic representation of it (b). (c) triangular wall of width w and (d) transverse wall of width $\frac{1}{2}w$. This case considers material parameters of Permalloy and a geometry of 30 nm thickness and 300 nm width for the wire.

In this way, the profile of the DW energy (per unit area) as a function of the DW position can be calculated. Additionally, the magnetoelastic field acting on the DW is straightforwardly obtained by deriving the DW energy profile in Eq. 2.37. For the calculations, the same material parameters used in Mumax simulations are considered.

2.4 Strain and mechanical deformation

It is virtually always the case that stresses are present in thin films and those stresses exist even though films are not externally loaded. The main area of interest in the mechanical properties of thin films concerns the negative effects that stress can have on films. For instance, film stresses influence band-gap shifts in semiconductors,[71] transition temperatures in superconductors,[72] and magnetic anisotropy.[73]

This has led to extensive research on the type, source, and extent of stress in thin films, as well as methods to reduce or manage it, while improving the mechanical properties of hardness and wear resistance for various coating applications. Also the packaging and attachment of semiconductor chips to circuit modules and boards, is known to cause structural-mechanics deformations.[74] The topic of stress in thin films has historically received the most attention and is the primary focus of this section.

2.4.1 Mechanical properties of materials and elastic regime

A wealth of knowledge about the mechanical properties of bulk materials exists, which can aid in understanding how thin films behave. The elastic regime represents one end of the spectrum and is based on the theory of elasticity, forming the foundation of structural mechanics and engineering design. In this regime, material strains are directly proportional to applied stresses and are reversible upon unloading. The other end of the spectrum is characterized by irreversible plastic effects induced when stress levels exceed the elastic limit[42](i.e. rolling, extrusion, fatigue, and fracture are manifestations of plastic-deformation effects). Unlike elasticity, plasticity is difficult to model mathematically due to the intrinsic non-linearity and hysteresis. In this section, the description of the mechanical behavior is limited to the elastic regime.

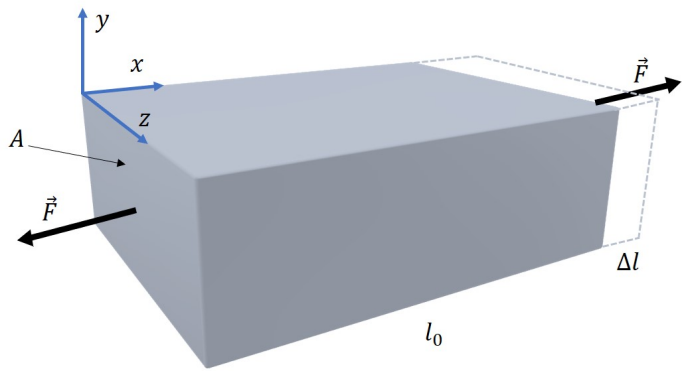

Figure 2.14: Tensile force $\boldsymbol{F}$ applied to a plate producing a change in the dimension from l_0 to $l_0 + \Delta l$.

Let us consider the situation depicted in Fig. 2.14, where a plate is stretched by equal and opposite forces F. When external forces are applied to a body's surface, they act directly on the surface atoms and are transmitted indirectly to the internal atoms through the network of bonds that are distorted by the stress field that develops inside. This distribution of internal forces throughout the plate results in a state of stress. In the depicted example, the tensile stress σ_x is defined as the normal force $\boldsymbol{F}$ divided by the area A. Similarly, normal stresses in the other two coordinate directions, σ_y and σ_z, can be envisioned under more complicated loading conditions. If the force is directed into the surface, a compressive stress arises, which is assigned a negative sign conventionally, in contrast to the positive sign for a tensile stress.

Applying tensile forces to the plate shown in Fig. 2.14 causes it to expand in the x direction by an amount Δl, resulting in a normal strain ε_x, which is defined as

$$\varepsilon_x = \frac{\Delta l}{l_0}, \tag{2.41}$$

where l_0 is the original length. Similarly, in other directions, the normal strains are ε_y and ε_z. Despite there being no stress in the y and z directions, the plate contracts laterally in those directions in conjunction with the longitudinal extension in the x direction. As a result, there is a strain in the y direction, denoted by $\varepsilon_y = -\nu\varepsilon_x$, and a strain in the z direction, denoted by $\varepsilon_z = -\nu\varepsilon_x$, where ν is Poisson's ratio, a measure of the lateral contraction of the material. Poisson's ratio typically has a value of around 0.3 for many materials. When subjected to shear stresses, the material experiences shear strains with mixed terms, e.g. ε_{ij}, which are essentially defined by the tangent of the shear distortion angle. In the elastic regime, all strains are small, and the system's response is dominated by Hooke's law

$$\sigma_x = Y\varepsilon_x, \tag{2.42}$$

where Y is the Young's modulus. If a three dimensional state of stress exists the following relation stands

$$\varepsilon_x = \frac{1}{Y}\left[\sigma_x - \nu(\sigma_y + \sigma_z)\right], \tag{2.43}$$

and can be extended analogously for ε_y and ε_z. The case of shear stress is similar, and reflects the case of mechanical equilibrium on internal surfaces cut at an arbitrary angle. This generally includes forces and stresses directed in the plane itself. For shear stresses γ_{ij}, Hooke's law also applies in the form

$$\tau_{xy} = Y\gamma_{xy}, \tag{2.44}$$

where τ_{ij} is the shear strain. This derivation is valid for isotropic materials, where the relation for the shear modulus $\mu = Y/2(1+\nu)$ stands. In anisotropic media, the elastic constants reflect the non-cubic symmetry of the crystal structure and have a tensorial form. A full description can be found, for example, in Ref.[75]

2.4.2 Origin of intrinsic stresses during thin-film growth

Thin-film materials have significant applications in various technological fields, such as microelectronics, photonics, magnetic devices, and surface coatings. However, due to the use of different fabrication and post-processing methods and varying intrinsic material properties, thin films often experience stress and strain imposed by their substrates. The origin of such stresses may be associated with several factors,[76] including: different thermal expansion coefficients of film and substrate, differences in lattice spacing, interatomic spacing or crystal size dislocations and re-crystallization processes. When a thin film and a substrate have different thermal expansion coefficients, temperature changes during film deposition and post processing will produce stress and strain, which are called thermal stress and thermal strain. The stresses resulting from the internal structure of a material during its deposition is generally regarded as intrinsic stresses (i.e. stresses that are present even without an external load) and are discussed in the current paragraph.

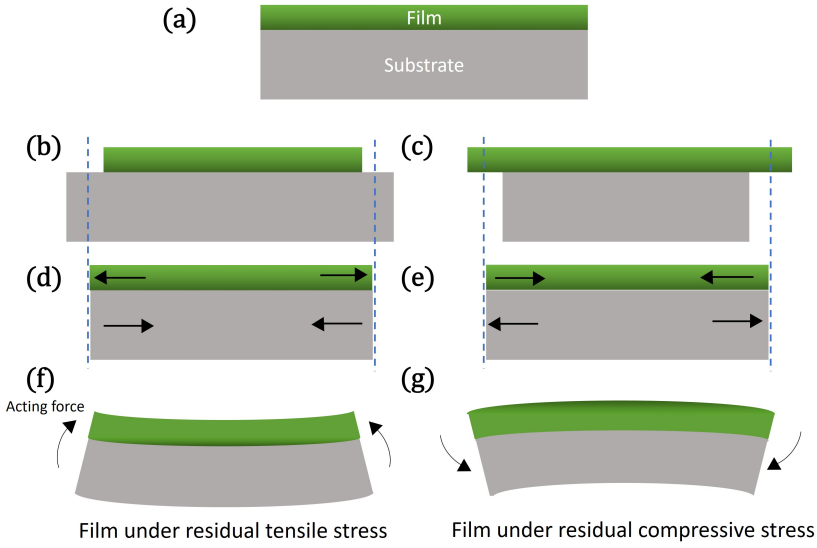

Figure 2.15: Schematic representation of the generation of built in stress during thin film deposition. The film is deposited at high temperature and cover the whole surface of the wafer (a). After cool down, the different thermal expansion coefficients of the film and the substrate causes different contraction (b) - (c). To conform to the film adhesion, forces are acing in the films (shown with black arrows) (d) - (e). These steps can lead to (f) residual tensile stress in the film or (g) residual compressive stress in the film.

In this thesis, the samples fabricated on a 5" wafers are covered with a SiN layer using Physical Vapor Deposition (PVD). This is commonly done in sensor and semiconductor industry to protect the chip from humidity and oxygen coming from the environment. The deposition of SiN on substrates is performed at high temperatures (250°C) during PVD processes and the film covers the wafer surface entirely, as shown in Fig. 2.15 (a). As the film/substrate composite cools down to room temperature, they undergo different amounts of contraction due to varying thermal expansion coefficients as shown in Fig. 2.15 (b) and (c). The film then experiences elastic strain in order to conform to the substrate and remain attached (Fig. 2.15 (d) and (e)), resulting in the combination of substrate and film bending (Fig. 2.15 (f) and (g)). If each layer of the thin film is assumed to be a linear elastic material, and the film/substrate system experiences minimal deformation during temperature changes. The thermal stresses σ_T that arise from this process are then described by Hooke's law

$$\sigma_T = Y\alpha(T - T_0), \tag{2.45}$$

where α is the coefficient of linear thermal expansion, Y is the Young's modulus (both assumed constant along the temperature change), T_0 and T are the initial and final temperatures. When the film and the substrate are together, mismatch forces arise at the interface to maintain the bonding states as schematically shown in Fig. 2.15 by the arrows direction. Regardless of the stress distribution that prevails, to maintain mechanical equilibrium the net force and the bending moment on the film - substrate cross section should compensate.[76] According to Fig. 2.15, two types of behavior are expected.

Considering Fig. 2.15 (f), the initial behavior of a growing film can cause it to shrink relative to the substrate. However, compatibility requires both the film and substrate to have the same length, resulting in the film being constrained and stretched while the substrate contracts. Tensile forces in the film are counteracted by compressive forces in the substrate, but unbalanced end moments prevent the combination from achieving mechanical equilibrium. If the film-substrate pair is not restrained, it elastically bends to counteract the unbalanced moments, causing films with internal tensile stresses to bend the substrate concavely upward. Conversely as shown in Fig. 2.15 (g), films that initially expand relative to the substrate develop compressive stresses that bend the substrate convexly outward. These results are general, regardless of the specific mechanisms causing film stretching or shrinking. The residual stress after material deposition can be calculated measuring with a laser the curvature of the substrate using a wafer bow.[77] The relationship between the radius of curvature and the internal stress σ is given by the Stoney formula[78] derived for our geometry (see Ref.[76] pp.418-420)

$$\sigma = Y\left[\frac{(R \pm d/2)\theta - R\theta}{R\theta}\right] = \pm\frac{Yd}{2R}, \tag{2.46}$$

where R is the beam radius of curvature, θ is the angle subtended and d is the film thickness. In the presence of a uniform stress inducing film, the stress distribution is also uniform, however, removing selected areas of the film (e.g. using reactive ion etching) locally relieves some of the stress at the interfaces, causing non-uniform stress. This phenomenon is predicted by finite element method simulations and confirmed experimentally within the work reported in the experimental chapter of this thesis, Sec. 5.2.

2.4.3 Voltage controlled strain - Piezoelectric effects

Piezoelectricity is a phenomenon that occurs in certain materials, which generates an electrical charge in response to mechanical stress or strain. In the same materials, an application of voltage alters the physical dimensions. This property has been exploited in a variety of applications, including sensors,[79] actuators,[80] and energy harvesting devices. With the deposition of magnetic materials onto piezoelectric substrates, the magnetization can be manipulated using electric field induced strain.[81]

Piezoelectric materials exhibit electrical polarization when subjected to mechanical stress. At the microscopic level, the displacement of atoms within the crystal's unit cell under deformation leads to the creation of electric dipoles in the medium. In specific crystal structures, this results in an overall macroscopic dipole moment or electric polarization. This phenomenon, referred to as the direct piezoelectric effect, is always accompanied by the converse piezoelectric effect, whereby the material becomes strained when exposed to an electric field. The coupling between the electric field and strain within a piezoelectric is determined by the constitutive relation in the strain-charge form

$$\begin{aligned} \boldsymbol{\varepsilon} &= \boldsymbol{s_E}\boldsymbol{\sigma} + d^T\mathbf{E} \\ \mathbf{D} &= \boldsymbol{d}\boldsymbol{\sigma} + \varepsilon_0\boldsymbol{\varepsilon_r}^T\mathbf{E}. \end{aligned} \tag{2.47}$$

In Eq. 2.47 $\boldsymbol{\varepsilon}$ is the strain, $\boldsymbol{\sigma}$ the stress, $\boldsymbol{E}$ the electric field and $\boldsymbol{D}$ is the electric displacement field. The material parameters $\boldsymbol{s_E}$, $\boldsymbol{d}$, and $\boldsymbol{\varepsilon_r}$, correspond to the material compliance, the coupling properties (or piezoelectric coefficients) and the permittivity. Those parameters have tensorial form (of rank 4, 3

and 2 - in order) but are highly symmetric for physical reasons, and they can be represented as matrices. For instance, the $\boldsymbol{d}$ tensor contains only 18 independent elements and can be written as a 3 by 6 matrix. According to the symmetry of the system, several matrix elements are zero, and eventually only few coefficients are sufficient to describe the piezoelectric properties of the material of interest, as described in the following paragraph.

2.4.3.1 Lithium niobate

In this thesis, the ferroelectric material lithium niobate ($LiNbO_3$) is used as a piezoelectric substrate. Lithium niobate is a human-made dielectric material that does not exist in nature. It is widely used in integrated and guided-wave optics and for the application of acoustic waves, as it is characterized by large piezoelectric coefficient. Details about the $LiNbO_3$ trigonal crystal structure are beyond the scope of this thesis, and can be found for example in the work of Weis et al.[82]

The piezoelectric effect in lithium niobate - with a 128° Y-cut, the one used in this thesis - can be described by four independent coefficients d_{15}, d_{22}, d_{31} and d_{33}. Measured values for these quantities are presented in Table 2.2.

d_{15}	d_{22}	d_{31}	d_{33}	
6.92	2.08	-0.085	0.6	Ref.[83]
6.8	2.1	-0.1	0.6	Ref.[84]
7.4	2.1	-0.087	1.6	Ref.[85]

Table 2.2: Piezoelectric strain coefficients of $LiNbO_3$ [$\times 10^{-11}$ C/N]. The values reported here are the ones relevant for a 128° Y-cut of the crystal used in this thesis.

Rotated cuts of quartz $LiNbO_3$ are suitable for the generation of surface acoustic waves.[86,87] A periodic electric field is produced when an RF source is connected to the electrode, thus permitting piezoelectric coupling to a traveling surface wave. There are therefore components of atomic displacement in the x and y directions that vanish at few wavelengths from the surface.

Variable strain - time and space dependent

In this thesis, a piezoelectric substrate is used to generate surface acoustic waves (SAW, see experimental chapter, Sec. 5.3). According to the scheme presented in Fig. 2.16 (a), this method involves launching two counter-propagating surface acoustic waves (SAWs) into a piezoelectric substrate using a set of interdigitated transducers (IDTs). This process creates a stationary stress/strain wave (SW)

between the transducers. In this paragraph, the strain profile of the strain waves that can be generated using IDTs[86] on a PZT substrate is presented.

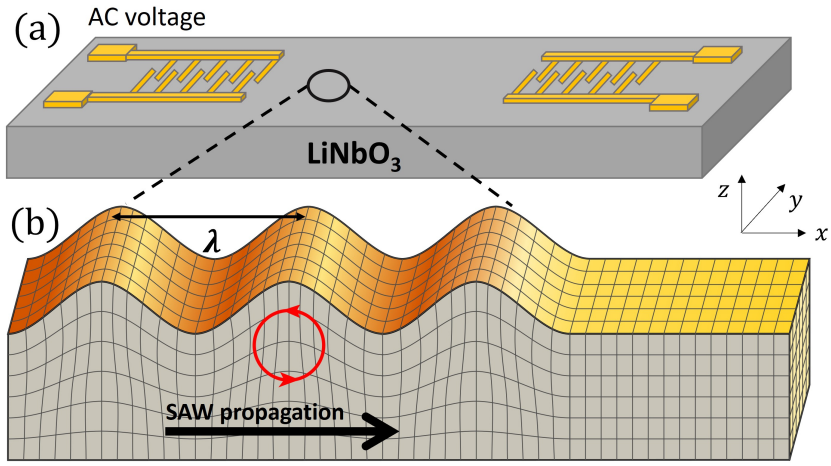

Figure 2.16: (a) Schematic representation of a pair of IDTs that can generate, upon AC voltage excitation, surface acoustic waves in a piezoelectric material. (b) Profile of a propagating Rayleigh wave / surface acoustic wave showing the position of node and anti-nodes at a distance λ between each other. The standing wave is the result of two counter propagating waves. Adapted from: commons.wikimedia.org.

If we assume that the SAWs take the form of pure Rayleigh waves, one can neglect the higher order piezoelectric corrections and solve the Rayleigh equation for a material with the elastic proprieties of an isotropic material.[87,88] If the same AC voltage with a frequency f_{IDT} is applied to the IDTs the form of the two counter-propagating stress (σ) waves is, accordingly

$$\begin{pmatrix} \sigma_{xx} \\ \sigma_{yy} \\ \sigma_{zz} \\ \sigma_{xy} \\ \sigma_{zx} \\ \sigma_{yz} \end{pmatrix} = \boldsymbol{A_{SAW}} \begin{pmatrix} sin(kx \mp \omega t) \\ 0 \\ -sin(kx \mp \omega t) \\ 0 \\ -\frac{3}{8} sin(kx \mp \omega t \pm \frac{\pi}{2}) \\ 0 \end{pmatrix}. \tag{2.48}$$

Here $\boldsymbol{A_{SAW}}$ is the amplitude of the stress wave, as determined by the strength of the excitation to the IDTs, $k = \frac{2\pi}{\lambda}$ (λ resonant wavelength of the stress wave), $\omega = 2\pi f_{IDT}$. Physically, Eq. 2.48 describes a rolling motion on the surface of the substrate and this profile of time variant and space variant strain can be visualized in Fig. 2.16 (b) by the red arrows. This rolling motion causes each point on the surface to trace an elliptical orbit within the x-z plane.

Therefore, the strain profile on the sample constitutes a series of nodes and anti-nodes, at a distance λ oscillating with a frequency ω.

3

Experimental techniques

This chapter describes and briefly introduces the experimental techniques used in this thesis work.

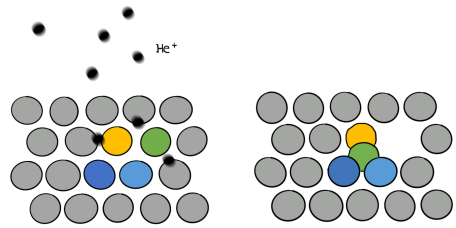

Contents

3.1 Sample fabrication

The realization of micro to nano-structures typically consists of a series of steps that, as a whole, go under the name of Nanofabrication. These Nanofabrication processes can follow a bottom-up (e.g. self-assembly) or a top-down (e.g. lithography) approach.[89] In the present work only lithographic methods are used, and the fabrication steps will be discussed in the following subsections.

3.1.1 PVD - Material deposition

Physical vapor deposition (PVD) methods[90] are processes for atomistic deposition in which the material is removed by a solid source (target) in forms of atoms. This material is subsequently moved by ballistic scattering through a vacuum or low pressure background atmosphere to a substrate where it then condensates. The DC magnetron sputtering technique is a type of PVD process used for the material deposition for metal and oxides in thin layers. In Fig. 3.1 a schematic of material deposition via magnetron sputtering method is shown.

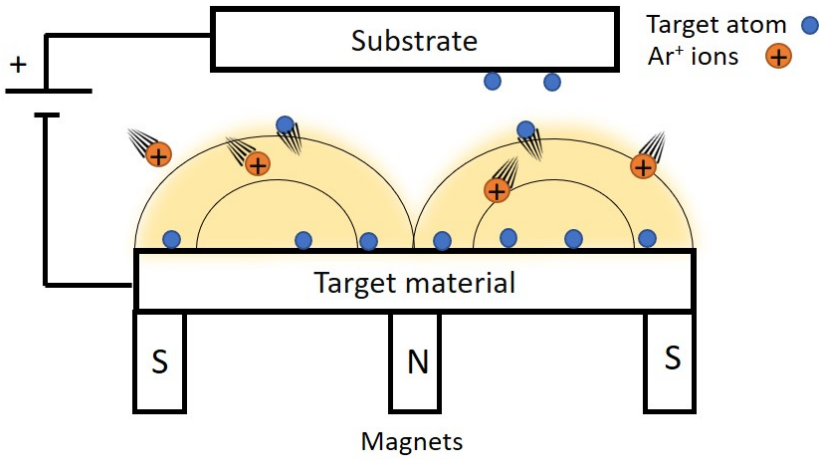

Figure 3.1: Schematic of the inside of a magnetron sputtering tool. A strong electric field is applied across the target and the sample that accelerate the ionized Ar^+ atoms to the target, thus sputtering the target atoms. The magnets on the back side of the target are used to confine the plasma and increase the sputtering rate.

Sputtering deposition exploits the kinetic energy of the ions of inert gases (e.g., argon or helium) that are accelerated by a DC voltage between substrate and target. The strong collision of these energetic ions with the target ejects target metal atoms into space. To increase the mean free path and ensure defect free deposition of the film, the process is performed at a typical base pressure of 10^{-8} mBar before injecting the inert gas into the chamber. These metal atoms are then deposited on the substrate material forming a metallic film. If the mean free path of the atoms is long enough, the ejected material recombines on the sample surface and agglomerate. The process is continued until the formation of a polycrystalline or film. Metals are easily sputtered in a DC configuration, on the other hand, insulators need to be sputtered in the AC settings (using RF voltage). This is due to the insulating nature of the target materials and to charge accumulation.

The target composition can be a single element, or an alloy - e.g. NiFe - and the sample can be rotated during deposition to improve the film uniformity. In general, the atomic composition of the alloy on the sample will reflect the one of the target. If the geometry of the sputtering chamber allows, the deposition of alloy of arbitrary composition is possible. To obtain this, a DC acceleration voltage is applied to different targets simultaneously, so that the different species will recombine on the sample surface - with a deposition rate proportional to the power applied to the target.

For our samples, we used the magnetron sputtering configuration. The name is due to the magnet that is added in this configuration at the back of the target. The generated magnetic field has the role of confining the plasma in the close proximity of the target. The electrons, confined by the magnetic field lines, provide a larger number of collisions with the Ar gas in the proximity of the target, creating a denser plasma and a higher deposition rate. The most advanced sputtering machines like the Singulus tool[91] used to fabricate most of our layers, have extraordinary precision, allowing deposition of sub-nanometers layers even in the amorphous phase.

Some of these machines, optimized for the deposition of magnetic materials, have the options to apply a uniform magnetic field across the substrate during sputtering,[92] that can be in the order of 10 mT. According to Fig. 3.2, two possible configurations of magnetic field are possible. In the first one (Fig. 3.2 (a)), the substrate where the target atoms will form the film is not rotated. If the magnetic material is soft enough, the magnetization of the clusters formed during growth will be well defined. Accordingly, a preferential direction of magnetization (easy axis) can be induced during growth in a static magnetic field in material such as $Co_{40}Fe_{40}B_{20}$ and Permalloy. If instead, the sample is rotated as indicated in the schematic of Fig. 3.2 (b), the magnetization of the magnetic layer will continuously change orientation during sputtering. As

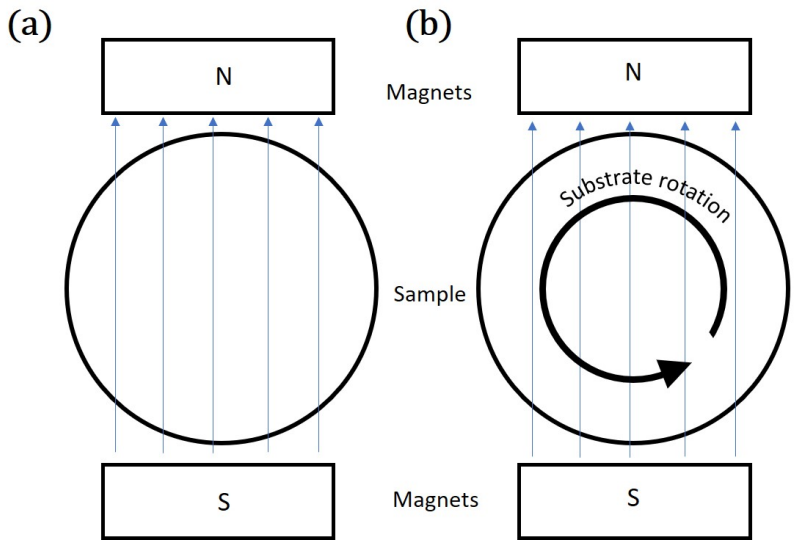

Figure 3.2: Schematic of top view of the substrate holder inside a magnetron sputtering tool, where a magnetic field is applied across the plane of the sample. (a) the magnetic field is static in the frame of reference of the substrate, which is not moving. (b) the sample is rotating with constant speed in the constant magnetic field imposed by the magnets across the sputtering chamber.

a result no preferential direction of magnetization will be induced by growth. On the contrary, the film anisotropy can be reduced. These configurations of magnetic fields during deposition are used in the work presented in Sec. 5.1.[93]

3.1.2 Lithography and structuring

In this section, a description of the two methods of lithography can be found: the photolithography and electron beam lithography. These two nanofabrication methods make use of a patterned resist, that will be described first. The detailed recipes used for fabrication are reported in the appendix of this thesis, Chap.A.

Lithography involves the patterning a surface through exposure to light, laser, or electrons followed by etching and or deposition of the material to form the desired structure.

Fig. 3.3 schematically shows the different steps involved during a lithographic process. Starting from the bare substrate - Fig. 3.3 (a) - structures with a

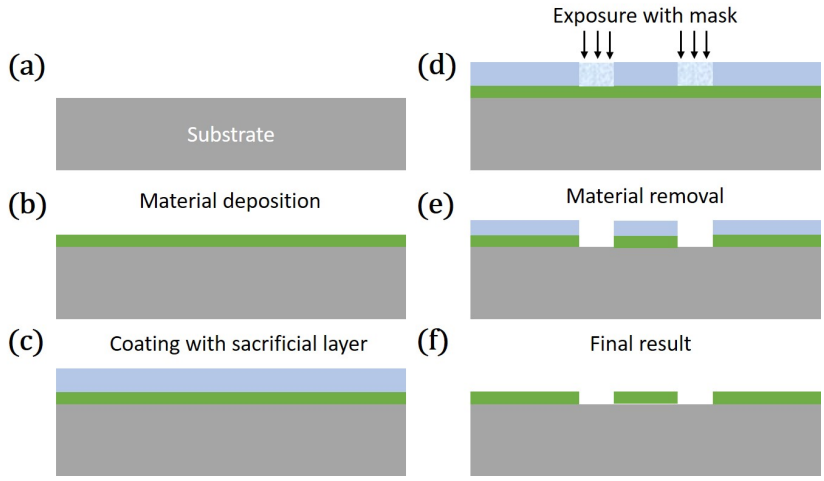

Figure 3.3: Schematic illustration of the process on lithography for the realization of micro to nano-structures on top of a rigid substrate. The substrate (a) is coated with the desired material (b) and with a sacrificial layer (c). At this point, the desired design is patterned first on the sacrificial layer (d) and then on the material (e) where selected areas are removed to obtain the final result (f).

resolution of tens of nm can be realized. A lithographic step can be repeated to create more complex structures.

3.1.2.1 Resist coating

As already presented in Fig. 3.3, the patterning of micro to nanostructures uses a sacrificial layer made of a polymeric matrix diluted in a solvent. This is commonly called resist and is used in the following steps like ion milling as a covering mask.

The definition of such mask starts with the coating of a uniform layer of resist on top of the sample. This step is called *spin coating* and consists in spreading the resist using the centrifugal force. The polymer+solvent is deposited on the sample surface in liquid form. By rotating the sample up to 5000 rpm the resist is distributing on the surface with a constant thickness, which is mainly defined by rotation speed and acceleration during spin-coating. At the same time, the solvent evaporates during the spinning making the polymer solid. An additional baking (c.a. 80-120°C) is usually performed to harden the resist. When the resist is coated on the sample different irradiations can be used to pattern it, step shown in Fig. 3.4 (a).

There are mainly two types of resist for lithography: the positive resist and the negative ones. A positive resist is made of long polymeric chains. When irradiated, the long chain will be divided in monomers. Accordingly, the portion of the resist that is exposed to radiation becomes more soluble to the resist developer. The unexposed portion of the resist remains insoluble to the resist developer. A negative resist instead, reacts to external radiation in the opposite way. This time the portion of the resist that is exposed to radiation becomes less soluble to the resist developer, and will stay after the development process. Figs. 3.4 (b) and (c) show the sample after development realized with a positive and negative resist, respectively. The same lithography mask is considered.

3.1.2.2 Patterning methods

Optical lithography

Optical (Photo) lithography is used in almost every aspects of modern microfabrication technology. The possibility to pattern arrays of nano-structures over large areas (wafer scale) in short time, is one of the reasons why this technique is widely used in industry-level production. Advances in this field have allowed to improve the resolution of the conventional photolithographic techniques, which is restricted by the diffraction limit.[94,95]

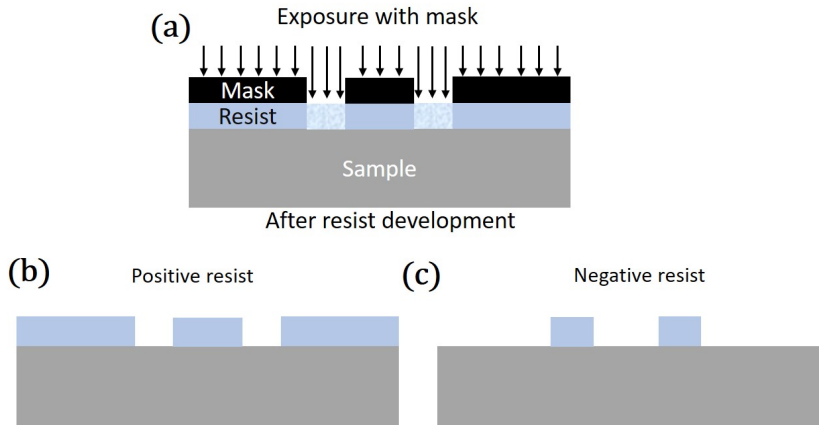

Figure 3.4: Schematic of the lithography step consisting in the resist exposure through a mask (a) and development (b) and (c). The dark rectangles indicate sections that are not transparent to Ultra-Violet light. Positive (b) and negative (c) resist on a sample after development. The exposed area is the same.

During optical lithography, the source of radiation that changes the resist properties locally are photons. To improve lateral resolution (diffraction limit),

UV light is typically used. Similarly to a conventional optical microscope, the light is guided through a path until it reaches the sample's surface. A mask, containing a non-transparent material (typically a metal like tungsten or chromium) shaped in the matrix to be imprinted, is placed in this optical path. The transfer of the pattern from the mask is then made onto the resist as shown in Fig. 3.4 (a). After the exposure of the resist, the resist is developed in a specific solvent, which dissolves the irradiated regions with different speed, compared to the non irradiated ones. Currently, the semiconductor foundries utilizes photons produced by plasma formed by extreme ultraviolet light and liquid immersion to manufacture elements of 10 nm pitch sizes. The tool used here is equipped with a light source of approximately 300 nm wavelength, which leads to a lateral resolution of 200 nm at best.

Electron-beam lithography

In many applications high resolution of sub-10 nm nanostructures is beneficial and sometimes required. For this reason, electron-beam lithography (EBL) is often used - especially in research and development - for its flexibility (mask-less patterning) and high resolution.[96,97] The wavelength of the electron (around 7 pm for an acceleration voltage of 30 kV) is much smaller than the one of the UV photons (300 nm), as a consequence the lateral dimensions of the structures that can be realized is massively reduced. Still the resolution of EBL is limited to few nm, limit imposed by the collimation and focusing of the electron beam.

The use of electrons for lithographic purposes is due to the fact that resists are not only sensitive to photons, but also to an incoming beam of electrons. EBL patterning can be described as follows. The sample coated with photo-resist is loaded in a vacuum chamber on a moving stage, that faces the electron gun. A beam of electrons is generated starting from a metallic filament and accelerated with acceleration energies in the range of few to tens of kV. The beam is then collimated with magneto-static lenses and can be focused on the sample surface. The beam of electrons can be deflected, exposing areas of the resist, according to the desired structures to be patterned. The great advantage of EBL is that no expensive mask is required, and any design can be quickly implemented. The major drawback of this technique, with respect to optical lithography, is the much longer exposure time.

3.1.2.3 Ion beam etching

Ion-beam etching is a technique in which the full surface of a sample is bombarded by a collimated beam of highly-accelerated ions. In a similar fashion

to sputtering, the highly energetic ions transfer kinetic energy to the surface atoms, that are subsequently removed. This time, as shown in Fig. 3.5 (a) the voltage is applied to the sample instead of the target. The etching rate - the amount of material that is removed from the surface in the unit time - is in general material dependent. If a hard mask is introduced using resist as in Sec. 3.1.2 with a etching rate much smaller than the material to be patterned, structuring is possible, as the material protected by the resist will survive the etching.

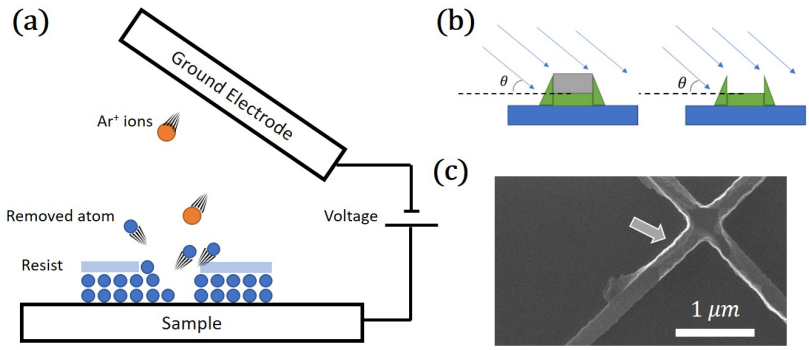

Figure 3.5: (a) Schematic of the inside of an ion milling tool during the carving of a wafer. The resist protects of the underlying material and allows the transfer of the desired structures to the material. (b) schematic representation of the fencing, created by re-deposition on the resist. (c) Scanning electron microscope image of a nanowire after etching. The re-deposition is indicated by the arrow.

The ion beam etching that is performed to create the devices used in this thesis is done using Ar^+ ions, and a rotating sample holder to promote homogeneous material removal.

A common phenomenon in nanofabrication is the formation of "sidewalls" after the etching step. This occurs especially for thick films and tiny structures. As shown in Fig. 3.5 (b) some of the removed material tends to re-deposit on the side of the resist building a vertical thin layer (mixture of your film and the substrate mostly). Typical solvents (e.g. Acetone) will dissolve the resist but leave the re-deposited material on top (Fig. 3.5 (c)). The formation of the sidewalls cannot be completely avoided, however, it can be reduced or partially removed tuning the parameters of the ion etcher. As schematically shown shown in Figs. 3.5 (a) and (b) the incidence angle of the incoming ions (in this case Ar) is not necessarily normal to the sample surface. Large angle (80°/90°) give straight and sharp profile, but also higher re-deposition (sidewalls) intermediate angles (50°) will lead to lower re-deposition rate, but also high etching rate and less sharp profile. The etching recipe (reported in the appendix of this thesis, Chap. A) can be optimized to reduce fencing using

different angles of the incident ions beam.

Mechanical removal can be also used to remove the fences created during etching e.g. a jet of high pressure CO_2 (*cryogenic dry cleaning*, more info at bruker.com).

3.2 Post-deposition material preparation

In thin films, the deposition conditions are not the sole degree of freedom for tailoring the material properties. Post deposition techniques like thermal treatments (annealing) or implantation of ions in the film are commonly used to promote crystallization,[98] rearrange atomic position,[99] dope the material[100] and for interface engineering.[101] In this sections, thermal annealing and ion irradiation are discussed as techniques for tailoring magnetic properties.

3.2.1 He^+ irradiation

Ion irradiation[102] is a technique for the modification of thin films properties by bombarding a target surface with high energy ions. The process involves the displacement of atoms in the film leading to different results, that will depend on the type of ion used for irradiation, its fluence and acceleration energy. As an example, formation of defects, disorder in the crystal structure but also increase in grain size and material texturing[103] are possible. When applied to thin magnetic films, ion irradiation can be used to alter the magnetic properties of the film, such as the magnetic moment, magnetic anisotropy, and domain structure.

An accelerated ion traveling within an atomic lattice can be engaged in two types of collisions: nuclear collisions, involving the nuclei of atoms in the lattice, and electronic collisions, involving the electrons in the solid. These collisions lead to energy loss and deflection of the ion's path as it travels through the lattice. The energy from these collisions is transferred to the atomic lattice through either direct nuclear collisions or indirect electronic collisions followed by electron-phonon coupling. Consequently, collisions increase the kinetic energy of the lattice atoms, enabling their displacement. Depending on the amount and type of energy that is deposited into the crystal, we can identify two regimes.[104] As shown in Fig. 3.6 (a) if primarily nuclear energy is deposited, mostly binary collisions take place between moving particles and stationary

target atoms. When the nuclear energy deposition is very large instead, a lot of ions are moving, and collisions now mostly take place between already moving atoms (cascade collisions) as shown in Fig. 3.6 (b). Accordingly, depending on the selected atomic species to perform irradiation, the ion acceleration energy, and its fluence (number of ions per unit area, ions/cm^2), these two different effects can be expected. In contrast to heavy ions (such as Xe or Pb) most of the structural effects of irradiation with light-ions (such as He^+) can be described by a simple ballistic recoil mechanism model (Fig. 3.6 (a)). During the irradiation process with light ions extended collision cascades are absent and the structural modifications are confined to the vicinity of the ion path in the metal. As a consequence of such a 'soft' irradiation process, the initial crystallographic structure is maintained.

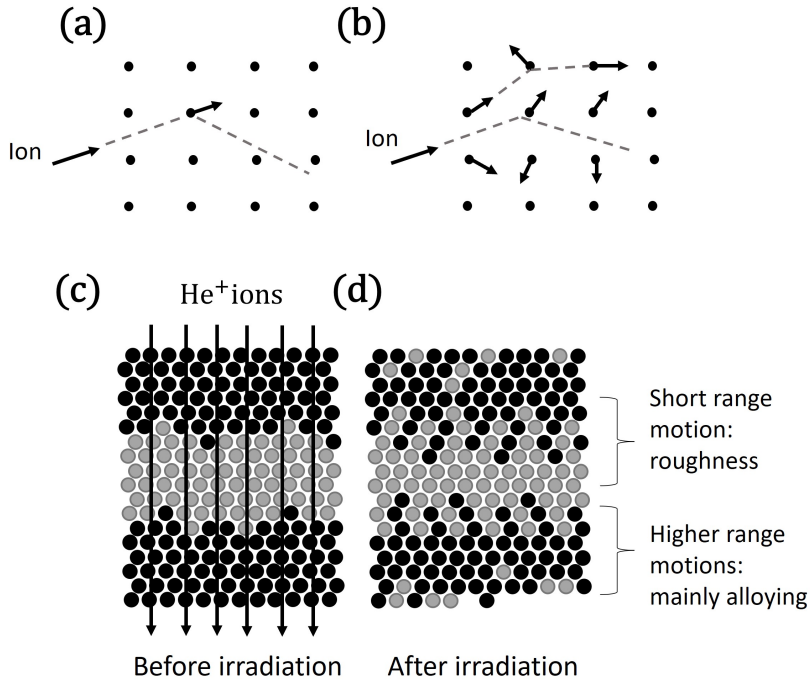

Figure 3.6: Sketches of the two different ballistic energy deposition regimes. (a) A linear collision cascade. (b) Non-linear collision cascade. Qualitative scheme of a sandwich structure before (c) and after (d) irradiation.

Depending on the acceleration energy, the penetration depth of the incoming ion in the target material will vary. If the ions do not have sufficient energy to reach the substrate, they will be implanted into the target layer. In this case, structural modification can be induced.[105] On the other hand, for the ions that have enough energy to penetrate through the whole film and reach

the substrate, the structural effects will be simply ballistic. At low fluences, it has been shown that room temperature irradiation can release strain, whereas, at high fluences, one major structural effect of irradiation is intermixing (Fig. 3.6 (d)).

In the work presented in this thesis, the irradiations on the magnetic material are performed using He^+ ion with an acceleration energy of 20 keV. If films with thickness $\simeq$50 nm are bombarded with helium ions (beam energy of typically 10–30 keV), all ions stop deep in the substrate and the irradiation process involves recoils limited to one (or rarely two) atomic distance(s) leading exclusively to substitution of atoms.[102]

A qualitative scheme of the effects of "soft" irradiation on a multilayer thin film is shown in Figs. 3.6 (c) and (d). As can be seen, displaced atoms moving in the ion direction travel for longer than one inter-atomic distance become isolated and give rise to alloying. Instead, atoms moving in the opposite direction travel for typically only one inter-atomic distance and contribute to roughness (local thickness fluctuations) of the layers. This mechanism can be explained by *Frenkel pair* creation (see Ref.[106] p. 49 for more details) as is shown by Fig. 3.7. The creation of a defect upon energy transferred to the lattice (Fig. 3.7 (a)) caused the presence of a vacancy (Fig. 3.7 (b)), that can either recombine in its original configuration, or can be taken by another atom. The latter is called a replacement collision, or substitution (Fig. 3.7 (c)).

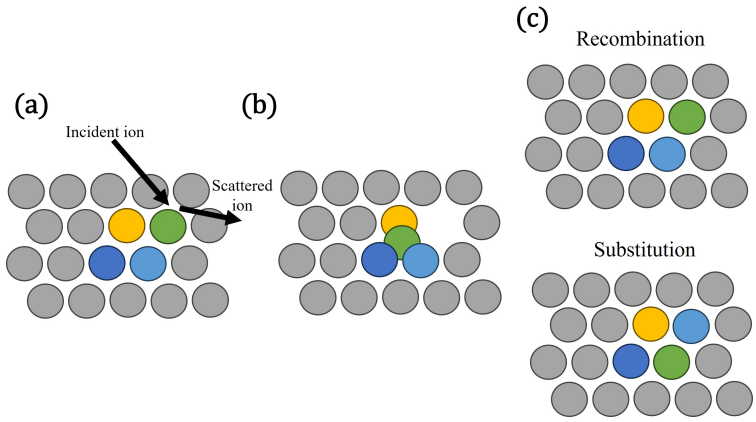

Figure 3.7: Schematic representation of the processes for *Frenkel pair* creation: (a) transfer of energy from incoming ion to the lattice, (b) creation of a vacancy and (c) resulting configuration of atomic position.

Another effect that is observed after ion irradiation in thin films, is the improvement in crystallization.[103] In some studies[107] the crystallite growth during irradiation and implantation is explained by collisions impacts at the grain

boundaries, where atomic rearrangement promotes the growth of the ordered phase. The added atomic mobility due to ion irradiation can induce the crystallization process at lower temperatures compared to annealing. It is worth noting that the orientation of the crystallites promoted is mostly isotropic.

One of the major advantages of irradiation (with respect to thermal annealing, discussed in Sec. 3.2.2), is the possibility to perform the treatment with a focused ion beam or with a mask, in a similar fashion to semiconductor doping. Due to the local nature of the interaction, magnetic patterning without affecting the surface topography becomes feasible. The irradiation treatment for the studies of this thesis were performed by J.W. van der Jagt from Spin Ion Technologies (France).

3.2.2 Magnetic annealing

Magnetic annealing has the scope to tailor the magnetization curve for a particular use or application.[108] The use of magnetic field in heat treatment of ferromagnetic materials is commonly employed to tailor the magnetic anisotropy (K_u) of a variety of soft magnetic materials.

The mechanism for field annealing can be described as follows. The magnetic material is heated in the presence of a magnetic field. To avoid oxidation, the process is performed in vacuum or in an inert gas atmosphere. If the annealing temperature T is sufficiently high to allow for atomic mobility, the process can rearrange atoms on a local scale. In the case of ferromagnetic materials, a preferred direction of magnetization can be imprinted in the sample by annealing in such a way as to favor magnetization in a given direction. This gives the possibility to create a magnetic anisotropy in favored / given direction. The external magnetic field in the chamber sets the magnetization in the sample and some atom pairs orient themselves relative to the direction of magnetization so that their magnetic anisotropy energy is minimized.

When the temperature is lowered to a level at which atomic diffusion is no longer taking palace, the frozen-in atomic pair directional ordering may be sufficient to override other anisotropies and hold the magnetization in the direction it had during annealing. It is commonly mistaken that simply the direction of the applied field is responsible for field-induced magnetic anisotropy while instead the direction of the magnetization in the sample during the heat treatment promotes the short range directional ordering. For this reason, the annealing temperature should not be above the Curie temperature $T < T_c$ (material no longer magnetic).

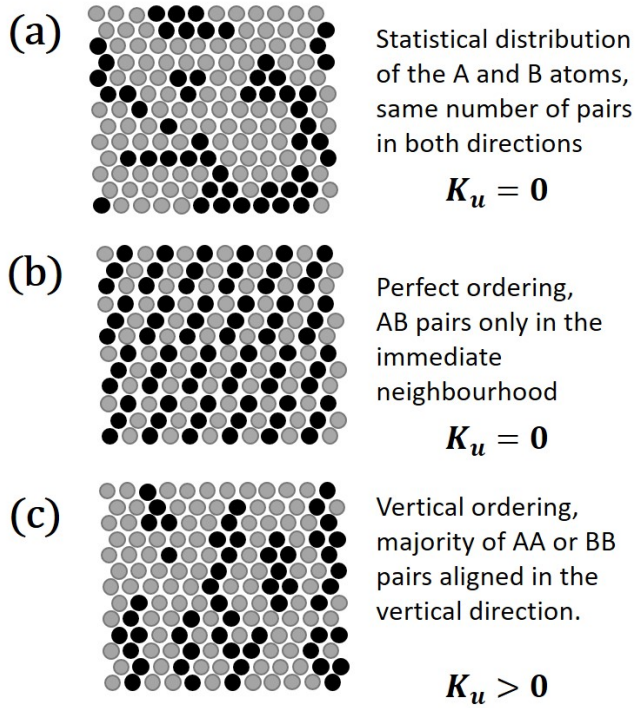

Figure 3.8: Possible results of isotropic or anisotropic pair interaction energies in atom arrangements of an alloy in a regular lattice (2D). (a) shows the case of a random distribution of ordered pairs and (b) a perfect order of the AB atoms. In (c) the pair ordering has a preferential orientation in the vertical direction. K_u indicates the uniaxial magnetic anisotropy.

A way to visualize the mechanism behind field annealing induced anisotropy is the atomic pair ordering, showed in Fig. 3.8 that considers a regular arrangement of two atomic species.[109,110] A nonmagnetic system will arrange its bond coordination, subject to packing constraints, to minimize the energy. In this case the number of pairs oriented in different directions will be equally distributed, as in Figs. 3.8 (a) and (b). In a magnetic material, e.g. Permalloy, the strength of the bond interaction can depend on the orientation of the A-A, B-B, and A-B bonds relative to the magnetization direction. Because the direction of magnetization can alter the energy of the system, the final configuration after magnetic annealing will have an orientational order similar to the illustration of Fig. 3.8 (c). This will impose a preferred axis of magnetization on the sample ($K_u > 0$).

Typical parameters for field annealing of $Ni_{80}Fe_{20}$ and $Co_{40}Fe_{40}B_{20}$ films used in this thesis are: temperature of 265°C and magnetic fields in the order of 10 - 100 mT. The corresponding induced anisotropy is typically in the order of 10

- 1000 J/m^3.

3.3 Measurements techniques

In the following section, the measurement techniques relevant for the content of this thesis is presented.

3.3.1 Magneto-optical (MO) effects

Magneto optical (MO) phenomena refer to alterations of electromagnetic wave properties upon interaction with a magnetized medium. One of the most well known MO effects, the Faraday effect, dates back to 1845 and marks the birth of magneto-optics. Michael Faraday observed that linearly polarized light's polarization axis rotates as it passes through a transparent medium placed in a magnetic field aligned with the light's propagation direction. John Kerr discovered a similar polarization change when linearly polarized light reflects from a magnetized material approximately thirty years later. As depicted in Fig. 3.9 (a), the reflected light gains ellipticity and rotation of its polarization axis when interacting with a magnetic thin film, known as the magneto-optical Kerr effect or MOKE.

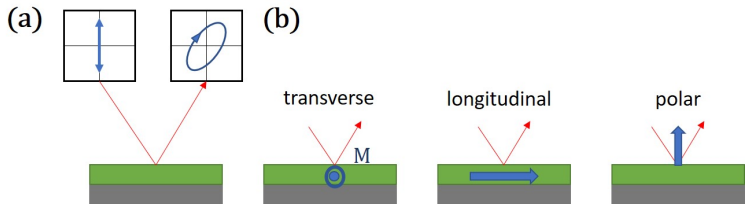

Figure 3.9: (a) Illustration of the magneto-optical Kerr effect (MOKE). A linearly polarized laser beam is reflected of a magnetic thin film. Upon reflection, the polarization of the laser beam is rotated, and gains a certain ellipticity. (b) Illustration of the different MOKE configurations, which are defined by the alignment of the magnetization (blue) with respect to both the sample surface and the plane of incidence of the laser beam (red).

The Kerr effect arises from a difference in the (complex) refractive index for right and left circularly polarized light in a magnetic material. When the incoming linearly polarized light travels a short distance through the material, at most 10

- 20 nm for metal, before it is reflected according to the refractive index of the material. As a result, the two circular modes of the reflected light will have a difference in the phase and amplitude. The phase difference results in a rotation of the polarization axis of the reflected light with respect to the incoming light, called the Kerr rotation θ, whereas the different amplitudes causes a change in ellipticity, denoted by the Kerr ellipticity ε. The Kerr rotation and the ellipticity can be combined in the complex Kerr angle $\Phi_K = \theta + \varepsilon$. In the case of MOKE, the Kerr angle is a function of the magnetization. This is due to the magnetic splitting of the energy bands at the Fermi level that leads to magnetic state dependent interactions with light (transitions probabilities correlated to the occupation of the states).

The interaction of light with a magnetic material can be described in a semi-classical approximation using the dielectric tensor.[111] When interacting with the electrons in a metal, the electric field of linearly polarized light will introduce a difference in the potential. The electrons that will oscillates in the electric field created by the light, will relax by producing photons with the same polarization. This process can be described projecting the components of the light beam on the dielectric tensor, which has the form of[112, 113]

$$\begin{bmatrix} E_s^r \\ E_p^r \end{bmatrix} = \begin{bmatrix} r_{ss} & r_{sp} \\ r_{ps} & r_{pp} \end{bmatrix} \begin{bmatrix} E_s^i \\ E_p^i \end{bmatrix}, \tag{3.1}$$

where $\boldsymbol{E^r}$ is the reflected light, $\boldsymbol{E^i}$ is the incident light, $\hat{r}$ is the reflectivity tensor and p and s are the standard notations for the electric field oscillating in the plane of incidence and perpendicular to it, respectively. For the case of a non-magnetic and optically isotropic material, the dielectric tensor is diagonal and with real coefficients. When interacting with a magnetic sample, the electrons that are oscillating with the linearly polarized light are subjected to a force that arises from the magnetization of the sample. This force is known as the Lorentz force $\mathbf{v} \times \mathbf{M}$, where v is the motion induced by the electric field. For non-collinear configurations of the trajectory and the magnetization vector, the Lorentz force causes a deviation in the linear trajectory of the electron. As a result, a new current is induced that is orthogonal to the original one, leading to photons with a different polarization. These photons, which are created by electrons affected by the Lorentz force, are reflected with the non-modified ones to produce the magneto-optical Kerr effect. This effect is incorporated in the dielectric tensor as off-diagonal imaginary coefficients.

There are three main MOKE configurations differing in the relative orientation of the magnetization direction $\mathbf{M}$ and the plane of incidence of the light. These three configurations are schematically depicted in Fig. 3.9 (b). If the magnetization of the sample is pointing in the direction perpendicular to the

sample plane, the MOKE configuration is called polar. Longitudinal MOKE considers instead the case of magnetization in the plane of the sample (in-plane magnetization) and in the plane of incidence. If eventually the in-plane magnetization is perpendicular to the plane of incidence, the configuration is called transverse MOKE.

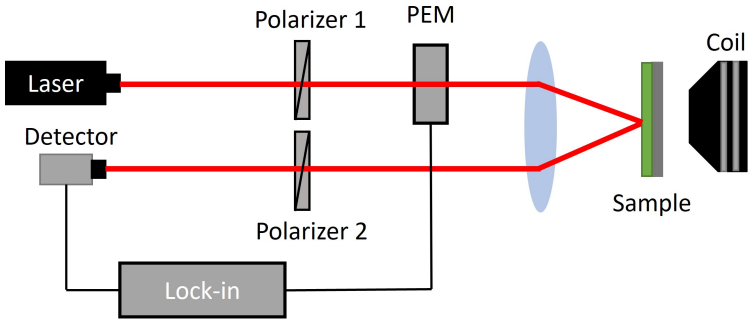

Figure 3.10: Sketch of a basic longitudinal MOKE setup showing the laser, the sample, two polarizers, the lenses employed to focus the beam onto the sample. PEM is the photo-elastic modulator. The polarization of the laser light lies in the direction perpendicular to the page.

Fig. 3.10 illustrates the setup for longitudinal MOKE. To improve the signal-to-noise ratio in the measurement, a signal modulation technique is utilized in combination with a lock-in amplifier. In this technique, a photo-elastic modulator (PEM) is placed between the first polarizer and the sample, as depicted in Fig. 3.10. The PEM comprises a wave-plate that oscillates its retardance over time, inducing a polarization oscillation in the light. By detecting the signal using a lock-in amplifier synchronized with the PEM's frequency (50 kHz in this thesis), only polarization-dependent effects are measured, and other effects are filtered out. It is important to note that MOKE techniques do not provide a quantitative measurement of the magnetization of the sample. However, by the shape of the hysteresis loops, the magnetization reversal process can be investigated accurately.

3.3.1.1 Kerr microscopy

In the MOKE setups previously discussed, the measured MO signal represents the average response to the magnetization in the entire probed region, weighted by the spatial intensity profile of the laser spot. However, some of the research presented in this thesis requires a spatially resolved magnetization image, such as investigating magnetic domains in a ferromagnetic thin film. To obtain

such an image, a Kerr microscope can be used, which is an optical microscope utilizing MOKE to produce an image with MO contrast.[114,115] A schematic representation of the Kerr microscope can be seen in Fig. 3.11.

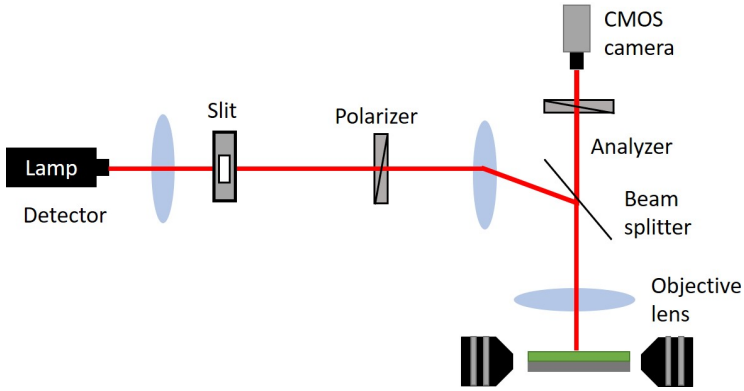

Figure 3.11: Sketch of a Kerr microscope. The use of a COMS camera as a detector for the reflected light allows spatial resolution of the magnetic contrast on the sample surface. The MOKE contrast can be optimized by setting the correct angle of the polarizer and the analyzer.

The Kerr microscope generates MO sensitivity by incorporating two almost crossed polarizers in the light path (see evicomagnetics.com). The angle of incidence of the light is controlled using an aperture between the light source and the objective (in this work, 50x magnification is used). To enhance the MO contrast in the images, a differential imaging technique is applied, where a background image is subtracted from the live image to eliminate non-magnetic contributions. Typically, the background image is captured with a saturated magnetization in the sample, ensuring that the differential image only detects magnetization changes relative to the saturated state. With a careful configuration of the microscope, structures down to 200 nm lateral dimension can be imaged. The diffraction limit remains challenging due to the reduced reflected light intensity and the thermal drift occurring at room temperature.

3.3.2 BH-looper

The BH (Hysteresis) looper instrument is a tool used to measure the magnetic properties of wafers. It operates by applying a small magnetic field to the wafer and measuring the resulting magnetic response, typically in the form of a hysteresis loop.

The BH-looper instrument, shown in Fig. 3.12 (a), consists of a sample holder that can hold the wafer in place, while the magnetic field is applied. The sample holder is typically equipped with a mechanism for applying a small rotation to the wafer, which allows for measurements of magnetic anisotropy. The instrument has a pair of Helmholtz coils, which generate a uniform magnetic field across the wafer. The magnetic response of the wafer is then measured by a second pair of coils, called pick-up coils.

The advantage of this technique is the short measurement time. The BH-looper can be used to measure magnetic properties such as the coercive field, the remanence, and the saturation magnetization, the anisotropy field, the anisotropy constant. As a limitation, this instrument is suitable only for measuring materials with a coercive field limited to 10 mT. This limit is set by the Helmholtz coils. Another significant drawback is the requirement of a rather large sample area to sense a large enough signal.

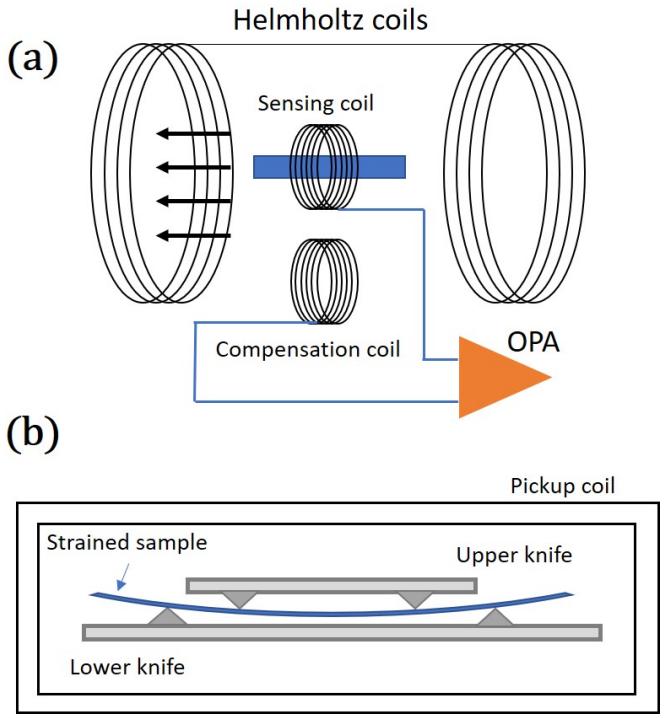

Figure 3.12: (a) schematic of the BH - Looper. The magnetic signal coming from the wafer is sensed by a pair of pickup coils while the Helmholtz coils are inducing an alternating in-plane magnetic field. (b) section of measurement head for performing magnetostriction measurements using the BH-Looper, showing the mechanism to apply mechanical strain to the wafer.

The operation of the BH-Loop is the following: the sample is placed in the

center of two Helmholtz coils.[116] An alternating current of frequency up to 100 Hz generates a oscillating magnetic field in the region o the wafer. The stray field coming from the magnetic sample is measured by a set of pickup coils (induced current): one sensing coil is placed in the sample proximity while the compensation coil is placed in the magnetic field produced by the two Helmholtz coils but at a larger distance form the sample. As only the sensing coil is subject to the stray field of the sample, subtracting the two signal will remove the contribution from the Helmholtz coils to the generated voltage.

The BH Looper model 109[117] used in this thesis has a sample holder (with embedded pickup coil) that is able to apply a mechanical force on the wafer during the measurement. These specialized pickups are used to measure the magnetostrictive effect in materials deposited on thin (200 to 600 µm) substrates. The sample is bent using a set of four equally-spaced non magnetic knife edges as illustrated in Fig. 3.12 (b), and the change in anisotropy field is then measured. The typical strain that can be induced on the wafer is 0.15%.

3.3.3 X-ray characterization techniques

X-ray diffraction

X-ray diffraction (XRD) is a technique that utilizes the interaction of X-rays with a sample to determine its crystal structure and composition.[118] When applied to thin films, XRD can provide information on the film's crystal structure, thickness, and crystalline perfection.

In X-ray diffraction, a beam of X-rays is directed at a sample, and the diffracted X-rays are then detected and analyzed to determine the sample's crystal structure. The diffraction pattern is a result of the constructive and destructive interference of the X-rays as they pass through the sample's crystal lattice.

The positions and intensities of the diffraction peaks in the XRD pattern are related to the crystal structure, and the spacing between the peaks is a direct measure of the inter-atomic distances within the crystal according to Bragg's law

$$2dsin\theta = n\lambda. \tag{3.2}$$

Here θ is the angle of incidence as schematically shown in Fig. 3.13, d indicates the distance between diffracting planes, λ is the wavelength of the beam and n is simply an integer. In general, the simplified picture of Bragg's law,

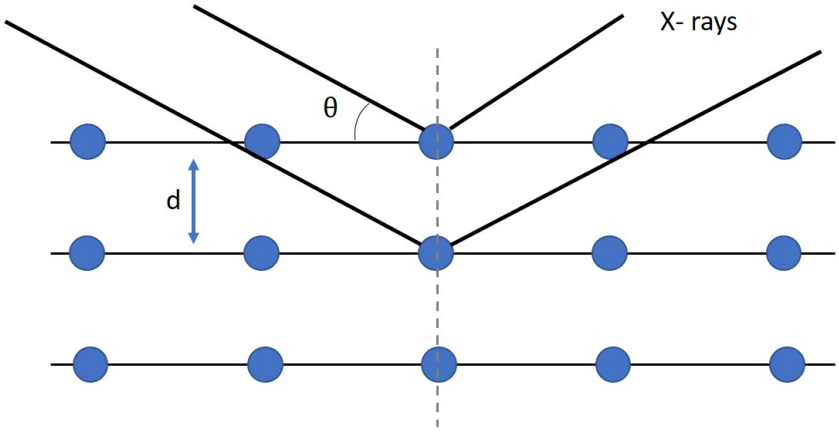

Figure 3.13: Schematic of an X-ray beam (black lines) interacting with the atoms of a crystal (blue circles). The angle between the plane of atoms and the angle of the X-ray beam is defined as θ. The distance between scattering planes (defined by the horizontal lines) is named d.

describes perfectly ordered lattice to extract information. In practice with X-ray diffraction in polycrystalline samples, the degree of crystalline perfection can be determined by analyzing the width of the diffraction peaks (broadening). The crystallite size (or size of a coherently diffracting domain in the material), is also a fundamental property that can be obtained from an XRD profile.[119] According to the Scherrer equation,[120]

$$D = \frac{K\lambda}{\beta cos\theta} \tag{3.3}$$

the size of coherently diffracting domains is inversely proportional to the FWHM of a diffraction peak. In the measurements conducted within this thesis, $K = 0.9$ is a dimensionless shape factor, D the crystallite size, λ the wavelength of the Cu-Kα radiation, θ the diffraction angle and β is the line broadening at FWHM of the XRD peak in radians, after subtracting the instrumental line broadening.

If the detector is set at a specific Bragg angle, and the sample is tilted, the measurement is called *Rocking curve*. This type of measurement results in a scan of intensity along the Θ angle. A sharp peak is only observed when the crystallographic direction is parallel to the diffraction vector, therefore a broad intensity profile is recorded if the sample contains multiple diffraction planes, making this a useful technique for evaluating crystal perfection.[121] To obtain more accurate measurements, the use of monochromator is suggested.

X-ray reflectometry

A last configuration of the X-rays that is used in this thesis is X-ray reflectometry (XRR) analysis. When X-rays are shined onto a material flat surface at grazing angles of incidence, total reflection will occur at or below a critical angle. With a material whose surface is ideally flat, the reflectivity suddenly decreases at angles above the critical angle. The measurement of the intensity pattern, as a function of the detector angle Θ can be used to obtain information about the vertical properties (layer thicknesses), as well as the lateral properties (roughness and correlation properties of interfaces or lateral layer structure). Specifically, film thickness can be determined from the periodicity of the oscillation and information on the surface and interface can be obtained from the angular dependency of the oscillation pattern's amplitude.[122] This technique is used in this thesis, in Sec. 4.1, to characterize multilayers of Ni and Fe.

3.3.4 ToF-SIMS

TOF-SIMS (Time-of-Flight Secondary Ion Mass Spectrometry) is a surface analysis technique that utilizes a primary ion beam to sputter material from the surface of a sample, creating secondary ions that are then analyzed using mass spectrometry.[123] The technique is able to provide chemical information at the atomic and molecular level for studying the composition and properties of surfaces. The high sensitivity (mass resolution $m/\Delta m$ of the secondary ion peaks typically between 5000 and 9000) of the technique allows for the detection of trace amounts of impurities or contaminants on a surface down to few ppm. Additionally, the high spatial resolution of TOF-SIMS enables the identification of the location of specific chemical compounds within a sample.

In the work presented here, TOF-SIMS are employed to determine the depth dependent composition profile of a thin film multilayer (2 nm repetitions). These measurements were performed by A. Lamperti at the CNR-IMM Unit of Agrate Brianza, (Italy).

3.3.5 Application of strain by substrate bending

Most of the work of this thesis is dedicated to the study the magnetostriction or magnetoelastic coupling. To obtain information about the magnetoelastic properties of the material, the magnetic response of the material needs to be

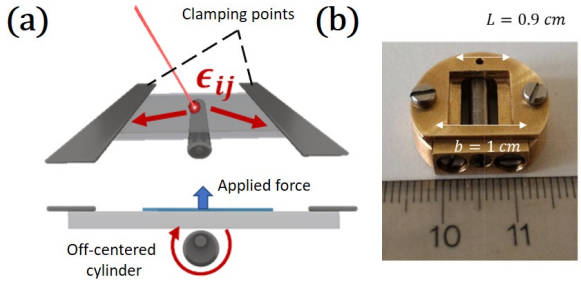

Figure 3.14: Schematic (a) and picture (b) of the sample holder used to apply uniform in-plane strain.

characterized in the presence of controlled strain. One possibility is the use of substrate bending. Deliberate strain can be transferred to the sample if the substrate (typically Si/SiOx) is bent mechanically with a 3 point bending sample holder, as shown schematically in Fig. 3.14 (a). A square sample of 1 by 1 cm is vertically constrained on two sides and pushed uniformly from below by a cylinder that has an off-centered rotation axis. The device generates a tensile strain in the plane of the sample up to 0.1 %, when the cylinder is rotated by 90°. The strain is mostly uniaxial and can be measured with a strain gauge on the substrate surface. The sample holder is suitable for pMOKE and Kerr microscope measurements.

Magnetostriction measurements using the substrate bending device

Magnetic hysteresis loops - recorded before and after the application of the tensile strain - can be used used to estimate the saturation magnetostriction of the material. As previously mentioned in the theory chapter, Sec. 2.2.4, the magnetic in-plane anisotropy K_u is linked to the energy stored in the magnetization curves. For example the (uniaxial) magnetic anisotropy energy is given by the area enclosed between the magnetic loops measured along two in-plane directions perpendicular to each other. If then the strain in the film is non-zero, the magneto-elastic coupling contributes in principle to the effective anisotropy. Indeed, if the directions of the crystalline and magnetoelastic uniaxial anisotropy are perpendicular to each other ($K_u \perp K_{ME}$), we can write the strain dependent effective in-plane anisotropy K_{eff} measured in the system as[105]

$$K_{eff} = K_u + K_{ME}. \tag{3.4}$$

In this case, two hysteresis loops measurements, before and after the application of strain, are sufficient to estimate λ_s. Accordingly, the total anisotropy of the system is $K_{eff} = K_u$ and $K_{eff} = K_u + K_{ME}$ before and after the application of strain, respectively. Different anisotropy contributions (crystalline, interfacial...) cancel out when the magnetic curves are subtracted. The magnetoelastic anisotropy $K_{ME} = \frac{3}{2}\lambda_s Y \varepsilon$ is linked to reversible part of the hysteresis loops (close to the saturation) according to

$$K_{ME} = \frac{1}{2} M_s \Delta E = \frac{3}{2} \lambda_s Y \varepsilon \tag{3.5}$$

where ΔE is the anisotropy energy measured by the difference in area below the strained and unstrained curves. This corresponds to the reversible part, i.e. the red marked area in Fig. 3.15. If the Young's modulus Y of the magnetic material and the strain magnitude ε are known, Eq. 3.5 can be made explicit with respect to λ_s to obtain its value.

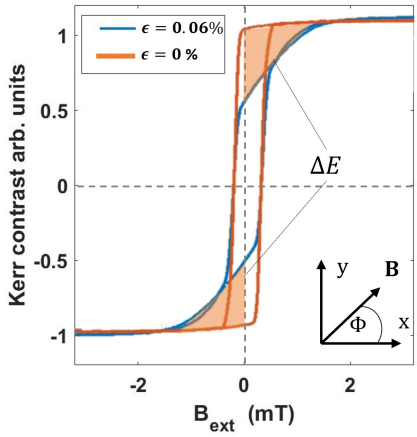

Figure 3.15: Hysteresis loops measured with Kerr microscopy that are used to estimate λ_s. The magnetic field is applied along the same direction of the in-plane strain, along x. The strained and unstrained hysteresis loops are plotted with an area ΔE marked in orange that represents the magnetoelastic anisotropy constant $\times \frac{2}{M_s}$ as evaluated using the area-integration method.

3.3.6 Room temperature transport measurements

To measure the AMR of our sample, the 4-point probe method is used, in which the direction of the current path is defined by the external contacts. As shown

in Fig. 3.16, the four gold contacts are evaporated 1 mm apart. The resistance is measured while the sample is rotated in a magnetic field of 10 mT, sufficient to saturate the magnetization along the field direction. A constant current of 1 mA is applied with a Keithley 2400 while the DC voltage is measured at the other two terminals with a Nanovoltmeter model 2182A. The magnetic material was not structured in our studies and a full film is considered.

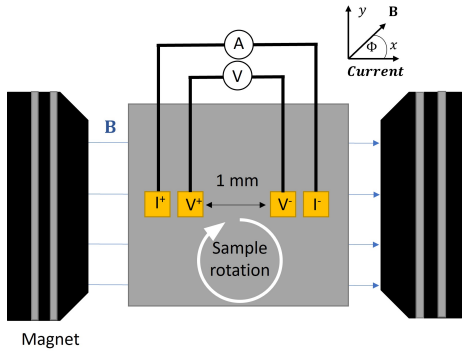

Figure 3.16: Schematic of the contacts during the AMR measurement. The sample (in gray) is a full film where gold contacts (in yellow) are used for electrical contacts. The sample is on a rotating stage and placed in a uniform magnetic field created by the coils.

As a result, the resistivity of the sample as a function of the angle Φ between the magnetization direction and the current flow can be recorded and fitted with the expression[15]

$$R(\Phi) = R_{\perp} + (R_{\perp} + R_{\parallel})cos^2\Phi = R_{\perp} + \Delta R cos^2\Phi. \tag{3.6}$$

The magnitude of the AMR effect can be quantified by the magnetoresistive coefficient

$$\frac{\Delta R}{R_{\parallel}}. \tag{3.7}$$

3.3.7 Application of Surface acoustic waves

Surface acoustic waves (SAWs) are elastic waves that propagate along the surface of solids and they found applications in sensing, communication, and signal processing. Piezoelectric substrates (introduced in the theory chapter of

this thesis, Sec. 2.4.3) are particularly interesting for SAW applications due to their ability to convert electrical signals into mechanical waves and vice versa. This property enables the generation and detection of SAWs on the surface of the substrate using interdigitated transducers (IDTs) that are fabricated on the surface. In the context of this thesis, SAWs can introduce time-varying (dynamic) strain waves in the magnetic thin films and, consequently leading to SAW-assisted magnetization switching[124–126] via the magnetoelastic coupling, discussed in Chap. 2. The piezoelectric material used is a 128 Y-cut lithium niobate ($LiNbO_3$) substrate. On top of it, a pair of interdigits is patterned using optical lithography as shown in Fig. 3.17 (b). The fringe pattern of the IDT will define the frequency of the emitted SAW. Typical frequencies that can be reached are 50-350 MHz, but higher frequencies (i.e. smaller transducers) can be reached using electron beam lithography.

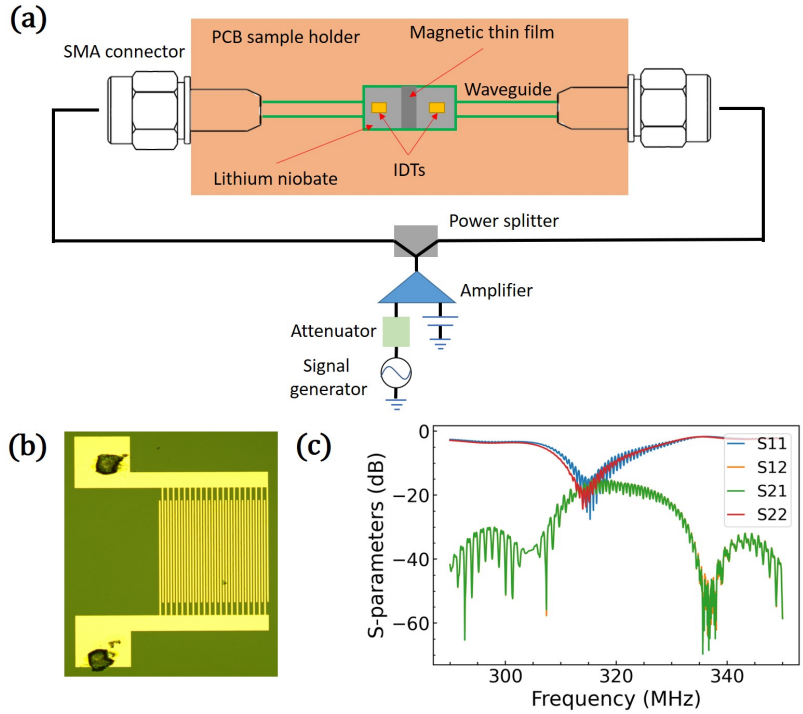

Figure 3.17: (a) Schematic of RF circuit used to generate standing SAW. The copper surface of the PCB board (in orange) is used as a ground plane. The the different components of the circuit are connected to the sample via a co-planar wave-guide and standard SMA connectors. (b) optical microscope image of the patterned IDTs. The signal generator, attenuator, amplifier and power splitter are removed and a VNA is attached to the SMA connectors for S-parameter measurements shown in (c). The different coefficients S_{ij} indicate the reflected ($i = j$) or transmitted ($i \neq j$) power between the two IDTs.

The RF circuit used to generate standing SAW is shown in Fig. 3.17 (a). An Agilent E5062A vector network analyzer (VNA) is utilized to determine the transmission loss and to excite standing SAWs by applying RF signals to both IDTs simultaneously.[88,127] To calculate the transmission loss, the VNA's two ports are connected to each IDT at both ends of the device through bond wires and SMA connectors. The four transmission parameters, including S21, are measured, allowing the determination of the peak value of transmission with respect to frequency. This point typically displayed 19 dB transmission loss at 319 MHz, as shown in Fig. 3.17 (c). The VNA is connected to the device using an attenuator and an amplifier (Fig. 3.17 (a)). This configurations ensures that the linear range of the amplifier is fully utilized. To excite standing SAWs, a power-splitter is used to divide the signals into two, which are then sent to each IDT. The RF power applied to the device is amplified to a range of approximately 23 to 28 dBm before being split, and the expected total RF power transduced into the standing SAW mode is estimated to be in the range of approximately 17.5 to 22.5 dBm, taking into account the measured losses at peak transmission. To generate instead propagating SAW, the power-splitter is removed and only one IDT is connected to the SMA connector, while the second IDT is floating.

The part of this thesis involving the use of SAWs was done with the help of J. Shuai - responsible for the IDTs patterning - during a collaboration with the University of Leeds (UK).

3.4 Simulation softwares

In the following section, the two software packages used in this thesis for simulations are briefly described. The software Mumax3 is used to simulate the static or time dependent magnetization in the domain-wall-based devices. Finite element method calculations have instead been used to estimate the stress and strain profiles induced by layer deposition on a silicon substrate.

3.4.1 Micromagnetic simulations

The micromagnetic approximation of a magnetic system - describing the magnetization by a continuous vector field and discussed in the theory Chap.2 - has equations that cannot be solved analytically except for a few very idealized

cases. Therefore, for most problems of interest, a solution has to be found numerically. Numerical solutions are based on the discretization of the system so that the magnetization is not continuous function of the position but is only defined in a discrete set of points. Commonly, most of the available software solve the Landau-Lifshitz-Gilbert (LLG) equation - Eq. 2.34 - with effective fields arising from the conventional micromagnetic energy terms. A so called static solution can be found by minimizing the energy functional, while a dynamic (time variant) one can be found solving the time variant LLG equation. While the problem is identically described in the available software solutions, the method to solve it differs. Finite element methods are used by MagPar (magpar.net), while software like OOMMF, Micromagnum and Mumax3 use the finite difference method.

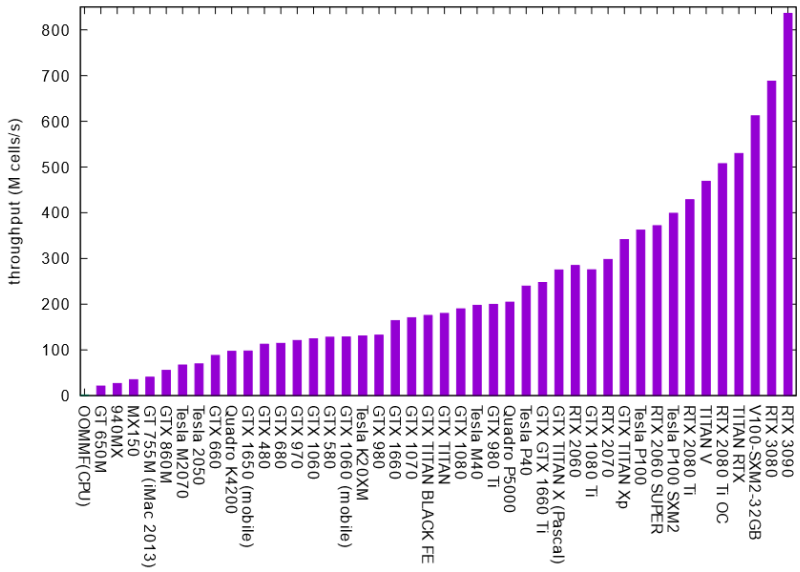

Figure 3.18: Mumax3 GPU perfomance for 2D simulations containing 4 million cells. CPU based simulations are reported for comparison. Source: mumax.github.io.

Due to its high computational speed and graphic user interface, the package used in this thesis is Mumax3. Mumax[128, 129] - developed by Arne Vansteenkiste at Ghent University's DyNaMat group in Belgium- uses Go language at a higher level, which allows to use simple readable scripts to run simulations, while its core is written in CUDA/C, a low level language that is harnessed to get high computational performance. The program utilizes Graphic Process Units (GPU) to perform simulations that are finite-difference based, resulting in remarkable speed advantages over CPUs. For GPU benchmark, see Fig. 3.18. Moreover, the program allows a script-based as well as a graphical user interface input and has gain high popularity in the scientific community over the past

years.

Most of the simulations carried out in this thesis are aimed to model the dynamics of magnetic domain walls. In this case, the Landau-Lifshitz-Gilbert equation takes into account various material properties, such as anisotropy, exchange interaction, applied magnetic fields, and is able to simulate the effects of thermal fluctuations and non-uniform magnetic fields. One additional aspect that Mumax3 is able to capture, is the effect of strain. In version 3.10 of mumax this is done by including a magnetoelastic field in the LLG equation.[130] An arbitrary value of the strain tensor can be considered in the system and strain can also be space and time dependent.

This allows to simulate strain induced by piezoelectric substrates and enables to simulate more complex behavior for magnetic domain walls and their pinning, in non-uniform strain profiles and strain gradients (see the experimental chapter Sec. 5.2).

To obtain physically consistent results, the discretization has to be chosen carefully. The cell size Δx has to be smaller than the exchange length in the magnetic material[131]

$$l_{ex} = \sqrt{\frac{2A_{ex}}{\mu_0 M_{sat}^2}}, \tag{3.8}$$

where A_{ex} is the exchange constant defined in the theory part, Sec. 2.2.2. The exchange length is a characteristic parameter of the ferromagnetic material and indicates the distance over which the parallel alignment of the spin magnetic moments is energetically favorable.[132] However, one has take into account that increasing system size and reducing cell size excessively will exponentially increase the computation time, particularly because reducing cell size also requires reducing the time step for the numerical integration scheme to be stable.

After the system geometry and the strain in the system is initialized, a possible simulation with domain wall in a nanowire is as follows. To initialize the magnetization -we place the domain wall close to the left edge of the sample as shown in Fig. 3.19 (b). The magnetic surface charges at the left and right edges of the computational region are removed to avoid the domain wall interacting with them. Once the system is prepared, the simulation commences, with the solver computing the time evolution of the magnetization according to the LLG equation for a time step, that can be either fixed or allowed to adapt dynamically depending on the stability conditions.

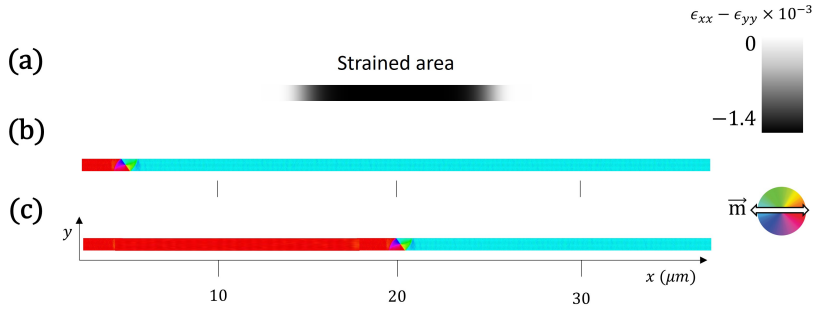

Figure 3.19: Example of a typical micromagnetic simulation for the work described in this thesis. The nonuniform strain profile (a) considers a compressive strain in the center of the nanowire, where a vortex wall is propagated (b). (c) vortex domain wall pinned at the center of the strained area, where the energy is minimum for $\lambda_s \sigma < 0$. The simulated system has a width of 800 nm and a thickness of 30 nm. Material parameters are the one of $Co_{40}Fe_{40}B_{20}$.

An example of a micromagnetic simulation to study the dynamics of a domain wall in a nanowire in the presence of strain can be seen in Fig. 3.19. In Fig. 3.19 (a) the strain profile, created with a "mask", indicates a compressive strain in the central area of the nanowire. The initial magnetization configuration, with an in-plane vortex wall on the left side of the wire, is shown in Fig. 3.19 (b). After the application of an external field, the time evolution of the magnetization is monitored until the DW reaches the pinning point (Fig. 3.19 (c)).

The micromagnetic simulations presented in the experimental chapter of this thesis, Chap. 5, have been performed with the help of M. Fattouhi, E. Martinez and L. Lopez-Diaz from the Department of Applied Physics of the Universidad de Salamanca (Spain).

3.4.2 FEM simulations

Finite element method (FEM) calculations are performed using COMSOL Multiphysics, a simulation software that enables the study of various physical phenomena, including mechanical and structural behavior and provides a wide range of pre-built physics interfaces that can be easily configured to simulate different types of problems. Additionally, the software offers a variety of post-processing tools that allow for the visualization and analysis of the simulation results.

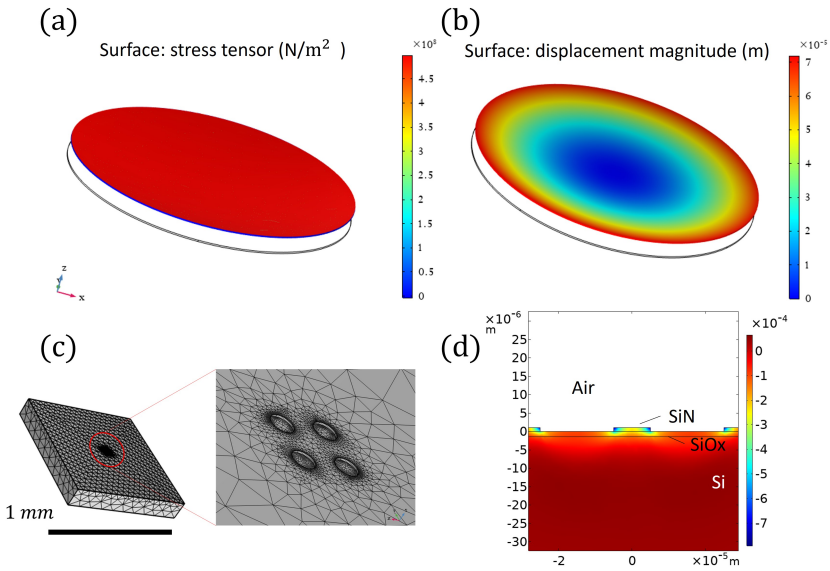

Figure 3.20: Stress tensor on a Si/SiOx wafer simulated using COMSOL Multi physics after deposition of SiN over-layer. (a) stress tensor on the surface of the wafer which is uniform. (b) surface displacement of a 5" wafer. (c) discretization and (d) x component of the strain tensor simulated in the proximity of a removed SiN layer.

One specific application of COMSOL is the simulation of strain and stress in materials and structures. The software uses the finite element method (FEM) to solve partial differential equations (PDEs) that describe the behavior of materials under various loading conditions. In the present study, the states of stress and strain on a Si wafer induced by SiN CVD deposition (source of intrinsic stress, discussed in Sec. 2.4.2) are simulated using the Structural Mechanics Module.

The system considered in this thesis is a Si(625 µm)/SiOx(1.5 µm) wafer covered by a SiN(1 µm) layer. The simulation computes the relaxed state of the system after the initial stress at the SiOx/SiN interface (-500 MPa, extracted form wafer-bow measurements) is imposed and assumed isotropic. This assumption does not consider anisotropic residual strain on the sample. To justify this assumption, the latter has been gauged and found to be 10 times smaller than the strain induced by the SiN openings. It is reasonable therefore to assume the residual strain as isotropic in our FEM simulations. An example of the output of our COMSOL simulation is shown in Fig. 3.20. Fig. 3.20 (a) presents an example of the uniform stress induced on a 5" wafer due to the SiN layer deposition, whereas Fig. 3.20 (b) shows the displacement magnitude.

When calculating the variation in the surface strain caused by the etched

areas in the SiN, the size of the system is reduced to 1×1 mm^2 to reduce computational time. Fig. 3.20 (c) shows a closer look to the holes created in the SiN layer, indicating the finer grid close to complex structures. The simulation in the presence of etched areas in the SiN shows a local strain relief in the close proximity of the openings (Fig. 3.20 (d)).

The FEM simulations presented in the experimental chapter of this thesis, Sec. 5.2, have been performed with the help of E. Spetzler, from the Institute for Materials Science of Kiel University (Germany).

4

Material preparation for magnetic field sensors

In this chapter, the first part of the experimental results of this thesis are contained. As the coupling between strain and magnetism is described by the magnetostriction, we present various studies that focus on characterizing and engineering strain-dependent material properties. Different magnetic systems are considered, ranging from standard free layers for MR to optically switchable ferrimagnetic layers.

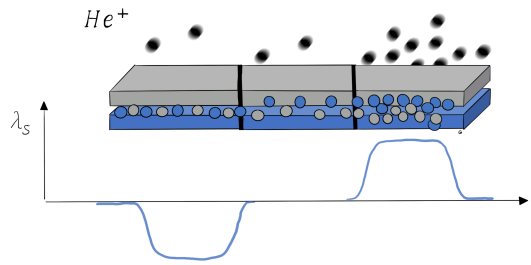

Contents

As it is discussed in the theory chapter - Sec. 2.2.4.1 - the magnetic properties are coupled to the elastic state of a material. The strength of this magnetoelastic interactions is determined by the magnetostriction λ_s, a constant whose value (in the order of 10^{-5}) can be positive or negative - if the tensile strain defines an easy or hard axis of the magnetization, respectively. The magnetoelastic properties of thin films are of major interest for technological use as well as for scientific investigations. As one could expect, the requirements for the magnetoelastic coefficient (λ_s) strongly depend on the application. Magnetic sensors often need, for example, strain immunity,[133] i.e. zero magnetostriction, to reduce strain cross-sensitivity. This is particularly important in the case of sensors on flexible substrates (see Chap. 1), where the strain-induced anisotropy can alter the sensitivity direction. On the other hand, actuators require giant strain effects, achieved in materials such as $TbFe_2$ (terfenol)[134] with large λ_s.

Considering the case of magnetic sensors, the strain anisotropy is nothing but one aspect of the optimization of the magnetic sensing layer. To give an example, AMR sensors have different requirements depending on their sensing application. Current sensors need a strong induced anisotropy, in order to well define the sensitivity direction with respect to the current flow. On the other hand, angle sensing in Wheatstone-bridge configuration needs a very low anisotropy and low hysteresis (magnetic softness maximized) in order to minimize the angle error.

In this chapter the attention is focused on the material preparation, one aspect in magnetic sensor development. In Sec. 4.1 and Sec. 4.2 two typical material platforms for in-plane magnetized sensors are considered. Respectively, a Ni(2 nm)/Fe(2 nm) multilayer and 30 nm Permalloy ($Ni_{81}Fe_{19}$ alloy). In both of these studies, He^+ ion irradiation - post deposition technique described in the experimental section, Sec. 3.2.1 - is employed to control the magnetostriction and to improve the magnetic softness of magnetic materials. These two studies were performed in collaboration with the startup company Spinion Technologies: the irradiations and the TRIM simulations were performed by J.W. van der Jagt.

In Sec. 4.3 the strain effects on a different material platform, Co/Gd synthetic ferrimagnets, are presented. This material, that recently gained attention, has the peculiarity that its magnetic state can be switched using a laser pulse.

4.1 Control of magnetostriction using He^+ irradiation

To achieve the optimal value of magnetostriction for a specific application, it is possible to use a combination of two or more materials that have different magnetic and magnetoelastic properties. Multilayer systems have been extensively studied to achieve a target value by exploiting the combination of different parameters such as λ_s, as presented in several studies.[135–138] These studies have identified that atomic intermixing at the interfaces of multilayer systems can greatly affect the total magnetostriction, and this interface magnetostriction has been utilized to engineer the total magnetoelastic coupling of the multilayer.[135,136] In the case of ion-sputtered films, where interface mixing naturally occurs, Nagai et al.[135] were able to modify the sign of the magnetostriction of a multilayer magnetic stack by adjusting the relative thickness of the layers. However, a limitation of this method is the lack of control over inter-layer roughness and intermixing degree, which are determined by the deposition conditions. This limitation restricts the ability to change the magnetostriction arbitrarily or locally.

As already discussed in Sec. 3.2.1, ion irradiation is a well-established technique for modifying magnetic properties[139–141] and inducing intermixing. As discussed in Sec. 3.2.1, by using light ions such as He^+ at energies between 10-30 keV, atomic displacements can be induced over short distances without causing surface defects in the material, which is a common issue when using heavy ions such as Ar^+ or Ga^+.[142] Unlike annealing, which is a uniform process, ion irradiation confines intermixing to the magnetic layer boundaries and prevents mixing with the non-magnetic seed layers. This allows for local magnetic patterning of multilayer film systems. For these reasons, ion irradiation is a promising approach for achieving a desired magnetostriction value in a multilayer by controlling the vertical extension of the intermixed region. Previous work[143] has demonstrated that magnetostriction changes induced by intermixing can be achieved using heavy ions and high energies (700 MeV). However, the use of highly energetic heavy ions can easily degrade PMA of thin layers and damage spacing layers in GMR spin valves or TMR junctions.[144] Furthermore, the presence of cascade collisions in the material and long-range atomic displacements[98] make precise control of the magnetic properties a challenging task.

The presented study investigates the impact of light-ion irradiation at different fluences on the interfaces of a Ni/Fe multilayer, particularly the effect of progressive intermixing. Our results indicate that by utilizing He^+ ion irradiation,

the magnetoelastic properties of the Ni/Fe multilayer can be adjusted locally. Additionally, this method improves the magnetic softness of the material, leading to a reduction of up to 70% in the coercive field and anisotropy.

The major part of the results of the present section are published in Applied Physics Letters[99] .

4.1.1 Sample structure and characterization

The samples are prepared by DC magnetron sputtering using a Singulus Rotaris system on a SiOx/Si substrate. A multilayer of [Ni(2 nm)/Fe(2 nm)]×8 is sputtered in the presence of a rotating magnetic field of 5 mT on a NiFeCr (5 nm) seed layer and capped with 4 nm of Ta. After that, optical lithography and ion etching are used to pattern arrays of circles (80 µm of diameter and 3 µm of spacing) on the samples in order to probe the local film properties.

Multiple copies of the samples are irradiated at an energy of 20 keV with different fluences of He^+ ions from 5×10^{13} to 1×10^{16} cm^{-2}.

A different method to promote atom diffusion in magnetic materials is the use of thermal energy provided by annealing.[145] We compare the effects of He^+ ion irradiation with the annealing in vacuum at 300°C for 4.5 hours of our magnetic multilayer.

In order to quantitatively estimate the formation of the alloy for increasing ion fluences and temperature during annealing, a series of experiments are conducted to investigate the changes in structure and chemistry occurring at the layer interfaces due to ion irradiation and annealing. Various techniques including X-ray diffraction, High-angle annular darkfield scanning transmission electron microscopy (HAADF-STEM, 80-200 mrad), nanoscale chemical analysis via energy dispersive X-ray spectroscopy (EDX) in STEM mode, and Time-of-Flight Secondary Ion Mass Spectrometry (TOF-SIMS) are utilized. The characterization of the intermixing is reported in Sec. 4.1.2.1

The thin film magnetic properties are measured with Kerr microscopy and Vibrating Sample Magnetometry (VSM). The Kerr microscope has a 20× objective and a white light source. Coils for in-plane magnetic field are used. We measure the hysteresis loops detecting differential contrast changes in the magneto-optical Kerr effect (MOKE) in a longitudinal configuration of the polarized light. Both longitudinal and transversal configuration are instead used to image the magnetization state (domains) in a gray scale sum image. The Kerr measurements are performed under uniaxial tensile strain using the

three pointing bending technique described in the experimental section, Sec. 3.3.5. The magnetic characterization and the estimation of magnetostriction are reported in Sec. 4.1.2.2.

4.1.2 Results and discussion

4.1.2.1 Intermixing - Structural modifications after irradiation

Montecarlo TRIM simulations

We used Montecarlo (TRIM[146]) simulations to investigate kinetic phenomena associated with ion energy loss, specifically target atom displacement (normalized by the incoming ion fluence) as a function of the vertical depth of the sample.

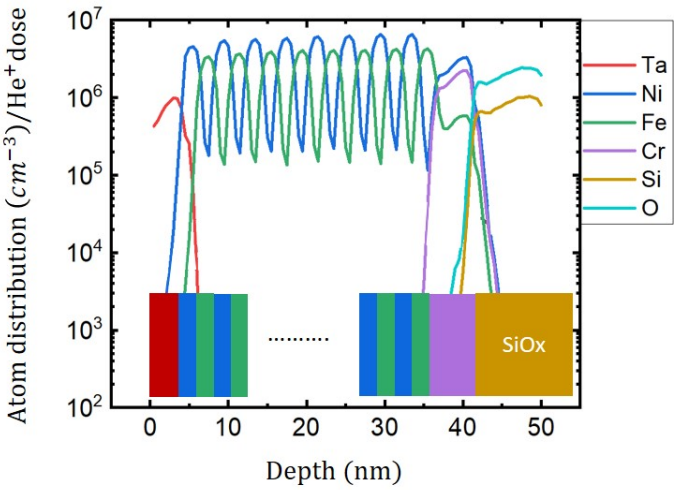

Figure 4.1: Montecarlo simulation obtained using the software TRIM.[146] The atomic recoil distribution of different elements after the collision with incoming ions is shown along the vertical depth of the multilayer. The results are normalized by the incoming fluence of ions.

The system is initialized with perfect interfaces and the kinetic energy of the incoming ions is set to 20 keV. Fig. 4.1 shows the results of TRIM simulations, with solid lines representing the recoil atomic distribution after collision with

He^+ ions. The overlapping region of two curves indicates coexistence of different atomic species, which corresponds to intermixing/alloying. The simulations suggest that the displacement is uniform through the magnetic stack for the selected ion energy, so we can expect similar amount of intermixing at each Ni/Fe interface.

According to our TRIM simulations, 95% of the ions reach the substrate, resulting in a uniform intermixing in the vertical direction of the sample. Additionally, the effect of ion implantation in the multilayer is negligible. Furthermore, we do not observe significant intermixing of the non-magnetic capping and seed layers with the magnetic stack. This is most likely due to the directional nature of collisions with He^+ ions.[102]

High resolution - TEM

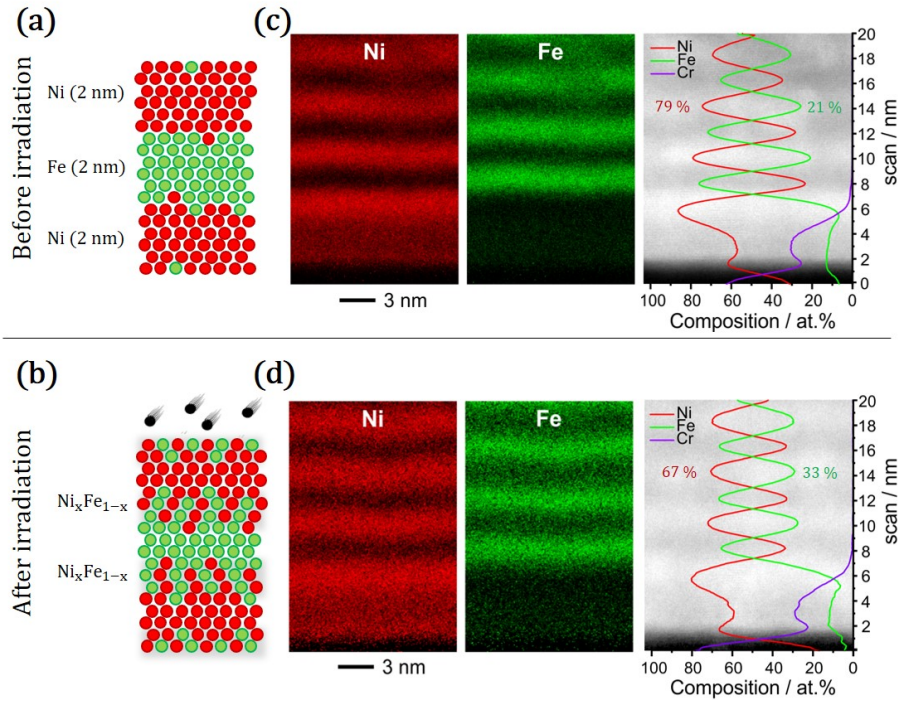

Figure 4.2: (a) - (b) Sketch of the intermixing due to light ion irradiation on a multilayer stack. STEM HAADF micrograph and EDX elemental maps of the Fe/Ni multilayer system before (c) and after (d) 1×10^{16} cm^{-2} He^+ ion irradiation measured across the first four repetitions on top of the NiFeCr seed layer. The HAADF micrograph is superimposed with a plot of the atomic composition quantified from the EDX measurements.

As reported elsewhere for similar irradiation conditions,[102] collision cascades are absent and the structural modifications are confined to the vicinity of

the ion path in the metal. According to Devolder et al.,[147] when exposed to radiation at low fluences, strain is released at room temperature. Conversely, at high fluences, intermixing becomes the primary structural effect of radiation, as illustrated in Figs. 4.2 (a) and (b).

To assess the degree of intermixing caused by our radiation, we utilized scanning transmission electron microscopy (STEM). To create cross sections (lamella) of Fe/Ni/NiFeCr on SiO_2/Si, we employed the focused-ion-beam technique (FIB). Our colleagues at the University of Kiel and the Leibniz Institute in Leipzig conducted these measurements using a probe CS-corrected Titan^3 G^2 60–300 microscope with an accelerating voltage of 300 kV. The HAADF mode is used to acquire STEM images, with a probe-forming aperture of 25 mrad and annular ranges of 80-200 mrad on the detector. These parameters were chosen to optimize resolution and contrast.[148]

Figures 4.2 (c) and (d) display a vertical EDX profile of the lower layers of the multilayer stack, along with corresponding EDX maps of the elemental distribution before and after He^+ irradiation with 1×10^{16} cm^{-2} fluence. After sputtering (Fig. 4.2 (c)), well-defined interfaces are observed between the magnetic layers. The EDX profile shows that the relative atomic composition contains 21(2)% of Fe in a Ni layer before irradiation, whereas after irradiation (Fig. 4.2 (d)), the ratio of Fe atoms in a Ni layer increases to 33(4)%. This stoichiometric change in layer composition is reflected in the EDX elemental maps, which show an increased scattering of signal intensity across the layer interfaces following irradiation. This indicates that an alloy of Ni_xFe_{1-x} is formed at the Ni/Fe interfaces due to the displacement of different atoms by incoming He^+ ions.

The inelastic scattering of the electron beam within a finite sample thickness results in the delocalization of X-ray signal intensity in EDX experiments at and near the atomic scale. Therefore, for meaningful results, a qualitative comparison of the X-ray signal distribution recorded for EDX maps on as-deposited and irradiated Ni/Fe multilayers can only be made for similar sample thicknesses (t). The sample thickness measurements determined by electron energy-loss spectroscopy (EELS) yields a much smaller finite thickness for the irradiated multilayer sample. Thus, the qualitative comparison of the measured EDX signal distribution and the interpretation of subtle chemical intermixing are justified.[149,150]

The structure of our multilayer before He^+-ion irradiation is polycrystalline with (110)-textured layers of Fe and (111)-textured layers of Ni as can be seen in Figs. 4.3 (a) and (c). The structural motif of [100] Fe with (110) out-of-plane orientation is evidenced by Fast Fourier Transforms (FFT) on a crystalline region within a Fe-layer. Within the Ni-layers, the dominant structural motif

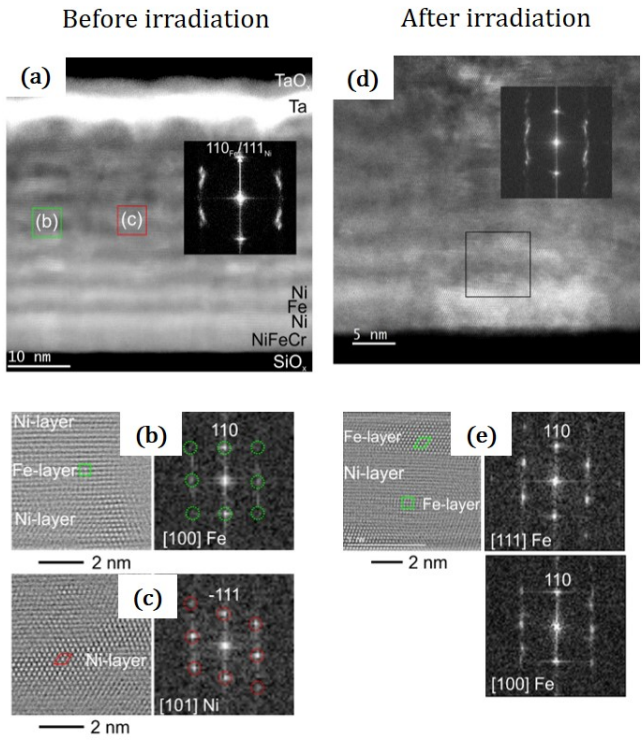

Figure 4.3: High-Resolution STEM micrographs of the Fe/Ni multilayer system before and after He^+-ion irradiation. (a) repetitions of (110)-textured layers of Fe and (111)-textured layers of Ni are evidenced by specific Z-contrast and individual Fast Fourier Transforms (FFT) of regions (b) and (c). (d) repetitions of Fe and Ni layers showing the identical crystalline texture after irradiation by comparison of FFT images.(e) Noise-filtered micrograph displaying the atomic structure of the multilayers. The structural motifs of [100] Fe and [111] Fe are shown for crystalline regions within the Fe-layers.

of [101] Ni is observed with (111) out-of-plane orientation as shown in Figs. 4.3 (a) and (c). We performed the same measurements after ion irradiation with a fluence of 1×10^{16} cm^{-2}. We found that the polycrystalline multilayers of Fe and Ni after irradiation (FFT images in Figs. 4.3 (d) -(e)) have the same crystalline texture as the as-deposited state (Figs. 4.3 (b) - (c)). Therefore, we conclude that the crystalline structure does not undergo significant changes after the irradiation treatment.

X-ray diffraction measurements

Figs. 4.4 (a) and (b) show the results of X-ray Diffraction (XRD) measurements performed to investigate the crystalline structure of the multilayer stack.

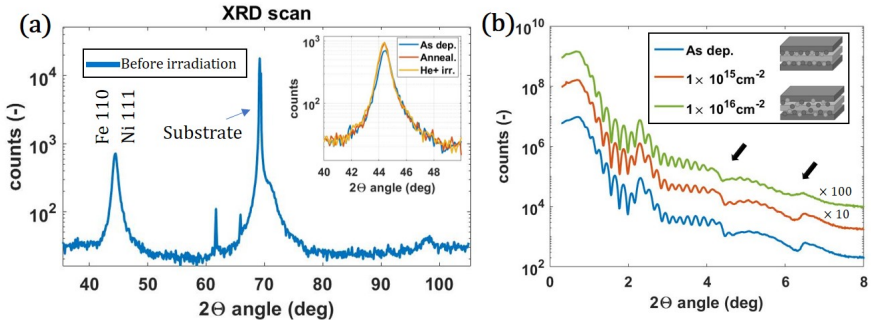

Figure 4.4: (a) XRD 2Θ/Θ angular scan of the Ni/Fe multilayer sample after sputtering. In the inset: Fe (110)/Ni (111) peak of the multilayer as-deposited, annealed and after irradiation. (b) X-Ray reflectometry (XRR) measurement for a multilayer of [Ni(2 nm)/Fe(2 nm)]× 8 irradiated with different He^+ fluences. The changes in the curves indicate increasing intermixing at the interfaces of our multilayer with increasing ion fluences.

In Fig. 4.4 (a), an XRD 2Θ/Θ angular scan of the Ni/Fe multilayer confirms, due to the presence of a diffraction peak at 44.3°, that the sputtered layers are textured. In the inset of Fig. 4.4 (a) the (110)/(111) reflection peak is compared for multilayer as-deposited, after annealing and after irradiation with fluence of 1×10^{16} cm^{-2}. As already shown by our STEM studies X-ray diffraction measurements indicate in our sample a polycrystalline structure of (110)-textured layers of Fe and (111)-textured layers of Ni which is not significantly altered by the process of irradiation nor by annealing.

Figure 4.4 (b) displays an X-ray reflectivity (XRR) angular scan for the as-deposited state and samples with varying irradiation fluences. More details about XRR measurements can be found in the experimental chapter, Sec. 3.3.3. The best fit of the data involves a relative roughness of the layers of approximately 1 nm for the as-deposited case. All curves exhibit two types of periodic oscillations. The short-period oscillations with a period of 0.2° correspond to the total thickness of the stack (which is 41 nm). The long-period oscillations around 2, 4, and 6° correspond to the repetitions of the multilayer with a thickness of $t_p = 4$ nm (black arrows in Fig. 4.4 (b)). The amplitude of these oscillations decreases progressively as the fluence of He^+ increases during irradiation. This effect is most noticeable in Figure 4.4 (b) for the peak at 6.2°. The data suggest that the Ni/Fe interfaces is degraded with increasing irradiation fluence, indicating an increased level of intermixing. This is qualitatively supported by a fitting model in which the layer roughness of Ni and Fe is increased, consistent with our other structural measurements.

ToF-SIMS measurements

Fig. 4.5 displays the atomic depth distribution measured by Time-of-Flight Secondary Ion Mass Spectrometry (ToF-SIMS).[123,151–154] This experiment was performed by A. Lamperti from CNR-IMM, unit of Agrate Brianza (Italy). The presence of Fe, Ni and Cr atoms in the multilayer is reported for samples as-deposited, irradiated with 1×10^{16} cm^{-2} fluence and after 300°C annealing, respectively. Observing Fig. 4.5 (a), it can be seen that the periodic oscillations of Ni and Fe are well-defined and have the same periodicity. The layer separation is reflected by the peak position and minima of Ni at the maxima of Fe. Fig. 4.5 (b) displays the atomic distribution after irradiation. In this case, the amplitude of Ni and Fe oscillations is significantly reduced compared to the as-deposited case. This is attributed to the intermixing of the neighboring magnetic layers, leading to the formation of Ni_xFe_{1-x} alloy.

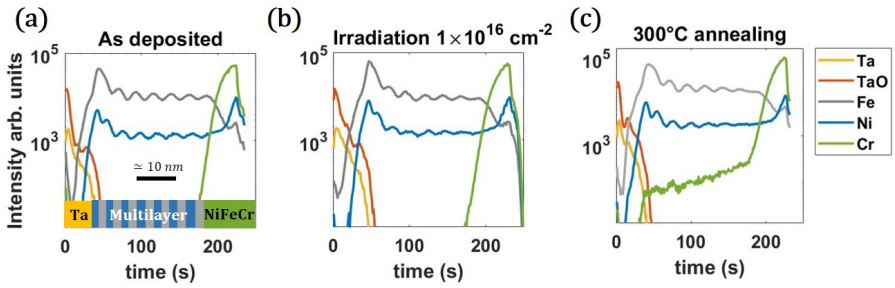

Figure 4.5: ToF-SIMS measurements for multilayer as-deposited (a), after irradiation (b) and thermal annealing (c).

The atomic diffusion, caused by the irradiation (Fig. 4.5 (b)), can be similarly observed in the ToF - SIMS measurements after the annealing treatment in Fig. 4.5(c). However, a clear difference between Fig. 4.5 (b) and Fig. 4.5 (c) can be seen in the signal of Cr (from the seed layer). After irradiation, the atomic diffusion is more directional and confined at the layer interface, instead after annealing the intermixing is long range and involves the non-magnetic NiFeCr seed layer. A more extensive comparison between the two mechanisms can be found in the experimental section, Sec. 3.2 and in our work on Permalloy layer described in the next section, Sec. 4.2.

4.1.2.2 Magnetic measurements - anisotropy and magnetostriction

In the previous section we have shown that He^+ irradiation of our Ni/Fe multilayer leads to proportional intermixing, most prominent at the interfaces.

In this section we present how such structural modification affects the magnetic properties of the system. Figs. 4.6 (a) and (b) show the in-plane hysteresis loops before and after ion irradiation. In Fig. 4.6 (a), it can be observed that the as-deposited sample exhibits distinct magnetization curves for different angular orientations of the in-plane magnetic field, indicating the presence of uniaxial crystalline anisotropy ($K_u \simeq 100$ J/m^3). The remanent magnetization plot in Fig. 4.6 (d) emphasizes this behavior. The coercivity measured along the easy axis of magnetization is 0.95(5) mT. Fig. 4.6 (b) shows the same magnetic measurements for the sample after He^+ irradiation at a fluence of 1×10^{16} cm^{-2}. We observe that the magnetic in-plane anisotropy is now negligible, as the hysteresis loops overlap. The reduction in anisotropy after irradiation can be seen in Fig. 4.6 (d) comparing the as-deposited state (orange diamonds) with the irradiated film (blue hexagrams). Furthermore, the coercivity is reduced to 0.25(5) mT.

The decrease in both coercivity and anisotropy in our multilayer after irradiation can be explained by an increased number of nucleation sites. This increase facilitates domain formation and magnetization switching at lower magnetic fields and is promoted by isotropic atomic mobility during irradiation. The coercive field and magnetic anisotropy remain unchanged after annealing. This difference between the two material treatment can be attributed to the different activation mechanism for atomic displacement: kinetic energy for irradiation and thermal energy for annealing. Similar effects are observed in a single Permalloy layer subjected to He^+ ion irradiation, as reported in Sec. 4.2 of this chapter.

Systematic measurements of the magnetic properties of our [Ni(2 nm)/Fe(2 nm)]×8 multilayer are shown in Fig. 4.6 (c) as a function of He^+ fluence during irradiation. The magnetic moment of the sample increases by approximately 15%, from 2.8(1) to 3.1(2)$\times10^{-3}$ emu, as the He^+ fluence increases. This increase is an indication of a higher level of intermixing between our Ni and Fe layers, as reported elsewhere.[155] If perfect interfaces existed between our Ni and Fe layers, the saturation magnetization M_s would be the average of the values for the two materials, namely $M_s(Fe) = 2.15$ T and $M_s(Ni) = 0.55$ T (see Table 4.1). In our case $M_s^{average}$ is equal to 1.35 T. Since $M_s(Ni_{50}Fe_{50}) = 1.5$ T, the increasing magnetic moment of our sample with ion fluence, as reported in Fig. 4.6 (c), indicates the creation of an alloy at the interfaces due to progressive intermixing.

In order to evaluate the potential of ion irradiation to finely tune the magnetoelastic properties of a magnetic multilayer, the effective magnetic anisotropy in our sample is measured under the application of mechanical strain by three-point bending method as described in the experimental chapter, Sec. 3.3.5. Here the substrate is bent to exert a uniaxial strain on the sample. Since

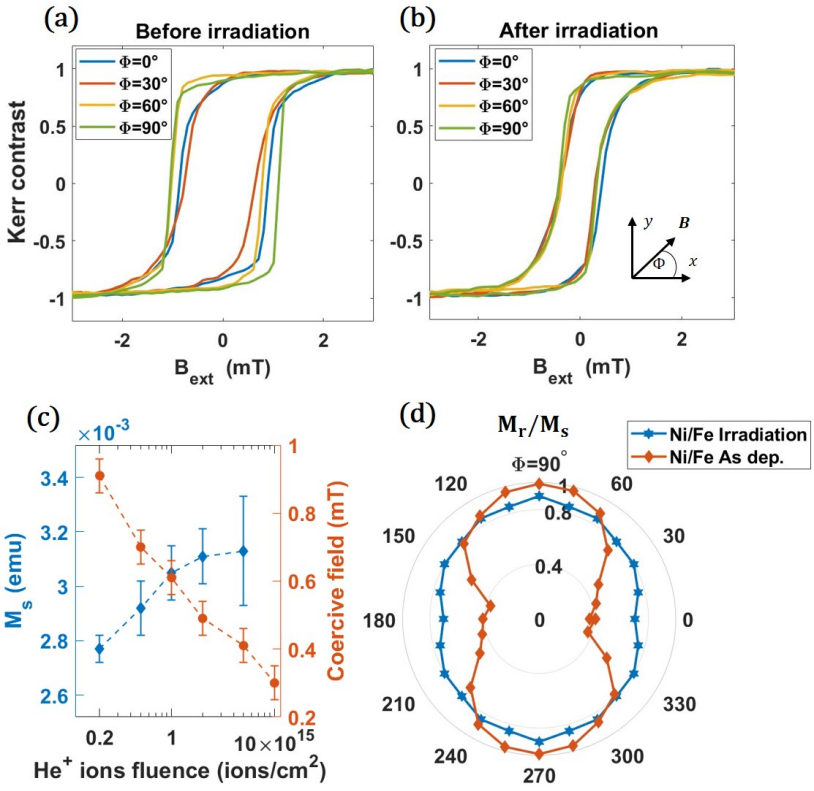

Figure 4.6: (a) - (b) Hysteresis loops as a function of the in-plane magnetic field direction measured by Kerr microscopy, respectively, before and after ion irradiation with a fluence of 1×10^{16} cm^{-2}. (c) Saturation magnetic moment (light blue) and coercive field (orange) as a function of the fluence of He^+ ions during irradiation measured with VSM. (d) Angular plot of the remanent magnetization M_r/M_s as a function of the magnetic field angle Φ.

Material	M_s (T)	λ_s x10^{-6}	Y (GPa)
Fe	2.15	-9	211
Ni	0.55	-30	180
$Ni_{50}Fe_{50}$	1.5	19	200

Table 4.1: Parameters from literature[135, 156–159] of the magnetic materials after deposition (no irradiation). Here, M_s is the saturation magnetization, λ_s is the saturation magnetostriction and Y is the Young's modulus. The same Y is considered for as-deposited and irradiated samples.

the magnetization is coupled to the external strain via the expression of the anisotropy energy[157] (see Sec. 2.2.4.1) one way to probe the effect of the strain

is to observe changes in the hysteretic behavior before and after mechanical deformation. The expression of the magnetoelastic anisotropy depends on the saturation magnetostriction λ_s of the material according to[73]

$$K_{ME} = \frac{3}{2}\lambda_s Y \varepsilon, \tag{4.1}$$

where Y is the Young's modulus and ε is the uniaxial tensile strain.

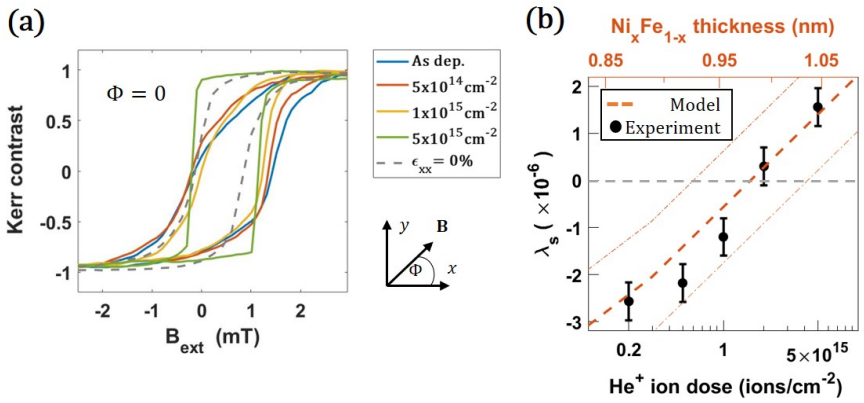

Figure 4.7: (a) Hysteresis loops measured along the direction of the applied strain ($\varepsilon_{xx} = 0.06\%$) for different fluences of He^+ ions (solid lines) are compared with the unstrained magnetic loop (dashed line). (b) Measured saturation magnetostriction λ_s (black dots) as a function of the ion fluence and calculated values using Eq. 4.2 (dashed line) as a function of the intermixed alloy thickness $t_{Ni_xFe_{1-x}}$. A central value of $\lambda_s^{Ni_xFe_{1-x}} = 19 \times 10^{-6}$ with $\pm 20\%$ variation is considered.

The sign of K_{ME} can be negative or positive, depending on the value of λ_s. Accordingly, the total magnetic anisotropy can increase ($\lambda_s < 0$) or decrease ($\lambda_s > 0$) in the presence of tensile strain. Since our magnetic system is considerably thick and primarily influenced by shape anisotropy (in-plane easy axis), we can ignore at a first order approximation any modifications in interface anisotropy that might result from ion irradiation for the purpose of our discussion and calculations.

Hysteresis loops are measured along the direction ($\Phi = 0°$) of the applied strain $\varepsilon_{xx} = 0.06\%$ and are reported for our samples in Fig. 4.7 (a) for different fluences of ions during irradiation. It can be observed that the magnetic anisotropy field in response to the applied strain is different for each irradiated sample. Two potential scenarios are identified by comparing the magnetization curve in the absence of strain (dashed line). When the tensile strain increases the anisotropy field in the direction parallel to ε_{xx}, K_{ME} and λ_s are negative.

The sample therefore displayed a negative magnetoelastic coupling in its as-deposited state. In the second scenario, when the strain direction becomes an easy-axis of magnetization (reduced anisotropy field), K_{ME} and λ_s are positive, as reported for larger fluences in the same magnetic stack.

The values of saturation magnetostriction of our magnetic multilayer - calculated using Eq. 4.1 - are shown in Fig. 4.7 (b) as a function of the fluence of He^+ ions. The value of magnetostriction of the as-deposited Ni/Fe multilayer is $-2.6(5)\times10^{-6}$. Larger fluences of He^+ ions, exceeding 5×10^{14} cm^{-2}, gradually reduce the absolute value of magnetostriction, which then increases after changing its sign to positive values. The change of sign of the magnetoelastic coupling occurs for fluences between 1×10^{15} and 2×10^{15} cm^{-2}. For details about the estimation of the magnetostriction with anisotropy methods, see the experimental chapter, Sec. 3.3.5.

An additional confirmation of the magnetic behavior of the magnetic stack under strain is obtained by imaging domain formation using the magneto-optical Kerr effect (MOKE).[160] A vector image of the in-plane magnetization is obtained by the sum of horizontal and vertical components of the magnetic contrast. The MOKE images in Figs. 4.8 (a)-(c) show the change in the preferred direction of magnetization before and after the application of a 0.06% uniaxial strain in 80 µm disk patterned samples. This particular shape is chosen to minimize the in-plane shape anisotropy.

Fig. 4.8 (a) shows the remanent magnetic domain pattern of the as-deposited multilayer, where the magnetization aligns to the crystalline anisotropy (left). After applying the strain (right), magnetic domains orient perpendicular to the uniaxial strain ε_{xx}, providing experimental proof of the development of stress-induced magnetic anisotropy $K_{ME} \simeq -450$ J/m^3 that overcomes the initial anisotropy direction. K_{ME} is perpendicular to the tensile strain direction due to the negative sign of the magnetostriction. Fig. 4.8 (b) displays the domain structure of the sample irradiated with a He^+ dose of 2×10^{15} cm^{-2}, where almost zero magnetostriction is measured. In this case, the orientation of the magnetization is almost unchanged by the presence of strain. Accordingly, K_{ME} is negligible compared to the crystalline anisotropy of the material $K_u \simeq 100$ J/m^3. For higher fluences, the clearly different domain pattern in Fig. 4.8 (c) demonstrates that the effects of strain on the remanent magnetization state become significant again. This time, the dominant magnetic anisotropy contribution in the system is again the magnetoelastic term. $K_{ME} \simeq 280$ J/m^3 is positive as the domains orient along the x direction, parallel to the applied strain ε_{xx}. Thus using ion irradiation, the magnetoelastic coupling of the stack is altered, obtaining values of magnetostriction ranging from negative to positive.

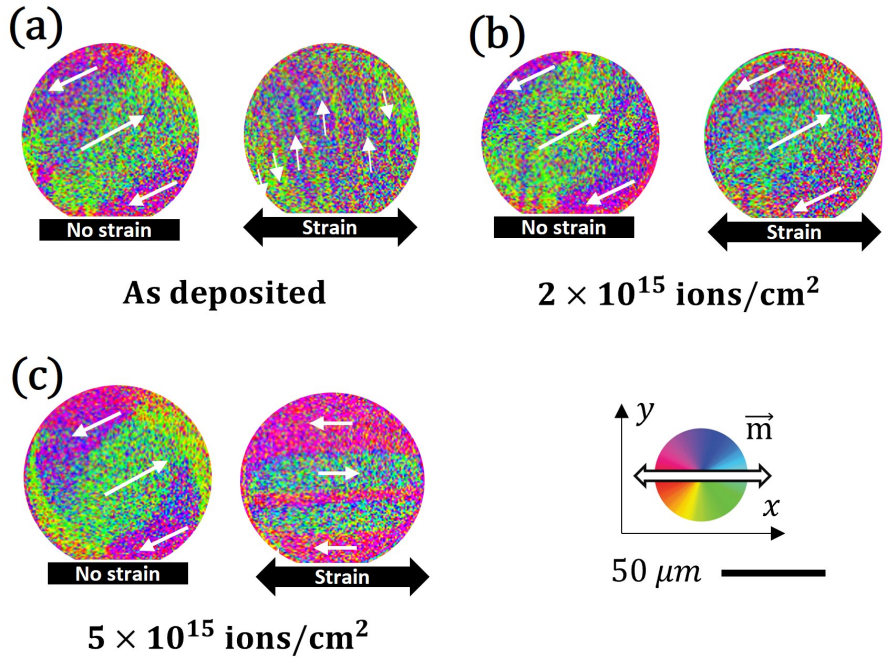

Figure 4.8: Kerr microscope images of the remanent magnetic domain state respectively before (left) and after (right) the application of strain are compared for (a) as deposited case, (b) intermediate value of irradiation and (c) strong value of irradiation. White arrows represent the direction of the in-plane magnetization in the domains according to the color wheel.

In a previous study,[136] it was found that the low magnetostriction observed in our periodic system can be explained by balance of the pristine and intermixed layers. Ni ($\lambda_s^{Ni} = -30 \times 10^{-6}$) and Fe ($\lambda_s^{Fe} = -9 \times 10^{-6}$) with a negative magnetostriction value are compensated by their 50% alloy with strongly positive magnetostriction[156,158] ($\lambda_s^{NiFe_{50}} = 19 \times 10^{-6}$) (see Table 4.1). Our STEM-EDX measurements - reported in Fig. 4.2 - shows that He^+ ion irradiation leads to the formation of a more intermixed interface region of Ni_xFe_{1-x}, resulting in an increase in the thickness of the positive magnetostrictive alloy. The thickness of the alloy increases proportionally to the fluence of He^+ ions during irradiation, as also confirmed by our ToF-SIMS measurements. This gradual shift in magnetostriction of the entire stack towards positive values can be described using the often adopted expression[135–138,161–163]

$$\lambda_s = \frac{\lambda_s^{Ni} + \lambda_s^{Fe}}{2} + \left(2\lambda_s^{Ni_xFe_{1-x}} - \lambda_s^{Ni} - \lambda_s^{Fe}\right) \frac{t_{Ni_xFe_{1-x}}}{t_p}, \tag{4.2}$$

where $t_p = t_{Ni} + t_{Fe} = 4\ nm$ is the period thickness, $t_{Ni_xFe_{1-x}}$ describes

the thickness of the alloy originated by the intermixing and $\lambda_s^{Ni_xFe_{1-x}}$ is the saturation magnetostriction of the intermixed alloy. With the appropriate magnetostriction values, Eq. 4.2 can be used to describe different material systems. The solution of Eq. 4.2 as a function of $t_{Ni_xFe_{1-x}}$ is shown in Fig. 4.7 (b) for the system investigated in this study. Fig. 4.7 (b) shows the solution of Eq. 4.2 as a function of $t_{Ni_xFe_{1-x}}$ for the investigated system. A central value of $\lambda_s^{Ni_xFe_{1-x}} = 19 \times 10^{-6}$ with $\pm 20\%$ variation is considered. These error-bars are added to take into consideration a more realistic intermixing profile of our multilayer. The predicted values reported in this thesis by Eq. 4.2 are obtained by considering a relative alloy composition $x = 50\%$ according to Table 4.1. In realistic conditions, the amount of intermixing changes gradually at the interface. Consequently $\lambda_s^{Ni_xFe_{1-x}} = \lambda_s^{Ni_xFe_{1-x}}(x)$ is not constant. The approximation used is justified by the fact that the value of magnetostriction of Permalloy - with relative Ni composition between $x = 40 - 70\%$ -does not deviate significantly from the value in Table 4.1. This happens because the magnetostriction of Permalloy has a local maximum around 50% relative composition.[164] Therefore, a constant value of $\lambda_s^{Ni_xFe_{1-x}}$ is expected to yield consistent results, as has been the case for previous works.[135]

After deposition in Ni/Fe multilayers prepared similarly to Nagai and coworkers,[135] the estimated $t_{Ni_xFe_{1-x}}$ is around 0.85 nm, under the assumption $t_{Fe}/t_p = 0.5$. Using this $t_{Ni_xFe_{1-x}}$ value, Eq. 4.2 returns a value of $\lambda_s = -2.8(2) \times 10^{-6}$, which is close to the measured value after deposition. Additionally, Eq. 4.2 can be used to estimate the amount of induced intermixing caused by He^+ ions. The calculated $t_{Ni_xFe_{1-x}}$ is 0.98(2) nm at the magnetostriction compensation value ($\lambda_s = 0$) and 1.05(2) nm for the highest fluence, where the magnetostriction is positive due to the dominant effect of the alloy. This increase in the alloy thickness induced by He^+ between 0.2×10^{15} and 5×10^{15} cm^{-2} is consistent with the information obtained from STEM-EDX and ToF-SIMS measurements.

Conclusions

In this section, an experimental investigation of the magnetoelastic properties of sputtered Ni/Fe multilayers after He^+ ion irradiation is presented. High resolution TEM, ToF-SIMS and X-ray diffraction techniques for structural analysis are used, revealing low roughness and alloying at the Ni/Fe interface in the as-deposited state, which can account for the small negative magnetostriction value observed. The polycrystalline structure of the layers is found to be unaffected by the irradiation conditions within the resolution of our measurements. Additionally, it is observed that intermixing of the sputtered layers at the interfaces is promoted by light ion irradiation in proportion to the ion fluence. Changes in the saturation magnetostriction of the magnetic stack with increasing the ion fluence during irradiation are observed, and a sign

change in the magnetoelastic coupling of the material from negative to positive for high fluences is achieved. Notably, strain insensitivity on the magnetic properties of the material can be achieved with ion fluences between 1×10^{15} and 2×10^{15} cm^{-2}. This behavior is due to the layers intermixing caused by the irradiation, in combination with the different sign of magnetostriction of the pristine layers and their alloy.

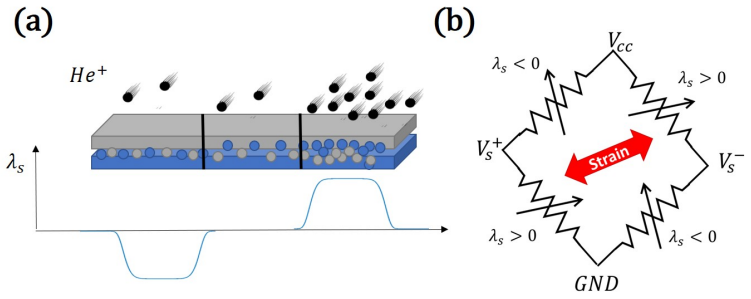

Figure 4.9: Outlook idea of a possible use of local tuning of magnetostriction using irradiation, realized irradiating a single film with different fluences (a). This could allow the straightforward realization of a Wheatstone bridge configuration for a strain magnetic sensor (b).

As a result, post-growth He^+ ion irradiation is demonstrated to be a useful tool for fine-tuning the magneto-elastic properties of multilayer magnetic samples. This technology allows for ion-induced "magnetic patterning", with focused ions or performing the irradiation through a mask in a similar fashion to semiconductor doping.[102,165] This method is well-suited for creating channels that facilitate the motion of magnetic domain walls[166,167] and skyrmions.[168,169] This is due to the ability of the local irradiation to generate gradients of magnetoelastic coupling.

This technique has the potential to be applied to multiple material combinations, and could be the next generation of material treatment offering precise and local patterning of magnetostriction, enabling the realization of novel and highly demanding applications. One example could be the realization of a magnetic strain sensor. By irradiating different areas of the magnetic layer with different fluences, as schematically shown in Fig. 4.9 (a), elements with opposite sensitivity to strain can be realized with a single irradiation step, starting from a single material. This paves a straightforward way to, e.g. realize a Wheatstone bridge configuration (as e.g., in Fig. 4.9 (b)).

4.2 Optimization of Permalloy for magnetic sensors

After considering a multilayer system as the one in Sec. 4.1 of the present chapter, we now focus our attention on the optimization of a ferromagnetic alloy, possible material for the free layer of magnetic sensors. Permalloy, a Ni-Fe alloy, is frequently used as an active sense layer in magnetoresistive (MR) sensor applications, due to its soft magnetic properties and low coercivity.[2] The composition of $Ni_{81}Fe_{19}$ has been found to be ideal for these devices, as it also possesses significant anisotropic magnetoresistance (AMR) and low magnetostriction. Previous studies have looked into optimizing Permalloy for AMR sensors,[170–172] with a focus on improving magnetic softness and reducing magnetostriction. To reach that, negligible induced anisotropy is firstly required. The sensor layer elements typically feature a stripe-shaped geometry to induce a strong shape anisotropy, providing the sensor with a well-defined orientation of sensitivity. Furthermore, this design ensures a fixed configuration of the magnetic domains, thus enabling a very high signal-to-noise ratio. Additional anisotropies of other sources, if not oriented in the same direction as the shape anisotropy, would hinder this sensitivity direction.[15] Low hysteresis and high AMR are also necessary for maximizing sensitivity,[173] along with low magnetostriction to avoid parasitic anisotropies. Low magnetoelastic anisotropy is particularly important for sensors on flexible substrates,[2,25,174–176] which have attracted much attention in recent years and are discussed in Chap. 1. Techniques such as growth optimization[177] and annealing[178] have been used to achieve low magnetostriction, but they do not allow for localized treatment of the film.

We have already discussed in Sec. 4.1 how ion irradiation can be used as a local technique for adjusting the magnetic and structural properties of thin films through interface intermixing. Studies on Permalloy films have demonstrated that ion irradiation can modify the magnetic anisotropy[179–181] and magnetoresistive response in the presence of exchange bias.[172,182] However, most of these investigations employ ion implantation[183–185] or heavy ions,[186] which can cause considerable damage to the sample for delicate structures as TMR. A preferable alternative is to use lighter ions, such as He^+ with energies ranging from 10-30 keV,[99,102] to avoid such damage. Additionally, no research has yet been reported comparing the effects of irradiation on the magnetoelastic properties of single Permalloy films with field-free ion irradiation and annealing.[187]

In the present section, we propose and explore the use of He^+ ion irradiation on sputtered layer of $Ni_{81}Fe_{19}$(30 nm) as material preparation for magnetic

field sensors. We compare this method to the standard field-free annealing approach, showing that irradiation with 20 keV He^+ ions leads to a significant reduction in coercivity and magnetic anisotropy.

We support our anisotropy measurements with a detailed comparison of the remanent domain pattern. Additionally, we demonstrate that the polycrystalline magnetostriction can be reduced by a factor of ten for irradiation doses of 5×10^{16} cm^{-2}. We attribute this reduction in magnetoelastic coupling to crystallization and changes to the interface magnetostriction resulting from intermixing at the boundaries of the magnetic layers. X-ray diffraction (XRD) analysis confirms an overall improvement in crystallization following irradiation and annealing. We suggest that the reduction in magnetic anisotropy is due to the absence of a preferential direction of atomic ordering and to stress relaxation during irradiation.

Considering that post growth He^+ ion irradiation enhances magnetic softness and minimizes strain sensitivity of Permalloy, we envisage high-sensitivity AMR magnetic sensors with low hysteresis even for integrated devices.

Most of the content of this section, Sec. 4.2 has been published in Physical Review Applied.[188]

4.2.1 Sample structure and characterization

The samples are prepared by DC magnetron sputtering at room temperature using a Singulus Rotaris system on a 1.5 µm thick, thermally oxidized SiOx on top of a 625 µm thick Si substrate. A NiFeCr (5 nm) seed layer is deposited first, followed by a layer of $Ni_{81}Fe_{19}$ (30 nm) with a base pressure of 5×10^{-8} mbar, a sputtering power of 1200 W and an Ar^+ flow of 90 sccm. A rotating magnetic field of 5 mT is used during sputtering, and a Ta layer of 4 nm is added as a cap layer, as shown in Fig. 4.11 (b). The seed layer helps promote a NiFe (111) texture and enhances magnetoresistance.[183] After deposition, the samples are patterned using optical lithography and ion etching to form arrays of disks with a diameter of 80 µm and a spacing of 3 µm in order to probe the local film properties. Several copies of the samples are exposed to He^+ ions at an energy of 20 keV with different fluences ranging from 5×10^{13} to 5×10^{16} cm^{-2}.

To determine the optimal irradiation parameters - in particular the ions energy - for our material system, we utilized Monte Carlo simulations (TRIM). These simulations allow us to calculate the ion's energy loss-related kinetic phenomena, such as target atom displacement (normalized by the incoming ion fluence) as

a function of the sample's vertical depth. The system is initialized with ideal interfaces, and the incoming ion's kinetic energy is varied between 15 and 60 keV. For these simulation we consider irradiation with 1×10^5 He^+ ions.

Figure 4.10 (a) shows the He^+ distribution as a function of sample depth, normalized by the dose and the total number of ions. The sample in question consists of NiFeCr (5 nm)/$Ni_{81}Fe_{19}$ (30 nm)/Ta (4 nm) on a SiOx substrate. Figure 4.10 (b) illustrates the percentage of He^+ ions that do not reach the substrate after irradiation as a function of the beam's acceleration energy. For our irradiation, the beam energy is 20 keV. Under these irradiation conditions, the majority of the ions reach the substrate (roughly 94% according to Figure 4.10 (b)), resulting in uniform irradiation of the whole layer stack. To process thicker Permalloy layers (100 nm) higher acceleration energy of the ions would be required.

The effect of back-scattering on the fluence can be neglected,[189] and the Permalloy film utilized is subjected to an irradiation fluence that is almost identical to the nominal fluence as reported. However, if the proposed irradiation technique is to be employed on different substrates or materials, it is recommended to conduct new simulations to confirm any possible variations. Nevertheless, the low mass of He^+ and the low cross-section for large-angle scattering events make it unlikely for there to be any significant changes in the results due to substrate variations, such as substituting SiOx with Si (111) or Kapton tape.

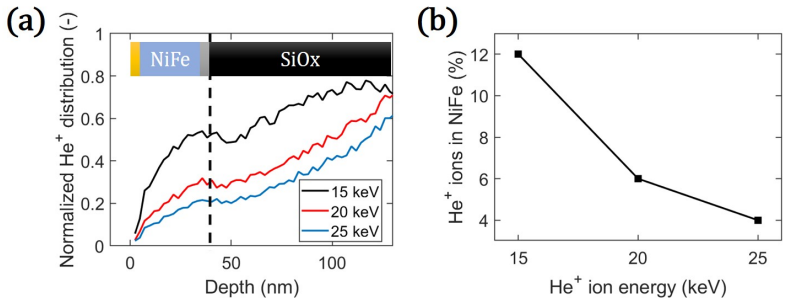

Figure 4.10: TRIM simulations for different energy of the incoming ions. 1×10^5 He^+ ions are considered. Normalized He^+ ions distribution along the vertical depth of the sample (a) and fraction of irradiating ions that do not reach the substrate (b) in a Permalloy sample 30 nm thick. The results are normalized by the incoming fluence of ions. The sample/substrate interface is marked with a black dashed line.

To compare the effect of ion irradiation to thermal annealing, the same magnetic material is consecutively annealed for three hours at 200, 265 and 300°C at a pressure of 10^{-7} mbar. To prevent preferential direction of ordering induced by magnetization,[184,190] external magnetic fields are minimized (i.e. shielded) during the irradiation and annealing processes. Kerr microscopy and VSM

are used to measure the thin film magnetic properties, which are summarized in Table 4.2. The Young's modulus value is assumed to be unaffected by the irradiation and annealing steps due to negligible implantation.[102] The anisotropic magnetoresistance (AMR) is measured electrically as explained in the experimental chapter, Sec. 3.3.6.

To apply strain to our devices, the substrate is bent mechanically with a three-point bending method. Structural modifications caused by ion irradiation and annealing are probed by X-ray Diffraction (XRD) using a Bruker D8 Discover system. Angular $2\Theta/\Theta$ scans and rocking curve measurements are performed on 1 by 1 cm samples.

4.2.2 Results and discussion

4.2.2.1 Structural modifications after irradiation

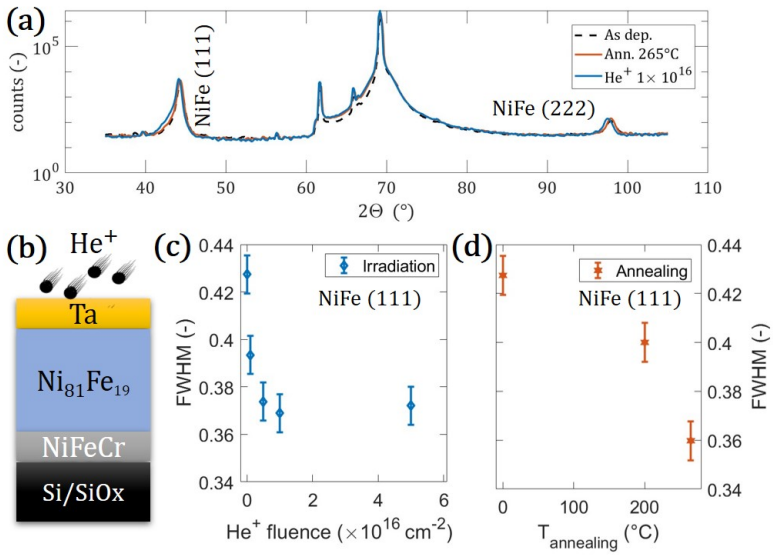

Figure 4.11: (a) $2\Theta/\Theta$ XRD angular scan of the NiFe samples for the sample in the as-deposited state, after annealing and after irradiation. (b) schematic of the NiFeCr(5 nm)/$Ni_{81}Fe_{19}$(30 nm)/Ta(4 nm) stack. (c) FWHM of the NiFe (111) peak as a function of He^+ fluence and (d) as function of annealing temperature.

To compare the structural modifications induced by different material treatment on a Ni-Fe alloy, XRD measurements are conducted on the $Ni_{81}Fe_{19}$ (30 nm) film in its as-deposited state, as well as after irradiation and annealing. The results of these measurements are shown in Fig. 4.11. Fig. 4.11 (a) displays the $2\Theta/\Theta$ angular scan of the Permalloy film. The material exhibits a well-defined crystalline texture of NiFe (111) (and its second-order peak) in its as-deposited state, this texture persists after irradiation and annealing in all the fluence and temperature ranges studied. The full width at half maximum (FWHM) of the (111) peak is presented in Fig. 4.11 (c) as a function of the irradiation fluence (blue diamonds) and in Fig. 4.11 (d) as a function of the temperature during annealing (orange pentagrams). In both cases, the FWHM of the (111) peak decreases by approximately 15% with increasing ion fluence and annealing temperature relative to the as-deposited state.

The FWHM of the (111) peak can be used to determine the the size of crystallites in our film. According to the Scherrer formula (Eq. 3.3, presented in the experimental chapter, Sec. 3.3.3), the size of the crystalline domains in our films increased after either annealing at 265°C or ion irradiation with a fluence of 5×10^{16} cm^{-2}. The estimated size of the diffracting domains is 22(1) nm for the as-deposited case and increased to 24(1) nm after the two material treatments, as calculated using Eq. 3.3. In both the irradiated and annealed samples, we observed a decrease in the FWHM of the rocking curve, indicating an improvement in the film's crystalline phase.[191]

Additionally, rocking curve measurements on our sample are reported in Fig. 4.12. In Fig. 4.12 (a) rocking curve measurements are presented in the as-deposited state, after annealing at 265°C, and after irradiation with a fluence of 1×10^{16} cm^{-2}.

After irradiation and annealing, the intensity of the rocking curve increases, while the full width at half maximum (FWHM) reduces in comparison to the as-deposited state. The dependence of the rocking curve FWHM on ion fluence during irradiation and on temperature during annealing is presented in Figs. 4.12 (b) and (c), respectively. Both treatments lead to a decrease in the FWHM of the rocking curve, which can be attributed to the reduction of defects by both material treatment methods. This indicates an improvement in the crystalline phase of the film.[191] The initial defects can result from mosaicity, dislocations, and curvature that disturb the ideal parallelism of atomic planes in our polycrystalline NiFe layer with (111) texture.

Previous studies have demonstrated that room temperature irradiation mainly improves material uniformity[192] and induces interface intermixing.[99] Similarly, thermal annealing is a common technique to promote atomic diffusion[193] and crystallization.[194] In the literature, similar effects have been reported for

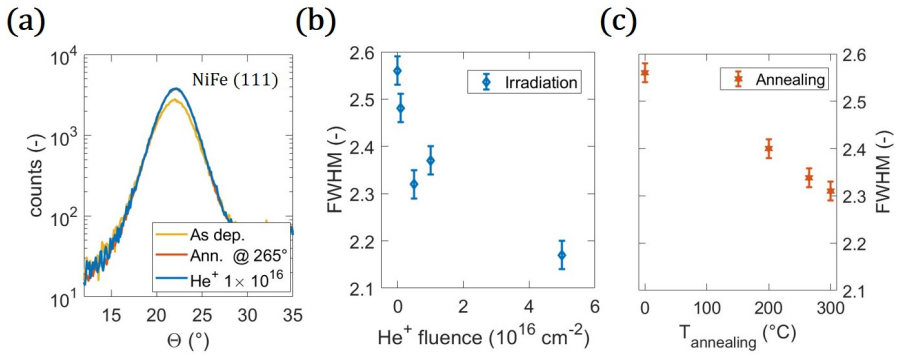

Figure 4.12: Details of the rocking curve measurements obtained with X-ray diffraction. (a) rocking curve of the NiFe (111) peak for the as deposited, irradiated and annealed samples. The fitted values of the FWHM of the rocking curves are reported as a function of ion fluence during irradiation (b) and as a function of temperature during annealing (c).

amorphous alloys where annealing[195] and He^+ irradiation[98,196] can enhance short range atomic mobility, enabling the growth of the ordered phase at the expense of its disordered or less ordered counterpart.

4.2.2.2 Magnetic measurements - anisotropy and coercivity

The thin film magnetic properties are measured with Kerr microscopy and are reported in Fig. 4.13. Figs. 4.13 (a) - (c) show the hysteresis curves for the NiFeCr(5 nm)/$Ni_{81}Fe_{19}$(30 nm)/Ta(4 nm) where the magnetic field is applied along two perpendicular in-plane directions: (a) for the as-deposited state, (b) after annealing and (c) after irradiation. The measurements refer to the magnetic contrast of the film structured into 80 µm disks.

Fig. 4.13 (a) shows the magnetic response of the Permalloy film in the as-deposited state. A weak uniaxial magnetic anisotropy K_u is present in the film, which can be associated with internal stresses during the material growth or asymmetries in the deposition system.[197] The value of $K_u = 80(7)\ \frac{J}{m^3}$ is determined by subtracting the area between the easy and hard axis loop of the as-deposited state as described in the experimental chapter, Sec. 3.3.5. The magnetic easy axis anisotropy direction can be inferred from the orientation of the magnetic domains at the remanent state (inset of Fig. 4.13 (a)). The in-plane magnetization direction is obtained by summing the horizontal and vertical components of the magnetic contrast. After annealing, the magnetic

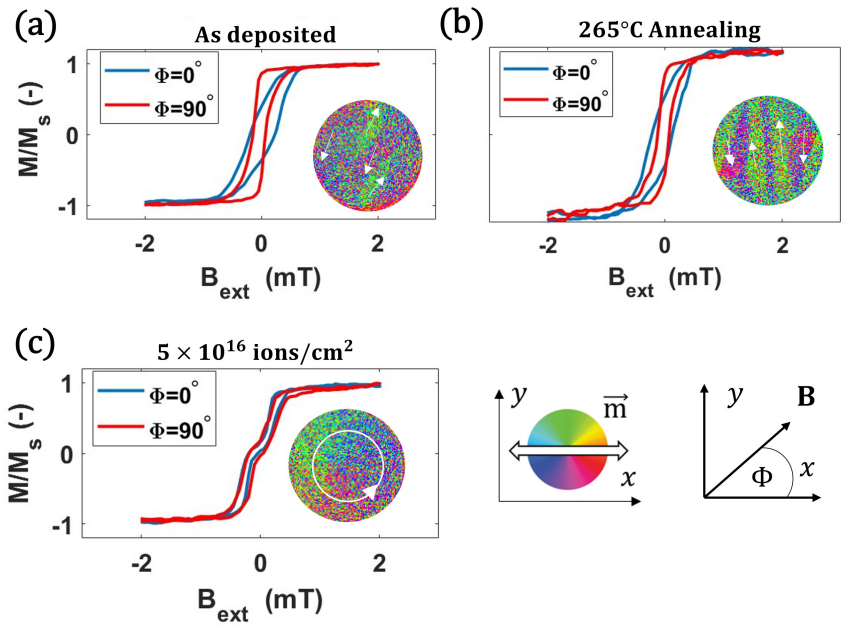

Figure 4.13: (a) - (c) in-plane hysteresis loops of NiFeCr(5 nm)/$Ni_{81}Fe_{19}$(30 nm)/Ta(4 nm) after sputtering, after thermal annealing and after He^+ ion irradiation, respectively. In the inset, the corresponding remanent magnetic state ($B_{ext} = 0$ mT) for 80 µm disks is shown. The field is applied along $\Phi = 0°$.

response of the film is measured again and is shown in Fig. 4.13 (b). The in-plane hysteresis loops still show the presence of uniaxial magnetic anisotropy, as confirmed by the remanent magnetic state (inset of Fig. 4.13 (b)) as the magnetic domains again orient along the easy axis direction $\Phi \simeq 90°$. The magnetic response of the irradiated Permalloy is shown in Fig. 4.13 (c) and is significantly different from the as-deposited and annealed cases. The low-field slope change observed in the hysteresis of Fig. 4.13 (c) is attributed to the creation of a magnetic vortex, as illustrated in the inset of Fig. 4.13 (c), accompanied by a sudden drop in magnetization upon decreasing the field from saturation.[198] Furthermore, the hysteresis loops now exhibit negligible angular dependence on Φ as can be seen from the overlapping curves in Fig. 4.13 (c). As a result of the reduced anisotropy after irradiation, the Permalloy exhibits a magnetization distribution in the form of a vortex at remanence, which is energetically preferred for disks with low induced anisotropy (inset of Fig. 4.13 (c)). Irradiation also lowers the hard-axis coercivity H_c since the linear movement of the vortex core in vortex structures minimizes hysteresis.[199]

Figure 4.14 (a) shows the angular dependence of the normalized remanent magnetization for the three samples. The as-deposited and annealed samples

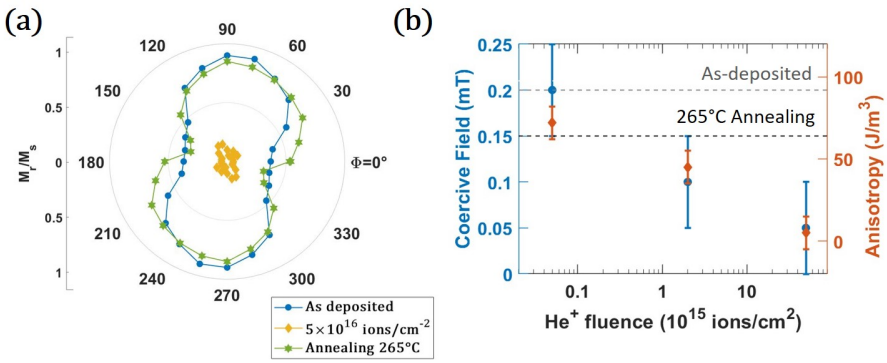

Figure 4.14: (a) angular plot of the normalized remanent magnetization M_r/M_s as function of the in-plane magnetic field direction Φ for as-deposited, irradiated and annealed samples. (b) coercive field (blue) and uniaxial magnetic anisotropy (orange) measured along the field direction $\Phi = 0°$ on a Permalloy sample irradiated with different fluences of ions during He^+ irradiation. For comparison, the values after annealing and in the as-deposited state are reported with dashed lines.

(shown in blue and green, respectively) exhibit uniaxial magnetic anisotropy with a sizable remanent magnetization at $\Phi \simeq 90°$. In contrast, the irradiated sample has a reduced remanent magnetization for all angles, which is typical for the vortex state seen that can be seen in the inset of Fig. 4.13 (c). To gain a better understanding of the enhancement of the magnetic softness of our Permalloy after irradiation, we gradually increased the He^+ fluence (cm^{-2}) while keeping the ion energy constant. The measurements of H_c and K_u as a function of He^+ ion fluence during irradiation are shown in Fig. 4.14 (b). The values for the as-deposited and annealed films are shown for comparison by dashed lines. No significant effects are observed for low fluences. However, at fluences larger than 5×10^{13} cm^{-2}, both the coercivity and anisotropy are progressively reduced as the He^+ fluence is increased. At the maximum fluence of 5×10^{16} cm^{-2}, H_c is reduced by a factor of five compared to the as-deposited state, while the induced anisotropy is decreased by a factor of ten. We do not observe a similar substantial reduction of these magnetic parameters after annealing.

One possible reason for the observed difference may be attributed to the distinct ordering mechanisms that occur during irradiation and annealing processes without magnetic field. Previous literature has reported improvements in atomic ordering in Permalloy films after annealing and irradiation with various ions.[186,200] Some studies on polycrystalline films[201,202] have shown that for temperatures ranging from 200 to 300° C, crystalline grain growth is more uniform for irradiation than for thermal annealing due to the differing mechanisms involved in altering the chemical ordering of the alloy.[203] These

$Ni_{81}Fe_{19}$	M_s (T)	K_u (J/m^3)	H_c (mT)	λ_s x10^{-6}	Y (GPa)
as-deposited	0.95(1)	78(5)	0.20(5)	-0.7(1)	200[159]
Ann. 265°C	0.95(1)	70(5)	0.15(5)	+0.04(9)	200[159]
He^+ 5 × 10^{16} cm^{-2}	0.91(1)	8(7)	0.05(5)	+0.01(9)	200[159]

Table 4.2: Parameters of the magnetic materials (thickness 30 nm) after deposition, annealing and He^+ ion irradiation. The values without reference are quantified experimentally. Here, M_s is the saturation magnetization, K_u is the uniaxial anisotropy constant, H_c is the coercive field, λ_s is the saturation magnetostriction and Y is the Young's modulus. The same value for Y is considered in all cases.

investigations suggest that radiation-induced mobility is more isotropic in the absence of a magnetic field compared to thermally-induced mobility.[180,203] The reader can refer to the experimental method chapter, Sec. 3.2.1. for more details. Accordingly, a stronger reduction in the magnetic anisotropy for the irradiated samples can be expected.

A first indication for the observed reduction in coercivity in our irradiated samples is the formation of a magnetic vortex in disk-patterned Permalloy (inset of Fig. 4.13 (c)). A recent study[192] compared ion irradiation with thermal annealing and analyzed the microscopic pinning parameters for domain wall (DW) motion. The annealed sample exhibited strong but widely distributed pinning sites, while the irradiated sample exhibited weaker defects with a higher density. As a result, the DW energy landscape is smoother after irradiation, allowing for domain formation and magnetization switching at lower magnetic fields. Additionally, the release of internal stresses in the film during irradiation[204,205] may also contribute to the improved soft magnetic properties of our Permalloy.

4.2.2.3 Strain dependent measurements - magnetostriction

In order to investigate the impact of ion irradiation and annealing on the magnetoelastic coupling of a thin magnetic Ni-Fe alloy, we have examined the strain-dependent magnetic properties of the material. Specifically, we applied uniaxial in-plane strain to a full film composed of NiFeCr (5 nm)/$Ni_{81}Fe_{19}$ (30 nm)/Ta (4 nm). The external strain is coupled to the magnetization via the anisotropy energy expression, so we used Kerr microscopy to measure the magnetic anisotropy before and after the strain application. The in-plane strain of $\varepsilon_{xx} = 0.06\%$ (tensile) is applied along the $\Phi = 0°$ direction. To determine the magnetostriction λ_s of the material we use Eq. 3.5 (see details in the

experimental chapter, Sec. 3.3.5) and the values of the Young's modulus in Table 4.2. The effective magnetostriction of the film for different He^+ fluences are reported in Fig. 4.15. In the as-deposited state and for He^+ fluences up to 10^{13} cm^{-2}, $\lambda_s = -7(2) \times 10^{-7}$ is negative, and an externally applied tensile strain increases the anisotropy field in the direction $\Phi = 0°$. As the fluence of ions during irradiation increases, the magnetostriction decreases and reaches values close to zero for a fluence of $5{\times}10^{16}$ cm^{-2}. In this case, the magnetoelastic anisotropy is negligible, and the material is insensitive to the applied strain. Accordingly the magnetization curves before and after the application of $\varepsilon_{xx} = 0.06\%$ are almost unchanged. The saturation magnetostriction of the magnetic layer after annealing is also measured and is reported in Fig. 4.15 for comparison. After annealing we also measure a value of magnetostriction $\lambda_s \simeq 0$ close to zero.

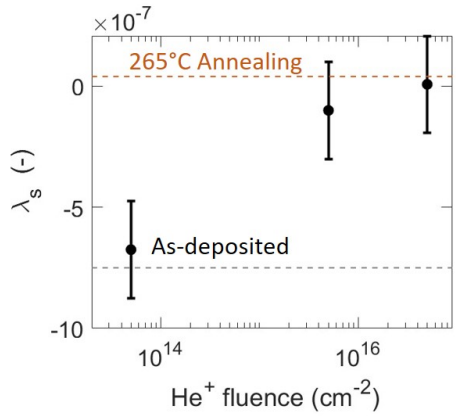

Figure 4.15: Saturation magnetostriction λ_s as a function of He^+ ions fluence during irradiation. The values as-deposited and after annealing are reported for comparison with dashed lines.

An additional confirmation of the magnetic behavior of the stack under applied strain is obtained by imaging domain formation using the magneto-optical Kerr effect (MOKE). The MOKE images in Figs. 4.16 (a) – (c) show how the magnetoelastic anisotropy affects the preferred direction of magnetic domains before and after the application of strain. In the as-deposited state (Fig. 4.16 (a)), the magnetization is aligned to the anisotropy easy axis induced during deposition. However, after the application of strain, the negative magnetostriction of the as-deposited sample causes the magnetic domains to orient themselves along the y direction, perpendicular to the uniaxial strain ε_{xx}. The domain pattern for a sample annealed at 265°C is shown in Fig. 4.16 (b). In this case, the remanent magnetic state is hardly affected by the applied strain due to the extremely low magnetostriction measured, resulting in negligible

magnetoelastic anisotropy $K_{ME} << K_u$. The sample irradiated with He^+ fluence 5×10^{16} cm^{-2} (Fig. 4.16 (c)) exhibits at remanence a magnetic vortex state that remains unchanged after the application of $\varepsilon_{xx} = 0.06\%$. The initial vortex state, which is unaffected by the application of strain, demonstrates that induced and magnetoelastic anisotropy are reduced to the point where only the shape anisotropy determines the remaining domain pattern.

In order to compare more quantitatively the MOKE images and the vortex state of the irradiated sample, the average radial magnetization is calculated for different in-plane Φ directions from the longitudinal component of the vector image, as described in the work of Gilbert et al.[206] The average contrast is determined for a single 80 µm disk from the images in Fig. 4.16 (c), and the results are shown in Fig. 4.16 (d). In the unstrained state, as shown in Fig. 4.16 (c) (left), the magnetization of the disk forms a circularly-symmetric vortex, and the average contrast varies periodically with the angular position on the disk, following the expression $a \sin(\phi b)$, which is shown as a black line in Fig. 4.16 (d). After the application of strain, due to the extremely small magnetostriction, the average contrast (red line in Fig. 4.16 (d)) still follows the same periodic behavior $a \sin(\phi b)$.

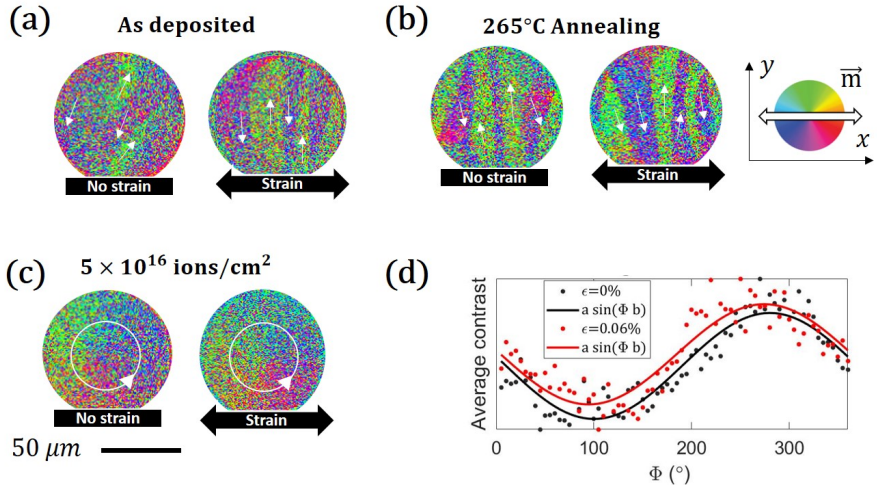

Figure 4.16: Remanent magnetic state for 80µm diameter disks before (left) and during (right) uniaxial strain 0.06% application for as-deposited (a), annealed (b) and irradiated Permalloy (c). (d) average contrast for 80 µm disks as a function of the in plane angle Φ for the irradiated sample in the remanent state (magnetic vortex state) before and after the application of strain.

One possible reason for the decrease in saturation magnetostriction observed after ion irradiation and annealing could be the increase in crystallite size in the NiFeCr(5 nm)/$Ni_{81}Fe_{19}$(30 nm)/Ta(4 nm) sample, which is highlighted in

Figs. 4.11 (c) and (d). The magnetostriction of isotropic cubic crystallites can be expressed as a combination of the saturation magnetostriction constants λ_{100} and λ_{111} in the (100) and (111) directions, respectively[158]

$$\lambda_s = \frac{2\lambda_{100} + 3\lambda_{111}}{5}. \tag{4.3}$$

In Permalloy, the two component of the magnetostriction change significantly over the relative Ni-Fe composition range altering the effective magnetostriction, λ_s. In our sample, which contains $Ni_{81}Fe_{19}$, the predicted λ_s value is close to zero.[164] Our XRD measurements show a 15% reduction in the (111) peak FWHM after ion irradiation and annealing, indicating crystallization along the thickness direction and therefore a possible change in the relative contribution of λ_{100} and λ_{111} in the magnetic layer. Following Eq. 4.3 the effective magnetostriction of the film can be affected by this change, as shown in Fig. 4.15, where the magnetostriction is progressively reduced with increasing fluence and annealing temperature as the size of crystallites increases due to irradiation and annealing. Additionally, increased intermixing at the boundaries of the magnetic layer could also alter the interface magnetostriction,[207] which is inversely proportional to the film thickness.[208,209] This could also play a role in the effective magnetostriction of the film as described in the multilayers system, Sec. 4.1.

4.2.2.4 Transport measurements - AMR

To assess the suitability of our Permalloy layer for sensing applications, we conducted transport measurements. The anisotropic magnetoresistance (AMR) effect occurs in $3d$ transition metals and can be observed macroscopically as a change in conductivity when a magnetic field is applied to a sample while current is flowing. The resistivity of the sample depends on the angle Φ between the magnetization direction and the current flow according to[15]

$$R(\Phi) = R_\perp + (R_\perp + R_\parallel)cos^2\Phi = R_\perp + \Delta R cos^2\Phi. \tag{4.4}$$

The magnitude of this effect can be quantified by the magnetoresistive coefficient

$$\frac{\Delta R}{R_\parallel}. \tag{4.5}$$

The AMR measurement of the film resistance as a function of the Φ angle are shown in Figs. 4.17 (a) and (b) for the as-deposited and irradiated sample, respectively. The results of the electrical characterization indicate that the NiFeCr(5 nm)/$Ni_{81}Fe_{19}$(30 nm)/Ta(4 nm) sample possesses a significant AMR of $\Delta R/R = 1.1(1)\%$ in the as-deposited state. Since the AMR does not change after irradiation, the proposed material treatment is appropriate for enhancing the magnetic properties of magnetic materials for sensing applications. For more information about the setup used for the AMR measurement, the reader can refer to Sec. 3.3.6 of this thesis.

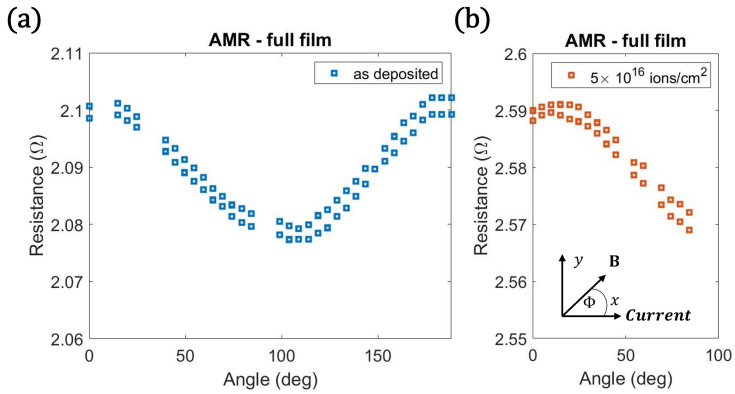

Figure 4.17: AMR measurements performed on a full film of $Ni_{81}Fe_{19}$ 30 nm before (a) and after (b) He^+ irradiation. A dose of 5×10^{16} cm^{-2} is considered.

Conclusions

In the study presented in Sec. 4.2, we examined and compared the impact of He^+ irradiation and thermal annealing on the magnetic properties of NiFeCr(5 nm)/$Ni_{81}Fe_{19}$(30 nm)/Ta(4 nm). According to our structural modification analysis using XRD, both treatments led to increased crystallization of the textured $Ni_{81}Fe_{19}$ alloy along the thickness direction. The irradiation resulted in a drastic reduction of the hard axis coercivity down to 0.05 mT and of the deposition-induced anisotropy by a factor of ten. This magnetic improvements can not be observed for the field-free annealing, that does not significantly enhance magnetic softness. We possibly attribute this to stress relaxation in the film after irradiation and to the completely isotropic mechanism for atomic ordering in the case of irradiation only. Additionally, we observed a significant decrease in the effective magnetostriction of the film by a factor of ten after irradiation and annealing, as confirmed by anisotropy measurement under in-plane strain. Importantly, we demonstrated that the sizable magnetoresistance is maintained after irradiation. Our results indicate that post-growth He^+ irradiation is a useful tool for enhancing magnetic softness and minimizing

strain cross-sensitivity of Permalloy. Unlike thermal annealing, ion irradiation enables local material treatment,[179,195,210] making it possible to adjust the anisotropy and directly write magnetic domain patterns into thin-film structured devices. This allows for the local tuning of magnetic material properties, making it suitable for applications such as high-sensitivity and low-hysteresis integrated AMR sensors that are insensitive to strain.

4.3 Strain effects of Co/Gd synthetic ferrimagnets

In the present section, we continue to investigate the strain dependent magnetic properties of magnetic materials. However, this time we focus on a different class of materials compared to those discussed in Sec. 4.1 and Sec. 4.2. Specifically, we investigate a ferrimagnetic system instead of a conventional ferromagnet. For a comprehensive review of ferrimagnets, interested readers are encouraged to consult the work of Kim et al.[211] We provide also a brief introduction to synthetic ferrimagnets in this section. The samples and the measurements for the work presented here were realized at TU/Eindhoven (NL) with the help of P. Li, T. J. Kools and A.A.D. Petrillo and the supervision of Prof. R. Lavrijsen.

Ferrimagnets are a class of magnets with unbalanced antiparallel-aligned sublattice moments. This unique combination of antiferromagnetic and ferromagnetic properties offers advantages such as finite Zeeman coupling, spin polarization, and non-adiabatic dynamics that could allow for all-optical switching (AOS) using femtosecond laser pulses.[211–213] AOS has been observed in rare earth-transition metal (RE-TM) ferrimagnetic alloys like GdFeCo and multilayer synthetic ferrimagnets such as Co/Gd and $[Co/Tb]_n$.[212,214,215] Synthetic ferrimagnets based on Co/Gd multilayers have particularly shown high potential for the use in integrated opto-spintronics devices, as they exhibit AOS without composition constraints imposed by alloy systems, as well as magnetic and angular momentum compensation that allows for ultrafast domain wall motion.[216–219] Current research has also reported the integration of Co/Gd synthetic ferrimagnets into optically switchable magnetic tunnel junctions.[220]

Recent advancements in spintronics have presented new possibilities for electronic applications beyond the standard CMOS, where ferrimagnets could be implemented. New concepts for high-density and ultrafast non-volatile data storage have been proposed in magnetic memories.[221,222] Over the years, ferrimagnets have been utilized in magnetic memories to enhance storage density,[223] as well as reading and writing speed,[224] and energy efficiency[225,226].[227,228] Additionally, single-pulse all optical-switching (AOS) of magnetization has enabled switching speeds below the ps timescale,[213,229–231] providing a promising foundation for a new generation of ultrafast data buffering in a single chip that integrates photonics with spintronics.[211,232–235]

When it comes to technological implementation, it is important to consider the effects of strain that may arise from processing steps like layer deposition and packaging.[236] The magnetic anisotropy of ferrimagnets can be affected by

intrinsic stresses and strain, which can alter the spin-orbit coupling (SOC) or the magnetization compensation, particularly in RE-TM alloys[237,238] where compensation temperature has been reported to be affected by strain.[239,240] Strain is omnipresent in applications,[241–243] it is therefore of interest to explore strain-dependent effects also in synthetic ferrimagnets.

The present section reports a systematic study of the effects of strain on Co/Gd synthetic ferrimagnets. By applying external strain through substrate bending, we investigate the impact on the perpendicular magnetic anisotropy (PMA) and magnetization compensation of [Co/Gd] and $[Co/Gd]_2$ multilayers. Using wedge samples and polar magneto-optic Kerr effect (pMOKE) measurements, we find that in-plane tensile strain increases the PMA, while a negative magnetostriction is observed. We also show that the effects of strain on the magnetization are mainly due to the modification of spin-orbit coupling within the magnetic layer and at the Pt/Co interface, which increases the magnetic anisotropy through magnetoelastic coupling. Furthermore, we find that the magnetization compensation point is not significantly affected by strain, as the magnetoelastic coupling influences the anisotropy rather than the magnetization of the two sublattices. These findings improve our understanding of magnetoelastic effects in ferrimagnetic multilayers and can aid in optimizing and developing spintronics devices, as well as in potential applications like magnetic memory and sensing.

The most part of the work reported in Sec. 4.3 has been published in the Journal of Applied Physics.[244]

4.3.1 Sample structure and characterization

The samples are grown on a 1.5 µm thick, thermally oxidized SiOx on top of a 625 µm thick Si substrate by DC magnetron sputtering in a chamber with a typical base pressure of 5×10^{-9} mBar. To obtain a wedge shaped thickness gradient, a shutter located near the sample is gradually closed during deposition. This enables the investigation of both compensation and spin reorientation transition (SRT) within a single sample. Two kinds of samples are produced. Firstly, a bilayer of Ta(4 nm)/Pt(4)/ Co(0-2)/Gd(t_{Gd})/TaN(4) with a constant Gd layer on top of a Co wedge is considered to study the SRT (Fig. 4.18 (a)). Secondly, a quadlayer of Ta(4)/Pt(4)/Co(0.6)/Gd(0-2)/Co(0.6)/Gd(1.5)/TaN(4) is grown, this time with a Gd wedge, to study the magnetization compensation (shown in Fig. 4.18 (b)).

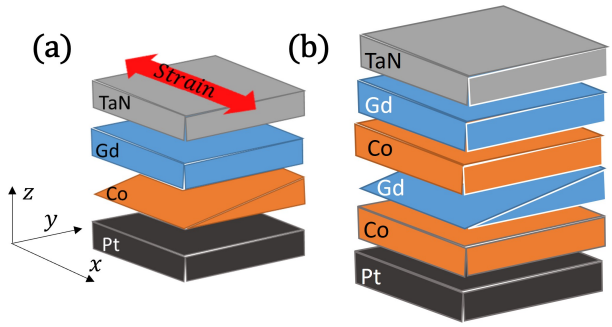

Figure 4.18: Sample sketch, red arrow indicates the direction of the applied strain. The bi-layer configuration (a) is used to investigate the SRT, while the configuration (b) is considered for studying the magnetization compensation.

The magnetic properties of these wedge samples are investigated by pMOKE, which is mostly sensitive to the out-of-plane (OOP) component of the Co magnetization at a wavelength of 658 nm. Fore more details about the pMOKE setup, the reader can refer to the experimental chapter, Sec. 3.3.1. According to Fig. 4.18 (a), the surface of the sample is scanned along the y-direction using a focused laser size with a spot-size of $\simeq$250 µm diameter. Accordingly, the local magnetic properties and hysteresis loops can be measured as a function of layer thickness, with a negligible thickness gradient < 0.025 nm within the used laser spot. All the measurements are performed at room temperature. To apply in-plane tensile strain to our multilayer, the substrate is mechanically bent using a three-point method used also for the studies in Sec. 4.1 and Sec. 4.2.

The in-plane strain with magnitude of 0.1% is measured with a strain gauge (RS PRO). The tensile strain is uniaxial along x and uniform in the measured area of the sample. More details about the strain generating device can be found in Sec. 3.3.5 of the experimental chapter.

4.3.2 Results and discussion

4.3.2.1 Spin reorientation transition in Co/Gd bilayers

The use of magnetic materials for high density data storage requires magnetic systems that are OOP magnetized.[245,246] In thin films, an OOP magnetic easy axis can be obtained by the anisotropy induced at the heavy metal

interface[247,248] (see also the theory chapter of this thesis, Sec. 2.2.4). Additionally, strain can influence the direction of the magnetic easy axis in systems with PMA.[249] To investigate the impact of external strain on Co/Gd systems with PMA, we examine bilayer samples consisting of Ta(4 nm)/Pt(4)/Co(0-2)/Gd(t_{Gd})/TaN(4). Specifically, we vary the Co thickness between 0 and 2 nm over a few mm along the y direction, while t_{Gd} remains constant (as shown in Fig. 4.18 (a)). In this system, the interfacial anisotropy energy (magnetocrystalline anisotropy energy at the Pt/Co interface) and demagnetization energy determine the effective magnetic anisotropy. The demagnetization energy increases with the thickness of the Co magnetic layer, and therefore, the magnetization shifts from OOP to IP. To measure the magnetization of our wedge sample, we record hysteresis loops from the pMOKE signal. We repeat the measurement by moving the laser spot along the wedge in the y direction. Initially, we examine a sample with t_{Gd}=0, and those measurements are shown in Figs. 4.19 (a) and (b). Fig. 4.19 (a) depicts the magnetic response of the Ta(4 nm)/Pt(4)/Co(0-2)/TaN(4) sample to an OOP magnetic film for different t_{Co}. The effective anisotropy K_{eff} is estimated[247] by recording hysteresis loops with a magnetic field applied OOP and IP, allowing us to determine the corresponding anisotropy energy per unit area K_s = 1.7 mJ/m^2. For t_{Co} = 1.35 nm, the square-shaped loop indicates PMA, with K_{eff}= 1.5(2)×10^5 J/m^3. A value of M_{Co} = 1.3 MA/m is used for the calculation. As the Co thickness is increased (moving the laser spot along the wedge direction - y), the remanence and squareness of the hysteresis loop decrease, along with the PMA of the system. For t_{Co} = 2.00 nm, the sample is IP magnetized, and K_{eff}= -0.8(2)×10^5 J/m^3 is negative. The OOP to IP transition occurs at t_{Co} = 1.85(2) nm in this system.

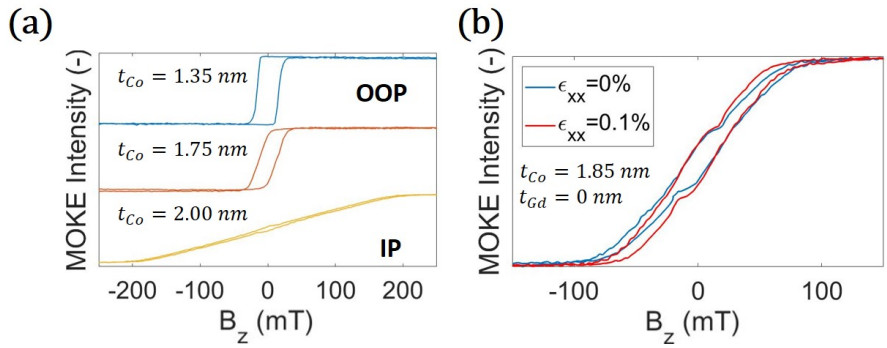

Figure 4.19: (a) Out of plane hysteresis loops of a Pt/Co/TaN stack for different Co thicknesses. (b) OOP hysteresis loops of Pt/Co(1.85 nm)/TaN before (blue) and after (red) application of 0.1% in-plane strain. The magnetic field was applied in the OOP direction, so along z.

To investigate the effects of externally applied in-plane strain, we perform the measurement again while bending the sample mechanically, as described in the experimental chapter, Sec. 3.3.5. The expression for the anisotropy energy can be used to describe the coupling between the magnetization and external strain.[93] When the strain in the film is non-zero, the magneto-elastic coupling of Co theoretically contributes to the effective anisotropy. Consequently, the total anisotropy K_{eff} of the magnetic stack is expected to change in the presence of external strain. In Fig. 4.19 (b), we present the OOP hysteresis loops of the Ta(4 nm)/Pt(4)/Co(1.85)/TaN(4) sample before (blue) and after (red) the application of a strain $\varepsilon_{xx} = 0.1\%$, where we observe a decrease in the anisotropy field following the application of in-plane strain. This occurs because of the positive strain-induced magnetoelastic anisotropy K_{ME} in this system, which we expect from a material with negative magnetostriction like Co.[249,250] Accordingly, the PMA is increased by the applied strain, allowing even a thicker Co system to reach OOP magnetization in contrast to the unstrained sample.

After this preliminary study on Pt/Co systems, we shift our focus to the magnetostriction of Co/Gd multilayers. The magnetostriction in Co-Gd alloys is reported to be heavily dependent on the composition[251,252] due to the structural changes caused by different atomic content. In contrast to this scenario, the effects of magnetostriction of a multilayer, are expected to be dependent on the magnetoelastic coupling of the individual layers.[99]

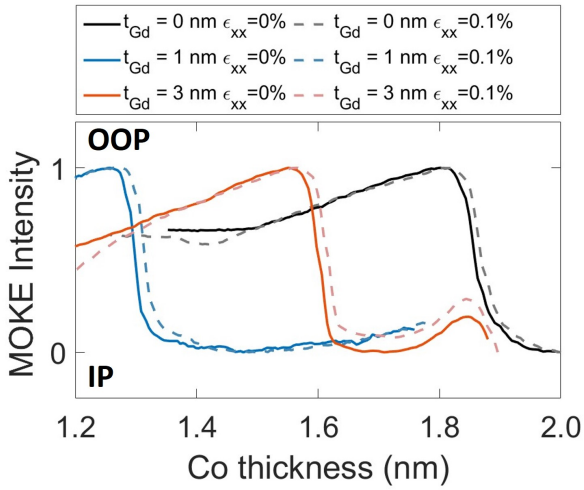

Figure 4.20: MOKE intensity scan at remanence (no applied field) of Pt/Co/Gd/TaN films along the Co wedge for different thicknesses of the top Gd layer. Solid (dashed) lines consider measurements before (during) the application of strain.

To investigate the magnetostriction of a Co/Gd multilayer, we add a constant

layer of Gd on top of the Co wedge with two different thicknesses, 1 nm and 3 nm, to perform thickness-dependent studies. The magnetization in the Gd layers is mainly induced at the interface with the Co layer, and couples anti-parallel to the Co magnetization.[214] Accordingly, the Co thickness t_{Co} required to reach SRT is expected to change with increasing t_{Gd}.[253] To compare the SRT of Ta(4 nm)/Pt(4)/Co(0-2)/Gd(t_{Gd})/TaN(4) samples with different t_{Gd}, we conducted remanent intensity scans along the Co wedge and hysteresis loop measurements. After saturating the sample with an out-of-plane (OOP) magnetic field of 1T, we determined the thickness-dependent remanence from the pMOKE signal without external magnetic field. These measurements are reported in Fig. 4.20. The normalized remanent intensity, which is sensitive to the OOP component of Co magnetization, drops to zero at the SRT, where the magnetization rotates in-plane (IP). We observed the SRT in samples with different Gd thicknesses before and after applying strain. The critical thickness $t_{Co} = t_c$ at which SRT occurs changes significantly in the presence of a Gd layer (previously reported by Kools et al.[253]), and the in-plane strain shifts the OOP to IP transition towards larger Co thickness (see Fig. 4.20), consistent for all investigated samples. This suggests that the effective magnetostriction of the Co/Gd bilayer is negative, and its value $\lambda_s = -10(5) \times 10^{-6}$ is not significantly altered by the thickness of the Gd layer.

To obtain a quantitative understanding of the shape of the spin reorientation boundary, we use an analytical model[253] to describe the magnetostatic free energy of the anisotropy, which is zero at the SRT boundary. The first energy terms of the model are the demagnetization energies of the Co layer

$$E_{d,Co} = \frac{1}{2}\mu_0 \int_0^y M_{Co}^2 \, dq = \frac{1}{2}\mu_0 M_{Co}^2 y \tag{4.6}$$

and of the Gd layer

$$\begin{aligned} E_{d,Gd} = \frac{1}{2}\mu_0 \int_0^x M_{Gd}^2 exp(-2q/\lambda_{Gd}) \, dq = \\ \frac{1}{4}\mu_0 M_{Gd}^2 \lambda_{Gd} \left(1 - \exp\left(\frac{-2x}{\lambda_{Gd}}\right)\right) \end{aligned} \tag{4.7}$$

where λ_{Gd} is the characteristic decay length of the Gd magnetization, which is induced at the Co/Gd interface, M_{Co} is the magnetization of the Co layer, M_{Gd} is the effective Gd magnetization at the interface between Co and Gd and x and y are, respectively, the Gd and Co thicknesses in the diagram of Fig. 4.21 (a). The magnetocrystalline anisotropy is included with the term

$$E_K = K_s - \Delta K \left(1 - \exp\left(\frac{-2x}{\lambda_K}\right)\right), \tag{4.8}$$

and it is also considered to decay with a characteristic decay length λ_K and magnitude ΔK. The second term in Eq. 4.8 represents the experimentally observed decay in effective anisotropy, which can result from the sputter-induced disordering of the Co.[254] In addition to this anisotropy term, the model also includes an energy term, E_{mix}, which accounts for mixing at the interfaces of the magnetic layers where the local net magnetization is zero. The expression is

$$\begin{array}{l} E_{mix} = \frac{1}{2}\mu_0 \int_0^{a_0 x} M_{Co}^2 + \left(M_{Gd} exp(-q/\lambda_{Gd})\right)^2 \, dq = \\ \frac{1}{2}\mu_0 a_0 M_{Co}^2 x + \frac{1}{4}\mu_0 \lambda_{Gd} M_{Gd}^2 \left(1 - \exp\left(\frac{-2a_0 x}{\lambda_{Gd}}\right)\right). \end{array} \tag{4.9}$$

In this model, the expression of the total free energy density per unit area is, considering all the terms mentioned so far:

$$E_{tot} = -E_K - E_{mix} + E_{d,Co} + E_{d,Gd}. \tag{4.10}$$

Therefore, the total energy E_{tot}, can be explicitly written as

$$\begin{array}{l} E_{tot} = -K_s + \Delta K \left(1 - \exp\left(\frac{-2x}{\lambda_K}\right)\right) - \frac{1}{2}\mu_0 a_0 M_{Co}^2 x \\ -\frac{1}{4}\mu_0 \lambda_{Gd} M_{Gd}^2 \left(1 - \exp\left(\frac{-2a_0 x}{\lambda_{Gd}}\right)\right) + \frac{1}{2}\mu_0 M_{Co}^2 y \\ +\frac{1}{4}\mu_0 M_{Gd}^2 \lambda_{Gd} \left(1 - \exp\left(\frac{-2x}{\lambda_{Gd}}\right)\right). \end{array} \tag{4.11}$$

The parameters λ_K, λ_{Gd} and ΔK for our Co/Gd bilayer are determined using a numerical fit. All the other parameters are either experimentally measured or taken from literature and are reported in Table 4.3. The magnetocrystalline anisotropy energy per unit area K_s, due to the Pt/Co interface is assumed to be constant. To fit this equation to the phase diagram obtained experimentally, it is convenient to find the Co-thickness (y) where the anisotropy energy (E_{tot}) is equal to zero (spin reorientation transition, SRT). Solving Eq. 4.11 for y yields:

$$\begin{array}{l} y_0(x) = \frac{2}{M_{Co}^2 \mu_0} \left(-\left(K_s - \Delta K \left(1 - \exp\left(\frac{-x}{\lambda_K}\right)\right)\right)\right) - \frac{1}{2}\mu_0 a_0 M_{Co}^2 x \\ -\frac{1}{4}\mu_0 \lambda_{Gd} M_{Gd}^2 \left(1 - \exp\left(\frac{-2a_0 x}{\lambda_{Gd}}\right)\right) + \frac{1}{4}\mu_0 M_{Gd}^2 \lambda_{Gd} \left(1 - \exp\left(\frac{-2x}{\lambda_{Gd}}\right)\right). \end{array} \tag{4.12}$$

Parameter	Value	Description
K_s	1.7 mJ/m^2	Interfacial anisotropy (from exp.)
K_{ME}	0.02 mJ/m^2	Magnetoelastic anisotropy (from exp.)
M_{Co}	1.3 MA/m	Cobalt magnetization (from exp.)
M_{Gd}	1.4 MA/m	Gadolinium magnetization at Co/Gd interface (from Ref.[253])
a_0	0.13 (-)	Growth parameter of intermixing region (from exp.)
λ_K	0.51(15) nm	Change of PMA energy characteristic decay length (Fit parameter)
λ_{Gd}	0.59(22) nm	Gd magnetization decay characteristic decay length (Fit parameter)
Δ_K	3.96(41)$\times 10^{-4}$ J/m^2	Change of PMA energy (Fit parameter)

Table 4.3: Parameters used in the model for the magnetostatics of uncompensated Co/Gd synthetic ferrimagnets used for the calculations of the SRT. The term K_{ME} is considered zero for when external strain is not applied to the sample.

Once the parameters are estimated, Eq. 4.11, describing the total energy of a Ta(4nm)/Pt(4)/Co(t_{Co})/ Gd(t_{Gd})/TaN(4) sample, can be solved for y (t_{Co}) by imposing $E_{tot} = 0$ (spin reorientation transition). The solution for the SRT obtained with the model described above is reported in Fig. 4.21 (a) using a blue solid line in a phase diagram where t_{Gd} (x) and t_{Co} (y) range from 0 to 3 nm and from 0 to 2 nm, respectively. The experimentally measured SRT without externally applied strain is also shown in Fig. 4.21 (a) with blue diamonds, and is in good agreement with the general trend of the model calculations. However, some discrepancies between the experimental and model values are observed for $t_{Gd} = 0$, which may be attributed to additional mixing between the layers.

To include the effects of strain, a magnetoelastic anisotropy $K_{ME} = -\frac{3}{2}\lambda_s Y \varepsilon$ is added to Eq. 4.10 that becomes

$$E_{tot} = -E_K - E_{mix} - K_{ME} + E_{d,Co} + E_{d,Gd}. \tag{4.13}$$

In our experiments, the value of $K_{ME} = 0.02$ mJ/m^2 corresponds to the magnetoelastic anisotropy induced by applying an in-plane strain of 0.1%. As shown in Fig. 4.20, we do not observe significant changes to K_{ME} with increasing t_{Gd}. To incorporate the magnetoelastic term, Eq. 4.13 is solved again for the SRT-boundary at $E_{tot} = 0$, and the solution is shown in Fig. 4.21 (a) with an orange solid line. Since the material has negative magnetostriction, K_{ME} adds to K_s, resulting in an enhancement of the PMA under in-plane

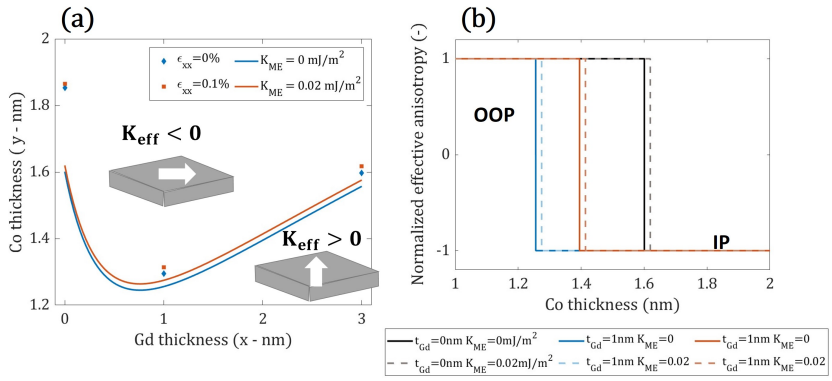

Figure 4.21: (a) 2D phase diagram of the SRT of the a $Ta(4nm)/Pt(4)/Co(t_{Co})/Gd(t_{Gd})/TaN(4)$ stack as a function of t_{Gd} (x) and t_{Co} (y). Blue diamonds and red squares correspond to the experimental data, reported without and with strain applied, respectively. The solid lines indicate the calculated values using the model for the magnetostatics and Eq. 4.13. A magnetoelastic anisotropy $K_{ME} = 0$ and 0.02 mJ/m^2 is considered, respectively, for the blue and orange curve. (b) Spin Reorientation Transition of a $Ta(4nm)/Pt(4)/Co(t_{Co})/Gd(t_{Gd})/TaN(4)$ sample calculated for values of $t_{Gd} = 0$, 1 and 3 nm and plotted as a function of t_{Co}. The SRT is represented here by a step function. Solid and dashed lines consider $K_{ME} = 0$ and 0.02 mJ/m^2, respectively.

strain. Therefore, the calculated SRT is shifted to larger values of t_{Co}. This trend is consistent with the experimentally determined SRT when an external strain of $\varepsilon_{xx} = 0.1\%$ is applied (shown as orange squares in Fig. 4.21 (a)).

To visualize the spin reorientation transition (SRT), Eq. 4.13 can be solved for fixed values of t_{Gd} to obtain the critical thickness of t_{Co} at which $E_{tot} = 0$. This approach generates a step function in the SRT diagram shown in Fig. 4.21 (b), which is equivalent to the MOKE remanence scan depicted in Fig. 4.20. The values of Gd thicknesses considered are $t_{Gd} = 0$, 1 and 3 nm and are plotted in Fig. 4.21 (b) with solid lines in black (0 nm), blue (1 nm) and orange (3 nm). Solid lines consider $K_{ME} = 0$ mJ/m^2. To include the effect of magnetoelastic anisotropy, dashed lines are used to represent the SRT models calculated with $K_{ME} = 0.02$ mJ/m^2, as shown in Fig. 4.21 (b). The SRT models can be correlated with the experimental remanent intensity scan in Fig. 4.20. The behavior predicted by the model is similar to the experimental results, showing that the SRT point shifts as the Gd layer thickness increases. The SRT point is also shifted due to the effect of magnetoelastic anisotropy and external strain, as seen in Fig. 4.21 (b) and Fig. 4.20, respectively. As we expect from a negative magnetostrictive material, K_s adds to K_{ME}, therefore the PMA is increased and the Co/Gd bilayer stays OOP magnetized for thicker Co (corresponding to larger $E_{d,Co}$). We confirm that the major effect of strain

on the Ta(4 nm)/Pt(4)/ Co(0-2)/Gd(t_{Gd})/TaN(4) sample is the change of the PMA.

In this section, we examined the impact of in-plane strain on the effective PMA of a Co/Gd ferrimagnetic bilayer. Our results indicate that the stack exhibits negative magnetostriction for the thickness values studied. To model the magnetostatics of this system, we base on a recent study that accounts for the influence of strain purely as magnetoelastic anisotropy. The outcomes of our experiments are consistent with the predictions obtained from this model, leading to a better comprehension of the response of this material to external strain.

4.3.2.2 Magnetization compensation in quadlayer systems

In ferrimagnetic materials, magnetization compensation is possible when the total magnetization $\boldsymbol{M_{tot}} = \boldsymbol{M_{Gd}} + \boldsymbol{M_{Co}}$ becomes zero due to the equal and opposite magnetization contributions from the two sub-lattices.

Previous studies have reported changes in saturation magnetization due to strain in epitaxial ferrimagnetic films[238] and rare earth-free ferrimagnets.[237] To investigate the effects of strain on magnetization compensation in synthetic ferrimagnets, we studied a quad-layer sample[253] consisting of Ta(4 nm)/Pt(4)/Co(0.6)/Gd(0-2)/Co(0.6)/Gd(1.5)/TaN(4), as shown in Fig. 4.18 (b). The thickness of the bottom Gd layer is varied between 0 and 2 nm over a few mm, while all other layers has a constant thickness. This choice of a quadlayer makes magnetization compensation easier to achieve. Compared to a Co/Gd bilayer, the quadlayer has two times the magnetic volume of the Co and three times the number of Co/Gd interfaces, where magnetization is induced in the Gd through direct exchange with the Co.

The growing thickness of Gd, increases the contribution of $\boldsymbol{M_{Gd}}$ to $\boldsymbol{M_{tot}}$. For this reason, some areas of the wedge sample are Co-dominated (for $t_{Gd} < t_{comp}$) and others are Gd-dominated (for $t_{Gd} > t_{comp}$) with $\boldsymbol{M_{tot}} = 0$ at $t_{Gd} = t_{comp}$. Here, t_{comp} is the thickness where magnetization compensation is achieved. When a magnetization compensation occurs, two effects are expected: a divergence of the coercivity and a sign change in the remanent pMOKE signal (Kerr rotation, normalized to its value in the absence of Gd). The coercivity data are extracted from hysteresis loops measured across the wedge direction (along y) and are reported in Fig. 4.22 (a). The sign change in the pMOKE signal is due to the alignment of the Gd magnetization along the field direction in the Gd-dominated regime. We observed magnetization compensation in this quad-layer for $t_{Gd} = 1.25$ nm.

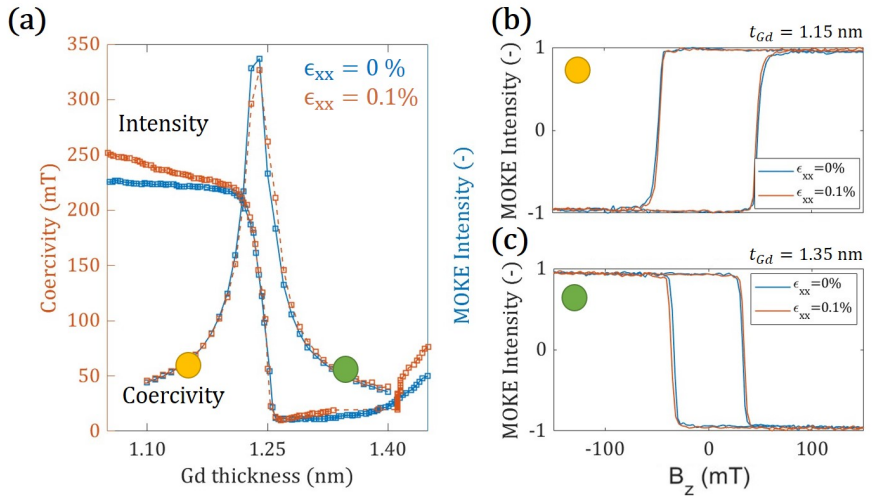

Figure 4.22: (a) remanent pMOKE intensity scan and coercivity as a function of t_{Gd}. Measurements before (blue) and after (orange) application of in-plane strain are reported. (b) hysteresis loops in the Co dominated and (c) Gd dominated state. Both curves with (orange) and without (blue) in-plane strain applied are shown. The magnetic field was applied in the OOP direction, so along z.

In a similar manner to what we have done investigating the PMA in the bilayer system, we repeated the measurement in the presence of ε_{xx} =0.1% in-plane strain. The results are shown in orange in Figure 4.22 (a). Notably, the Co/Gd quadlayer compensation point remains unaltered despite the application of external strain.

Figs. 4.22 (b) and (c) show OOP hysteresis loops of Ta(4 nm)/Pt(4)/Co(0.6)/Gd(t_{Gd})/Co(0.6)/Gd(1.5)/TaN(4) samples for $t_{Gd} = 1.15$ nm and $t_{Gd} = 1.35$ nm, respectively, and highlight the effect of magnetization compensation. The sample is in this case OOP magnetized. As the thickness of Gd is increased, the magnetization of the sample goes from being Co-dominated (Fig. 4.22(b)) to Gd-dominated (Fig. 4.22(c)). The hysteresis loops invert because for $t_{Gd} > 1.25$ nm, the Co-magnetization aligns antiparallel to the field, resulting in a change in the sign of the pMOKE signal. When the measurement is conducted again in the presence of 0.1% strain (orange line), there are no significant changes to the remanent intensity or coercivity compared to the unstrained case (blue line). These findings suggest that multilayer systems can achieve magnetization compensation under external strain, and importantly, the magnetization compensation point remains unaffected. This is in contrast to recent observations in ferrimagnetic alloys, where the compensation temperature changes with strain.[239,240]

In the recent study by Wang et al.,[240] strain was observed to induce alterations in the compensation temperature of GdFeCo ferrimagnetic alloys, which were attributed to variations in lattice constant caused by strain. First principle calculations indicated that this lattice strain affects the exchange coupling strength in GdFeCo and the moment of Gd. However, in the case of synthetic ferrimagnets, the ferromagnetic coupling within each layer is not strongly influenced by in-plane strain.

Synthetic ferrimagnets consist of two sublattices confined to separate layers, and Gd magnetization is induced at the Co/Gd interface, where the exchange energy is highest.[214,216] In other words, the composition gradient (where magnetization is primarily induced) occurs in the z-direction. Therefore, magnetization compensation in synthetic ferrimagnets arises from the balance between Co magnetization and Gd magnetization within the individual layers.[218,253] The total magnetic moment per unit area, denoted as $\boldsymbol{M_{tot}}$, is obtained by integrating the magnetization of the Co and Gd sublattices over their respective layer thicknesses.

In multilayer samples with perpendicular magnetic anisotropy (PMA), the main effect of in-plane strain, typically on the order of 0.1%, is the modification of spin-orbit coupling within a single layer.[255] This alteration affects the magnetocrystalline anisotropy energy of the system,[256] rather than the magnetic moment of Co and Gd within a single layer. Consequently, in a ferrimagnetic multilayer, in-plane strain is not expected to impact the induced magnetic moment from Co to Gd, thereby preserving magnetization compensation. This observation aligns with our experimental results, demonstrating strain-independent magnetization compensation in a synthetic ferrimagnet within the range of strain magnitudes investigated.

Conclusions

To summarize, the content of section Sec. 4.3 contains our strain dependent studies on synthetic ferrimagnets. Our study focuses on the effect of external strain on PMA and magnetization compensation of Co/Gd systems at room temperature. We have grown wedge samples with varied magnetic layer thickness to determine thickness-dependent transitions in the magnetostatics of this multilayer system, and applied deliberate in-plane strain to the samples.

In a bilayer Pt/Co/Gd system, we experimentally measure a significant magnetoelastic coupling that changes the SRT in the presence of strain. We included the contribution of the strain-anisotropy in a model for the magnetostatics, which describes the experimental observations well if an effective negative magnetostriction is considered.

In a Pt/Co/Gd/Co/Gd quadlayer, we achieved magnetization compensation of the two sub-lattices by varying the thickness of the bottom Gd layer. We found that the application of in-plane strain does not affect the magnetization compensation, as the induced magnetic moment from the Co onto the Gd is an interface effect in a multilayer system that is not altered by mechanical deformation. Overall, Sec. 4.3 provides a comprehensive understanding of the magnetoelastic properties of these multilayer systems. As PMA and magnetic compensation are maintained in the presence of externally applied strain, these materials are promising for technological implementation of ferrimagnets, where strain can be induced by layer deposition and packaging.

5

Strain effects in domain-wall-based sensors

In the present chapter, the second part of the results of this thesis are presented. The findings highlight the manipulation and positioning of magnetic domain walls using different types of strain for sensors and other applications. It is shown how controlled strain can improve and even realize new functionalities of these devices.

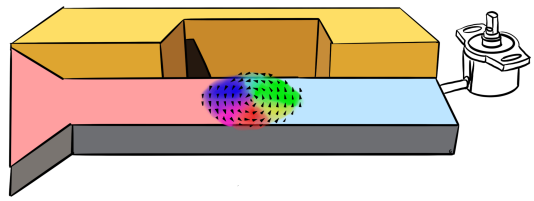

Contents

As described in Chap. 1, domain walls have long been valued for their static and dynamic properties in the context of spintronics for data storage and logic devices.[257–259] With the ability to create and study magnetic nanostructures over the past 15 years, researchers have been able to explore diverse spin textures, their formation, and stability. This extensive investigation has resulted in the incorporation of DWs in memory devices[54,222] and a variety of magnetic sensors.[15,260–262] For instance, a DW - delimiting two magnetic domains - has the potential to store information about the angular position of an object and to count the number of rotations performed in a non-volatile manner.[61,263,264] The benefit of magnetic sensors that employ DWs is their robustness, allowing for their non-volatile positioning in a variety of applications. Additionally, no external electrical power is required to alter the magnetic state in the sensor, rendering it ideal for energy-efficient systems, including those that may experience power outages. Although the functioning of the sensor is understood under ideal conditions, other factors come into play in actual devices that were previously overlooked. As explained in this study, mechanical strain or stress on these sensing components is recognized as a crucial concern among the external factors.

In contrast to Chap. 4, where the focus is the improvement and manipulation of magnetoelastic material properties, in this chapter the effects of different types of strain on a DW sensor device are discussed. In Sec. 5.1, uniform strain - equivalent to the one induced by dice packaging - is considered, and its effects on the magnetization are found to be strongly compensated with careful material preparation. A spatially varying strain (space dependent, constant in time) is used in Sec. 5.2. This leads to the conceptualization and realization of a new type of magnetic sensor. The possibility to have time dependent strain is exploited in Sec. 5.3 where DW devices are tested in the presence of surface acoustic waves.

5.1 Strain-controlled domain wall injection

The magnetic field conditions that allow a DW based sensor to function reliably is known as the field operating window.[265] This requires the successful creation and propagation of a DW into the nanowire, setting the minimum operation field value. However, the uncontrolled nucleation of domain walls at higher fields needs to be avoided, setting the maximum operation field value. Previous studies have examined the propagation and nucleation fields and their dependence on material parameters and device geometry.[61, 69, 70, 265–267]Instead of describing this sensor system as idealized, we consider in this study the presence of uniform strain. Such strain occurs during packaging as well as sensor operation, with potentially strong impact on the device performance.[268]

Strain in magnetic materials induces a preferential direction of magnetization, known as anisotropy (see Sec. 2.2.4.1), due to magnetoelastic coupling, and can even pin a DW in a nanowire.[269] In DW based devices, a common approach to generate a DW is to use a larger magnetic pad attached to the nanowire (as shown in as shown in Fig. 5.1 (c) - (d)), exploiting the reduced shape anisotropy.[267, 270, 271] Recent simulations have shown that strain-induced anisotropy can overcome the shape anisotropy in the nucleation pad, which governs the switching of the magnetic state.[272] However, previous studies did not report experiments on strain effects in a sensor relevant system.

In this section, we investigate experimentally the impact of externally applied strain on the injection of a 180° domain wall from a nucleation pad in a magnetic nanowire. We use MOKE microscopy to image the DW creation, pinning, and injection from the pad for different external strain configurations. The injection field strongly depends on the effective anisotropy of the magnetic material, which is modified by strain. Simulations are used to identify the switching mechanism and the spin structure of a pinned DW just before its injection into the wire.

The content of Sec. 5.1 has been published in the Journal of Applied Physics.[93]

5.1.1 Sample structure and characterization

Three different samples consisting of the following layers are considered, and are deposited using DC magnetron sputtering: $Co_{40}Fe_{40}B_{20}$ (30 nm)/Ta(4),

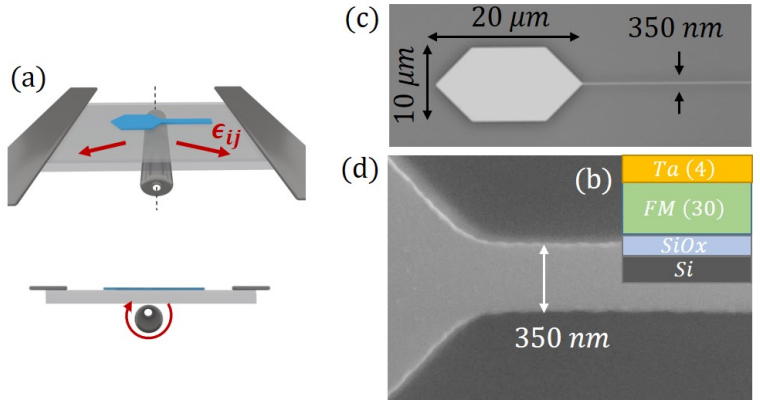

Figure 5.1: (a) Schematic of the mechanism to apply mechanical strain by three-point substrate bending. (b) Layer cross-section used for the investigated devices. FM indicates the magnetic material, the numbers correspond to the thickness in nm. The SiOx and Si thicknesses are 1.5 µm and 625 µm respectively. Device shown in an optical microscope (c) and scanning electron microscope image(d).

$NiFe_{11}Cr_{42}(4)/Ni_{82}Fe_{18}(30)/Ta(4)$, and Ni(30)/Pt(2). The substrate is made of thermally oxidized SiOx that is 1.5 µm thick, on top of 625 µm Si. To improve magnetic softness and deposition uniformity, we use a rotating magnetic field of 50 Oe during the sputtering of the magnetic material. As result, we obtain a soft magnetic material with low intrinsic anisotropy and coercive fields. The magnetic characteristics of our films, as deposited, are provided in Table 5.1. Our X-ray diffraction measurements suggest that the values for Young's modulus and saturation magnetostriction are unaffected by the annealing step. We utilize a BH-Looper to characterize our material and for measuring magnetostriction as described in Sec. 3.3.2.

Material	M_s (T)	B_k (mT)	B_c (mT)	λ_s x10^{-6}	Y (GPa)
$Co_{40}Fe_{40}B_{20}$	1.40(5)	0.20(5)	0.10(5)	27(1)	187^{273}
$Ni_{82}Fe_{18}$	0.95(5)	0.10(5)	0.10(5)	-0.5(1)	200^{159}
Ni	0.60(5)	2.00(5)	2.00(5)	$-32^{156,274}$	180^{157}

Table 5.1: Parameters of the magnetic materials (thickness 30 nm) after deposition (no annealing). The values without reference are quantified experimentally by measuring the magnetic film on 5" wafers. Here, M_s is the saturation magnetization, B_k is the anisotropy field, B_c is the coercive field, λ_s is the saturation magnetostriction and Y is the Young's modulus. The same Y and λ_s are considered for as deposited and annealed samples.

In order to create a preferred direction of magnetization in $Co_{40}Fe_{40}B_{20}$, a static magnetic field of 120 mT is applied while annealing the sample in N_2 at a temperature of 265°C for 2 hours. This treatment induces a uniaxial

anisotropy, resulting in an easy axis of magnetization in the direction of the applied field[275–277] (see Sec. 3.2.2). The anisotropy field and constant after annealing are B_k=2.7 mT and K_{film}=1.54(2) kJ/m^3, respectively. The as-deposited $Co_{40}Fe_{40}B_{20}$ material already has a weak uniaxial anisotropy of $K_{film} < 50(5)$ J/m^3, likely due to internal stresses during material growth or asymmetries in the deposition system.[278] This value is 30 times smaller compared to the anisotropy field induced by thermal annealing with a magnetic field, allowing to ignore its contribution in this study. A comparison of the angular dependence of the remanent magnetization and hysteresis loops before and after annealing are shown for $Co_{40}Fe_{40}B_{20}$, respectively in Figs. 5.2 (a) and (b) - (c).

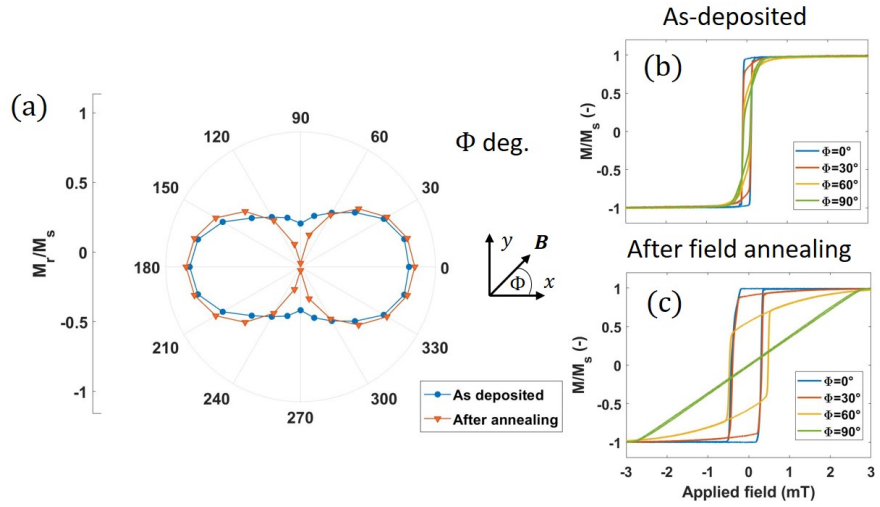

Figure 5.2: Characterization of the full film 5" wafers of $Co_{40}Fe_{40}B_{20}$ using a BH Looper before structuring. (a) The angular dependence of the remanent magnetization M_r/M_s shows the effects of thermal annealing in presence of magnetic field (orange triangles), that induces a uniaxial anisotropy with easy axis in the direction $\Phi = 0°$. Error bars are within the data points. The magnetic curves of the sample as deposited (b) and after annealing (c) show a easy axis and a hard axis of magnetization in blue and green, respectively. Orange and yellow are intermediate direction of applied magnetic field.

To create the devices used in this study, photolithography and Ar ion milling are used to pattern the structures. The devices consist of a nucleation pad (20 µm × 10 µm) attached to a nanowire that varied in width from 350 nm to 800 nm with an overall length of 200 µm. The geometry of the pad is designed to narrow the field distribution and allow for a domain wall (DW) nucleation at low fields.

To switch the magnetization in the devices, an external in-plane magnetic

field in the x-direction is applied. As the magnitude of the field increased, the nucleated DW is depinned from the pad and is injected into the nanowire. The injection field, B_{inj} is measured by imaging differential contrast changes in the magneto-optical Kerr effect (MOKE) in a longitudinal configuration of the polarized white light using a 50x magnification objective. The injection field is measured at fields lower than the spontaneous domain nucleation field in the wire (around 40 mT[265]) to ensure that the DW is injected from the pad into the wire and not from structure defects or nucleated at the edge of the wire. To apply strain to the devices, the substrate is mechanically bent using a three-point method that applied an out of plane force, resulting in a tensile strain in the plane of the sample up to 0.12%. This device is schematically shown in Fig. 5.1(a) and is described in Sec. 3.3.5. The strain is mostly uniaxial[279] and uniform in the central area of the sample, and the intensity of the strain is measured using a strain gauge. The stack is thin enough to assume that the strain is entirely transferred to the device, and shear strain is negligible.[280]

5.1.2 Results and discussion

5.1.2.1 Injection field in nanowires

The minimum field required to generate and propagate a domain wall (DW) in a magnetic sensor device is known as the injection field. However, to ensure a dependable and repeatable injection, a comprehensive understanding of the entire DW injection process is required. By using MOKE imaging (as shown in Fig 5.3), we can observe the gradual switching of magnetization in the nucleation pad, which leads to the creation of a DW at its end, as well as the moment when the DW starts to propagate into the wire.

In the absence of strain, the shape anisotropy mainly governs the domain configuration in the pad and does not vary significantly for the materials studied, resulting in similar images for all measured devices. Figs. 5.3 (a) - (c) illustrate the injection process. When the substrate is not under any strain, a pattern with multiple magnetic domains is formed (Fig. 5.3 (b) and Fig. 5.5 (b)), with a DW at the entrance of the nanowire for fields as low as 1 mT. However, the DW is unable to propagate into the nanowire at such low fields and is pinned at its entrance due to the difference in geometry between the pad and wire, which creates a local pinning site for the DW. It is this wall that

can then be injected to propagate along the wire.[281] To achieve injection into the wire, the external field must be increased.

If the substrate of our device is mechanically deformed (strained), an additional anisotropy is induced in the magnetic system. This strain-induced anisotropy competes with the shape anisotropy to determine the domain configuration and the switching mechanism in the injection pad. The expression of the free energy[282] reveals how the magnetization is coupled to the uniform macroscopic strain. In the theory section, Sec. 2.2.4.1, we have described how the magnetoelastic energy simplifies to a uniaxial magnetic anisotropy constant according to

$$K_{ME} = \frac{3}{2}\lambda_s Y|\varepsilon_{xx} - \varepsilon_{yy}|, \tag{5.1}$$

reported here for convenience. In Eq. 5.1 λ_s is the saturation magnetostriction, Y is the Young's modulus of the ferromagnetic layer and ε_{xx}, ε_{yy} are the components of the uniaxial in-plane strain along, respectively, x and y. In our experiments, we apply a strain magnitude of $\varepsilon_{ii} = 0.06\%$, where ii indicates the direction of uniaxial strain. This particular strain magnitude is chosen because it avoids sample breaking and is sufficient to probe strain effects on the injection field. Assuming that the strain is uniaxial and tensile, we can neglect the other direction ($\varepsilon_{yy} << \varepsilon_{xx}$ and vice versa). This implies that the strength and direction of the uniaxial anisotropy contribution is determined by the magnitude and sign of the saturation magnetostriction, respectively. In a positive magnetostrictive material such as $Co_{40}Fe_{40}B_{20}$, the easy axis follows the direction of the tensile strain, while a negative magnetostrictive material like Ni has an hard axis in this direction.

Our experimental observations show that strain modifies the conditions for nucleation and injection of domain walls (DWs). When the wire's easy axis of magnetization is aligned with the wire's length (i.e., in the x-direction), the coercive field of the pad increases, causing a sudden rotation of the magnetization from left to right, as depicted in Figs. 5.3 (d)-(f). In this case, there is no intermediate multi-domain state present in the pad, and the DW is not pinned at the wire's entrance because the coercive field coincides with the injection field. The second case is represented in Figs. 5.3 (g)-(i), where the easy axis of magnetization is induced perpendicular to the field direction (i.e., along the y-direction). In this case, the multi-domain state (Fig. 5.3 (h)) that minimizes the energy in the pad prefers a spin aligned along the y-axis, and a DW is nucleated at the entrance of the pad. The nucleated DW remains pinned at the entrance even for higher fields than in the unstrained case.

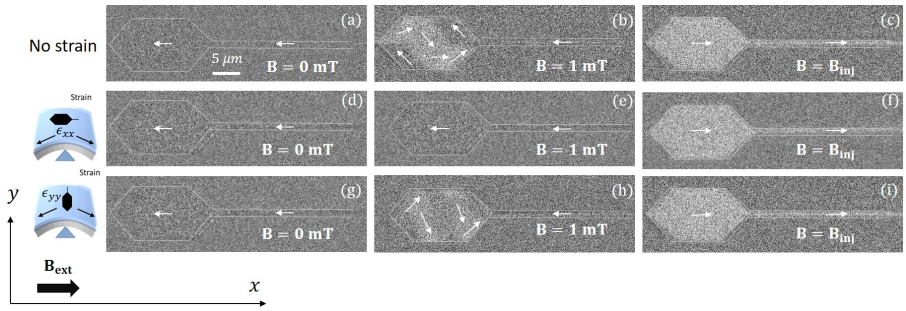

Figure 5.3: Kerr microscope images of the device made of $Co_{40}Fe_{40}B_{20}$ as deposited (no annealing). The white arrows indicate the local direction of the magnetization. The width of the nanowire is 350 nm. The field is applied along the x direction and progressively increased (from left to right) until the DW nucleated in the pad is injected into the nanowire. In (a) - (c) the sample is not strained, (d) - (f) tensile strain is applied along the wire $\varepsilon_{xx} = 0.06\%$, and (g) - (i) tensile strain is applied perpendicular to the wire $\varepsilon_{yy} = 0.06\%$.

By using the values in Table 5.1 and Eq. 5.1, we can calculate the uniaxial anisotropy constant due to the magnetoelastic term, denoted by K_{ME}. For $Co_{40}Fe_{40}B_{20}$, K_{ME} is calculated to be 3.6(1) kJ/m^3, for Ni it is $K_{ME} = -4.3(1)$ kJ/m^3, and for $Ni_{82}Fe_{18}$ it is $K_{ME} = -7(1) \times 10^{-2}$ kJ/m^3. The sign of K_{ME} is determined by the magnetostrictive constant. Therefore, the energetically favorable state for the magnetization direction is along the x-direction for $Co_{40}Fe_{40}B_{20}$ or perpendicular to the direction of tensile strain for Ni. The effects of strain are expected to be more than 50 times smaller in devices made of $Ni_{82}Fe_{18}$.

Fig. 5.4 presents experimental results for the injection field B_{inj} of three different materials, and it is observed that materials with strong magnetoelastic coupling - in Figs. 5.4 (a) and (c) - display the largest strain effects. As a result, for $Ni_{82}Fe_{18}$, which has low magnetoelastic coupling, the three curves overlap within the error bars, confirming that the observed changes in the injection field are caused by strain.

One observation is that in magnetostrictive materials, strain always increases the injection field, setting a lower limit for sensor operation. When an easy axis along the x direction is created, the pad coercivity increases, leading to a higher injection field, such as in the case of ε_{xx} for $Co_{40}Fe_{40}B_{20}$ and ε_{yy} for Ni. Conversely, when the easy axis is oriented along the y direction (ε_{yy} for $Co_{40}Fe_{40}B_{20}$ and ε_{xx} for Ni), the DW created at the mouth of the pad finds this position more energetically favorable than the wire, thus requiring a larger injection field.

Another observation relates to the wire width dependence of the injection field.

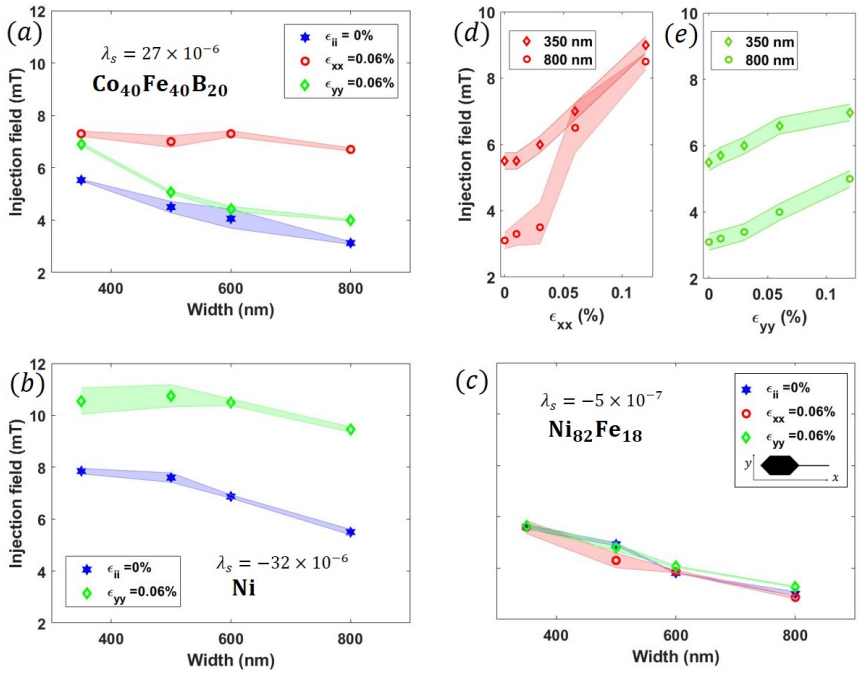

Figure 5.4: Experimental results of the injection field B_{inj}. Three different ferromagnetic materials (thickness 30 nm) are measured: (a) $Co_{40}Fe_{40}B_{20}$, (b) Ni and (c) $Ni_{82}Fe_{18}$. The experimental values are plotted as a function of the nominal width of the nanowire. For the blue data points no strain is applied. Uniaxial strain ε_{ii} is applied in the x or in the y direction for the red and green curve, respectively as schematically shown in the inset. (d) - (e) B_{inj} for $Co_{40}Fe_{40}B_{20}$ is plotted as a function of the intensity of the strain applied along the x and the y direction respectively, for selected wire widths.

When no strain is applied ($\varepsilon_{xx} = \varepsilon_{yy} = 0$), the injection field decreases as the wire width increases, regardless of the material. This is because the injection field in soft magnetic wires is mainly determined by the cross section (width and thickness[283–285]). However, when magnetoelastic anisotropy energy is introduced, deviations from this dependence are observed. When K_{ME} favors a spin orientation along the x direction, the injection field is determined by the coercivity of the pad, and the dependence of the injection field on the wire width is negligible for thin wires (Fig. 5.4 (a), red circles and Fig. 5.4 (b), green diamonds). In all other cases, the DW stays pinned at the edge of the pad, and a dependence of B_{inj} on the wire width is observed. Interestingly, when the strain-induced easy axis of magnetization is perpendicular to the wire, the dependence of B_{inj} on the wire width is maintained (Fig. 5.4 (a), green diamonds).

We can explain this behavior considering the different contributions to the free energy of the system F_{tot} which measures the angular dependence of the magnetic hardness. In a system with no net crystalline anisotropy, the free energy is given by[274, 286]

$$F_{tot} = F_{zeeman} + F_{demag} + F_{magel}. \tag{5.2}$$

F_{zeeman} describes the influence of the external magnetic field, and F_{demag} depends on the shape of the device (shape anisotropy). The last term describes the influence of the lattice strain to the magnetic anisotropy $F_{magel} = K_{ME} sin^2(\phi)$ according to Eq. 5.1, where ϕ is the angle between the magnetization and the easy axis. As described in the theory chapter, Sec. 2.3, the easy axis of magnetization corresponds with minima in the expression of F_{tot}.

Let us compare the case where there is no strain ($F_{magel} = 0$) to the case where there is strain ($K^y_{ME} \neq 0$) with the easy axis aligned with the y-axis. The strain-induced uniaxial anisotropy favors a spin configuration with wider domain walls in the nucleation pad, where a large part of the magnetization is pointing along the y-axis. Both MOKE images and simulated spin structures confirm this observation. The injection field, which is determined by the energy difference between a domain wall at the edge of the pad and inside the wire[284] ($\Delta E^{DW} = E^{DW} wire - E^{DW} pad$), depends on the energy barrier ΔE^{DW}, which is larger when $K^y_{ME} \neq 0$ due to the preference for a narrow domain wall inside the wire.[287] This explains why a larger external applied field is needed to inject the domain wall, as seen in the experiments. The experimental data in Figs. 5.4 (d) - (e) provide additional information about the different energy terms in Eq. 5.2. When B_{inj} for $Co_{40}Fe_{40}B_{20}$ is plotted against the intensity of the applied strain (shown in Fig. 5.4 (d) - (e)), the behavior is consistent with the magnetoelastic energy term F_{magel} calculated using Eq. 5.1, where a linear dependence of B_{inj} against the applied strain is expected. These data also demonstrate that the impact of the device shape (energy term F_{demag}) becomes insignificant in the presence of large strain along the wire (ε_{xx}), while it remains significant if the strain is perpendicular to the device (ε_{yy}).

5.1.2.2 Micromagnetic simulation of domain wall injection

Micromagnetic simulations using *Mumax* are conducted to better comprehend the impact of strain on the injection field. More details about the micromagnetic simulations can be found in Sec. 3.4.1 of this thesis. The material parameter used (experimentally measured) are $\lambda_s = 2.7 \times 10^{-5}$ and $M_s = 1.0 \times 10^6$ A/m

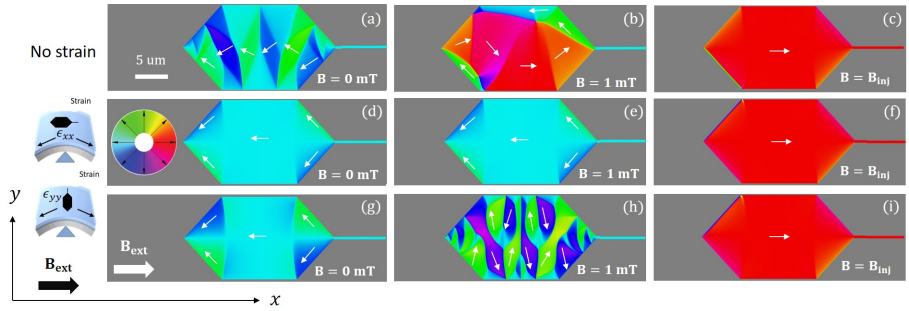

Figure 5.5: Snapshots of the simulations performed with the $Mumax^3$ framework. We used material parameters of amorphous $Co_{40}Fe_{40}B_{20}$. The field is applied along the x direction and progressively increased (from left to right) until the DW nucleated in the pad is injected into the nanowire (300 nm wide). (a) - (c) strain is not included, (d) - (f) uniform tensile strain along the wire is applied, $\varepsilon_{xx} = 0.06\%$, and (g) - (i) uniform tensile strain is applied perpendicular to the wire, $\varepsilon_{yy} = 0.06\%$. The order of the images follows Fig. 5.3, and a comparison confirms the same switching mechanism observed in the experiments.

for saturation magnetostriction and magnetization, respectively, whereas for the exchange and elastic constants typical values for $Co_{40}Fe_{40}B_{20}$ reported in the literature are used:[273] $A_{ex} = 1.5 \times 10^{-11}$ J/m, $c_{11} = 2.8 \times 10^{11}$ N/m^2, $c_{12} = 1.4 \times 10^{11}$ N/m^2 and $c_{44} = 0.7 \times 10^{11}$ N/m^2. Since the anisotropy for the as-deposited samples is below 50 J/m^3, the first-order uniaxial anisotropy constant is disregarded in the simulations as its energy effect is negligible.

The simulations are performed on a pad with the same dimensions as the physical system (Fig. 5.1 (c)), except for the nanowire that is shortened to 2.5 µm. The computational region is divided into $5 \times 5 \times 15$ nm^3 cells, and mechanical stress is modeled by adding a magnetoelastic field contribution to the effective field.[36,288] The magnetization is initialized uniformly oriented along the $-x$ direction, and the equilibrium state is calculated for a series of increasing applied fields. The results of the simulations are shown in Fig. 5.5 and can be compared with the Kerr microscope images in Fig. 5.3. The double vortex pattern in the absence of strain (Fig. 5.3 (b) and Fig. 5.5 (b)) is reproduced by the simulations, as well as the almost uniform configuration for $\varepsilon_{xx} = 0.06\%$ (Figs. 5.3 (e) and 5.5 (e)) and the multi-domain state favoring the magnetization pointing along y for $\varepsilon_{yy} = 0.06\%$ (Figs. 5.3 (h) and 5.5 (h)).

In addition to the equilibrium magnetic state, also B_{inj} is calculated using simulations for different strain directions. The computed injection fields as a function of the wire width are plotted in the lower part of Fig. 5.6 together with the experimental ones. Simulations and experiments show good quantitative agreement except for the cases where the tensile strain is applied along x, in which the computed values are significantly below the experimental ones.

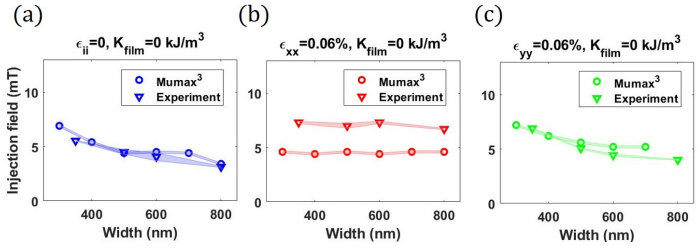

Figure 5.6: (a) - (c) comparison between the calculated and measured B_{inj} for the indicated strain configurations.

Both the decrease in the injection field for increasing the wire width - cases of no strain (Fig. 5.6 (a)) and $\varepsilon_{yy} = 0.06\%$ (Fig. 5.6 (c)) - as well as the negligible dependence for $\varepsilon_{xx} = 0.06\%$ in Fig. 5.6 (b) are well captured by the simulations, supporting our interpretation of the experimental results.

In summary, we report that the injection field is proportional to the uniaxial strain ε_{xx} or ε_{yy} for a positive magnetostrictive material such as $Co_{40}Fe_{40}B_{20}$ (ε_{xx} Fig. 5.4 (d) or ε_{yy} Fig. 5.4 (e)), and only when the easy axis of magnetization is aligned along the wire, the injection field coincides with B_c of the pad, and the wire width dependence is low. The overview of the effects of strain on the injection field is presented in Fig. 5.4 (a) and our interpretation is supported by micromagnetic simulations.

5.1.2.3 Effects of field induced anisotropy

So far, our study has focused on isotropic and magnetically soft ferromagnetic materials, where the main contribution to the anisotropy energy is a strain-induced uniaxial anisotropy constant of $K_{ME} \simeq 3 - 5$ kJ/m^3 in the film. To further investigate into the DW nucleation and injection mechanism, we fabricated our devices using $Co_{40}Fe_{40}B_{20}$ that is thermally annealed in the presence of a uniform magnetic field, as described in Sec. 3.2.2 of the experimental chapter. The numerical value for the Young's modulus listed in Table 5.1 is used for this case as well. This preparation method resulted in a preferential orientation or easy axis (EA) for the magnetization, aligned with the applied magnetic field direction during annealing. The uniaxial anisotropy K_{film} is experimentally determined to be 1.54(2) kJ/m^3 from the full film hysteresis loops reported in Figs. 5.2 (b) and (c). To include this contribution, an additional term is added to the free energy Eq. 5.2 that becomes

$$F_{tot} = F_{zeeman} + F_{demag} + F_{magel} + F_{film}, \tag{5.3}$$

where $F_{film} = K_{film} sin^2(\phi)$ is the free energy term of the induced anisotropy, which may compete with strain-induced anisotropy and alter the magnetization orientation effects.

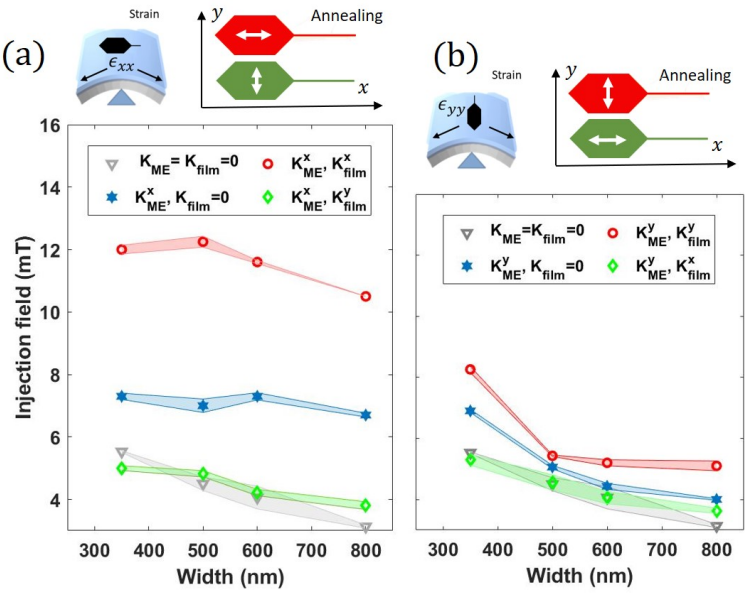

Figure 5.7: Experimentally determined injection field for $Co_{40}Fe_{40}B_{20}$. Here samples with and without annealing are compared. (a) $\varepsilon_{xx} = 0.06\%$ in-plane strain is applied and (b) $\varepsilon_{yy} = 0.06\%$. K_{ME} and K_{film} are the uniaxial magnetic anisotropy constants due to strain and annealing, respectively. The apexes indicate the in-plane direction of the uniaxial anisotropy. Grey triangles are, for comparison, the reference case where no strain is applied. The scheme on the right shows the direction of the magnetic field applied during annealing (white arrows) relative to the tensile strain (black arrows).

Based on this information, the experiment described in Sec. 5.1.2.1 is repeated using annealed $Co_{40}Fe_{40}B_{20}$ samples. Notably, significant effects are observed when both the magnetoelastic anisotropy K_{ME} and K_{film} are superimposed. The results of this experiment are presented in Fig. 5.7, which compares the annealed films with the as-deposited samples. When the directions of K_{ME} and K_{film} are parallel, the effective uniaxial anisotropy is increased (as indicated by a larger injection field for the red points in Fig. 5.7). When two different uniaxial anisotropy contributions point in the same direction, the resulting film anisotropy is still uniaxial but now has an equivalent anisotropy constant $K_{eq} \propto K_{ME} + K_{film}$, as experimentally confirmed by an increase in

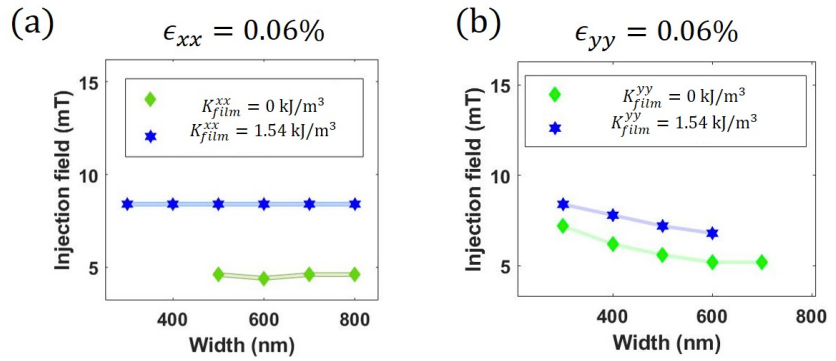

Figure 5.8: The calculated values for B_{inj} (using Mumax simulations) are reported for induced easy axis along the x and y directions in (a) and (b), respectively. The simulations considered the strain effects on a as deposited sample (green diamonds) or a sample annealed with magnetic field in the strain direction (blue stars).

the anisotropy field B_k measured along the hard axis of magnetization. Two distinct scenarios can be observed for parallel anisotropies: when K^x_{ME} and K^x_{film} are oriented along x, the resulting easy axis is along the wire (red circles in Fig. 5.7(a)), which increases the coercive field of the pad and, consequently, also grows the injection field. When K^y_{ME} and K^y_{film} are oriented with the easy axis along y, the resulting anisotropy energetically favors the positioning of the DW at the extremity of the pad. As a result, ΔE^{DW} and B_{inj} are larger (red circles in Fig. 5.7(b)).

The effects of magnetoelastic and annealing induced anisotropy on the injection field have also been corroborated using micromagnetic simulations. In Fig. 5.8 the simulated B_{inj} is reported for a device where the easy axis directions of K_{ME} and K_{film} are parallel and along x (Fig. 5.8 (a)) or y (Fig. 5.8 (b)). In both cases it is evident how the increased effective anisotropy (blue hexagram, where the deposition induced anisotropy is non-zero) makes B_{inj} larger which is in agreement the experimental data shown in Fig. 5.7. In addition to that, the dependence of B_{inj} as function of the device width is well captured by those simulations. The negative slope in Fig. 5.8 (b) agrees with Fig. 5.7 (b) while the negligible dependence in Fig. 5.8 (a) agrees with Fig. 5.7 (a). The negligible slope is attributed to the direction of the nanowire, patterned along the easy axis of magnetization.

The scenario for two anisotropy contributions, K_{ME} and K_{fim}, having perpendicular easy axis directions to each other is the nontrivial case. In this situation, the injection field values are experimentally reduced (green points in Fig. 5.7) and are close to those of the non-strained sample (gray triangles in Fig. 5.7). This is a significant result as it indicates that the impact of

effective anisotropy on the device (increased by the strain) can be mitigated through material preparation. This outcome may seem surprising, considering the difference in strength between the two contributions, $K_{ME} = 3.6$ kJ/m^3 and $K_{film} = 1.54$ kJ/m^3. However, it should be noted that the concept of an "effective" uniaxial magnetic anisotropy K_{eq} is not applicable unless the anisotropies are oriented in identical directions.

In order to understand these findings, a comprehensive characterization of the entire film material is conducted using MOKE hysteresis loops in the presence of strain and annealing-induced anisotropy. The most general case considers a magnetic energy represented by two perpendicular uniaxial magnetic anisotropy axes. We measured the angular dependence of the normalized remanent magnetization M_r/M_s as a function of the angle Φ between the external magnetic field and the magnetization's easy axis. Fig. 5.9 compares the cases of K^x_{ME}, K^x_{film} and K^x_{ME}, K^y_{film}. In both cases, the strain is determining the dominant easy axis, as $K_{ME} > K_{film}$. However, differences are observed in the angular plots of M_r in the vicinity of the hard axis ($\Phi = 90°$) in Fig. 5.9. The precise identification of the magnetic easy axis is achieved by fitting the normalized magnetic hysteresis M_r/M_s curves as a function of Φ. Since the projection of the in-plane magnetization vector to the plane of incidence of light during our MOKE measurements is a cosine-like function (as evident from the inset in Fig. 5.9), the following fitting function is chosen:[289]

$$\frac{M_r}{M_s} = \frac{M_r^{max}}{M_s}|cos(\Phi)| + \frac{M_r^{off}}{M_s} \tag{5.4}$$

where $\frac{M_r^{max}}{M_s}$ is the maximum normalized magnetic remanence, and $\frac{M_r^{off}}{M_s}$ is the offset in magnetic remanence M_r. The strength of the uniaxial magnetic anisotropy is the amplitude of the fitting parameter, and the offset originates from the isotropic contribution of the film.

The fit confirms that the easy axis aligns with the strain direction $\Phi = 0°$. Nonetheless, when K_{ME} is perpendicular to K_{film}, the strength of the predominant magnetic easy axis substantially diminishes. To be more precise, a comparison between the two scenarios of K_{ME} being parallel and perpendicular to K_{film} reveals that the ratio of the offset $\frac{M_r^{off}}{M_s}$ increases from 0.02 to 0.21, whereas the maximum remanence reduces from 1.00 to 0.75. This implies that the annealing-induced anisotropy, counteracts the strain-induced easy axis anisotropy, when the relative orientation of these two contribution is 90°. The pure uniaxial anisotropy is therefore modified and its strength reduced.

The observed results and consideration on the full film material properties can explain the experimentally determined injection field. As shown by green

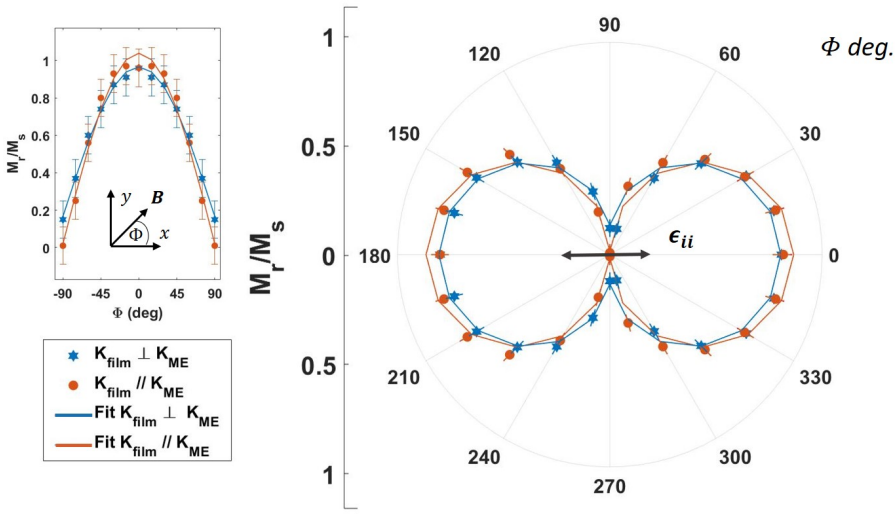

Figure 5.9: Angular dependence of the normalized remanent magnetization of full film $Co_{40}Fe_{40}B_{20}$. The material is strained along Φ =0° and measured with MOKE contrast. In orange (circles) and blue (stars) the magnetic field during annealing is applied along Φ =0° and 90° respectively. The experimental values are fitted using Eq. 5.4 of M_r, and are here showed with lines. The offset of M_r along the hard axis (Φ =90°) shows the overlap of two perpendicular uniaxial anisotropy directions (biaxial anisotropy), where the magnetoelastic contribution is dominant $K_{film} < K_{ME}$. On the left, the data are displayed in a 2D plot.

diamonds in Fig. 5.7, the effects of strain on B_{inj} can be strongly reduced by annealing $Co_{40}Fe_{40}B_{20}$ with a magnetic field perpendicular to the strain direction. In a material with a larger $\frac{M_r^{off}}{M_s}$ ratio, the coherent rotation of the magnetization requires less energy, which results in a decrease of the anisotropy field and coercive field. Consequently, the film becomes magnetically softer, and the magnetic properties of the blue points in Fig. 5.9 are closer to the ones of the unstrained as-deposited state depicted in Fig. 5.2 (a). These findings support the results displayed in Fig. 5.7, where the green ($K_{ME} \perp K_{film}$) and gray (no anisotropy) data points overlap.

The softness of the material has therefore a direct impact on the creation and nucleation of the domain wall in the nucleation pad, as well as on the injection field, because the energy difference between the DW at the mouth of the pad and in the nanowire is affected by the film properties. It is worth noting that the DW energy in the thin long wire remains unaffected by the presence of an annealing-induced anisotropy, as the strong shape anisotropy[290] is approximately 10^4 J/m^3. However, in the nucleation pad (with lower shape anisotropy), if the strength of the uniaxial magnetic anisotropy decreases, the

magnetization can rotate freely in the field direction, similar to the unstrained as-deposited state.

Conclusions

To summarize, the study presented in Sec. 5.1 explores how mechanical strain impacts the injection of a domain wall into a nanowire using MOKE microscopy and Mumax micromagnetic simulations. By considering $Co_{40}Fe_{40}B_{20}$, Ni, and $Ni_{82}Fe_{18}$ films we find that the effects of strain are proportional to the material's magnetoelastic coupling, which is represented by the saturation magnetostriction λ_s. Uniaxial strain leads to a uniaxial magnetic anisotropy and increases the injection field up to 30%, particularly in materials with high magnetostriction. Our experimental results indicate that the DW injection mechanism depends primarily on DW creation in the pad. Additional experiments involved thermal annealing with a magnetic field for $Co_{40}Fe_{40}B_{20}$, which introduces another uniaxial magnetic anisotropy that contributes to the injection field. The strain-induced uniaxial anisotropy K_{ME} can be strengthened or weakened using annealing-induced uniaxial anisotropy K_{film}, respectively parallel or perpendicular to the strain contribution. If the magnetization's easy axis is along the wire direction, the coercive field of the nucleation pad increases considerably. Conversely, low anisotropy facilitates magnetization switching and leads to DW creation at low fields at the pad's extremity. The DW stays pinned at the wire entrance until the energy difference $\Delta E^{DW} = E^{DW}_{wire} - E^{DW}_{pad}$ is comparable with the Zeeman energy (higher external fields). E^{DW} is a combination of different anisotropies that can be tailored through the device design and material preparation. Micromagnetic simulations validate our results and can identify the lower limit for reliable DW injection. Thus, during optimization and development of magnetic sensors and devices based on domain walls, the impact of strain and material preparation has to be considered. Our findings demonstrate that a magnetostrictive-free behavior of DW-based devices can be achieved even in systems with finite magnetostriction. Careful material preparation, can counteract the magnetoelastic effects and increase the device robustness against strain. This can be best understood and using the model of an effective anisotropy.

5.2 Imprinted strain gradients for spintronics

Nanomagnetic and spintronic devices are considered as promising "Beyond CMOS" technology due to their non-volatile nature, high operating speed, low power consumption, and established methods for data reading and writing.[291] An example of this technology is nanomagnetic networks, which use soft ferromagnetic nanowires to propagate and manipulate information stored in domain walls (DWs) through dipolar interaction.[292,293] Manipulating DWs has been a focus of research for a long time, with a current-controlled magnetic DW shift register (racetrack memory)[294] being a significant milestone in this area. As discussed in Sec. 5.1, DW-based memories,[295] logic devices,[296] sensors,[2,12,297] and neuromorphic computing[298,299] have been suggested using domain walls. Although magnetic domain walls are a relatively mature technology compared to other spin structures (e.g., skyrmions[300]), there are still many obstacles to overcome before full technological realization is achieved. Ensuring the feasibility of the fabrication processes and compatibility with existing CMOS devices are major challenges that need to be addressed for these technologies to be established.

Manipulating DWs is a major challenge in these devices and has been researched for many years. One commonly used method for pinning DWs involves using geometric constraints like notches[301–303] or the local manipulation of magnetic anisotropy through magnetoelastic coupling and strain.[66,93] Magnetostrictive/piezoelectric systems are commonly used to generate controllable strain, but their high production cost and complexity make them unattractive for most sensor manufacturers. For example, achieving high-resolution notches or depositing multiferroic stacks would require expensive investments in tools for high-resolution lithography and layer deposition. Furthermore, piezoelectric actuation via metallic contacts increases design complexity and area usage, making the system even more expensive to manufacture. Additionally, it is challenging to confine electric fields to realize an arbitrary shape of strain and strain gradients down to the micrometer range with piezoelectric substrates.[304] An alternative method for transferring strain to a thin film is to use an additional layer at the interface.[105] Capping layers are widely used in the semiconductor and photovoltaic industries to provide protection from hostile environments, but some of these layers are known to induce severe stresses when deposited on Si/SiOx wafers.[305,306]

In Sec. 5.2, we make one step forward with respect to Sec. 5.1 as we do not consider a uniform strain anymore, but the strain is made a spatially variable quantity along the domain-wall device. To create such local strain, we

demonstrate an inexpensive and CMOS-compatible method that is based on removing certain areas of the passivation layer. The magnitude and profile of the strain are determined through anisotropy and stress measurements and finite element simulations. We also take advantage of the magnetoelastic effect to alter the energy of a magnetic domain wall in a nanowire by removing portions of the passivation layer near a magnetic strip. Using Kerr microscopy, we show that this approach allows for precise control of domain wall pinning in a racetrack-type element for different materials, as verified through micromagnetic simulations and 1D model calculations for vortex domain walls. This method offers several advantages, including ease of fabrication, flexibility in creating strain magnitudes and gradients, and the ability to avoid high-resolution lithography or piezoelectric substrates. Additionally, we propose and validate the use of this technology in a nonvolatile magnetic peak field sensor to demonstrate its technological relevance.

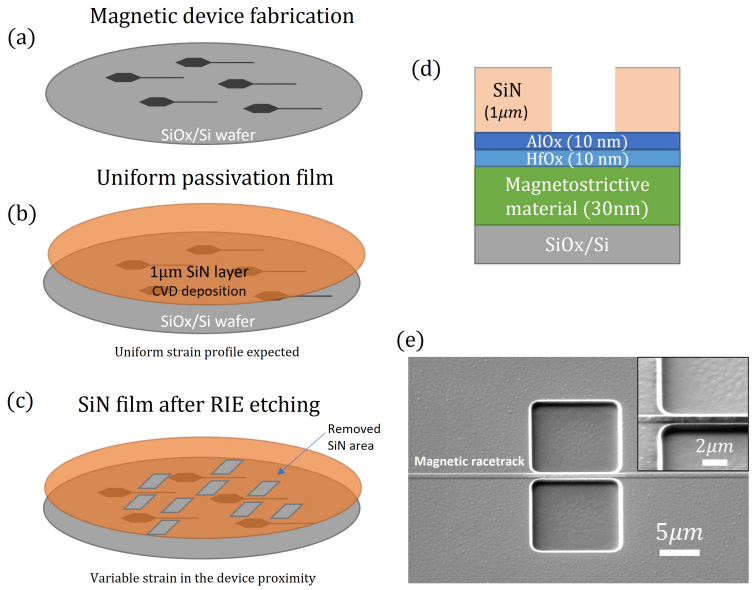

Figure 5.10: Schematic of the proposed method for imprinting strain on a Silicon wafer. After the magnetic racetrack are structured (a), a SiN layer deposited on top of a Si/SiOx wafer generates a uniform strain at the interface (b). The local strain is relieved (c) if areas of the SiN are removed using RIE. (d) section of the layers used in this work. (e) SEM image of a pair of openings in the SiN in the proximity of a magnetic nanowire (racetrack).

The work presented in Sec. 5.2 has been published in Applied Physics Letters[307] and filed as a German patent application.

5.2.1 Sample structure and characterization

Samples of $Co_{70}Fe_{30}$(30 nm) and $Co_{40}Fe_{40}B_{20}$(30 nm) were prepared by DC magnetron sputtering using a Singulus Rotaris system on a SiOx(1.5 µm)/Si(625 µm) substrate. The ferromagnetic layers were capped with AlOx(10 nm)/HfOx(10) layers to preserve their functionalities during the fabrication process. Using optical lithography and ion etching, nanowires are fabricated with a variable width - between 800 and 500 nm - and a length of 70 µm using a negative resist. The nanowires in our experiment also have a reservoir at the left end to create DWs at lower fields and avoid the formation of reversed domains in the middle of the nanowires (method also used in Sec. 5.1). After that, the entire wafer is covered with a 1 µm thick SiN layer by plasma-enhanced chemical vapor deposition (PECVD) at a temperature of 250°C. The residual stress on the wafer is quantified using a standard wafer bow measurement. A second optical lithography step is used in combination with positive resist and reactive ion etching (RIE) to remove selected areas of the SiN layer (openings) without damaging the magnetic layer, as is shown in Figs. 5.10 (a) - (d). After this process, only small areas (up to 20×20 µm^2) of the SiN are removed, while the surface is still largely covered. The hysteresis loops of the thin films are measured using a BH-looper with a setup to measure magnetostriction and the magneto-optic Kerr effect (MOKE) is used to image the magnetization state in the devices.

5.2.2 Results and discussion

5.2.2.1 Strain characterization

When a thin film is deposited onto a substrate with a different coefficient of thermal expansion, the temperature changes during growth produce intrinsic stresses and strains called thermal stresses and thermal strain.[76] The SiN layer deposited on the substrate shrinks at a different rate due to the varying coefficients of thermal expansion, resulting in elastic deformation of the film to conform to the substrate and remain attached (Figs. 5.10 (a)-(b)). This causes substrate and film bending, which can be measured through wafer curvature to determine the residual stress.[77] This source of stress is explained in more details in the theory chapter, Sec. 2.4.2. The measured in-plane stress is

uniform and in our case has a magnitude of −495(5) MPa (compressive stress). To create a non-uniform stress on the substrate surface, selected areas of the SiN are removed to create openings in the passivation layer (Fig. 5.10 (c)). It is worth noting that the etching is monitored to stop the process at the AlOx/SiN interface, as shown in Fig. 5.10 (d), to preserve the integrity of the magnetic layer. The resulting device is shown in a scanning electron microscopy image (SEM) in Fig. 5.10 (e) for a pair of square apertures with a size of 10×10 µm^2 in size. Sub-micrometer resolution can be achieved in the creation of apertures of arbitrary shapes, sizes, and spacing by using an appropriate lithography mask. In the work presented in this section - as shown in Fig. 5.10 (e) - we are able to create the openings 1 µm apart and etch the SiN layer without causing any damage to the 800 nm wide magnetic track underneath.

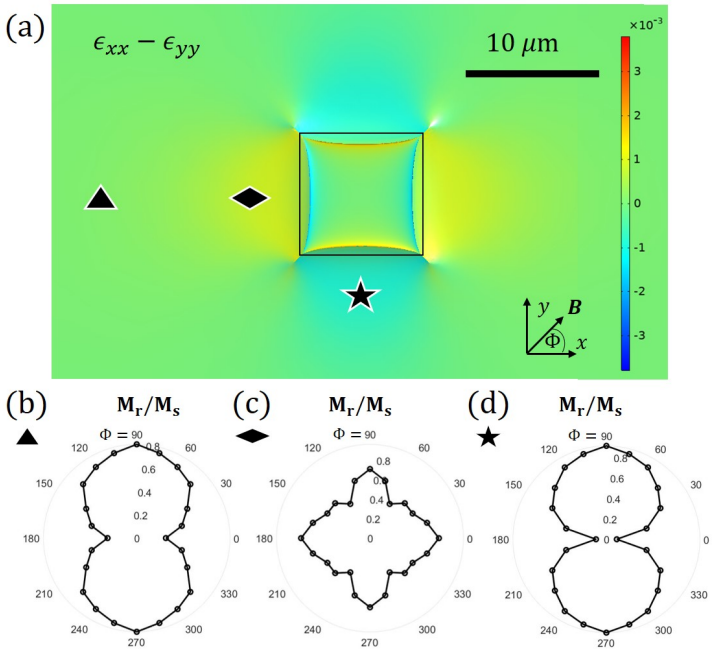

Figure 5.11: (a) surface strain ($\varepsilon_{xx} - \varepsilon_{yy}$) for a single square-shaped opening obtained from COMSOL multiphysics simulations. (b) - (d) angular plot of the normalized remanent magnetization M_r/M_s as a function of the in-plane angle Φ of the magnetic field measured with Kerr microscopy on a full film of $Co_{40}Fe_{40}B_{40}$ (30 nm) for a single opening in the SiN. The measurements are taken in different locations around the etched area in the passivation layer as indicated by the markers. Namely, an area far from the opening (b), on the left side where $\varepsilon_{xx} - \varepsilon_{yy} > 0$ (c) and on the lower side where $\varepsilon_{xx} - \varepsilon_{yy} < 0$ (d) are considered.

In order to determine the magnitude of stress relief achieved by removing selected regions of the SiN layer, FEM calculations are carried out.[308] Further

details on the FEM simulations can be found in Sec. 3.4.2 of the experimental section of this thesis. The calculated values of surface strain $\varepsilon_{xx} - \varepsilon_{yy}$ at the SiN/SiOx interface are presented in Fig. 5.11 (a), for the simplest case of a single square aperture of size 10×10 µm^2. The surface strain remains constant at distances greater than 20 µm from the etched regions, with $\varepsilon_{xx} - \varepsilon_{yy}$ approaching zero, consistent with residual stress measurements. However, near the openings (shown as black lines), the strain profile changes and reaches values of $\varepsilon_{xx} - \varepsilon_{yy} \simeq 0.2\%$. The $\varepsilon_{xx} - \varepsilon_{yy}$ strain is positive (tensile) to the right and left of the opening, while it is negative (compressive) above and below the opening, according to the symmetry of the system.

In order to validate the local strain magnitude and direction, we measured the magnetization curves of a full film of AlOx/HfOx/$Co_{40}Fe_{40}B_{20}$(30 nm) underneath the patterned SiN. Using a Kerr microscope, we measured the hysteresis loops at several spots on the sample, selecting a region of interest of 5×5 µm^2 in size within the microscope's field of view. Due to significant $Co_{40}Fe_{40}B_{20}$ magnetostriction ($\lambda_s \simeq 30 \times 10^{-6}$), the film's strain is linked to its magnetization through the magnetoelastic effect, which is expressed in the anisotropy energy in Eq. 2.31 (see the theory chapter of this thesis, Sec. 2.2.4.1).

As described in the experimental chapter, Sec. 3.3.5, the in-plane magnetoelastic anisotropy K_{ME} and the local strain can be estimated using Kerr microscopy. The angular dependence of the normalized remanent magnetization (M_r/M_s) is plotted as a function of the in-plane angle of the applied magnetic field (Φ), as shown in Figs. 5.11 (b) - (d) for three different positions with respect to a square-shaped opening in the SiN. This allows us to identify the direction of the effective in-plane magnetic anisotropy (K_{eff}) in the material.[309] In Fig. 5.11 (b), the measurement of M_r/M_s at a location 20 µm to the left of the opening (triangle in Fig. 5.11 (a)) is presented. By measuring the anisotropy in a point far from the opening, we get a reference point for the strain measurement. A uniaxial magnetic anisotropy with an easy axis along $\Phi = 90°$ is found, and $M_r/M_s(\Phi = 0°) \simeq 0.2$ along the hard axis. According to COMSOL simulations, the effective uniaxial strain along x in this area is close to zero, indicating that the observed anisotropy is likely deposition-induced rather than strain-induced.[310] Interestingly, in regions of the sample close to the opening where $\varepsilon_{xx} - \varepsilon_{yy} \neq 0$, the measured film magnetic anisotropy is altered compared to the case in Fig. 5.11 (b). Figs. 5.11 (c) and (d) consider areas where the local uniaxial strain along x is tensile (diamond) or compressive (star), respectively. In Fig. 5.11 (c), the angular plot of M_r/M_s indicated the presence of two uniaxial magnetic anisotropies with the easy axes oriented along 0° (dominant) and 90°. The first easy axis along 90° is deposition-induced, while the strain-induced easy axis is along the direction

of the tensile uniaxial strain, which is along x ($\Phi = 0°$) in this case. This is consistent with our COMSOL simulations, which gave $\varepsilon_{xx} - \varepsilon_{yy} = +0.15\%$ in the area marked by a diamond in Fig. 5.11 (a), since $Co_{40}Fe_{40}B_{20}$ has a positive magnetostriction. The same measurement for M_r/M_s is performed in an area where the effective strain along x is compressive and is reported in Fig. 5.11 (d). In this region (marked by a star in Fig. 5.11 (a)), the strain-induced easy axis is expected to be along y ($\Phi = 90°$) i.e. along the same direction of the deposition-induced anisotropy. Accordingly, the measured effective anisotropy is larger with $M_r/M_s(\Phi = 0°) \simeq 0$ along the hard axis of magnetization (Fig. 5.11 (d)). Our calculations report $\varepsilon_{xx} - \varepsilon_{yy} = -0.15\%$ (compressive) in this area, marked by a star in Fig. 5.11 (a).

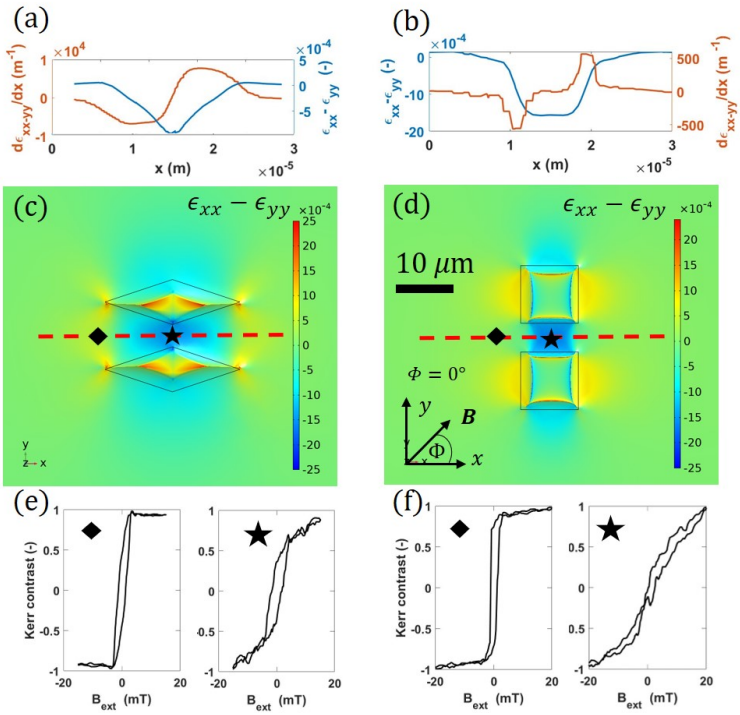

Figure 5.12: (a) - (b) effective strain ($\varepsilon_{xx} - \varepsilon_{yy}$) and strain gradient for, respectively, a triangular and a square pair of opening obtained from simulations. The x axis refers to the red dashed line. (c) - (d) surface strain $\varepsilon_{xx} - \varepsilon_{yy}$ obtained with COMSOL multipysics. The geometry is highlighted with black lines. (e) - (f) in-plane hysteresis loops obtained with Kerr microscopy on a full film of $Co_{70}Fe_{30}$ (30 nm) for, respectively, a triangular and a square pair of opening. The contrast is measured before the opening (diamond) and between them (star) according to the symbol position. To record hysteresis loops, the external magnetic field is applied along x.

In order to utilize the strain gradient produced by SiN structures in a magnetic racetrack, it is convenient to consider a pair of openings on the side of a

magnetic nanowire, creating a well-defined strained region. Computed values of surface strain $\varepsilon_{xx} - \varepsilon_{yy}$ at the interface between SiN/SiOx for two different opening geometries are shown in Figs. 5.12 (a) - (d). Similar to the case of a single opening, the effective surface strain is nearly zero far from the etched areas and becomes non-uniform in their proximity as demonstrated in Figs. 5.12 (c) and (d). The geometry of the opening determines the strain profile, which is illustrated in Figs. 5.12 (a) and (b) where a line plot of the surface strain is taken along a dashed line between two openings. For a square pair of openings (Fig. 5.12 (b)), the effective uniaxial strain profile $\varepsilon_{xx} - \varepsilon_{yy}$ is mostly flat and contained between the openings, with strain gradient maxima (minima) at the exit (entrance) of the strained area. In the case of a diamond-shaped pair of openings, the strain is once again contained between the openings but its magnitude increases nearly linearly towards the center (Fig. 5.12 (a)), while the strain gradient remains constant. Additionally, the magnitude of the strain can be increased by reducing the spacing between the etched areas.

In Figs. 5.12 (e) - (f) hysteresis loops of a full film, this time of SiN/AlOx/HfOx/$Co_{70}Fe_{30}$(30 nm) are reported. The magnetic contrast is measured again on an area of 5×5 µm^2 as indicated by the markers and to record hysteresis loops, the external magnetic field is applied along x. The opening geometry matched that of Figs. 5.12 (c) - (d), respectively. By comparing the magnetization curves next to (diamond) and in between (star) the square openings in Fig. 5.12 (f), it is found that the anisotropy field is increased. This increase is indicative of (uniaxial) magnetoelastic anisotropy. As $Co_{70}Fe_{30}$ exhibits positive magnetostriction, the increase of the anisotropy field ($K_{ME} \simeq 8.9(2)$ kJ/m^3) is attributed to negative (compressive) $\varepsilon_{xx} - \varepsilon_{yy}$ strain, in agreement with the COMSOL simulation. Using Eq. 2.31 and the difference of magnetoelastic anisotropy, the estimated strain for a square opening of this size is $\varepsilon_{xx} - \varepsilon_{yy} \simeq -0.05(1)\%$. The same measurement can be performed for a diamond-shaped pair of openings and is reported in Fig. 5.12 (e). The calculated maximum strain difference for this case is $\varepsilon_{xx} - \varepsilon_{yy} \simeq -0.02(1)\%$.

To summarize Sec. 5.2.2.1, the proposed method allows for the creation and design of local strain gradients on a SiOx/Si wafer. The profile of the strain, which is entirely transferred at the SiN/SiOx interface, can be simulated with FEM simulations. The strain magnitude can be probed experimentally using Kerr microscopy, if a magnetostrictive magnetic material is deposited underneath the SiN layer. As of now, we have considered the effect of magnetoelastic coupling on a full film. In the next section , Sec. 5.2.2.2, we consider the effects of the strain gradients described above on domain walls propagating in a magnetic nanowire.

5.2.2.2 Domain Wall pinning

The reliable control of DWs presents a significant challenge for applications that utilize racetrack technology. To drive magnetic domains in sensors, external magnetic fields are commonly employed.[12,93] In addition to that, implementing a mechanism to change direction, or stop a DW is necessary. Various methods have been proposed and all of them act on the DW energy making it a spatially variable quantity. In analogy with the conventional field-driven case, the magnetoelastic field can be considered as a force that - in a quasi-particle model - pushes the DW along the direction of decreasing energy, i.e., increasing compressive strain if $\lambda_s > 0$ for the in-plane strain-gradient case. As already discussed in the theory chapter, Sec. 2.3.3, this force is often dependent on the gradient of the spatially variable quantity,[66,311,312] which acts as an effective (magnetoelastic) field

$$B_{ME} = -\frac{1}{M_s}\frac{du_{ME}}{dx}, \tag{5.5}$$

where u_{ME} is the magnetoelastic DW energy per unit area.

For this study, a 500 nm wide magnetic nanowire made by $Co_{70}Fe_{30}$(30 nm) is considered together with a pair of square openings. The openings in the SiN layer are 10×10 µm^2 in size, which creates a channel with nonuniform strain in the center. We utilize Kerr microscopy in transverse mode to observe the magnetic state of the device while applying an in-plane magnetic field parallel to the wire along the x-axis. Figs. 5.13 (a)-(c) depict the position of a DW along the magnetic racetrack as a function of the applied magnetic field. When the field is strong enough, the DW is injected from the reservoir (Fig. 5.13 (a)) into the magnetic wire. As shown in Fig. 5.13 (b), the wall remains pinned in the region between the SiN openings, which corresponds to the strained area, and does not propagate to the end of the magnetic channel. The corresponding surface strain is shown with a simulation in Fig. 5.12 (d). Only with larger magnetic fields, the wall can continue to propagate to the other end of the magnetic channel, as seen in Fig. 5.13 (c).

The pinning strength observed in the device is assumed to be caused by the magnetoelastic energy landscape, which creates a favorable energy state for the DW. To verify this, we conduct the same experiment on devices with varying distances between the racetrack and openings. According to COMSOL simulations, the absolute value of the compressive strain increases as the opening distance d is reduced. As a result a larger depinning field should be required, if the magnetoelastic energy is the dominant cause of pinning. Our

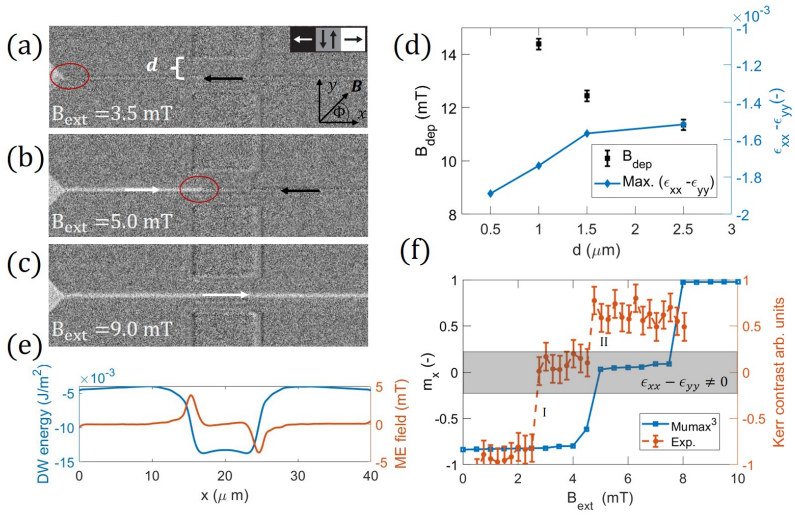

Figure 5.13: MOKE images showing a DW (a) injected, (b) pinned in the strained area and (c) continuing to move for larger magnetic fields. (d) experimental values of depinning field (black squares) and maximum strain $\varepsilon_{xx} - \varepsilon_{yy}$ (blue diamonds) for different distances between a pair of square openings. The values consider a 500 nm wire of $Co_{70}Fe_{30}$ with 30 nm thickness. (e) 1D model calculations of energy profile and effective magnetoelastic field for a vortex wall in a nonuniform strain profile. (f) micromagnetic simulations of m_x (proportional to the DW position) as a function of the applied field together compared with the experimental case, the strained area created by the openings is highlighted. A 800 nm wide nanowire is considered.

results show an increase in the depinning field from 11.0(2) mT to 14.5(2) mT for a distance between the opening and the magnetic racetrack decreasing from 2.5 to 1 µm, as depicted by black circles in Fig. 5.13 (d). The magnetoelastic origin of this pinning force, is additionally confirmed by the patterning of low magnetostrictive magnetic racetrack. The same geometry of opening is considered, and the DW position is again monitored as a function of the external magnetic field in a Permalloy wire ($Ni_{81}Fe_{19}$). For this case, no DW pinning in between the opening is reported above the injection field (1 mT for this case).

To corroborate our findings, we conduct micromagnetic simulations and 1D model calculations using the realistic strain profile obtained from COMSOL (see also Sec. 2.3.3 of theory chapter). The results, shown in Figs. 5.13 (e) and (f), consider nanowires made of 30 nm thick $Co_{40}Fe_{40}B_{20}$ and summarize the discussion about magnetoelastic fields. The 1D analytical model is used to calculate the DW energy per unit area and the corresponding magnetoelastic field, as shown in Fig. 5.13 (e) for a vortex wall in a 500 nm wide nanowire.

Comparing Fig. 5.13 (e) with Fig. 5.13 (b), the point where the DW is pinned coincides with the minimum of DW energy, in agreement with the Kerr images. At the sides of the pinning site, the effective magnetoelastic field is non-zero, and opposite to the applied external field. This equivalent force prevents the DW to move forward unless the external applied field is increased.

Material	M_s (T)	λ_s x10^{-6}	Y (GPa)
$Co_{40}Fe_{40}B_{20}$	1.40	30	187
$Co_{70}Fe_{30}$	2.0	80	180

Table 5.2: Parameters from literature[156,158,273] of the magnetic materials after deposition and used for the estimation of the magnetoelastic anisotropy. Here, M_s is the saturation magnetization, λ_s is the saturation magnetostriction and Y is the Young's modulus.

For the Mumax[129] micromagnetic simulations, a wire of 800 nm width is instead considered. The simulated system is a nanowire 30 nm thick. System size are 40×0.8 µm^2 and the cell size of 5 nm is below the exchange lenght of CoFeB. The material parameters (see also Table 5.2) used[313,314] are the one for $Co_{40}Fe_{40}B_{20}$: the elastic constants are C_{11}=280 GPa, C_{12}=140 GPa, C_{44}=75.5 GPa, the magnetostriction is λ_s=2.9×10^{-5}, saturation magnetization M_s=1×10^6 A/m, the exchange constant A_{ex}=15×10^{-12} and the damping is set to α=0.015. Disorder in the system is introduced by varying the material parameters A_{ex} and M_s of 5% over the grain distribution (grain size 20 nm). A realistic edge roughness of 30 nm is considered and the temperature of the simulations is 300 K. The applied strain is extracted from COMSOL simulations for the corresponding SiN opening geometry. The system magnetization is initialized with a DW on the left side of the strained area and a magnetic field is subsequently applied. Several simulations are conducted at varying external magnetic field strengths, and the outcomes are summarized in Fig. 5.13 (f). It can be observed from Fig. 5.13 (f) that in case of the external field lower than B_{dep}, the average magnetization in the x direction (which is proportional to the DW position) matches that of the strained area (state I). When the applied magnetic field is increased beyond B_{dep}, the DW is free to move and reaches the right end of the wire (state II). Fig. 5.13 (f) also contains the experimental DW position values as a function of B_{ext} for an 800 nm wide $Co_{40}Fe_{40}B_{20}$ wire, for comparison. The pinning position (y-axis value in Fig. 5.13 (f)) coincides with the simulations while the field strength value (x-axis in Fig. 5.13 (f)) differs. Discrepancies between the simulations and experiments for the value of B_{dep} can be due to roughness and defects that are not fully captured by micromagnetic simulations.

To summarize, we have experimentally shown how the magnetoelastic energy landscape created by the openings in the device allows the creation of pinning

points for in-plane vortex walls. We report sizable pinning fields up to 15 mT for different ferromagnetic materials with positive magnetostriction. The strain magnitude and profile (and therefore B_{dep}) is set by the opening distance and geometry. This allows for the control of DWs in magnetic racetrack using a simple lithography step. Using FEM and micromagnetic tools, this method for DW control can be also simulated.

5.2.2.3 Opening on top of a racetrack and bi-stable device

The creation of a local strain using openings in the SiN layer can be used in DW-based devices not only if the removed area is in the device proximity, but also directly on top of it. This is the case of a device like the one presented in Fig. 5.14 (a). Such a structure can be realized without damaging the magnetic wire as the RIE process used to create the openings does not affect the racetrack. As the magnetic layer is capped by AlOx(10 nm)/HfOx(10 nm), protection from oxidation is still ensured.

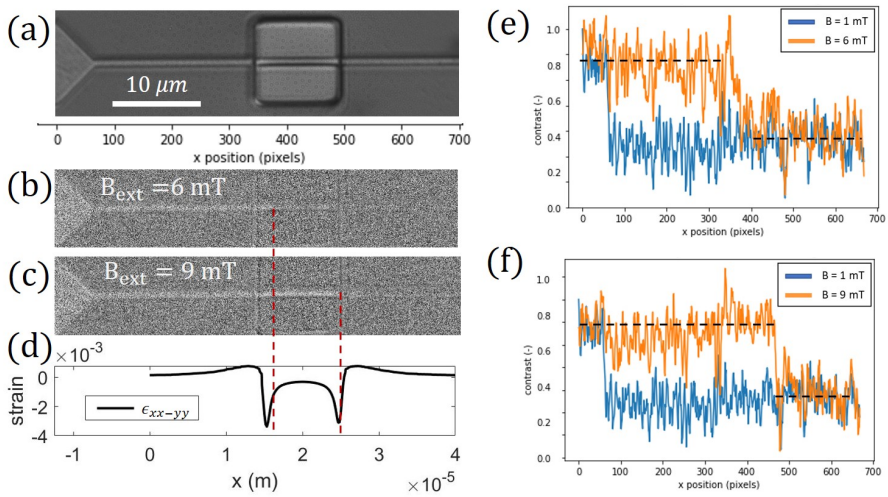

Figure 5.14: (a) optical microscope image of an opening on top of the magnetic wire made by $Co_{40}Fe_{40}B_{20}$. (b) and (c) Kerr microscope image showing the two pinning points at which a DW is pinned, corresponding to the side of the opening where the strain magnitude is the maximum. (d) effective strain $\varepsilon_{xx} - \varepsilon_{yy}$ calculated with FEM along the wire for a single squared opening geometry. (e) and (f) consider the magnetic contrast (proportional to the DW position) averaged over 10 measurements for two values of magnetic field, respectively.

This opening geometry creates a particular strain profile - shown in Fig. 5.14 (d) - characterized by the presence of two minima of strain. Accordingly,

the corresponding magnetoelastic energy in the racetrack presents two energy minima for a DW traveling in the magnetic channel. Figs. 5.14 (b) and (c) show a field driven DW pinned at the two sides of the opening. The measured B_{dep} is larger at the second side (9 mT) than at the left side of the opening (6 mT). This is attributed to the magnetoelastic energy difference (and the corresponding effective strain difference) which is larger when a DW exits the area uncovered by the SiN with respect to the point where it enters it. To give an accurate estimation of the depinning field and the pinning position, the magnetic contrast along the magnetic wire (corresponding to the DW position) is averaged over ten measurements. This is reported in Figs. 5.14 (e) and (f) and again confirms that the DW is located in one of the two areas where the strain is maximum.

A possible use for this type of strain (which is much more localized than the example of the opening pair Fig. 5.12) is the realization of a bi-stable device.

Solid state magnetic memory devices typically assign a 1 or 0 by orienting the remanent magnetization of ferromagnetic elements in one of two opposite directions. As a result, there is ongoing research into the magnetic properties of small particles to reliably and reversibly switch between two nonvolatile states. In previous works Koo and co-workers[315] used current pulses for storing and reading binary information in magnetic systems. Their idea involved the use of a bi-stable remanent domain configuration of a ferromagnetic island, which can be chosen by passing a current pulse through the material. Similarly for our case, the patterning of an opening on top of a racetrack could be a viable option for magnetic random access memory and unconventional computing applications.[316] This could be realized, if the energy barrier between the two states is reduced to $\simeq k_b T$, for example by changing the opening geometry.

5.2.2.4 A nonvolatile peak field sensor concept

As is commonly known, external magnetic fields can drive the motion of magnetic DWs, and the Sec. 5.2.2.2 demonstrated the creation of trapping points using local strain. By altering the aperture design, the maximum strain value and thus the depinning field can be adjusted, as illustrated in Fig. 5.13 (d). This allows for the creation of a novel magnetic sensor that can detect discrete magnetic field values. Previous research[303] has proposed similar concepts, but our approach presented in Sec. 5.2 involves fabrication techniques that are compatible with most sensor manufacturers production lines, as sub-100 nm lithography resolution is not required. We propose a non-volatile magnetic

field peak detection method. In addition, current peaks can also be detected using Oersted fields, if the sensor is place in close proximity of wires or coils.

The diagram in Fig. 5.15 illustrates the design of the peak field sensor, which consists of a magnetic nanowire with several pinning sites. By reducing the edge-to-edge distance between the pinning sites, as depicted in Figs. 5.15 (a) and (b), the strain magnitude increases gradually. The depinning field B_{dep} required to propagate a DW also increases from left to right, as indicated in Figure 5.15 (d). The device considered in this study has four pairs of openings, which allow it to detect four distinct levels of external magnetic fields, corresponding to the four energy minima along the wire where the DW can be found.

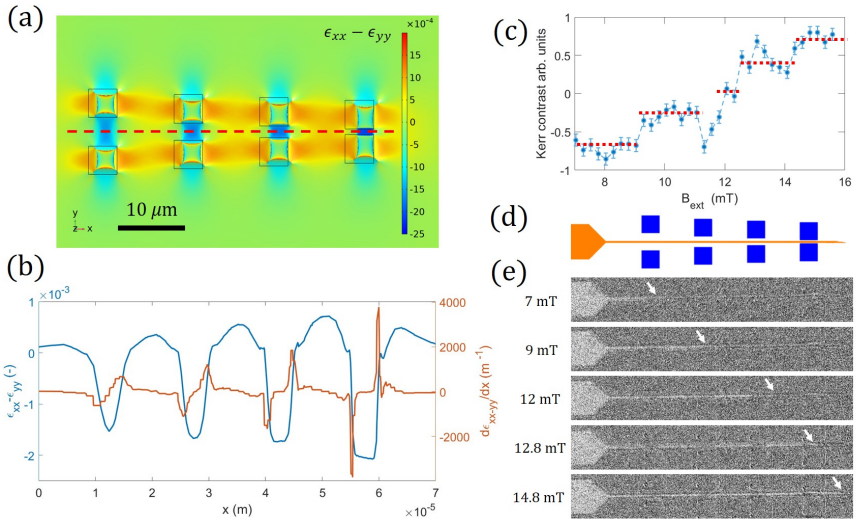

Figure 5.15: Different aspects for the conceptualization and realization of a peak field sensor based on DWs. (a) COMSOL simulations of the surface strain and (b) plot of the strain value and strain gradient along the racetrack path, that is highlighted with a dashed line in (a). (c) magnetic contrast obtained with Kerr microscopy of the racetrack indicating the well defined position of the DW as a function of applied magnetic field. The sample is made of $Co_{70}Fe_{30}$ and the width of the wire is 500 nm. (d) sketch of the magnetic stricture (orange) and of the etched areas in the SiN (blue). (e) MOKE images of the DW position in the device for different magnetic field steps. The position of the DW is indicated with a white arrow.

Figs. 5.15 (c)-(e) depict the operating principle of the device implemented in this study. The magnetic wire used in this case has a $Co_{70}Fe_{30}$ (30 nm thickness) magnetic layer and a wire 500 nm in width. The openings have a size of 5×5 µm^2, and the edge-to-edge distances between the pairs are 5, 3, 2, and 1 µm, as illustrated in Fig. 5.15 (d).

The device is initialized with large, negative magnetic field in the x direction and a uniform magnetic state is realized. Subsequently, the magnetic field is gradually increased to positive values while Kerr microscopy is used to monitor the magnetic state of the wire. As shown in the magnetic contrast image in Fig. 5.15 (c), discrete levels of magnetization are obtained as the magnetic field is increased. This occurs because the DW that propagates into the nanowire stops at specific positions along the x axis. The pinning point for the DWs can be observed in the sequence of Kerr microscope images shown in Fig. 5.15 (e). The DW, created in the nucleation pad, gradually moves as the external magnetic field is increased until it reaches the following strained area between the openings and becomes pinned.

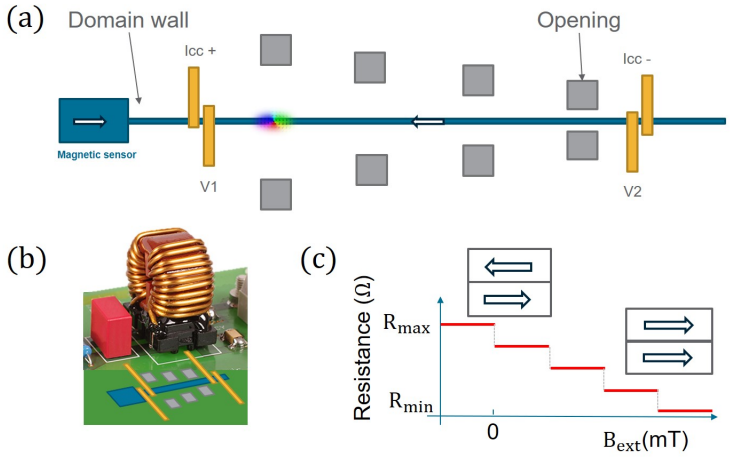

Figure 5.16: (a) sketch of the nonvolatile sensor concept proposed, where the readout con be realized with electrical contacts in combination with a GMR stack. (b) if placed next to a coil, the proposed prototype could detect discrete Oersted fields. The output signal of the sensor (if realized with GMR stack) is a step function as shown in (c). The arrows indicate the magnetization of the free layer (top) and of the pinned layer (bottom). Adapted from stock.adobe.com.

The position of the DW in the magnetic channel (output) indicates the maximum field (input) experienced by the device after initialization. In the presented case, optical methods are used to measure the magnetic state in Fig. 5.15 (c). Alternatively, the position of the DW can be electrically detected using two electrical contacts in combination with a full Giant Magnetoresistive (GMR - spin valve configuration) stack[12] as shown in Figs. 5.16 (a) - (b). In this configuration, the DW moves in the free-layer of the stack, while the pinned layer would either be oriented parallel or anti-parallel to the wire. This sensing solution is particularly suitable for energy-efficient devices or inaccessible measurement conditions due to the non-volatile nature of the magnetic state.

The device only requires electrical power for initialization and readout and the read value of resistance of the proposed device, if realized with GMR stack, is shown in Fig. 5.16 (c).

Conclusions

In Sec. 5.2, a technique is proposed and validated for producing a local strain on a rigid substrate that is compatible with standard CMOS technologies. This is achieved by selectively removing regions of the passivation layer through etching, which modifies the intrinsic stress occurring at the substrate/layer interface during SiN deposition. FEM simulations demonstrated that the strain is only affected in the vicinity of the removed material. The magnitude and gradient of the in-plane strain can be adjusted by varying the geometry and location of the openings in the stress-generating layer. Using in-situ measurements of magnetoelastic anisotropy, the uniaxial strain is experimentally determined to be up to 0.05(1)%.

The potential of using these strain gradients for manipulating magnetic domain walls in spintronic devices through magnetoelastic coupling in magnetostrictive materials is also validated. The magnetoelastic energy landscape in the device is shown to create pinning points for in-plane vortex walls. The DW position is determined using Kerr microscopy. Pinning fields of up to 15 mT are reported for various ferromagnetic materials with positive magnetostriction. Our findings are supported by micromagnetic simulations and 1D model calculations using a realistic strain profile. All of these observations are attributed to the magnetoelastic energy contribution in the system, which creates local energy minima for the DW at the desired location. This approach offers an alternative for generating DW-based devices that are compatible with wafer-level production. An example of a discrete magnetic field or current sensor using imprinted strain gradients is also demonstrated.

The work presented in Sec. 5.2 offers a valid alternative for the generation of local strain, whose usability is not limited to spintronics and to the realization of new magnetic sensor concepts as discussed in our manuscript. Instead, such strain can also be used in manipulation of quantum dots,[317] band structure in 2D materials[318] and mobility in semiconductors.[319]

5.3 Control of domain walls using SAWs

After starting with simple uniaxial and static strain in Sec. 5.1, we realized static but spatially varying (i.e. non-local) strain in Sec. 5.2. In the present section, the dynamic behavior of strain is considered, as the strain does not only change with the position along the sample surface (space variant), but also in time (time variant). To do this, the experimental setup and the sample structure increases in complexity since an AC voltage source in combination with a piezoelectric substrate are utilized. The strain is realized using surface acoustic waves (SAWs), as discussed in the theory chapter, Sec. 2.4.3 and in the experimental method section, Sec. 3.3.7.

This method involves launching two counter-propagating surface acoustic waves (SAWs) into a piezoelectric substrate using a set of interdigitated transducers (IDTs) and creates a stationary stress/strain wave (SW) between the transducers. SAWs have a wide range of application. For instance the control of particles in overlaid microfluidic systems[320,321] has been demonstrated, while in spintronics, the coupling of magnetostrictive/ ferromagnetic material (multiferroic) can be employed to reduce coercivity of thin films,[127] to control and move skyrmions[322] and to pin DWs.[88] SAW-based control of magnetism offers several potential advantages compared to other techniques. Firstly, SAWs can be generated by voltage, which is more energy-efficient than using current. Secondly, SAWs can propagate over long distances, with minimal power loss, allowing for a single pair of electrodes to control multiple devices. Additionally, pinning sites can be created remotely using electrodes, potentially enabling precise control of domain walls without intricate designs. Within the scope of this thesis, our focus is on utilizing SAWs to regulate the injection of a domain wall into a magnetic racetrack, commonly employed in sensing or logic applications (see Sec. 5.1).

In this section, a frequency dependent study of SAWs effects is reported. To start with, the magnetic switching of different ferromagnetic materials with different magnetoelastic coupling is compared in the presence of standing SAWs. Strong reduction of the coercive field in the presence of sanding SAWs is observed, with proportionality to the applied power and to the material magnetostriction. This is compatible with the interpretation of a strain activated magnetization reversal. When investigating the effects of strain in magnetic domain walls injectors, we observe a strong reduction in the magnetic field required to inject a DW into the device up to 50%. This time, the reduction is strongly dependent on the frequency of the AC voltage applied to generate the SAW. We attribute this dependency to the resonant match of the RF signal and the dynamics of

the spin structure of the DWs in the nanowires, that are likely to be in a vortex state due to the device shape anisotropy. Moreover, we observe stronger effects both in magnetization reversal and in DWs injection if the central frequency of the AC voltage is changed in time (frequency modulation). By doing so, we realize standing SAWs with moving node/anti-node position. This might be an additional energy transfer channel from the strain to the magnetoelastic energy of the wall as a previous report suggests.[323]

The work contained in the present section was done in strong collaboration with the University of Leeds (UK), where the IDTs have been fabricated and the samples have been measured with the help of J. Shuai under the co-supervision of Prof. T. Moore.

5.3.1 Sample structure and characterization

Figs. 5.17 (a) - (b) show a schematic of the SAW device used in this study. Films of $Co_{40}Fe_{40}B_{20}$ (30 nm), $Co_{70}Fe_{30}$ (30 nm) and $Ni_{81}Fe_{19}$ (30 nm) with in-plane anisotropy are deposited using DC magnetron sputtering on a 128° Y-cut lithium niobate ($LiNbO_3$) substrate with dimensions $10\times10\times0.5$ mm^3. A seed layer of 5 nm of Ta is used to reduce roughness related effects and the ferromagnetic layers are capped with 4 nm Ta to reduce aging effects. The magnetic films are structured using electron beam lithograhy (EBL) and ion etching into disks of 80 µm diameter and into nanowires with 800 nm width and 100 µm long. To facilitate DW injection, a nucleation pad (20×10 µm^2) is realized at the one end of the magnetic racetrack. All the devices are realized within the SAW beam path of one IDTs pair.

At the terminations of the devices, a set of IDTs made of Ti (10 nm) and Au (90 nm) are fabricated using optical lithography. Metal evaporation and liftoff techniques are employed during the fabrication process. Each IDT consisted of 20 electrode pairs. The length of the electrodes, referred to as the IDT aperture, is 500 µm, while the distance between the two IDTs, known as the SAW propagation distance, measured 3 mm. The electrode width and pitch are varied between 10 and 7.5 µm, resulting in an approximate SAW wavelength (λ) between 40 µm and 15 µm. This corresponds to a resonant frequency of the IDTs between 100 and 320 MHz.

The determination of scattering parameters (S-parameters) is carried out using an Agilent E5062A vector network analyzer. Figure 5.17 (c) illustrates the reflection (S11 and S22) and transmission (S21 and S12) characteristics of the surface acoustic wave (SAW) transducers and substrate, with a central

frequency of 173 MHz. To generate standing SAWs (SW), RF signals are simultaneously applied to both IDT1 and IDT2 as shown in Fig. 5.17 (a). For launching standing SAWs with moving node position, the frequency of the RF signal applied to the two IDTs simultaneously is swiped around the resonant frequency of ±25 MHz in 111 ms (milliseconds) (0.45 MHz/ms). To ensure equal power delivered to the IDTs for standing SAWs, the power loss along the circuit is carefully examined and compensated. Further details regarding the RF circuit used for determining S-parameters and launching SAWs can be found in the experimental section, Sec. 3.3.7.

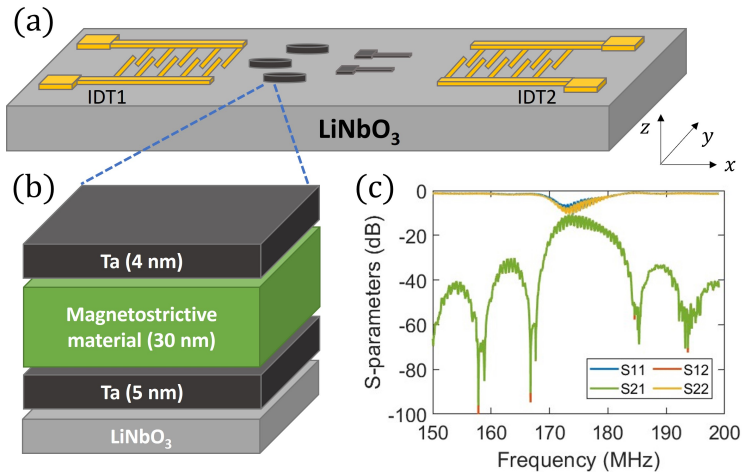

Figure 5.17: Experimental setup used to apply SAW. (a) scheme (not to scale) of the sample used to investigate SAW effects on in-plane magnetostrictive materials. The devices (in black) are patterned between the two IDTs well within the beampath of the SAW. The contacts in yellow are used to apply the RF voltage. (b) layerstack used in this study. (c) S-parameters, both in reflection and in transmission, for the IDTs used to launch SAWs. The delay line comprising both IDTs and the substrate shows a center frequency of 173 MHz.

The magnetic properties and hysteresis loops of the films (structured in disks) are measured using a Kerr microscope with a 20x objective and an in-plane magnetic field applied. For the domain wall injection measurements, a 50x objective is used instead.

5.3.2 Results and discussion

5.3.2.1 SAW assisted magnetic switching

Hysteresis loops are measured with Kerr microscopy from an array of disk structures to probe the local magnetic properties of the film. The magnetic field is applied in-plane, along x according to the scheme of Fig. 5.17 (a). During the measurement a RF voltage is applied to the IDTs to launch a standing SAW parallel to the applied magnetic field (along x). To compare the magnetization reversal process in the presence of SAW, the coercive field H_c is measured as a function of the RF power applied to the IDTs and is reported in Fig. 5.18 for different magnetic materials. IDTs with a resonant frequency of 238 MHz are considered for our coercivity measurements reported in Fig. 5.18.

A significant coercivity reduction is observed in the presence of standing SAWs for $Co_{70}Fe_{30}$ and $Co_{40}Fe_{40}B_{20}$ films. For $Co_{70}Fe_{30}$ (Fig. 5.18 (a)), H_c decreases from 17.0(1) mT in the absence of SAW to 14.5(1) mT with 3 mW RF power, while for $Co_{40}Fe_{40}B_{20}$ films (Fig. 5.18 (b)) H_c decreases from 0.4(1) mT to 0.1 mT with 3 mW RF power applied. The coercivity decreases with increasing applied power and similar reductions to H_c are observed for IDTs with resonant frequency between 100 and 300 MHz, without significant dependence on the applied SAW frequency. The measured reduction in coercivity is compatible with previous studies.[124]

In thin films with perpendicular magnetic anisotropy (PMA) standing SAWs are reported to facilitate the quasi-static magnetization reversal process.[124,127] The decrease in coercivity can be attributed to alterations in anisotropy induced by strain, as reported in previous studies[88,127] and discussed in Sec. 5.1 for the uniform strain case. Surface acoustic waves (SAWs) function as dynamic strain waves, capable of locally modifying the energy landscape of thin films. This periodic modulation raises and lowers the anisotropy of the thin film, eventually leading to magnetization reversal when the anisotropy reaches low values. These changes in anisotropy are associated with magnetoelastic anisotropy, which depends on the applied strain tensor component ε_{ii} and the material saturation magnetostriction λ_s. In piezoelectric materials, the magnitude of strain is directly related to the applied voltage. Consequently, larger reductions in coercivity (H_c) are expected with higher applied power, consistent with the observed trends in Figs. 5.18 (a) - (b). In addition, the large magnetostriction of $Co_{70}Fe_{30}$, $\simeq 80\times10^{-6}$, explains the more significant changes to H_c with respect

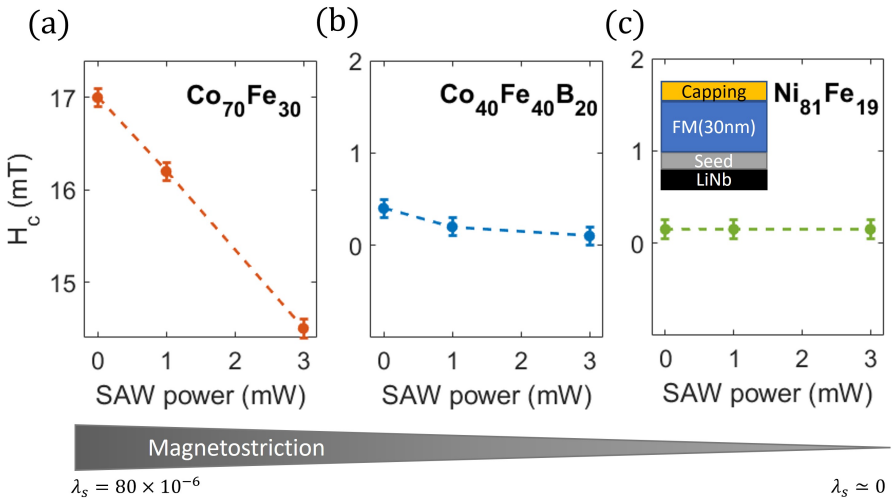

Figure 5.18: Measurements of coercivity (H_c) in the presence of standing SAW as a function of the applied RF power. The frequency of the strain wave is 238 MHz, resonant frequency of the patterned IDTs. The measurements for (a) Ta(5 nm)/$Co_{70}Fe_{30}$(30)/Ta(4), (b) Ta(5 nm)/$Co_{40}Fe_{40}B_{20}$(30)/Ta(4) and (c) Ta(5 nm)/$Ni_{81}Fe_{19}$(30)/Ta(4) films are reported with the same y-axis scale for comparison. The field is applied in-plane along the same direction of the SAW. The film is patterned into 80 µm diameter disks.

to $Co_{40}Fe_{40}B_{20}$ films, where the magnetostriction is $\simeq 30 \times 10^{-6}$. According to Eq. 2.31, the value of this strain anisotropy can be obtained by the value of magnetostriction and the applied strain. In LiNbO the calculated strain is expected[324] to be in the order of 0.8×10^{-4} for the largest voltage amplitude used. Using this value of strain the changes to the anisotropy are expected to be 1.9(1) kJ/m^3 for $Co_{70}Fe_{30}$, 1.0(1) kJ/m^3 for $Co_{40}Fe_{40}B_{20}$ and only 50 J/m^3 for Permalloy.

It is important to consider that the introduction of RF power to generate surface acoustic waves (SAWs) may lead to an increase in temperature, potentially resulting in a decrease in coercivity. For the studied devices and power range used, the heat-induced temperature changes are expected to be in the order of 5 to 10K.[325] Off resonant dependent studies[127] suggested that the reduction in coercivity is directly attributed to the standing SAW rather than RF power-induced heating. In addition to this previous report, we measured RF power dependent coercivity of a Permalloy ($Ni_{81}Fe_{19}$) film as reported in Fig. 5.18 (c). The saturation magnetostriction of $Ni_{81}Fe_{19}$ is below -1×10^{-6}. As its value of magnetostriction in nearly zero, the film magnetic anisotropy is not expected to be modified by the SAW. No changes to the coercivity of Permalloy are measured even for the largest RF power of 3 mW, thus confirming that

magnetoelastic effects are dominating over thermal activated magnetization reversal.

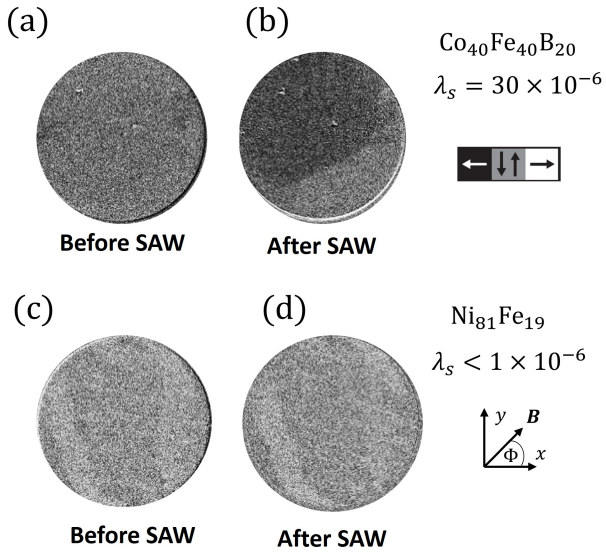

Figure 5.19: Remanent state of magnetization (no applied magnetic filed) imaged before (left) and after (right) applying a standing SAW with 3 mW power and a frequency of 238 MHz. The SAW is applied for 1 second along the x direction. (a) and (b) refer to magnetic disks made of Ta(5 nm)/$Co_{40}Fe_{40}B_{20}$(30)/Ta(4) while (c) and (d) refer to Ta(5 nm)/$Ni_{81}Fe_{19}$(30)/Ta(4) disks. The Kerr microscope is operated in longitudinal mode to probe the x direction of magnetization.

In addition to hysteresis loops, the remanent magnetic state (i.e. in the absence of magnetic field) in the disks is imaged using Kerr microscopy in longitudinal configuration[114] and is reported in Fig. 5.19. For this measurement, the magnetization of the sample is saturated in one direction. After background subtraction the magnetic field is gradually reduced to zero and the images in Figs. 5.19 (a) and (c) are recorded. After that, RF power of 3 mW (strain amplitude $\simeq 0.8 \times 10^{-4}$) at 238 MHz (resonant IDTs frequency) is applied for 1 second and switched off. At this point a second image is recorded (Figs. 5.19 (b) and (d)). Figs. 5.19 (a) and (b) consider the remanent state of a Ta(5 nm)/$Co_{40}Fe_{40}B_{20}$(30)/Ta(4) disk. Before the application of RF power (Fig. 5.19 (a)) the magnetic state is for its most part in the previously saturating direction. After the application of the SAW, large parts of the magnetization have reversed the in-plane direction. This can be explained by the reduction of H_c that is almost reduced to zero during the application of a standing SAW, therefore allowing for magnetic domain nucleation and propagation in magnetostrictive $Co_{40}Fe_{40}B_{20}$. If instead a material with negligible magnetostriction such as Permalloy is considered, the application of

RF power leaves the remanent magnetic domain pattern unaffected, as shown in Figs. 5.19 (c) and (d). Again, this suggests that the dominant effect of the SAW on the magnetization is the magnetoelastic anisotropy contribution.

Off-resonant RF signal

So far, the RF power applied to the IDTs during the experiment is at a constant frequency, f_0, the resonant frequency of the patterned IDT defined as the point of the maximum in $S12$ and $S21$ parameters. This configuration, called single standing surface acoustic wave (SSAW), creates a standing SAW with fixed node and anti-node position. We will now expand this technique by using frequency-modulated SSAWs.[323] By changing the frequency of the two coherent counter propagating SAWs, which interfere coherently to form the standing wave, the nodal position is shifted. To realize frequency modulation of SSAWs the RF signal at the IDTs is swiped around the resonant frequency f_0 of the transducers between $f_0 - \Delta f$ and $f_0 + \Delta f$. Δf is set to be 25 MHz and the sweep time is set to 111 ms.

Fig. 5.20 shows hysteresis loops measurements with in-plane magnetic field along the x direction. For each material the respective measurements are reported with different colors: without RF power applied to the IDTs, with a SSAWs f_0=238 MHz and in the presence of frequency modulated SSAWs $f_0 \pm \Delta f$=238±25 MHz. By comparing the case with no SAW (blue) and the standing SAW (orange) in Fig. 5.20 (a) and (b) a reduction in the coercive field is observed. As the two materials considered have sizable magnetostriction, the magnetization reversal is assisted (facilitated) in the presence of SAWs, as discussed in Fig. 5.19.

Remarkably, the frequency modulation of SSAWs additionally reduces H_c for the same RF power applied (3 mW) compared to a non modulated SAW. For $Co_{70}Fe_{30}$ (Fig. 5.20 (a)) the coercivity is reduced to 14.5(1) mT in the presence of SSAWs and to 12.0(1) mT with frequency modulation. For $Co_{40}Fe_{40}B_{20}$ instead the additional frequency modulation of SSAWs reduces the coercivity to a value below the resolution of our measurement (0.1 mT), as can be seen in the inset of Fig. 5.20 (b).

To explain this result, we consider the effect of frequency modulation as an additional mechanism to promote domain walls propagation and magnetization switching in our film. A change in frequency of the RF signal applied to the two IDTs creates a standing SAW (with respect to magnetization dynamics) with a slightly difference wavelength according to

$$\lambda_{SAW} = \frac{\nu_{SAW}}{f} \tag{5.6}$$

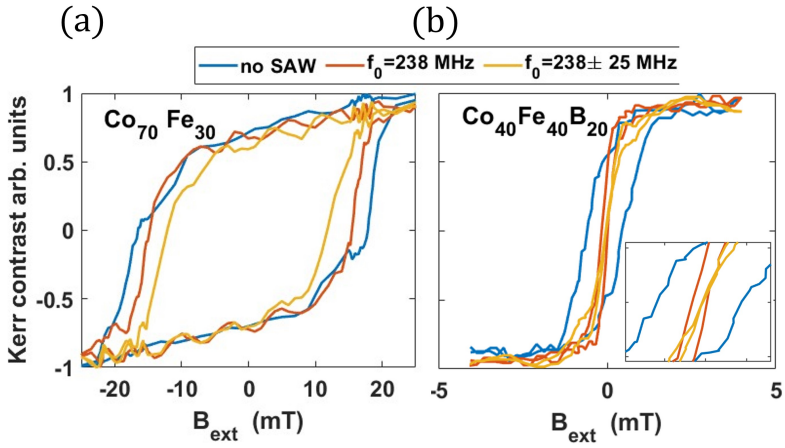

Figure 5.20: Hysteresis loops measured with Kerr microscopy of (a) Ta(5 nm)/$Co_{70}Fe_{30}$(30)/Ta(4) and (b) Ta(5 nm)/$Co_{40}Fe_{40}B_{20}$(30)/Ta(4) films patterned into disks. Three independent measurements are reported as a comparison: in the absence of RF power (no SAW, in blue), in the presence of f_0=238 MHz standing SAW (resonant IDTs frequency, in red) and in the presence of an off resonance SAW swiped between $f_0 - \Delta f$=213 MHz and $f_0 + \Delta f$=263 MHz. The magnetic field is applied along the direction of SAW (x direction), SAW power is 3 mW and the frequency is swiped within 111 ms.

where ν_{SAW} is the acoustic velocity (3997 m/s[326]) and f is the applied high-frequency signal. Major effects of the frequency modulation are expected within the 3 dB pass-band of the IDTs which is in the order of 10 MHz. As the distance between the interdigits is fixed, this also leads to a change in the anti-node position,[320] where the anistotropy (i.e. the energy landscape of the film) is locally reduced by the time varying strain. The change of the anti-node position, can be seen as an additional mechanism that facilitates magnetization switching and can explain the reduction in H_c observed in Fig. 5.20. Further investigation with systematic speed of frequency sweep variation should be performed in future studies to improve our understanding on this effect.

To summarize this section, standing surface acoustic waves, are found to reduce coercive field of magnetostrictive materials due to local anisotropy variations of the time variant strain, in agreement with previous studies. The magnetoelastic effect is dominant over thermal effects of the RF power heating, as SAWs do not alter the magnetic state of low magnetostrictive $Ni_{81}Fe_{19}$. In addition to the static case, we performed frequency modulation of SSAWs, and found that for the same RF power, the frequency modulation additionally reduces the coercive field of our films improving the efficiency of the strain coupling with the system.

5.3.2.2 SAW assisted domain wall injection

After studying the effects of SSAWs on the magnetization reversal mechanism of films, we employ SSAWs to improve a figure of merit of domain wall based sensors and devices, which is the injection field, B_{inj}. This quantity, already defined in Sec. 5.1, is the magnetic field required to inject a DW into the magnetic racetrack, as shown in the sketch of Figs. 5.21 (a) - (b). Ideally, in a device B_{inj} should be as low as possible[93] to reduce the lower boundary of the field operating window.

A viable option to lower this boundary is the use of SAWs, in combination with an external applied field. It was shown that SSAWs can increase the DW velocity in nanowires[324] and assist the depinning[327] due to the modulation of the pining barrier with magnetoelastic anisotropy modulation. If this modulation is at the mouth of the pad, where the DW is pinned before injection (Fig. 5.21 (a)), then the energy barrier, mainly provided by the shape anisotropy, is lowered (lower B_{inj}).[93]

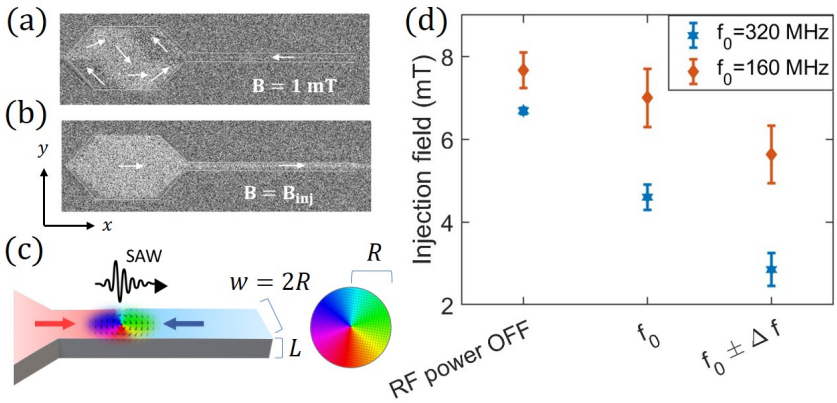

Figure 5.21: Kerr microscope images of a domain wall injection process, from a nucleation pad (a) into a nanowire (b) where the DW propagates. (c) schematic of a vortex DW in the wire geometry considered whose dimension are $L = 30$ nm and $R = w/2$=400 nm. (d) measurements for B_{inj} in the presence of SSAWs. Two central RF frequencies of the IDTs are considered, f_0 =320 MHz and f_0 =160 MHz, in blue and orange, respectively. The measurements refer to a Ta(5 nm)/$Co_{40}Fe_{40}B_{20}$(30)/Ta(4) sample on top of $LiNbO_3$ substrate. The RF power applied is 3 mW.

According to the sketch of Fig. 5.21 (c), we design the IDTs for a SAW propagation along x, same direction of the applied magnetic field. The wire has a width of $w = 2R$=800 nm and a thickness of L =30 nm. This approximately defines the size of the vortex-type wall, with radius R.

To measure the injection, a magnetic field of 20 mT along $-x$ direction initializes the device magnetization (pointing left). After subtraction, the magnetic field is reduced to zero and increased to positive values. The contrast changes are monitored with a Kerr microscope until the injection (as Fig. 5.21 (b)) is reached. Measured values of B_{inj} are reported for a Ta(5 nm)/$Co_{40}Fe_{40}B_{20}$(30)/Ta(4) sample in Fig. 5.21 (d) in the presence of SSAWs with different IDTs resonant frequency f_0. Two different set of samples are realized for the two frequency measurements.

In the absence of SSAWs (no RF power applied to the IDTs) the injection field is B_{inj}=7.0(5) mT. In the presence of a SSAWs with frequency f_0=320 MHz (blue stars in Fig. 5.21 (d)) B_{inj} is reduced to 4.5(2) mT. B_{inj} is reduced further to 2.8(2) mT in the presence of frequency modulated SSAW $f_0 \pm \Delta f$=320±25 MHz. The stronger reduction in the case of frequency modulation, is justified by decrease in H_c reported in Fig. 5.20. Interestingly, the use of a lower central frequency f_0=160 MHz (orange diamonds in Fig. 5.21 (d)) has smaller influence on B_{inj}. For 160 MHz, in the case of unmodulated SSAW, the injection field is unaltered. B_{inj} is only affected during frequency modulation ($f_0 \pm \Delta f$=160±25 MHz), where the maximum reduction to B_{inj} is 1 mT with respect to the reference case (no RF power). The observed reduction in B_{inj} in the presence of SSAWs can be compared with our study on DW injection using uniform strain[93] (see Sec. 5.1). As shown in Fig. 5.4 for similar device geometry, a uniform tensile strain changes the injection field in $Co_{40}Fe_{40}B_{20}$ nanowires from 3 mT to 9 mT. In that study, the estimated strain anisotropy is 3.6(1) kJ/m^3. A strain anisotropy of 1.0(1) kJ/m^3 is estimated for the SAW amplitude used. Accordingly, a reduction up to 4 mT in the value of B_{inj} is in agreement with our published studies using uniform strain.

This significant frequency dependence observed in Fig. 5.21 (d), suggests that, in contrast to the H_c measurements, the effect of SAWs on DW injection strongly depends on the wavelength of the strain modulation. A possible explanation for this dependence is the spin structure of the domain wall injected. For the used wire geometry, the DW is a vortex type.[328] It is known that a magnetic vortex is subject to motion of the core under external field excitation and these excitations have eigenfrequencies ω_0 (i.e. resonant modes) of the vortex translational motion.[329,330] The value of ω_0 is dependent on the size of the vortex, i.e. on the geometry of the system according to[329]

$$\omega_0 \simeq \gamma M_s \left(\frac{L}{R}\right) \tag{5.7}$$

where γ is the gyromagnetic ratio, M_s the saturation magnetization, R the radius of the vortex and L the thickness of the magnetic layer. Eq. 5.7 is valid

in the limit of aspect ration $\frac{L}{R} << 1$ and assumes a vortex spin structure. The latter is valid only for applied fields below the walker breakdown. This is not the case of our experiment, however the a qualitative comparison is possible at a first level of approximation. Considering the parameters of $Co_{40}Fe_{40}B_{20}$ and an aspect ratio $\frac{L}{R} = 0.075$, we find a value of $\omega_0 \simeq$300 MHz. ω_0 can be considered as the resonant frequency of a vortex type wall in a wire of width $w = 2R$, equivalent to the one of a vortex in a disk with diameter $d = 2R$ and same thickness.

The lowest frequency transnational (or gyrotropic) mode can be excited by an in-plane magnetic field and has an eigenfrequency that is a result of the finite wire size and is determined not by exchange but by long range dipolar interactions.[329] Intuitively, the use of a strain induced modulation of the anisotropy, with a frequency closer to the vortex equivalent resonant mode $f_0 \simeq \omega_0$=300 MHz drives the vortex wall more efficiently, and therefore explains a larger reduction of the injection field, with respect to the use of lower RF frequency of the SAWs. However, a more complete study, including different values of frequencies and different geometries of the nanowire would be required to confirm our claims.

Conclusions

This section contains the final experimental part of this thesis, where we focus on investigating the effects of time-variant strain on magnetostrictive ferromagnets. To achieve this, we design devices on a piezoelectric substrate, enabling the generation of standing strain waves through interdigitated transducers when an RF voltage is applied. By utilizing Kerr microscopy to measure magnetization switching, we obtain the following key findings.

Firstly, a reduction in the coercivity in the presence of SSAWs is observed in materials exhibiting non-zero magnetoelastic coupling. The modulation of the RF voltage around the IDTs central frequency leads to further reductions in the coercive field at the same output power. We attribute this to the modulation of the anti-node position where the largest strain anisotropy is induced, additionally contributing to the magnetization reversal.

Secondly, in devices for domain wall injection, a significant decrease in the injection field is reported in the presence of SSAWs and this reduction is most pronounced in the presence of frequency modulation. Interestingly, we report the reduction of B_{inj} to be dependent on the central frequency of the IDTs. Upon comparing the frequency of the surface acoustic waves (SAWs), denoted as f_0, with the resonant frequency, ω_0, of a magnetic vortex having the same aspect ratio as our nanowire, we speculate that the coupling between the SAW and the injected domain wall is more significant when $f_0 \simeq \omega_0$.

This section further explored the effects of frequency modulated strain on magnetic domain walls. These promising results give motivation to continue exploring the effects of dynamic strain - using time resolved Kerr microscopy and considering more values of RF frequency - as it holds potential for future developments in domain wall devices.

6

Conclusions and Outlook

The conclusions of this work are here presented. If strain cross sensitivity needs to be minimized for most applications, controlled strain can be used to realize new magnetic sensor concepts. Possible implications are illustrated in the outlook to this thesis work.

Contents

6.1 Conclusion

As discussed in the theory chapter, Sec. 2.2.4.1, the magnetization is coupled to the elastic state of a material. The strength of this magneto-elastic interaction is determined by the magnetostriction, a constant whose value can be positive or negative if the tensile strain defines an easy or hard axis of magnetization, respectively. The magnetoelastic properties of thin films are therefore of major interest for technological use as well as for scientific investigations. The optimization of the magnetic sensing layer is crucial for magnetic sensors, and depending on the application, different requirements exist. These requirements can be met if the magnetoelastic coefficient can be controlled.

This is the focus of the fist experimental chapter, Chap. 4 of this thesis, whose attention is the optimization of the free layer of magnetic sensors with emphasis on the strain effects. The chapter begins by discussing two typical material platforms for in-plane magnetized sensors: a Ni(2 nm)/Fe(2 nm) multilayer and a 30 nm Permalloy ($Ni_{81}Fe_{19}$ alloy). In both cases, He^+ ion irradiation, a post-deposition technique, is employed to control the magnetostriction and improve the magnetic softness of the materials. The irradiations and Monte Carlo simulations are performed in collaboration with the startup company Spinion Technologies.

In the first study presented in Sec. 4.1, the magnetoelastic properties of sputtered Ni/Fe multilayers after He^+ ion irradiation are investigated. Various techniques for structural analysis are used, revealing limited roughness and alloying at the Ni/Fe interface in the as-deposited state. The study finds that intermixing of the sputtered layers at the interfaces is promoted by light ion irradiation in proportion to the ion fluence. The saturation magnetostriction of the magnetic stack is observed to change with increasing ion fluence, leading to a sign change in the magnetoelastic coupling from negative to positive for high fluences. The study also demonstrates that strain insensitivity of the sensor free layer can be achieved within a specific range of ion fluences.

The impact of He^+ irradiation and thermal annealing on the magnetic properties of Permalloy samples are explored instead in Sec. 4.2. Structural modification analysis using XRD revealed increased crystallization of the $Ni_{81}Fe_{19}$ alloy along the thickness direction after both treatments. The irradiation has led to a drastic reduction in the hard axis coercivity and the deposition-induced anisotropy, while the field-free annealing did not significantly enhance magnetic softness. The study attributes this difference to stress relaxation in the film after irradiation and the completely isotropic mechanism for atomic ordering

in the case of irradiation alone. The effective magnetostriction of the film decreases significantly after both irradiation and annealing. Importantly, the sizable magnetoresistance is maintained after irradiation, indicating that post-growth He^+ irradiation can enhance magnetic softness and minimize strain cross-sensitivity in Permalloy. Unlike thermal annealing, ion irradiation enables local material treatment, making it possible to adjust the anisotropy and directly write magnetic domain patterns into thin-film structured devices. This technique holds promise for high-sensitivity and low-hysteresis integrated AMR sensors designed to be insensitive to strain.

Sec. 4.3, presents a study on the strain-dependent properties of synthetic ferrimagnets. The study focuses on the effect of external strain on perpendicular magnetic anisotropy (PMA) and magnetization compensation of Co/Gd systems at room temperature. In order to verify they suitability when integrated in standard CMOS technologies, wedge samples with varied magnetic layer thickness are grown to determine thickness-dependent transitions in the magnetostatics and magnetization compensation of the multilayer system. The study experimentally measures a significant magnetoelastic coupling in a bilayer Pt/Co/Gd system, which changes the spin-reorientation transition (SRT) in the presence of strain. By varying the thickness of the bottom Gd layer in a Pt/Co/Gd/Co/Gd/Pt multilayer structure, the magnetization compensation is found to be unaffected by external strain. This research contributes to the understanding of strain-induced effects in synthetic ferrimagnet, showing their superior resilience to strain if compared to ferrimagnetic alloys.

The second experimental chapter, Chap. 5, delves into the effects of different types of strain (uniform, non-local and time variant strain) on magnetic sensors and devices based on magnetic domain walls. Sec. 5.1 investigates the injection of domain walls into nanowires under uniform strain. The study focuses on the effects of strain on the domain wall injection field in magnetostrictive materials. The results show that the strain effects depend on the material magnetoelastic coupling, and that uniaxial strain can increase the injection field. The study emphasizes also that material preparation and careful design are critical for optimizing the injection mechanism and improving the robustness of devices against strain disturbances. The findings show that a deposition-induced uniaxial anisotropy, can reduce the effective uniaxial anisotropy in the nucleation pad, keeping the injection field low even in the presence of external strain. These findings suggest that tailored engineering of the magnetic anisotropy can make domain wall-based devices more robust to external strain.

A novel technique for generating local strain on a substrate to manipulate magnetic domain walls is proposed and validated in Sec. 5.2. By selectively removing regions of the passivation layer, strain gradients are created, enabling the controlled manipulation of magnetic domain walls. The approach offers

an alternative for generating domain wall-based devices that are compatible with wafer-level production. Due to its relevance for sensing applications, it is submitted as a patent application. The technique's feasibility is demonstrated through experiments on submicron magnetic nanowires, which successfully show the pinning of domain walls using the locally-induced strain gradients. This innovative approach has the potential to advance the field of magnetic domain wall devices. This is shown with a new sensor concept, a device able to detect discrete values of magnetic field in a nonvolatile way.

Finally, the effects of time-variant strain on magnetostrictive ferromagnets are explored in Sec. 5.3. The section focuses on devices fabricated on piezoelectric substrates, which generate standing strain waves controlled by AC voltage. The effects of these strain waves on the coercivity and domain wall injection are investigated. The results reveal reductions in both the coercive field and the injection field under the influence of the strain waves. Additionally, frequency modulation of the strain waves leads to more pronounced effects and those effects are found to be dependent on the frequency of the RF excitation voltage in the case of vortex type domain walls. Insights for the design and optimization of strain-driven domain wall devices are therefore highlighted, but a more systematic study has to be conducted to draw additional conclusions.

In conclusion, this thesis presented comprehensive insights into material preparation techniques, ion irradiation, in order to understand the effects of strain on the free layer of conventional magnetoresistive sensors and domain wall devices. On the one hand, the studies showed that the fine-tuning of magnetoelastic coupling is possible using ion irradiation and this can allow for strain insensitivity of the magnetic free layer of the sensor. This represent a crucial advantage as an (ideally) zero magnetostriction material is desirable in most magnetic sensing applications. On the other hand, by deliberate application of strain we realize a new magnetic sensor concept. If the magnetoelastic coupling of the free layer is significant, the strain can control the position of magnetic domain walls and stabilize the magnetization through the magnetic anisotropy. Different forms of strain can be created, with the use of substrate bending, etched passivation layers and using a piezoelectric substrate, paving the way for the development of novel magnetic sensors and devices with improved performance and versatility.

6.2 Outlook

In this section, some outlook remarks are presented, starting from the conclusions on the topics that we consider more promising.

For what concerns the irradiation as a tuning mechanism for magnetostriction, one avenue for further investigation is performing the irradiation locally. This could offer the possibility to realize on single-deposited film, areas with opposite sensitivity to strain, and therefore could allow strain detection in a Wheatstone bridge configuration arrangement. Local irradiation could also be employed to create strain activated pinning sites or racetracks for DW motion and control of skyrmions, by patterning channels for propagation (e.g. with lower anisotropy) using "ion-beam" lithography. The use of ion irradiation as a method to reduce the magnetostriction in Permalloy, should be tested on flexible substrates (e.g. kapton), where minimization of strain effects is crucial.

About the most relevant part of the thesis for technological implementation, the generating of CMOS compatible strain gradients for spintronics, many promising research directions appear. A first option would be realizing uniform strain in close proximity of a magnetoresistive element of the sensor (e.g. TMR junction or AMR stripe). The pinning of the magnetostrictive free layer, provided by the opening in the SiN, could stabilize the magnetization and suppress the magnetic noise - especially the $1/f$ component - with a limited sensitivity reduction. The local strain that is realized using the SiN opening, could also be used to improve the closed loop design of the multi-turn counter. As presented in the work of Borie et al.,[62,265] the reliable propagation of a vortex DW in a cross-shaped geometry can be improved using a curved wire (*siphon*). In analogy with the *siphon* element, the control of the DW position before entering the wire intersection could be controlled using local strain to achieve reliable propagation.

For what concerns the sensor concept proposed, the next step would be to realize the same design using a GMR material for the racetrack, thus enabling electrical detection of the domain wall position. This would allow large scale testing, and to obtain more statistic on the pinning event. Exploring opportunities for commercialization and identifying specific market needs could drive the development of cutting-edge magnetic sensors with this technology.

Eventually, the work on surface acoustic waves that has been started, should be pursued with a more systematic frequency dependent study to explain the frequency dependent vortex domain wall injection observed. The use of time resolved Kerr microscopy, would undoubtedly be of use especially if extended

to other spin structures like skyrmions or domain walls in perpendicularly magnetized systems.

This page has been intentionally left blank.

A

Appendix - Sample fabrication details

This chapter contains the lithography recipes used for structuring of the different samples used in the present thesis.

A.1 Realization of disks using optical lithography

The structures are realized using a negative resist (type AR-N7520.073) in combination with etching. The following steps were used starting from a SiOx/Si substrate with the desired material already sputtered (see Sec. 3.1.1) on top.

• Cleaning procedure:

Dip the sample in Acetone or Ethanol for 60s, then in Isopropanol 60s and finally in high-purity water for more than 60 s. Use a hotplate >120°C for 1 min for water desorption and let the sample cool down for 1 min.

• Coating procedure:

Use a spin coater and the resist AR-N7520.073 (allresist.de) 0,1 ml using a pipette. The following setting are used: prespin 1s at 500 rpm then Spin for 50s at 5000 rpm so that the resulting thickness is 100 nm. Soft-bake the resist at T = 85°C for 1 min and cool down for 1 min.

• Exposure using optical lithography:

use 10s of UV exposure using hard contact between sample surface and optical mask.

• Development:

Use the developer AR300-47 by immersion for 60 s, then use DI water for development break by 30s immersion.

• Ion Beam etching:

The best results are obtained using variable angles of the incident ions to avoid fencing. Sample rotation is set to 60 rpm. Use 30 seconds under 80°, close the shutter then 30 seconds under 10° and close shutter and do the loop until sample is completely etched etch and 20 seconds under 10° when completely done. Resist has a etching rate of roughly 5nm/min. To avoid heating use 1 min of break with the shutter close between each of the steps.

• Resist removal:

Put the sample in acetone over night and use Ultrasound with the sample in acetone for a few minutes the next day. Then use IPA and water and blow dry the sample.

A.2 Realization of nanowires using EBL

Same procedure for sample cleaning and resist coating as described in Sec. A.1. The following recipe considers a Raith lithography system (raith.com).

• Exposure:

use acceleration of 30 kV EHT and 10 µm aperture. Select the resolution of 4 nm stepsize. The suggested electron dose is 170 μC/cm^2 for crosses and 280 μC/cm^2 for nanowires.

• Development:

Use the developer AR300-47 immersing for 23 s. To have development break use 30s high-purity water rinsing.

For ion etching see Sec. A.1.

A.3 Realization of electrical contacts using lift-off

This is a liftoff recipe for standard Cr/Au (5nm /55nm) contacts and marker. This time a positive resist is used in combination with sputtering after the development. A double layer of PMMA/MMA (allresist.de) is here considered for undercut realization and facilitate liftoff.

• Coating procedure (after sample cleaning):

Use resist MMA (8.5) MAA EL6 0,1 ml and pin coat with pre-spin 2s at 500 rpm (acceleration set to 500) then spin for 60s at 3000 rpm (acceleration set to 3000).

• Soft-bake:

use hotplate at 180°C for 90s then cool down substrate for 1 min.

• Second coating:

use resist PMMA 950k A4 and pre-spin for 1s 500 rpm then Spin for 45s at 3000 rpm. Perform again a soft-bake, as described for MMA layer. Optional: spin coat E-spacer for PMMA if your sample is insulating (use setting 2000 rpm 30 s). E-spacer is a conductive resist that avoids charging of insulating amples during SEM imaging and EBL lithography.

• Exposure:

use acceleration of 10 kV EHT and 30 µm aperture. Select the resolution of 50 nm stepsize. The suggested electron dose is 160 μC/cm^2 and the *meander mode* setting.

• Development:

Optional: if you used E-spacer remove it by dipping the sample in water. Use the solution of MIBK:IPA in ratio of 1:1 and use dive development for 30s. For development break dip 30s into IPA. The blow-dry using Nitrogen and the sample is ready for contact sputtering.

• Lift off:

immerse the sample in acetone and use ultrasound for 1 min.

B

Appendix - published papers

This chapter contains the published articles during this thesis.

Publication list:

1. **Giovanni Masciocchi**, Mouad Fattouhi, Andreas Kehlberger, Luis Lopez-Diaz, Maria-Andromachi Syskaki, Mathias Kläui *Strain-controlled domain wall injection into nanowires for sensor applications*, Journal of Applied Physics **130**, 183903 (2021)
2. **Giovanni Masciocchi**, Johannes Wilhelmus van der Jagt, M-A Syskaki, Alessio Lamperti, Niklas Wolff, Andriy Lotnyk, Jürgen Langer, Lorenz Kienle, Gerhard Jakob, Benjamin Borie, Andreas Kehlberger, Dafine Ravelosona, Mathias Kläui, *Control of magnetoelastic coupling in Ni/Fe multilayers using He^+ ion irradiation*, Applied Physics Letters **121**, 182401 (2022)
3. **Giovanni Masciocchi**, Johannes Wilhelmus van der Jagt, Maria-Andromachi Syskaky, Jürgen Langer, Gerhard Jakob, Jeffrey McCord, Benjamin Borie, Andreas Kehlberger, Dafine Ravelosona, Mathias Kläui, *Optimization of Permalloy properties for magnetic field sensors using He^+ irradiation*, Phys. Rev. Applied **20**, 014001 (2023)
4. **Giovanni Masciocchi**, Thomas J Kools, Pingzhi Li, Adrien Petrillo, Bert Koopmans, Reinoud Lavrijsen, Andreas Kehlberger, Mathias Kläui, *Strain effects on magnetic compensation and spin reorientation transition of Co/Gd synthetic ferrimagnets*, J. Appl. Phys. **134**, 013904 (2023)
5. **Giovanni Masciocchi**, Mouad Fattouhi, Elizaveta Spetzler, Maria-Andromachi Syskaki, Ronald Lehndorff, Eduardo Martinez, Jeffrey McCord, Luis Lopez-Diaz, Andreas Kehlberger, Mathias Kläui, *Generation of imprinted strain gradients for spintronics*, Appl. Phys. Lett. **123**, 022404 (2023)
6. **Giovanni Masciocchi**, Andreas Kehlberger, Mathias Kläui, Ronald Lehndorff, *Spannungsbeeinflussungseinrichtung zum Erzeugen einer lokalen Veränderung einer inneren mechanischen Spannung*, German Patent application - submitted (2023)

Journal of Applied Physics ARTICLE scitation.org/journal/jap

Strain-controlled domain wall injection into nanowires for sensor applications

Cite as: J. Appl. Phys. **130**, 183903 (2021); doi: 10.1063/5.0069661
Submitted: 1 September 2021 · Accepted: 17 October 2021 ·
Published Online: 9 November 2021

Giovanni Masciocchi,[1,2,a)] Mouad Fattouhi,[3] Andreas Kehlberger,[2] Luis Lopez-Diaz,[3] Maria-Andromachi Syskaki,[1,4] and Mathias Kläui[1]

AFFILIATIONS

[1]Institute of Physics, Johannes Gutenberg-University Mainz, 55099 Mainz, Germany
[2]Sensitec GmbH, 55130 Mainz, Germany
[3]Department of Applied Physics, Universidad de Salamanca, E-37008 Salamanca, Spain
[4]Singulus Technologies AG, 63796 Kahl am Main, Germany

[a)]**Author to whom correspondence should be addressed:** gmascioc@uni-mainz.de

ABSTRACT

We investigate experimentally the effects of strain on the injection of 180° domain walls (DWs) from a nucleation pad into magnetic nanowires, as typically used for DW-based sensors. In our study, the strain, generated by substrate bending, induces in the material a uniaxial anisotropy due to magnetoelastic coupling. To compare the strain effects, $Co_{40}Fe_{40}B_{20}$, Ni, and $Ni_{82}Fe_{18}$ samples with in-plane magnetization and different magnetoelastic coupling are deposited. In these samples, we measure the magnetic field required for the injection of a DW, by imaging using differential contrast in a magneto-optical Kerr microscope. We find that strain increases the DW injection field and that the switching mechanism depends strongly on the strain direction. We observe that low magnetic anisotropy facilitates the creation of a domain wall at the junction between the pad and the wire, whereas a strain-induced magnetic easy axis significantly increases the coercive field of the nucleation pad. Moreover, we find that these effects of strain-induced anisotropy can be counteracted by an additional magnetic uniaxial anisotropy perpendicular to the strain-induced easy axis. We perform micromagnetic simulations to support the interpretation of our experimental findings showing that the above described observations can be explained by the effective anisotropy in the device. The anisotropy influences the switching mechanism in the nucleation pad as well as the pinning of the DW at the wire entrance. As the DW injection is a key operation for sensor performances, the observations show that strain is imposing a lower limit for the sensor field operating window.

I. INTRODUCTION

Domain walls (DWs) have always been of importance for their static and dynamic properties since the use of magnetic materials for logic devices and data storage.[1–3] In the last 15 years, the possibility to realize and characterize magnetic nanostructures has allowed one to explore complex spin textures, their creation, and stability. This intense research has enabled the use of DWs in memory devices[4,5] and diverse magnetic sensors.[6–9] For example, a DW can be used to carry information about the angular position of an object and to count the number of rotations performed in a non-volatile way.[10–12] The interest in magnetic sensors based on DWs is in their stability, making their non-volatile positioning suitable to many applications. No external electrical power is required to manipulate the magnetic state in the sensor, making it ideal for energy efficient systems even where power failures can occur.

The magnetic field conditions under which a DW-based sensor can reliably operate are called the field operating window.[13] For the sensor to work, a DW needs to be successfully created and propagated into the nanowire, setting the minimum operation field value. At the same time, uncontrolled nucleation of domain walls at higher fields needs to be avoided, thus setting the maximum operation field value. Previous studies about DW sensors investigated the propagation and nucleation fields and showed how they depend on material parameters and device geometry.[12–17] While the field operation window in idealized operation conditions is known, in real devices further factors play a role and have been previously neglected.

Among the external factors, strain or mechanical stress on these sensing elements is known to be a key issue. Such strain occurs during packaging as well as sensor operation, with strong

impact on the device performance.[18] Strain in magnetic materials is known to induce a preferential direction of magnetization (anisotropy) due to magnetoelastic coupling[19,20] and even pin a DW in a nanowire.[21] In DW-based devices, a common approach to generate a DW is to use a larger magnetic (nucleation) pad attached to the nanowire exploiting the reduced shape anisotropy[17,22,23] as shown in Figs. 1(c) and 1(d). It has been shown recently using simulations how, in the nucleation pad, strain-induced anisotropy can overcome the shape anisotropy governing the switching of the magnetic state.[24] However, these previous studies did not report experiments on strain effects in a sensor relevant system as ours.

In the work presented here, we investigate experimentally the impact of externally applied strain on the injection of a 180° domain wall from a nucleation pad in a magnetic nanowire. We employ magneto-optical Kerr effect (MOKE) microscopy to image the DW creation, pinning, and injection from the pad for different external strain configurations. The injection field is strongly affected by the effective anisotropy of the magnetic material, which is modified by strain. Simulations are used to identify the switching mechanism and the spin structure of a pinned DW just before the injection into the wire.

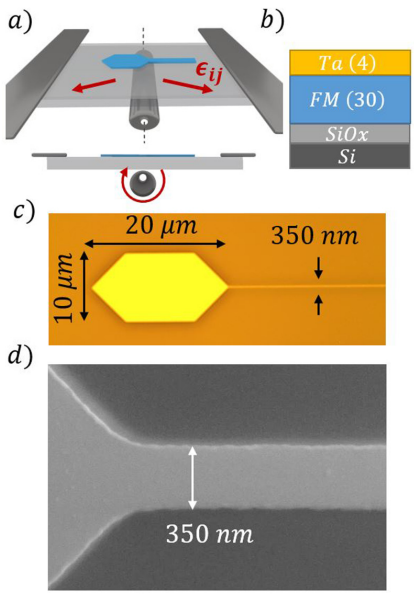

FIG. 1. (a) Schematic of the mechanism to apply mechanical strain by three-point substrate bending. (b) Layer cross section used for the investigated devices. FM indicates the magnetic material, the numbers correspond to the thickness in nm. The SiO_x and Si thicknesses are 1.5 and 625 μm, respectively. Device shown in an optical microscope (c) and scanning electron microscope image (d).

II. EXPERIMENTAL METHODS

We investigate three different samples: $Co_{40}Fe_{40}B_{20}$ (30 nm)/Ta (4 nm), $NiFe_{11}Cr_{42}$(4 nm)/$Ni_{82}Fe_{18}$(30 nm)/Ta (4 nm), and Ni (30 nm)/Pt (2 nm), and all layers are deposited by magnetron sputtering. The substrate is 1.5 μm thick, with thermally oxidized SiO_x on top of 625 μm undoped Si. To improve magnetic softness and deposition uniformity, the magnetic material was sputtered in a rotating magnetic field of 50 Oe. The result is a soft magnetic material with intrinsically low anisotropy field and low coercive field. The magnetic properties of our films, as deposited, are summarized in Table I. The values for Young's modulus and the saturation magnetostriction are assumed to be unaffected by our annealing step as our x-ray diffraction measurements suggest. For the characterization of our material, we used a BH-Looper, a hysteresis loop tracer, where B is the measured magnetic flux and H is the applied magnetic field (Shb Instruments—Model 109). This tool includes a setup for measuring magnetostriction.[25–27]

To induce a preferential direction of magnetization in the $Co_{40}Fe_{40}B_{20}$, the sample was annealed in N_2 for 2 h at $T = 265\,^{\circ}C$, while a static field of 120 mT is applied. This treatment induces a uniaxial anisotropy, where the easy axis of the magnetization is in the direction of the applied magnetic field. One plausible model to explain its mechanism is the migration of atoms. The applied magnetic field drives an anisotropic distribution of atom pairs among Co, Fe, and B[33–35] that increases the uniaxial anisotropy constant. The anisotropy field after annealing is $B_k = \frac{2K_{film}}{\mu_0 M_s} = 2.7$ mT and the uniaxial anisotropy constant is $K_{film} = 1.54(2)$ kJ/m^3, where M_s is the saturation magnetization of the magnetic material. A comparison of the angular dependence of the remanent magnetization and hysteresis loops before and after annealing are shown for $Co_{40}Fe_{40}B_{20}$, respectively, in Figs. 2(a)–2(c). A weak uniaxial anisotropy, $K_{film} < 50(5)$ J/m^3, is present even in the as-deposited $Co_{40}Fe_{40}B_{20}$ and might be associated with internal stresses during the material growth or asymmetries in the deposition system.[36] Since this value is 30 times smaller than the anisotropy field induced by thermal annealing with magnetic field, it is neglected in our study.

The structures are then patterned using photolithography and Ar ion milling. The devices used in this study can be seen in Fig. 1(c). A nucleation pad ($20 \times 10\,\mu m^2$) is attached to a 200 μm long nanowire with different widths from 350 to 800 nm. The specific geometry of the pad is designed to narrow the field

TABLE I. Parameters of the magnetic materials (thickness 30 nm) after deposition (no annealing). The values without reference are quantified experimentally by measuring the magnetic film on 5 in. wafers. Here, M_s is the saturation magnetization, B_k is the anisotropy field, B_c is the coercive field, λ_s is the saturation magnetostriction, and Y is Young's modulus. The same Y and λ_s are considered for as-deposited and annealed samples.

Material	M_s (T)	B_k (mT)	B_c (mT)	$\lambda_s \times 10^{-6}$	Y (GPa)
$Co_{40}Fe_{40}B_{20}$	1.40(5)	0.20(5)	0.10(5)	27(1)	187[28]
$Ni_{82}Fe_{18}$	0.95(5)	0.10(5)	0.10(5)	−0.5(1)	200[29]
Ni	0.60(5)	2.00(5)	2.00(5)	−32[30,31]	180[32]

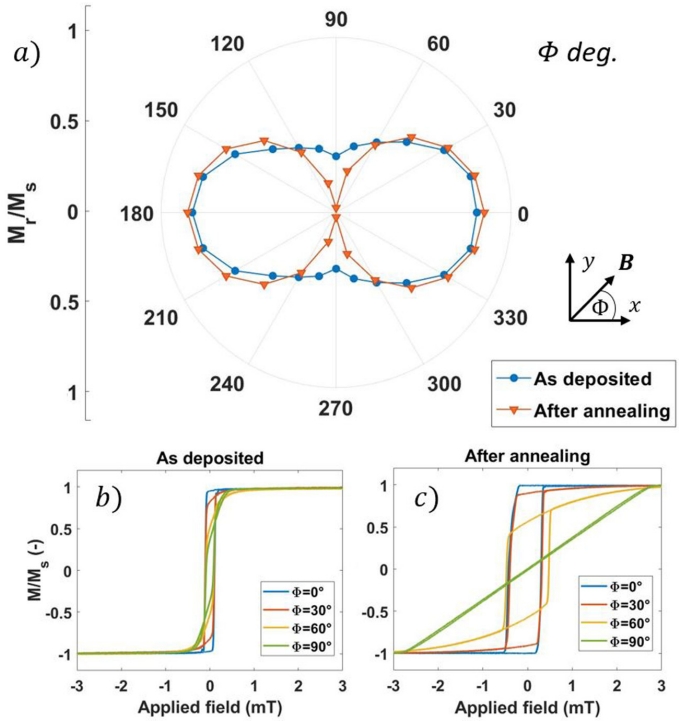

FIG. 2. Characterization of the full film 5 in. wafers of $Co_{40}Fe_{40}B_{20}$ using a BH-Looper before structuring. (a) The angular dependence of the remanent magnetization M_r/M_s shows the effects of thermal annealing in the presence of a magnetic field (orange triangles), which induces a uniaxial anisotropy with easy axis in the direction $\Phi = 0°$. Error bars are within the data points. The magnetic curves of the sample as-deposited (b) and after annealing (c) show an easy axis and a hard axis of magnetization in blue and green, respectively. Orange and yellow are the intermediate directions of the applied magnetic field.

distribution for injecting magnetic domains into the wire and to allow for a DW nucleation at low fields.

To switch the magnetization in the device, we applied an external in-plane magnetic field in the x direction (aligned with the nanowire). As the magnitude of the field is increased, the nucleated DW depins from the pad and is injected into the nanowire (injection field, B_{inj}). We measure the injection field by imaging differential contrast changes in the magneto-optical Kerr effect (MOKE) in a longitudinal configuration of the polarized white light. To image and detect the switching event, a 50× magnification objective was used. The magnetic contrast, without structural contrast, is accomplished by subtracting a reference image in the saturated stage, at the beginning of the measurement. We have conducted our experiment at fields lower than the spontaneous domain nucleation field in the wire, which is reported to be around 40 mT.[13] This ensures us that a DW is injected from the pad into the wire and not from structural defects or nucleated at the edge of the wire.

To apply strain to our devices, the substrate was bent mechanically with a three-point bender that applies an out of plane force as shown schematically in Fig. 1(a). A square sample of 1 by 1 cm is vertically constrained on two sides and pushed uniformly from below by a cylinder that has off centered rotation axis. The device generates a tensile strain in the plane of the sample up to 0.12% when the cylinder is rotated. The strain is mostly uniaxial[27] and uniform in the central area of the sample and thus in the measured area. The intensity of the strain induced on the surface of the *SiOx* has been measured with a strain gauge (RS PRO). The stack is thin enough to assume that the strain is entirely transferred to our device and that shear strain is negligible.[37]

III. RESULTS AND DISCUSSION

A. Injection field in nanowires

The injection field is the minimum field required to create and propagate a DW in the magnetic sensor device. However, to obtain reliable and a repeatable injection, one needs to understand the whole process of the DW injection. The MOKE images allow us to observe how the magnetization is gradually switched in the nucleation pad, creating a DW at its end, and also, captures the moment when a DW starts propagating into the wire.

In the absence of strain, the domain configuration in the pad is mostly dominated by the shape anisotropy and is not varying strongly for the materials studied. We indeed obtain similar images for all the measured devices. The process of injection can be observed in Figs. 3(a)–3(c). When no strain is applied to the substrate, a pattern with six domains is formed, with a domain wall at

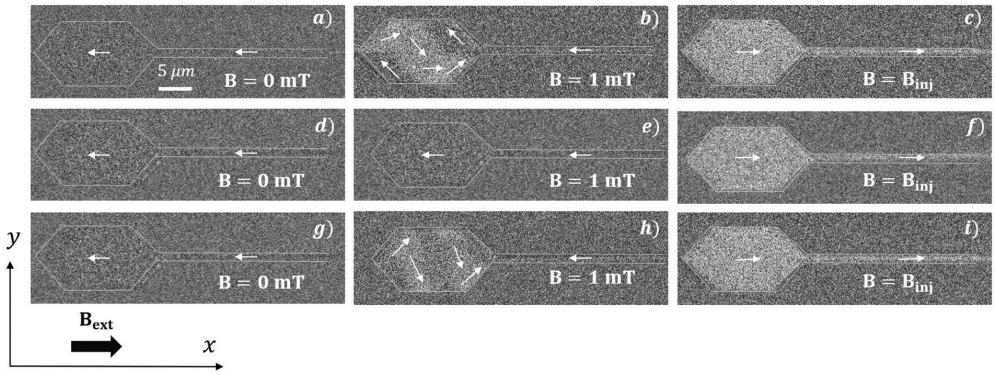

FIG. 3. Kerr microscope images of the device made of $Co_{40}Fe_{40}B_{20}$ as deposited (no annealing). The white arrows indicate the local direction of the magnetization. The width of the nanowire is 350 nm. The field is applied along the x direction and progressively increased (from left to right) until the DW nucleated in the pad is injected into the nanowire. In (a)–(c), the sample is not strained, (d)–(f) tensile strain is applied along the wire $\varepsilon_{xx} = 0.06\%$, and (g)–(i) tensile strain is applied perpendicular to the wire $\varepsilon_{yy} = 0.06\%$.

the entrance of the nanowire for fields as small as 1 mT. However, at such low fields, the DW cannot propagate into the nanowire and is pinned at its entrance. The difference in geometry between the pad and the wire creates a local pinning site for the DW. The pad has a lower coercivity than the nanowire due to the shape anisotropy, therefore, changes in the magnetization distribution of the pad result in the creation of a wall in the vicinity of the pad/wire interface. It is this wall that can then subsequently be injected to propagate along the wire.[38] To obtain the injection, the external field is increased.

If, on the other hand, the substrate of our device is mechanically deformed (strained), an additional anisotropy is induced in the magnetic system. Strain-induced anisotropy will compete with the shape anisotropy and exchange to determine the domain configuration and the switching mechanism in the injection pad. It is known how the magnetization is coupled to the uniform macroscopic strain in the expression of the free energy.[39] As reported in previous studies,[20,32] the magnetoelastic energy simplifies to a uniaxial magnetic anisotropy constant defined as

$$K_{ME} = \frac{3}{2}\lambda_s Y|\varepsilon_{xx} - \varepsilon_{yy}|, \tag{1}$$

where λ_s is the saturation magnetostriction, Y is Young's modulus of the ferromagnetic layer, and ε_{xx} and ε_{yy} are the components of the uniaxial in-plane strain along, respectively, x and y. In our experiments, the magnitude of the strain is equal to $\varepsilon_{ii} = 0.06\%$, where ii indicates the direction of uniaxial strain. This particular strain magnitude is chosen since it avoids sample breaking (at $\varepsilon > 0.12\%$) and is large enough to probe strain effects on the injection field. Since the strain is uniaxial, we assume that the other direction can be neglected ($\varepsilon_{yy} \ll \varepsilon_{xx}$ and vice versa). This means the strength and the direction of the uniaxial anisotropy contribution will be determined by, respectively, the magnitude and the sign of the saturation magnetostriction λ_s. In a positive magnetostrictive material ($Co_{40}Fe_{40}B_{20}$), the easy axis will follow the direction of the tensile strain, while there will be a hard axis in this direction for a negative magnetostrictive material (Ni).

We experimentally observe that the conditions for the DW nucleation and injection are modified by the strain. When the easy axis of magnetization is along the wire (x direction), the coercive field of the pad is increased and the magnetization rotates suddenly from left to right. This can be seen in Figs. 3(d)–3(f). No intermediate multi-domain state is present in the pad and the DW is not pinned at wire entrance since the coercive field coincides with the injection field. The second case is represented in Figs. 3(g)–3(i). Here, the easy axis of magnetization is induced perpendicular to the field direction (along y). In this case, the multi-domain state that minimizes the energy in the pad prefers spin aligned along the y axis, and a DW is nucleated at the entrance of the pad. In this case, the nucleated DW stays pinned at the entrance even for a higher field with respect to the unstrained case.

Using the values in Table I and Eq. (1), one can calculate the uniaxial anisotropy constant due to the magnetoelastic term which is $K_{ME} = 3.6(1)$ kJ/m^3 for $Co_{40}Fe_{40}B_{20}$, $K_{ME} = -4.3(1)$ kJ/m^3 for Ni and only $K_{ME} = -7(1) \times 10^{-2}$ kJ/m^3 for $Ni_{82}Fe_{18}$. The sign is determined by the magnetostrictive constant. The energetically favorable state for magnetization direction will, therefore, be along ($Co_{40}Fe_{40}B_{20}$) or perpendicular (Ni) to the direction of tensile strain. The strain-induced effects are expected to be more than 50 times smaller in the devices made of $Ni_{82}Fe_{18}$.

In Fig. 4, the injection field B_{inj} is experimentally reported for three different materials. As expected, materials with strong magnetoelastic coupling (i.e., large $|\lambda_s|$) will show the largest strain effects as can be seen in Figs. 4(a) and 4(c). This is why, for $Ni_{82}Fe_{18}$, with low magnetoelastic coupling, the three curves overlap within the

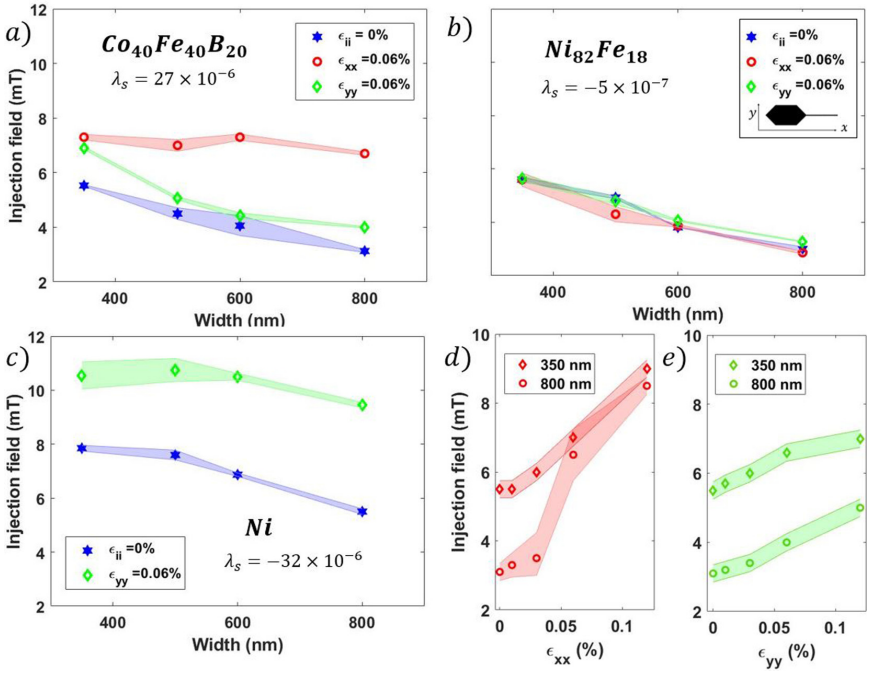

FIG. 4. Experimental results of the injection field B_{inj}. Three different ferromagnetic materials (thickness 30 nm) have been measured: (a) $Co_{40}Fe_{40}B_{20}$, (b) $Ni_{82}Fe_{18}$, and (c) Ni. The experimental values are plotted as a function of the nominal width of the nanowire. For the data points in blue, no strain is applied. Uniaxial strain ε_{ii} was applied in the x or in the y direction for the red and green curves, respectively, as schematically shown in the inset. (d) and (e) B_{inj} for $Co_{40}Fe_{40}B_{20}$ is plotted as a function of the intensity of the strain applied along the x and the y direction, respectively, for selected wire widths.

error bars in Fig. 4(b). This also confirms that the observed changes in the injection field are caused by strain.

A first observation is that in magnetostrictive materials strain is always increasing the injection field, thus imposing a lower limit for the sensor operation field. When an easy axis along x is created, the pad coercivity grows, thus also increasing the injection field. This is the case of ε_{xx} for $Co_{40}Fe_{40}B_{20}$ and ε_{yy} for Ni. When instead the easy axis is oriented along the y direction (ε_{yy} for $Co_{40}Fe_{40}B_{20}$ and ε_{xx} for Ni), the DW created at the mouth of the pad finds this position more energetically favorable than the wire. Therefore, a larger injection field is required. Due to small magnetic contrast in Ni, some experimental points in 4(c) are missing.

A second observation concerns the wire width dependence of the injection field. Regardless of the material, when strain is not applied ($\varepsilon_{xx} = \varepsilon_{yy} = 0$), we find that the injection field decreases with the increasing width of the wire. As reported elsewhere,[40,41] the injection field in soft magnetic wires is mainly determined by the shape of the cross section (width and thickness) and the monotonic behavior of B_{inj} is the consequence of different sizes of DWs governed by different wire widths. Therefore, we expect that in the absence of strain, the de-pinning field from the extremity of the pad is mainly due to shape anisotropy.[42] However, when magnetoelastic anisotropy energy is introduced in the system, we observe deviation from this dependence. When K_{ME} favors a spin orientation along the x direction, the injection field is determined by the coercivity of the pad and the dependence of the injection field on the wire width is negligible for thin wires [Fig. 4(a), red circles and 4(c), green diamonds]. This is because B_c in the pad is large enough to inject and propagate the DW through the nanowire. In all the other measured cases, instead, the DW stays pinned at the edge of the pad, and a net dependence of B_{inj} on the wire width is observable. Interestingly, when the strain-induced easy axis of magnetization is perpendicular to the wire, the dependence of B_{inj} on the wire width is maintained [Fig. 4(a), green diamonds].

An explanation for this can be found in the different competing contributions to the system energy. To describe the impact of strain on the magnetization orientation and injection field, we use the free energy of the system F_{tot} that is a measure for the angular dependence of the magnetic hardness. In a system with no net crystalline anisotropy, the free energy is given by[31,43]

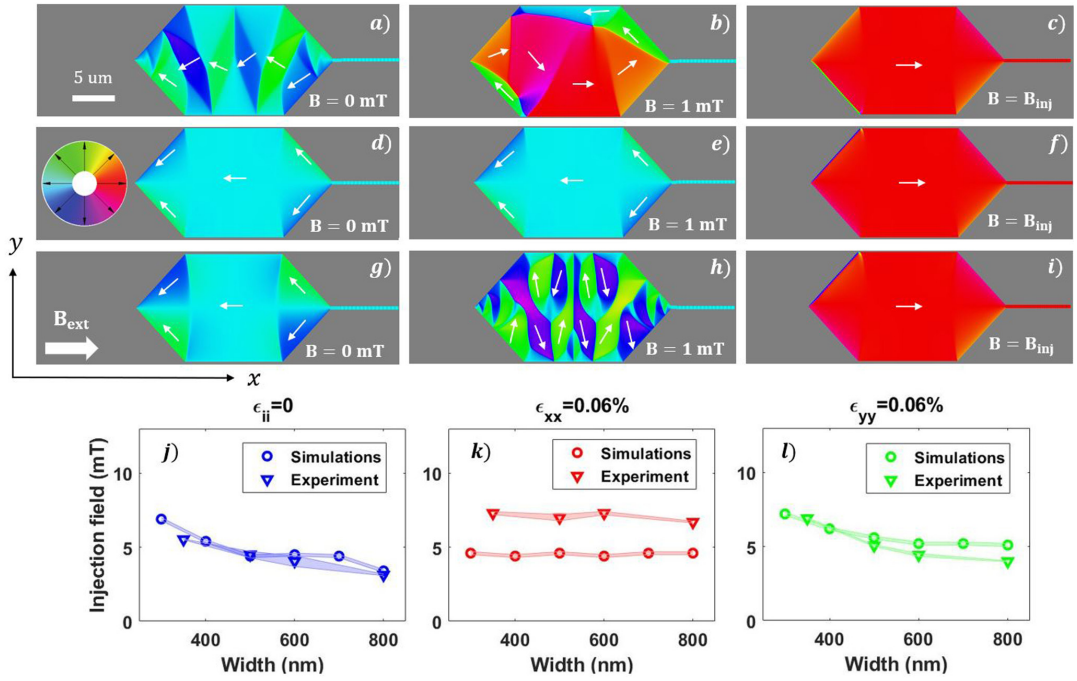

FIG. 5. Snapshots of the simulations performed with the *Mumax*[3] framework. We used material parameters of amorphous $Co_{40}Fe_{40}B_{20}$. The field is applied along the *x* direction and progressively increased (from left to right) until the DW nucleated in the pad is injected into the nanowire (300 nm wide). (a)–(c) Strain is not included, (d)–(f) uniform tensile strain along the wire is applied, $\varepsilon_{xx} = 0.06\%$, and (g)–(i) uniform tensile strain is applied perpendicular to the wire, $\varepsilon_{yy} = 0.06\%$. The order of the images follows Fig. 3, and a comparison confirms the same switching mechanism observed in the experiments. (j)–(l) Comparison between the calculated and measured B_{inj} for the indicated strain configurations.

$$F_{tot} = F_{zeeman} + F_{demag} + F_{magel}. \quad (2)$$

F_{zeeman} describes the influence of the external magnetic field, and the demagnetization term F_{demag} depends on the shape of the device. The last term describes the influence of the lattice strain to the magnetic anisotropy $F_{magel} = K_{ME}\sin^2(\phi)$ according to Eq. (1), where ϕ is the angle between the magnetization and the easy axis. Minima in the expression of F_{tot} correspond to magnetic easy directions.

Let us now compare the case of $F_{magel} = 0$ (no strain) and $K^y_{ME} \neq 0$ with the easy axis along *y*. This strain-induced uniaxial anisotropy tends to favor a spin configuration with wider DW in the nucleation pad, where a large part of magnetization is pointing along *y*. This is observed both in the MOKE images and in the simulated spin structure. What determines the injection field[41] is the energy difference between a DW sitting at the extremity of the pad and inside the wire $\Delta E^{DW} = E^{DW}_{wire} - E^{DW}_{pad}$. Since in the wire a narrow DW is preferred,[44] the energy barrier ΔE^{DW} will be larger if $K^y_{ME} \neq 0$. Therefore, a larger external applied field is required to inject the DW wall, as we experimentally observe. Additional experimental data reported in Figs. 4(d) and 4(e) allow the identification of the different energy terms in Eq. (2). When B_{inj} for $Co_{40}Fe_{40}B_{20}$ is plotted as a function of the intensity of the strain applied, the behavior is monotonic in qualitative agreement with the magnetoelastic energy term F_{magel} calculated using Eq. (1). At the same time, these data reaffirm how the impact of device shape (energy term F_{demag}) becomes negligible in the presence of a large strain along the wire (ε_{xx}), while it remains significant if the strain is perpendicular to the device (ε_{yy}).

To get a better understanding of the effect of strain on the injection field, we performed micromagnetic simulations using the GPU-based *Mumax*[3] framework.[45] The material parameter values measured for our sample were considered, namely, $\lambda_s = 2.7 \times 10^{-5}$ and $M_s = 1.0 \times 10^6$ A/m for saturation magnetostriction and magnetization, respectively, whereas for the exchange and elastic constants, typical values for $Co_{40}Fe_{40}B_{20}$ reported in the literature were used:[28] $A_{ex} = 1.5 \times 10^{-11}$ J/m, $c_{11} = 2.8 \times 10^{11}$ N/m^2, $c_{12} = 1.4 \times 10^{11}$ N/m^2, and $c_{44} = 0.7 \times 10^{11}$ N/m^2. As the anisotropy for

as-deposited samples is less than 50 J/m^3, the first order uniaxial anisotropy constant is set to zero in the simulations as its energy contribution is negligible.

In the simulations, the dimensions of the pad are the same than in the physical system [Fig. 1(c)], whereas the nanowire is shortened to 2.5 μm. The computational region is divided into $5 \times 5 \times 15$ nm^3 cells. The mechanical stress is modeled by adding a magnetoelastic field contribution to the effective field.[46,47] The system is initialized with uniform magnetization pointing in the $-x$ direction and the equilibrium state is calculated for a series of increasing applied fields in steps of 0.2 mT. The results of the simulations are shown in Fig. 5. Some snapshots of the magnetization are presented to be compared with the Kerr microscope images in Fig. 3. As noticeable, the main features observed at $B = 1$ mT are reproduced by the simulations, namely, the double vortex pattern in the absence of strain [Figs. 3(b) and 5(b)], the quasi-uniform configuration for $\varepsilon_{xx} = 0.06\%$ [Figs. 3(e) and 5(e)], and the multidomain state favoring the magnetization pointing along y for $\varepsilon_{yy} = 0.06\%$ [Figs. 3(h) and 5(h)]. The computed injection fields as a function of the wire width are plotted in the lower part of Fig. 5 together with the experimental ones, showing good quantitative agreement except for the case where the tensile strain is applied along x, where the computed values are significantly below the experimental ones. Both the decrease in the injection field when increasing the wire width for the cases of no strain [Fig. 5(j)] and $\varepsilon_{yy} = 0.06\%$ [Fig. 5(l)] and the negligible dependence for $\varepsilon_{xx} = 0.06\%$ are well captured by the simulations, supporting our interpretation of the experimental results.

To summarize, an overview of the effects of the strain on the injection field can be observed in Fig. 4(a). We report that for a positive magnetostrictive material such as $Co_{40}Fe_{40}B_{20}$, the injection field is proportional to the uniaxial strain ε_{xx} [Fig. 4(d)] or ε_{yy} [Fig. 4(e)]. Only in the case when the easy axis of magnetization is aligned along the wire, the injection field coincides with B_c of the pad and the wire width dependence is low [Fig. 4(a), red circles].

B. Effects of growth-induced anisotropy

Up to now, we have considered isotropic and magnetically soft ferromagnetic materials. In this case, a strain-induced uniaxial anisotropy with constant of $K_{ME} \simeq 3$–5 kJ/m^3 was the only anisotropy energy contribution in the full film material. To further investigate the mechanism and the limits for DW nucleation and injection, we structured our devices using thermally annealed $Co_{40}Fe_{40}B_{20}$. In this section, again the numerical value of Young's modulus reported in Table I is assumed. This material preparation induces a preferential orientation (easy axis, EA) for the magnetization, according to the direction of the applied magnetic field during annealing. The uniaxial anisotropy $K_{film} = 1.54(2)$ kJ/m^3 has been measured experimentally from the full film hysteresis loops. To take this contribution into account, an additional term to the free energy is added, and Eq. (2) becomes

$$F_{tot} = F_{zeeman} + F_{demag} + F_{magel} + F_{film}, \tag{3}$$

where $F_{film} = K_{film} \sin^2(\phi)$ is the free energy term of the crystalline magnetic anisotropy, which may compete with strain-induced anisotropy and alter the magnetization orientation effects.

In light of this, the experiment described in Sec. II has been repeated for annealed $Co_{40}Fe_{40}B_{20}$ samples. Sizable effects are found when K_{film} and the magnetoelastic anisotropy K_{ME} are superimposed. In Fig. 6, the results for this experiment are shown, and the annealed films are compared with the as-deposited samples. One can observe how, when the directions of K_{ME} and K_{film} are parallel, the effective uniaxial anisotropy grows (larger injection field for red points in Fig. 6). On the other hand, the injection field is reduced if K_{ME} and K_{film} have perpendicular easy axis direction (green points in Fig. 6). When two different uniaxial anisotropy contributions point in the same direction, the resulting anisotropy of the film is still uniaxial, but now has an equivalent anisotropy constant $K_{eq} \propto K_{ME} + K_{film}$. This is experimentally confirmed by an increase in the anisotropy field B_k, measured along

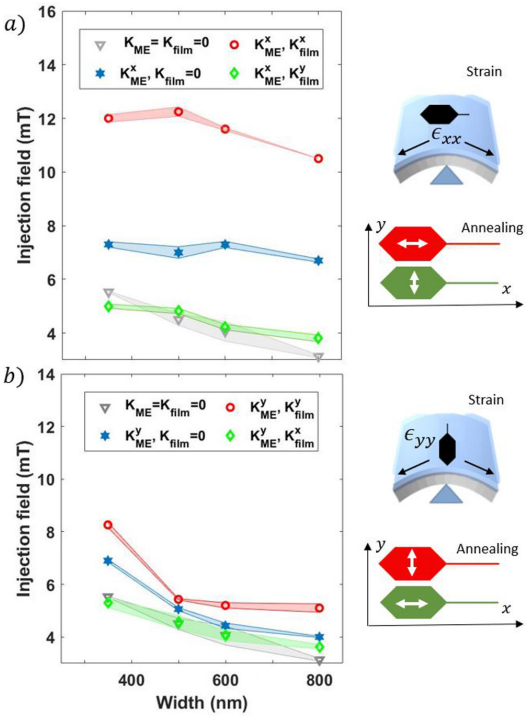

FIG. 6. Experimental injection field for $Co_{40}Fe_{40}B_{20}$. Here, samples with and without annealing are compared. (a) $\varepsilon_{xx} = 0.06\%$ in plane strain is applied and (b) $\varepsilon_{yy} = 0.06\%$. K_{ME} and K_{film} are the uniaxial magnetic anisotropy constants due to strain and annealing, respectively. The apexes indicate the in plane direction of the uniaxial anisotropy. Gray triangles are, for comparison, the reference case where no strain is applied. The scheme on the right shows the direction of the magnetic field applied during annealing (white arrows) relative to the tensile strain (black arrows).

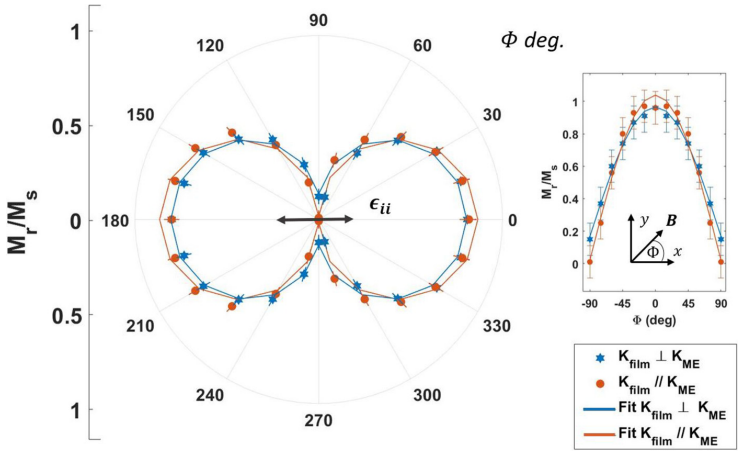

FIG. 7. Angular dependence of the normalized remanent magnetization of full film $Co_{40}Fe_{40}B_{20}$. The material was strained along $\Phi = 0°$ and measured with MOKE contrast. In orange (circles) and blue (stars), the magnetic field during annealing was applied along $\Phi = 0°$ and 90°, respectively. The experimental values were fitted using Eq. (4) of M_r and are here showed with lines. The offset of M_r along the hard axis ($\Phi = 90°$) shows the overlap of two perpendicular uniaxial anisotropy directions (biaxial anisotropy), where the magnetoelastic contribution is dominant $K_{film} < K_{ME}$. In the inset, the data are displayed in a 2D plot.

the hard axis of magnetization. Again, we can distinguish two situations. When K^x_{ME} and K^x_{film} are oriented along x, the resulting EA is along the wire [Fig. 6(a), red circles]. This increases the coercive field of the pad and consequently the injection field also grows. When K^y_{ME} and K^y_{film} are oriented with EA along y, the resulting anisotropy favors energetically the DW to be positioned at the extremity of the pad. Consequently, ΔE^{DW} and B_{inj} are larger [Fig. 6(b), red circles].

The nontrivial case is the situation when the two contributions of anisotropy, K_{ME} and K_{fim}, are perpendicular to each other. Experimentally, the values of the injection field are reduced and are close to the non-strained sample (gray triangles in Fig. 6). This result is important since it shows that the impact of the effective anisotropy on the device can be attenuated by material preparation. This outcome might seem unexpected, due to the difference in the strength of the two contributions $K_{ME} = 3.6\,\mathrm{kJ/m^3}$ and $K_{film} = 1.54\,\mathrm{kJ/m^3}$. However, one should keep in mind that the idea of an "effective" uniaxial magnetic anisotropy K_{eq} is not applicable, unless the anisotropy are oriented along identical directions.

To understand these results, a characterization of the full film material has been done in the presence of strain and annealing-induced anisotropy with MOKE hysteresis loops. The most general case considers a magnetic energy described by two perpendicular uniaxial magnetic anisotropies axes. We have measured the angular dependence of the normalized remanent magnetization M_r/M_s as a function of the angle Φ between the external magnetic field and the easy axis of magnetization. In Fig. 7, the cases K^x_{ME}, K^x_{film} and K^x_{ME}, K^y_{film} are compared. In both cases, the strain is defining the dominant easy axis, since $K_{ME} > K_{film}$. However, in Fig. 7, we observe differences in the angular plots of M_r in the vicinity of the hard axis ($\Phi = 90°$). The precise determination of the magnetic easy axis is carried out by fitting the normalized magnetic hysteresis M_r/M_s curves as a function of Φ. The projection of the in-plane magnetization vector to the plane of incidence of light during our MOKE measurements is a cosine-like function (as is evident from the inset in Fig. 7); therefore, the following fitting function is chosen:[48]

$$\frac{M_r}{M_s} = \frac{M_r^{\max}}{M_s}|\cos(\Phi)| + \frac{M_r^{off}}{M_s}, \tag{4}$$

where $\frac{M_r^{\max}}{M_s}$ is the maximum normalized magnetic remanence, and $\frac{M_r^{off}}{M_s}$ is the offset in magnetic remanence M_r. The strength of the uniaxial magnetic anisotropy is the amplitude of the fitting parameter, and the offset originates from the isotropic contribution of the film.

The fitting confirms that the easy axis is along $\Phi = 0°$ (strain direction). However, the strength of the dominant magnetic easy axis is strongly reduced when $K_{ME} \perp K_{film}$. More quantitatively, if we compare the two cases $K_{ME} \parallel K_{film}$ and $K_{ME} \perp K_{film}$, the offset $\frac{M_r^{off}}{M_s}$ increases from 0.02 to 0.21 while the maximum remanence decreases from 1.00 to 0.75, respectively. This means the annealing-induced anisotropy can contribute to the effective magnetic anisotropy of the system. The pure uniaxial anisotropy is modified by the presence of an isotropic part.

The observed results and consideration on the full film material properties can explain the experimentally determined injection field. In Fig. 6, we showed how the effects of strain can be compensated by annealing $Co_{40}Fe_{40}B_{20}$ with a magnetic field perpendicular to the strain direction. In a material with larger $\frac{M_r^{off}}{M_s}$, the coherent rotation of the magnetization requires less energy: the anisotropy field decreases and the coercive field is reduced at the same time. Therefore, the film becomes magnetically softer, and the magnetic properties of the blue points in Fig. 7 are closer to the ones of the unstrained as-deposited state, shown in Fig. 2(a). This supports the findings displayed in Fig. 6, where the green ($K_{ME} \perp K_{film}$) and gray (no anisotropy) data points overlap.

The material softness directly influences not only the creation and nucleation of the DW in the nucleation pad but also the

injection field, due to the fact that the energy difference between the DW at the mouth of the pad and in the nanowire is affected by the film properties. We can indeed say that the DW energy in the thin long wire is unchanged by the presence of an annealing-induced anisotropy, because here the strong shape anisotropy[49] is of the order of $\simeq 10^4\ \mathrm{J/m^3}$. On the other hand, in the nucleation pad, if the strength of the uniaxial magnetic anisotropy is reduced, the magnetization is free to rotate in the field direction similarly to the unstrained as-deposited state.

IV. CONCLUSIONS

In conclusion, we have investigated the effects of mechanical strain on the injection of a DW into a nanowire using MOKE microscopy and *Mumax*[3] micromagnetic simulations. We have measured in-plane magnetized $Co_{40}Fe_{40}B_{20}$, Ni, and $Ni_{82}Fe_{18}$ films structured by optical lithography. We find that the effects of the strain are proportional to the magnetoelastic coupling of the material, quantified by the saturation magnetostriction λ_s. We report that uniaxial strain, regardless of the direction, induces a uniaxial magnetic anisotropy in the material and increases the injection field. The changes are up to 30% in materials with $|\lambda_s| \simeq 30$ ppm, while they are negligible in low magnetostrictive $Ni_{82}Fe_{18}$. The experimental results show how the mechanism of DW injection depends primarily on the creation of the DW in the pad. Further measurements involved different material preparation introducing a thermal annealing step with a magnetic field for $Co_{40}Fe_{40}B_{20}$. With this, another uniaxial magnetic anisotropy is introduced and contributes together with strain effects to the B_{inj}. We find that the strain-induced uniaxial anisotropy, K_{ME}, can be enhanced or weakened using annealing-induced uniaxial anisotropy, K_{film}, respectively, parallel or perpendicular to the strain contribution. If the easy axis of magnetization is along the wire direction, the coercive field of the nucleation pad increases significantly. In the same way, low anisotropy will facilitate the magnetization to switch and create a DW at low fields ($\simeq 1mT$) at the extremity of the pad. The DW stays pinned at the wire entrance until the energy difference $\Delta E^{DW} = E^{DW}_{wire} - E^{DW}_{pad}$ is comparable with the Zeeman energy (higher external fields). This energy barrier is the combination of different anisotropies and can be tailored by device design and material preparation. The validity of these results is verified by micromagnetic simulations, which can help us to identify the lower limit for reliable DW injection. The optimization and development of magnetic sensors and devices based on domain walls needs to consider, therefore, the effects of strain and material preparation. Our results of the DW injection mechanism show that a magnetostrictive free behavior of the DW-based device can even be reached in systems with finite magnetostriction. A careful material preparation can reduce the effective anisotropy caused by strain in the magnetic layer, thus keeping the DW injection field low in these devices. This provides, therefore, a way to improve the robustness of these types of magnetic sensors against strain disturbances.

ACKNOWLEDGMENTS

The authors would like to acknowledge Dr. R. Lehndorff for the fruitful discussions. This project has received funding from the European Union's Horizon 2020 research and innovation program under the Marie Skłodowska-Curie Grant Agreement No. 860060 "Magnetism and the effect of Electric Field" (MagnEFi) and the Austrian Research Promotion Agency (FFG). The authors also acknowledge support by the chip production facilities of Sensitec GmbH (Mainz, DE), where part of this work was carried out, the German Research Foundation (SFB TRR 173 Spin + X #268565370), the BMBF (ForLab MagSens Center), and the Max-Planck Graduate Centre with Johannes Gutenberg University.

AUTHOR DECLARATIONS

Conflict of interest

The authors have no conflicts to disclose.

DATA AVAILABILITY

The data that support the findings of this study are available from the corresponding author upon reasonable request.

REFERENCES

[1]M. Kläui, "Head-to-head domain walls in magnetic nanostructures," J. Phys.: Condens. Matter **20**, 313001 (2008).
[2]R. Spain, "Domain tip propagation logic," IEEE Trans. Magn. **2**, 347–351 (1966).
[3]D. A. Allwood, G. Xiong, C. Faulkner, D. Atkinson, D. Petit, and R. Cowburn, "Magnetic domain-wall logic," Science **309**, 1688–1692 (2005).
[4]S. S. Parkin, M. Hayashi, and L. Thomas, "Magnetic domain-wall racetrack memory," Science **320**, 190–194 (2008).
[5]D. Atkinson, D. Eastwood, and L. Bogart, "Controlling domain wall pinning in planar nanowires by selecting domain wall type and its application in a memory concept," Appl. Phys. Lett. **92**, 022510 (2008).
[6]L. Jogschies, D. Klaas, R. Kruppe, J. Rittinger, P. Taptimthong, A. Wienecke, L. Rissing, and M. C. Wurz, "Recent developments of magnetoresistive sensors for industrial applications," Sensors **15**, 28665–28689 (2015).
[7]P. Vavassori, V. Metlushko, B. Ilic, M. Gobbi, M. Donolato, M. Cantoni, and R. Bertacco, "Domain wall displacement in Py square ring for single nanometric magnetic bead detection," Appl. Phys. Lett. **93**, 203502 (2008).
[8]M. Donolato, P. Vavassori, M. Gobbi, M. Deryabina, M. F. Hansen, V. Metlushko, B. Ilic, M. Cantoni, D. Petti, S. Brivio *et al.*, "On-chip manipulation of protein-coated magnetic beads via domain-wall conduits," Adv. Mater. **22**, 2706–2710 (2010).
[9]E. Rapoport and G. S. Beach, "Dynamics of superparamagnetic microbead transport along magnetic nanotracks by magnetic domain walls," Appl. Phys. Lett. **100**, 082401 (2012).
[10]M. Diegel, R. Mattheis, and E. Halder, "Multiturn counter using movement and storage of 180 magnetic domain walls," Sens. Lett. **5**, 118–122 (2007).
[11]R. Mattheis, S. Glathe, M. Diegel, and U. Hübner, "Concepts and steps for the realization of a new domain wall based giant magnetoresistance nanowire device: From the available 24 multiturn counter to a 212 turn counter," J. Appl. Phys. **111**, 113920 (2012).
[12]B. Borie, J. Wahrhusen, H. Grimm, and M. Kläui, "Geometrically enhanced closed-loop multi-turn sensor devices that enable reliable magnetic domain wall motion," Appl. Phys. Lett. **111**, 242402 (2017).
[13]B. Borie, A. Kehlberger, J. Wahrhusen, H. Grimm, and M. Kläui, "Geometrical dependence of domain-wall propagation and nucleation fields in magnetic-domain-wall sensors," Phys. Rev. Appl. **8**, 024017 (2017).
[14]E. Martinez, L. Lopez-Diaz, O. Alejos, L. Torres, and C. Tristan, "Thermal effects on domain wall depinning from a single notch," Phys. Rev. Lett. **98**, 267202 (2007).
[15]E. Martinez, L. Lopez-Diaz, O. Alejos, L. Torres, and M. Carpentieri, "Domain-wall dynamics driven by short pulses along thin ferromagnetic strips:

Micromagnetic simulations and analytical description," Phys. Rev. B **79**, 094430 (2009).
[16]F. Garcia-Sanchez, A. Kakay, R. Hertel, and P. Asselin, "Depinning of transverse domain walls from notches in magnetostatically coupled nanostrips," Appl. Phys. Express **4**, 033001 (2011).
[17]D.-Q. Hoang, X.-H. Cao, H.-T. Nguyen, and V.-A. Dao, "Creation and propagation of a single magnetic domain wall in 2D nanotraps with a square injection pad," Nanotechnology **32**, 095703 (2020).
[18]W. Van Driel, J. Janssen, G. Zhang, D. Yang, and L. Ernst, "Packaging induced die stresses-effect of chip anisotropy and time-dependent behavior of a molding compound," J. Electron. Packag. **125**, 520–526 (2003).
[19]E. W. Lee, "Magnetostriction and magnetomechanical effects," Rep. Prog. Phys. **18**, 184 (1955).
[20]S. Finizio, M. Foerster, M. Buzzi, B. Krüger, M. Jourdan, C. A. Vaz, J. Hockel, T. Miyawaki, A. Tkach, S. Valencia *et al.*, "Magnetic anisotropy engineering in thin film Ni nanostructures by magnetoelastic coupling," Phys. Rev. Appl. **1**, 021001 (2014).
[21]N. Lei, T. Devolder, G. Agnus, P. Aubert, L. Daniel, J.-V. Kim, W. Zhao, T. Trypiniotis, R. P. Cowburn, C. Chappert, D. Ravelosona, and P. Lecoeur, "Strain-controlled magnetic domain wall propagation in hybrid piezoelectric/ferromagnetic structures," Nat. Commun. **4**, 1378 (2013).
[22]R. Cowburn, D. Allwood, G. Xiong, and M. Cooke, "Domain wall injection and propagation in planar permalloy nanowires," J. Appl. Phys. **91**, 6949–6951 (2002).
[23]K. Shigeto, T. Shinjo, and T. Ono, "Injection of a magnetic domain wall into a submicron magnetic wire," Appl. Phys. Lett. **75**, 2815–2817 (1999).
[24]H. Zhou, S. Shi, D. Nian, S. Cui, J. Luo, Y. Qiu, H. Yang, M. Zhu, and G. Yu, "Voltage control of magnetic domain wall injection into strain-mediated multiferroic heterostructures," Nanoscale **12**, 14479–14486 (2020).
[25]G. Choe and B. Megdal, "High precision magnetostriction measurement employing the BH Looper bending method," IEEE Trans. Magn. **35**, 3959–3961 (1999).
[26]C. Hill, W. Hendren, R. Bowman, P. McGeehin, M. Gubbins, and V. Venugopal, "Whole wafer magnetostriction metrology for magnetic films and multilayers," Meas. Sci. Technol. **24**, 045601 (2013).
[27]A. Raghunathan, J. E. Snyder, and D. Jiles, "Comparison of alternative techniques for characterizing magnetostriction and inverse magnetostriction in magnetic thin films," IEEE Trans. Magn. **45**, 3269–3273 (2009).
[28]R.-C. Peng, J.-M. Hu, K. Momeni, J.-J. Wang, L.-Q. Chen, and C.-W. Nan, "Fast 180 magnetization switching in a strain-mediated multiferroic heterostructure driven by a voltage," Sci. Rep. **6**, 1–9 (2016).
[29]E. Klokholm and J. Aboaf, "The saturation magnetostriction of permalloy films," J. Appl. Phys. **52**, 2474–2476 (1981).
[30]B. D. Cullity and C. D. Graham, *Introduction to Magnetic Materials* (John Wiley & Sons, 2011), Chap. 8, pp. 243–257.
[31]M. Weiler, A. Brandlmaier, S. Geprägs, M. Althammer, M. Opel, C. Bihler, H. Huebl, M. S. Brandt, R. Gross, and S. T. Gönnenwein, "Voltage controlled inversion of magnetic anisotropy in a ferromagnetic thin film at room temperature," New J. Phys. **11**, 013021 (2009).
[32]A. Bur, T. Wu, J. Hockel, C.-J. Hsu, H. K. Kim, T.-K. Chung, K. Wong, K. L. Wang, and G. P. Carman, "Strain-induced magnetization change in patterned ferromagnetic nickel nanostructures," J. Appl. Phys. **109**, 123903 (2011).
[33]Y. Zhang, X. Fan, W. Wang, X. Kou, R. Cao, X. Chen, C. Ni, L. Pan, and J. Q. Xiao, "Study and tailoring spin dynamic properties of CoFeB during rapid thermal annealing," Appl. Phys. Lett. **98**, 042506 (2011).
[34]G. V. Swamy, R. Rakshit, R. Pant, and G. Basheed, "Origin of 'in-plane' and 'out-of-plane' magnetic anisotropies in as-deposited and annealed CoFeB ferromagnetic thin films," J. Appl. Phys. **117**, 17A312 (2015).
[35]A. Deka, B. Rana, R. Anami, K. Miura, H. Takahashi, Y. Otani, and Y. Fukuma, "Electric-field control of interfacial in-plane magnetic anisotropy in CoFeB/MgO junctions," Phys. Rev. B **101**, 174405 (2020).
[36]B. Cui, C. Song, Y. Wang, W. Yan, F. Zeng, and F. Pan, "Tuning of uniaxial magnetic anisotropy in amorphous CoFeB films," J. Phys.: Condens. Matter **25**, 106003 (2013).
[37]O. Thomas, Q. Shen, P. Schieffer, N. Tournerie, and B. Lépine, "Interplay between anisotropic strain relaxation and uniaxial interface magnetic anisotropy in epitaxial Fe films on (001) GaAs," Phys. Rev. Lett. **90**, 017205 (2003).
[38]D. McGrouther, S. McVitie, J. Chapman, and A. Gentils, "Controlled domain wall injection into ferromagnetic nanowires from an optimized pad geometry," Appl. Phys. Lett. **91**, 022506 (2007).
[39]J. Wang, "Mechanical control of magnetic order: From phase transition to skyrmions," Annu. Rev. Mater. Res. **49**, 361–388 (2019).
[40]M.-Y. Im, L. Bocklage, P. Fischer, and G. Meier, "Direct observation of stochastic domain-wall depinning in magnetic nanowires," Phys. Rev. Lett. **102**, 147204 (2009).
[41]L. Bogart, D. Atkinson, K. O'Shea, D. McGrouther, and S. McVitie, "Dependence of domain wall pinning potential landscapes on domain wall chirality and pinning site geometry in planar nanowires," Phys. Rev. B **79**, 054414 (2009).
[42]D. Backes, C. Schieback, M. Kläui, F. Junginger, H. Ehrke, P. Nielaba, U. Rüdiger, L. J. Heyderman, C.-S. Chen, T. Kasama *et al.*, "Transverse domain walls in nanoconstrictions," Appl. Phys. Lett. **91**, 112502 (2007).
[43]A. Brandlmaier, S. Geprägs, M. Weiler, A. Boger, M. Opel, H. Huebl, C. Bihler, M. S. Brandt, B. Botters, D. Grundler *et al.*, "*In situ* manipulation of magnetic anisotropy in magnetite thin films," Phys. Rev. B **77**, 104445 (2008).
[44]R. D. McMichael and M. J. Donahue, "Head to head domain wall structures in thin magnetic strips," IEEE Trans. Magn. **33**, 4167–4169 (1997).
[45]A. Vansteenkiste, J. Leliaert, M. Dvornik, M. Helsen, F. Garcia-Sanchez, and B. Van Waeyenberge, "The design and verification of MuMax3," AIP Adv. **4**, 107133 (2014).
[46]R. Yanes, F. Garcia-Sanchez, R. Luis, E. Martinez, V. Raposo, L. Torres, and L. Lopez-Diaz, "Skyrmion motion induced by voltage-controlled in-plane strain gradients," Appl. Phys. Lett. **115**, 132401 (2019).
[47]A. Hubert and R. Schäfer, *Magnetic Domains: The Analysis of Magnetic Microstructures* (Springer Science & Business Media, 2008).
[48]S. A. Mollick, R. Singh, M. Kumar, S. Bhattacharyya, and T. Som, "Strong uniaxial magnetic anisotropy in Co films on highly ordered grating-like nanopatterned Ge surfaces," Nanotechnology **29**, 125302 (2018).
[49]A. Kumar, S. Fähler, H. Schloerb, K. Leistner, and L. Schultz, "Competition between shape anisotropy and magnetoelastic anisotropy in Ni nanowires electrodeposited within alumina templates," Phys. Rev. B **73**, 064421 (2006).

Applied Physics Letters ARTICLE scitation.org/journal/apl

Control of magnetoelastic coupling in Ni/Fe multilayers using He^+ ion irradiation

Cite as: Appl. Phys. Lett. **121**, 182401 (2022); doi: 10.1063/5.0107942
Submitted: 7 July 2022 · Accepted: 8 October 2022 ·
Published Online: 31 October 2022

G. Masciocchi,[1,2,a)] J. W. van der Jagt,[3,4] M.-A. Syskaki,[1,5] A. Lamperti,[6] N. Wolff,[7] A. Lotnyk,[8] J. Langer,[5] L. Kienle,[7] G. Jakob,[1] B. Borie,[3] A. Kehlberger,[2] D. Ravelosona,[3,9] and M. Kläui[1]

AFFILIATIONS

[1]Institute of Physics, Johannes Gutenberg University Mainz, Staudingerweg 7, 55099 Mainz, Germany
[2]Sensitec GmbH, Walter-Hallstein-Straße 24, 55130 Mainz, Germany
[3]Spin-Ion Technologies, 10 Boulevard Thomas Gobert, 91120 Palaiseau, France
[4]Université Paris-Saclay, 3 rue Juliot Curie, 91190 Gif-sur-Yvette, France
[5]Singulus Technologies AG, Hanauer Landstrasse 107, 63796 Kahl am Main, Germany
[6]CNR-IMM, UoS Agrate Brianza, Via Olivetti 2, 20864 Agrate Brianza, Italy
[7]Faculty of Engineering, Institute for Material Science, Synthesis and Real Structure, Kiel University, Kaiserstraße 2, 24143 Kiel, Germany
[8]Leibniz Institute of Surface Engineering (IOM), Permoserstraße 15, Leipzig 04318, Germany
[9]C2N, CNRS, Université Paris-Saclay, 10 boulevard Thomas Gobert, 91120 Palaiseau, France

[a)]**Author to whom correspondence should be addressed:** gmascioc@uni-mainz.de

ABSTRACT

This study reports the effects of post-growth He^+ irradiation on the magneto-elastic properties of a Ni/Fe multi-layered stack. The progressive intermixing caused by He^+ irradiation at the interfaces of the multilayer allows us to tune the saturation magnetostriction value with increasing He^+ fluences and even to induce a reversal of the sign of the magnetostrictive effect. Additionally, the critical fluence at which the absolute value of the magnetostriction is dramatically reduced is identified. Therefore, insensitivity to strain of the magnetic stack is nearly reached, as required for many applications. All the above-mentioned effects are attributed to the combination of the negative saturation magnetostriction of sputtered Ni and Fe layers and the positive magnetostriction of the Ni_xFe_{1-x} alloy at the intermixed interfaces, whose contribution is gradually increased with irradiation. Importantly, the irradiation does not alter the layer polycrystalline structure, confirming that post-growth He^+ ion irradiation is an excellent tool to tune the magneto-elastic properties of multilayer samples. An alternative class of spintronic devices can be envisioned with a material treatment able to arbitrary change the magnetostriction with ion-induced "magnetic patterning."

The magnetoelastic properties of thin films are of major interest for technological use as well as for scientific investigations. The requirements for the magnetoelastic coefficient (λ_s) strongly depend on the application. Magnetic sensors often need, for example, strain immunity,[1] i.e., zero magnetostriction, to reduce strain cross-sensitivity, while actuators require giant strain effects, achieved in materials such as $TbFe_2$ (terfenol).[2] One way to obtain the optimal value of the magnetostriction for a specific application is to use the combination of two or more materials with different magnetic and magnetoelastic properties. Multilayer systems have widely been investigated exploiting the combination of different parameters λ_s to achieve a target value.[3–6] In these studies, atomic intermixing at the multilayer interfaces has been identified to severely influence the total magnetostriction and this interface magnetostriction has been exploited to engineer the total magnetoelastic coupling of the multilayer.[3,4] In ion-sputtered films, where interface mixing naturally occurs, Nagai *et al.*[3] were able to change the sign of the magnetostriction of a multilayer magnetic stack by changing the relative thickness of the layers. However, a clear limit to this obsolete approach is the lack of control of the inter-layer roughness and degree of intermixing. The latter is, indeed, fixed by the deposition conditions. This imposes limitations to the usability of this method, as the magnetostriction can neither be arbitrarily nor be locally changed.

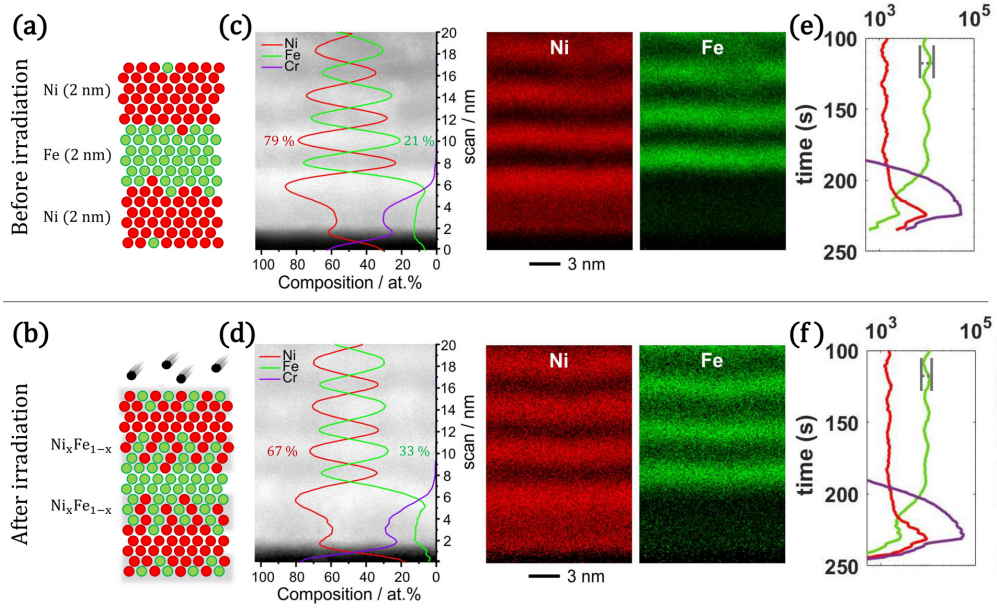

FIG. 1. (a) and (b) Sketch of the intermixing due to light ion irradiation on a multilayer stack. STEM HAADF micrograph and EDX elemental maps of the Fe/Ni multilayer system before (c) and after (d) 1×10^{16} cm^{-2} He^+ ion irradiation measured across the first four repetitions on top of the NiFeCr seed layer. The HAADF micrograph is superimposed with a plot of the atomic composition quantified from the EDX measurements. (e) and (f) Depth distribution of the elements composing the multilayer structure obtained with ToF-SIMS in the as-deposited and irradiated samples, respectively.

A widely used technique to modify magnetic properties[7–9] and induce mixing at interfaces[10,11] is ion irradiation. Specifically, the use of light ions such as He^+ at energies in the range of $10 - 30$ keV induces short range atomic displacements without generation of surface defects in the material, which instead is more prevailing for heavy atoms,[12] such as Ar^+ or Ga^+. If compared to alternative techniques to promote atomic diffusion, e.g., annealing, the use of ion irradiation confines the intermixing to the magnetic layer boundaries and avoids mixing with the nonmagnetic seed layers (for details, see Fig. S1 of the supplementary material). In addition, annealing is a uniform process while the local nature of irradiation interaction can be applied to the magnetic patterning of the multilayer film system. For these reasons, ion irradiation is an excellent candidate to obtain a desired value of the magnetostriction in a multilayer, by controlling the vertical extension of the intermixed part. A previous work[13] reported intermixing induced magnetostriction changes using heavy ions and high energies (700 MeV). However, the use of these type of atoms can be harmful for thin magnetic layers,[14] whose magnetic properties, such as saturation magnetization or perpendicular magnetic anisotropy, can be easily degraded. Moreover, the presence of cascade collisions in the material and long-range atomic displacements[15] makes the precise control of magnetic properties a difficult task.

In this work, we study the effect of progressive intermixing at the interfaces of a Ni/Fe multilayer caused by light-ion irradiation at different fluences. We report that He^+ ion irradiation can be used to tune locally the magnetoelastic properties of in-plane magnetized Ni/Fe multilayers, changing the saturation magnetostriction λ_s of the magnetic stack from negative to positive. Importantly, we confirm that the above-mentioned method not only preserves the layers polycrystalline structure but also improves the magnetic softness of the material, reducing the coercive field up to 70% and the anisotropy. The key advantages of the proposed method are the high repeatability of the process and the surface uniformity of the magnetic properties. Moreover, this technology allows for ion-induced "magnetic patterning," with focused ions or performing the irradiation through a mask in a similar fashion to semiconductor doping.[11,16] Accordingly, this technique is suitable to prepare channels for magnetic domain wall motion[17,18] and skyrmions[19,20] as it provides the creation of magnetoelastic coupling gradients.

The samples have been prepared by magnetron sputtering using a Singulus Rotaris system on a SiOx/Si substrate. A multilayer of $[\mathrm{Ni}(2\,\mathrm{nm})/\mathrm{Fe}(2\,\mathrm{nm})] \times 8$ is sputtered in the presence of a rotating magnetic field of 5 mT on a NiFeCr (5 nm) seed layer and capped with 4 nm of *Ta*. After that, optical lithography and ion etching have been used to pattern arrays of circles (80 μm of diameter and 3 μm of spacing) on the samples in order to probe the local film properties. Multiple copies of the samples have been irradiated at an energy of 20 keV with different fluences of He^+ ions from 5×10^{13} to 1×10^{16} cm^{-2}. As reported elsewhere for similar irradiation

conditions,[11] collision cascades are absent and the structural modifications are confined to the vicinity of the ion path in the metal.

At low fluences, it has been shown[21] that room temperature irradiation releases strain, whereas, at high fluences, one major structural effect of irradiation is intermixing, as schematically presented in Figs. 1(a) and 1(b) and confirmed by Monte Carlo (TRIM) simulations (Fig. S4 of the supplementary material). X-ray diffraction and scanning transmission electron microscopy (STEM) studies indicate a polycrystalline structure of (110)-textured layers of Fe and (111)-textured layers of Ni in our sample which is not significantly altered by the process of irradiation. In-depth investigation on the structural changes induced by He^+ irradiation and annealing can be found in Sec. S1 of the supplementary material, where atomic diffusion activated by thermal energy is compared with ion irradiation. According to TRIM simulations,[22] the majority (95%) of the ions reaches the substrate; therefore, a uniform intermixing in the vertical direction of the sample is expected; moreover, the effect of ion implantation into the multilayer is negligible.

To have a more quantitative estimation of the formation of the alloy for increasing ion fluences, a series of experiments to probe structural and chemical modifications occurring at the layer interfaces caused by ion irradiation were performed and are summarized in Fig. 1. Cross sections of Fe/Ni/NiFeCr on SiO_2/Si were prepared using the focused-ion-beam method (FIB). STEM electron energy-loss spectroscopy (EELS) was performed on a JEOL JEM-ARM200F "Neoarm" microscope operated at 200 kV to determine the thickness of the prepared multilayers samples. High-angle annular dark-field scanning transmission electron microscopy (HAADF-STEM, 80–200 mrad) images were acquired and nanoscale chemical analysis via energy dispersive x-ray spectroscopy (EDX) was performed in the STEM mode on a probe Cs-corrected Titan G2 60–300 microscope operating at 300 kV accelerating voltage. A vertical EDX profile across the bottom layers of the multilayer stack is shown in Figs. 1(c) and 1(d) together with corresponding EDX maps of the elemental distribution recorded on multilayers before and after He^+ irradiation with 1×10^{16} cm^{-2} fluence, respectively. After sputtering [Fig. 1(c)], the interfaces between the magnetic layers are well defined. The EDX profile of the relative atomic composition indicates 21(2)% of Fe in a Ni layer before the irradiation. After irradiation [Fig. 1(d)], the ratio of Fe atoms in a Ni layer increases to 33(4)%. This measured stoichiometric change in the layer composition is reflected in the displayed EDX elemental maps by the increased diffuse scattering of signal intensity across the layer interfaces after irradiation. This suggests the formation of an alloy of Ni_xFe_{1-x} at the Ni/Fe interfaces when the different atoms are displaced under the effect of incoming He^+ ions.

Figures 1(e) and 1(f) display the atomic depth distribution measured by Time-of-Flight Secondary Ion Mass Spectrometry (ToF-SIMS).[23–27] The presence of Fe, Ni, and Cr atoms in the multilayer is reported for samples as-deposited and irradiated with 1×10^{16} cm^{-2} fluence, respectively. Looking at Fig. 1(e), the position of the periodic oscillations of Ni and Fe appear well defined and has the same periodicity. The peak position, minima of Ni at maxima of Fe, reflects the layer distribution. The atomic distribution after irradiation is shown in Fig. 1(f). In this case, the amplitude of Ni and Fe oscillations is significantly attenuated with respect to the as-deposited case. This is again attributed to the intermixing of the atoms in the neighboring magnetic layers, leading to the formation of Ni_xFe_{1-x} alloy. More details about simulations and measurements to probe structural modifications can be found in Sec. S1 of the supplementary material.

The thin film magnetic properties have been measured with Kerr microscopy and Vibrating Sample Magnetometry (VSM). Figures 2(a) and 2(b) show in-plane hysteresis loops before and after the ion irradiation, respectively. In Fig. 2(a), the as-deposited sample presents different magnetization curves for different angular directions of the magnetic field, indicating the presence of uniaxial crystalline anisotropy $K_u \simeq 100\,\mathrm{J/m^3}$ as can be observed in the inset. The coercivity measured along the easy axis of magnetization is 0.95(5) mT. Analogous magnetic measurements are reported in Fig. 2(b) for the sample after He^+ irradiation of 1×10^{16} cm^{-2}. The magnetic in-plane anisotropy is now negligible, as the different hysteresis loops overlap. The coercivity is reduced to 0.25(5) mT. The reduction in coercivity and anisotropy might be related to a possible increase in the concentration of nucleation sites after irradiation, which allows domain formation and switching of the magnetization at lower magnetic fields.

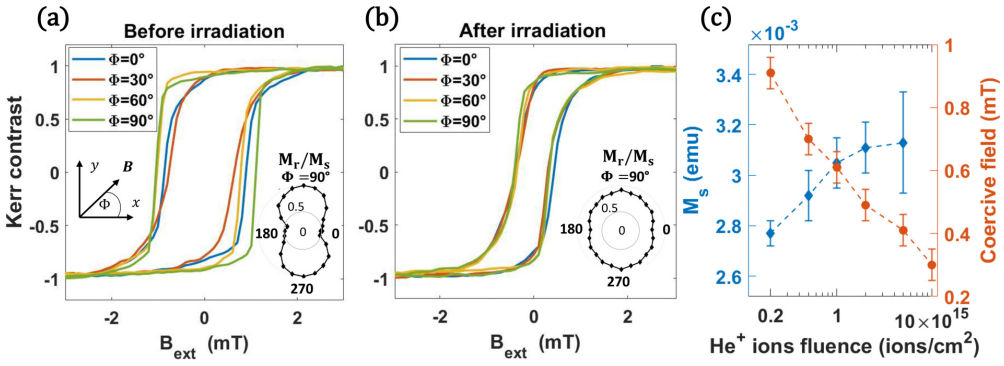

FIG. 2. (a) and (b) Hysteresis loops as a function of the in-plane magnetic field direction measured by Kerr microscopy, respectively, before and after ion irradiation with a fluence of 1×10^{16} cm^{-2}. The inset shows the angular plot of the remanent magnetization M_r/M_s as a function of the magnetic field angle Φ. (c) Saturation magnetic moment (light blue) and coercive field (orange) as a function of the fluence of He^+ ions during irradiation measured with VSM.

As the H_c and the magnetic anisotropy are reduced, the magnetic softness of our multilayer is improved by this material treatment. Figure 2(c) reports systematic measurements of the magnetic properties of our $[Ni(2\,\mathrm{nm})/Fe(2\,\mathrm{nm})] \times 8$ multilayer as a function of the He^+ fluence during irradiation. With increasing He^+ fluence, the magnetic moment of the sample increases by about 15%, from 2.8(1) to 3.1(2) $\times 10^{-3}$ emu. As reported elsewhere,[28] this is an indication of increased level of intermixing of our magnetic layers (Ni and Fe).

In order to evaluate the potential of ion irradiation to finely tune the magnetoelastic properties of a magnetic multilayer, the effective magnetic anisotropy in our sample has been measured under the application of mechanical strain by three-point bending method as previously reported.[29] Here, the substrate is bent to exert a uniaxial strain on the sample. Since the magnetization is coupled to the external strain via the expression of the anisotropy energy,[30] one way to probe the effect of the strain is to observe changes in the hysteretic behavior before and after mechanical deformation. More details can be found in Sec. S2 of the supplementary material. The expression of the magnetoelastic anisotropy depends on the saturation magnetostriction λ_s of the material according to[31]

$$K_{ME} = \frac{3}{2}\lambda_s Y \varepsilon, \tag{1}$$

where Y is the Young's modulus and ε is the uniaxial tensile strain. If the directions of the crystalline and magnetoelastic uniaxial anisotropy are such that $K_u \perp K_{ME}$, the strain dependent effective in-plane anisotropy K_{eff} measured in the system can be written as sum of two terms according to[32]

$$K_{eff} = K_u + K_{ME}. \tag{2}$$

As the sign of K_{ME} can be negative or positive, depending on the value of λ_s, the total magnetic anisotropy can, respectively, increase or decrease in the presence of strain. To quantify K_{eff}, hysteresis loops are measured using Kerr microscopy, where the magnetic field and the tensile strain are applied along the fixed direction $\Phi = 0°$. As the considered relatively thick magnetic system is dominated by shape anisotropy and, thus, in-plane magnetized, changes to interface anisotropy caused by ion irradiation can be neglected in our calculations.

The hysteresis loops measured along the direction of the applied strain $\varepsilon_{xx} = 0.06\%$ are reported in Fig. 3(a) for samples irradiated with different fluences of ions. In response to the applied strain, the irradiated samples have a different magnetic anisotropy field. By comparison with the magnetization curve in the absence of strain (dashed line), two potential scenarios are identified. When a tensile strain increases the anisotropy field in the direction parallel to ε_{xx}, K_{ME} and λ_s are negative. Our sample exhibits negative magnetoelastic coupling in the as-deposited state. On the other hand, if the strain direction becomes an easy-axis of magnetization (reduced anisotropy field), K_{ME} and λ_s are positive. This behavior is reported for larger fluences in the same magnetic stack.

As the difference between magnetic loops before and after the application of strain is proportional to the magnetoelastic anisotropy, the saturation magnetostriction (λ_s) of our magnetic multilayer can be estimated[33–35] using Eqs. (1) and (2). Figure 3(b) shows the saturation magnetostriction as a function of the fluence of He^+ ions. In agreement with the behavior of the magnetic hysteresis loops, the value of

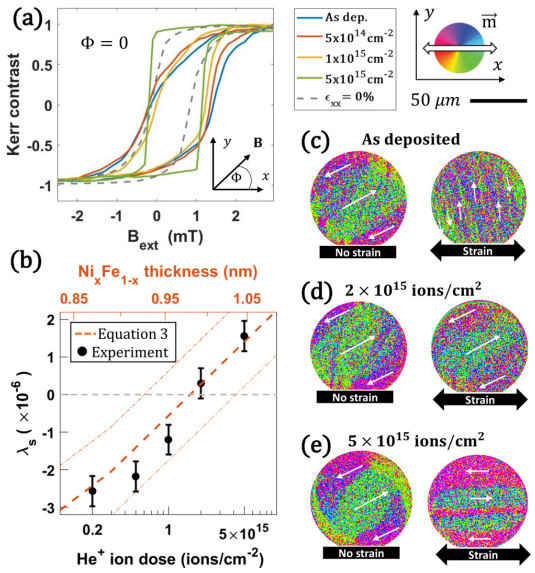

FIG. 3. (a) Hysteresis loops measured along the direction of the applied strain ($\varepsilon_{xx} = 0.06\%$) for different fluences of He^+ ions (solid lines) are compared with the unstrained magnetic loop (dashed line). (b) Measured saturation magnetostriction λ_s (black dots) as a function of the ion fluence and calculated values using Eq. (3) (dashed line) as a function of the intermixed alloy thickness $t_{Ni_xFe_{1-x}}$. A central value of $\lambda_s^{Ni_xFe_{1-x}} = 19 \times 10^{-6}$ with ±20% variation is considered. Kerr microscope images of the remanent magnetic domain state, respectively, before (left) and after (right) the application of strain are compared for (c) as deposited case, (d) intermediate value of irradiation, and (e) strong value of irradiation. The white arrows represent the direction of the in-plane magnetization in the domains according to the color wheel.

magnetostriction of the as deposited Ni/Fe multilayer is $-2.6(5) \times 10^{-6}$. He^+ fluences larger than $5 \times 10^{14}\,\mathrm{cm}^{-2}$ gradually reduce the absolute value of magnetostriction that then increases through positive values. The change in sign of the magnetoelastic coupling occurs for fluences between 1×10^{15} and $2 \times 10^{15}\mathrm{cm}^{-2}$.

An additional confirmation of the magnetic behavior of the magnetic stack under strain is obtained by imaging domain formation using the magneto-optical Kerr effect (MOKE). A vector image of the in-plane magnetization is obtained by the sum of horizontal and vertical components of the magnetic contrast. The MOKE images shown in Figs. 3(c)–3(e) present how the preferred direction of magnetization changes before and after the application of 0.06% uniaxial strain in 80 μm disk patterned samples. This particular shape has been chosen since it minimizes the in-plane shape anisotropy. The remanent magnetic domain pattern of the multilayer as-deposited is presented in Fig. 3(c). Before the application of strain (left), the magnetization aligns to the crystalline anisotropy easy axis. After the application of strain, magnetic domains orient along the y direction, perpendicular to the uniaxial strain ε_{xx}. This is a clear experimental proof of the development of stress induced magnetic anisotropy $K_{ME} \simeq -450\,\mathrm{J/m^3}$ that overcomes the initial anisotropy direction. K_{ME} is perpendicular to the

tensile strain direction due to the negative sign of the magnetostriction. The domain structure of the sample irradiated with a He^+ dose of 2×10^{15} cm^{-2} is displayed in Fig. 3(d), where a value of magnetostriction close to zero is measured. In this case, the orientation of the magnetization is almost unchanged by the presence of strain, meaning that K_{ME} is negligible, compared to the crystalline anisotropy of the material $K_u \simeq 100\,\mathrm{J/m^3}$. For higher values of fluences as reported in Fig. 3(e), the effects of strain on the remanent magnetization state become again significant. This time the dominant magnetic anisotropy contribution in the system is $K_{ME} \simeq 280\,\mathrm{J/m^3}$ as the domains orient along the x direction, parallel to the applied strain ε_{xx}. Thus, the magnetoelastic coupling of the stack has been altered using ion irradiation obtaining values of magnetostriction that range from negative to positive.

As previously reported,[4] the small value of magnetostriction in our (as-deposited) periodic system is caused by the balance among the negative magnetostriction of Ni ($\lambda_s^{Ni} = -30 \times 10^{-6}$) and Fe ($\lambda_s^{Fe} = -9 \times 10^{-6}$) and the strongly positive magnetostriction of the Ni_xFe_{1-x} alloy film ($\lambda_s^{NiFe_{50}} = 19 \times 10^{-6}$) with a relative composition close to 50%.[36,37] As shown by STEM-EDX measurements, a more intermixed interface region of Ni_xFe_{1-x} is formed at the boundary between Ni and Fe layers by He^+ ion irradiation. Hence, the thickness of the positive magnetostrictive alloy increases proportionally to the fluence of the He^+ ions during irradiation, as also confirmed by ToF-SIMS measurements. This gradually shifts the magnetostriction of the full stack to positive values. A common way to describe the effective magnetostriction in the presence of intermixing is[3–6,38–40]

$$\lambda_s = \frac{\lambda_s^{Ni} + \lambda_s^{Fe}}{2} + \left(2\lambda_s^{Ni_xFe_{1-x}} - \lambda_s^{Ni} - \lambda_s^{Fe}\right)\frac{t_{Ni_xFe_{1-x}}}{t_p}, \qquad (3)$$

where $t_p = t_{Ni} + t_{Fe} = 4$ nm is the period thickness, $t_{Ni_xFe_{1-x}}$ describes the thickness of the alloy originated by the intermixing, and $\lambda_s^{Ni_xFe_{1-x}}$ is the saturation magnetostriction of the intermixed alloy. With the appropriate magnetostriction values, Eq. (3) can be used to describe different material systems. The solution of Eq. (3) as a function of $t_{Ni_xFe_{1-x}}$ is shown in Fig. 3(b) for the system investigated in this study. A central value of $\lambda_s^{Ni_xFe_{1-x}} = 19 \times 10^{-6}$ with ±20% variation is considered. More details about the calculations are reported in Sec. S1 of the supplementary material. After deposition in similarly sputtered Ni/Fe multilayers,[3] $t_{Ni_xFe_{1-x}}$ has been estimated to be around 0.85 nm, under the assumption $t_{Fe}/t_p = 0.5$. Using this value of $t_{Ni_xFe_{1-x}}$, Eq. (3) returns $\lambda_s = -2.8(2) \times 10^{-6}$, close to the measured value after deposition. Moreover, the amount of induced intermixing caused by He^+ ions can be estimated using Eq. (3). The calculated $t_{Ni_xFe_{1-x}}$ is 0.98(2) nm at the magnetostriction compensation value ($\lambda_s = 0$) and 1.05(2) nm for the highest fluence, where the magnetostriction is positive due to the dominant effect of the alloy. This corresponds to 20% increase in the alloy thickness induced by He^+ between 0.2×10^{15} and 5×10^{15} cm^{-2}, in agreement with the information extracted from STEM-EDX and ToF-SIMS measurements.

In conclusion, this manuscript presents an experimental investigation into the magnetoelastic properties of sputtered Ni/Fe multilayers after controlled He^+ ion irradiation. Using different experimental techniques for structural analysis, the presence of moderate roughness and alloying is observed after sputtering at the Ni/Fe interface. This can justify the small negative value of magnetostriction in the as-deposited state. In the same way, it was found that light ion irradiation promotes the intermixing of the sputtered layers at the interfaces proportional to the ion fluence. This process can explain the reported changes in the saturation magnetostriction of the magnetic stack. The increasing fluence of the irradiating ions progressively changes the saturation magnetostriction inducing a change in sign of the magnetoelastic coupling of the material, from negative to positive for high fluences. Remarkably, strain insensitivity on the magnetic properties of the proposed material can be obtained with ion fluences between 1×10^{15} and 2×10^{15} cm^{-2}. Importantly, the polycrystalline structure of the layers is confirmed to be unchanged after the used irradiation conditions.

As a result, post growth He^+ ion irradiation has been demonstrated to be an excellent tool that allows to fine-tune the magnetoelastic properties of multilayer magnetic samples and we expect this method to be applicable for several material combinations. Accordingly, this technique can be foreseen to be the next generation of material treatment offering the possibility to have local patterning of magnetostriction with high control and flexibility, allowing the realization of highly demanding applications.

See the supplementary material for the complete characterization of the intermixing, the alloy composition, and for details on the calculation of the magnetostriction.

The authors acknowledge Professor J. McCord from Kiel University for fruitful discussions. This project has received funding from the European Union's Horizon 2020 research and innovation program under the Marie Skłodowska-Curie (Grant Agreement No. 860060) "Magnetism and the effect of Electric Field" (MagnEFi), the Deutsche Forschungsgemeinschaft (DFG, German Research Foundation)—TRR 173-268565370 (projects A01 and B02), the DFG funded collaborative research center (CRC)1261/project A6, and the Austrian Research Promotion Agency (FFG). The authors acknowledge the support by the chip production facilities of Sensitec GmbH (Mainz, DE), where part of this work was carried out and the Max-Planck Graduate Centre with Johannes Gutenberg University.

AUTHOR DECLARATIONS

Conflict of Interest

The authors have no conflicts to disclose.

Author Contributions

Giovanni Masciocchi: Conceptualization (lead); Data curation (lead); Formal analysis (lead); Investigation (lead); Validation (lead); Writing – original draft (lead); Writing – review & editing (lead). **Benjamin Borie:** Supervision (equal); Writing – review & editing (equal). **Andreas Kehlberger:** Project administration (equal); Resources (equal); Supervision (lead); Writing – review & editing (equal). **Dafine Ravelosona:** Project administration (equal); Resources (equal); Supervision (supporting); Writing – review & editing (supporting). **Mathias Kläui:** Resources (equal); Supervision (equal); Writing – review & editing (equal). **Johannes Wilhelmus van der Jagt:** Conceptualization (lead); Data curation (equal); Formal analysis (equal); Investigation (lead); Validation (lead); Writing – original draft (lead); Writing – review & editing (equal). **Maria-Andromachi Syskaki:** Data curation (supporting); Formal analysis (supporting); Investigation (supporting); Writing – review & editing (equal). **Alessio Lamperti:** Data curation (supporting); Formal analysis (supporting);

Investigation (supporting). **Niklas Wolff:** Data curation (supporting); Formal analysis (supporting); Writing – review & editing (equal). **Andriy Lotnyk:** Data curation (supporting); Formal analysis (supporting); Investigation (supporting); Methodology (supporting); Writing – review & editing (supporting). **Juergen Langer:** Investigation (supporting); Methodology (supporting); Resources (supporting); Supervision (supporting); Writing – review & editing (supporting). **Lorenz Kienle:** Resources (supporting); Supervision (supporting). **Gerhard Jakob:** Supervision (supporting).

DATA AVAILABILITY

The data that support the findings of this study are available from the corresponding author upon reasonable request.

REFERENCES

[1]S. Ota, A. Ando, and D. Chiba, "A flexible giant magnetoresistive device for sensing strain direction," Nat. Electron. **1**, 124–129 (2018).
[2]H. García-Miquel, D. Barrera, R. Amat, G. Kurlyandskaya, and S. Sales, "Magnetic actuator based on giant magnetostrictive material Terfenol-D with strain and temperature monitoring using FBG optical sensor," Measurement **80**, 201–206 (2016).
[3]Y. Nagai, M. Senda, and T. Toshima, "Properties of ion-beam-sputtered Ni/Fe artificial lattice film," J. Appl. Phys. **63**, 1136–1140 (1988).
[4]M. Senda and Y. Nagai, "Magnetic properties of Fe/Co, Fe/CoFe, and (Fe/Co)/SiO_2 multilayer films," J. Appl. Phys. **65**, 3151–3156 (1989).
[5]S. Rengarajan, E. Yun, W. Kang, and R. Walser, "Effect of intermixing on the magnetic properties of $Co_{50}Fe_{50}/Ni_{80}Fe_{20}$ multilayers," J. Appl. Phys. **81**, 4761–4763 (1997).
[6]S. Jen and C. Lin, "Magnetostriction and Young's modulus of [$Fe_{15}Ni_{85}$/$Fe_{25}Ni_{75}$] multilayers," Thin Solid Films **471**, 218–223 (2005).
[7]M. C. De Jong, M. J. Meijer, J. Lucassen, J. Van Liempt, H. J. Swagten, B. Koopmans, and R. Lavrijsen, "Local control of magnetic interface effects in chiral Ir/Co/Pt multilayers using Ga^+ ion irradiation," Phys. Rev. B **105**, 064429 (2022).
[8]L. H. Diez, M. Voto, A. Casiraghi, M. Belmeguenai, Y. Roussigné, G. Durin, A. Lamperti, R. Mantovan, V. Sluka, V. Jeudy *et al.*, "Enhancement of the Dzyaloshinskii-Moriya interaction and domain wall velocity through interface intermixing in Ta/CoFeB/MgO," Phys. Rev. B **99**, 054431 (2019).
[9]L. Koch, F. Samad, M. Lenz, and O. Hellwig, "Manipulating the energy balance of perpendicular-anisotropy synthetic antiferromagnets by He^+-ion irradiation," Phys. Rev. Appl. **13**, 024029 (2020).
[10]X. Zhao, B. Zhang, N. Vernier, X. Zhang, M. Sall, T. Xing, L. H. Diez, C. Hepburn, L. Wang, G. Durin *et al.*, "Enhancing domain wall velocity through interface intermixing in W-CoFeB-MgO films with perpendicular anisotropy," Appl. Phys. Lett. **115**, 122404 (2019).
[11]J. Fassbender, D. Ravelosona, and Y. Samson, "Tailoring magnetism by light-ion irradiation," J. Phys. D: Appl. Phys. **37**, R179 (2004).
[12]B. Terris, L. Folks, D. Weller, J. Baglin, A. Kellock, H. Rothuizen, and P. Vettiger, "Ion-beam patterning of magnetic films using stencil masks," Appl. Phys. Lett. **75**, 403–405 (1999).
[13]J. Juraszek, A. Grenier, J. Teillet, N. Tiercelin, F. Petit, J. B. Youssef, and M. Toulemonde, "Swift ion irradiation of magnetostrictive multilayers," Nucl. Instrum. Methods Phys. Res., Sect. B **245**, 157–160 (2006).
[14]W. F. Cureton, C. L. Tracy, and M. Lang, "Review of swift heavy ion irradiation effects in CeO_2," Quantum Beam Sci. **5**, 19 (2021).
[15]T. Devolder, I. Barisic, S. Eimer, K. Garcia, J.-P. Adam, B. Ockert, and D. Ravelosona, "Irradiation-induced tailoring of the magnetism of CoFeB/MgO ultrathin films," J. Appl. Phys. **113**, 203912 (2013).
[16]T. Devolder, C. Chappert, Y. Chen, E. Cambril, H. Launois, H. Bernas, J. Ferre, and J. Jamet, "Patterning of planar magnetic nanostructures by ion irradiation," J. Vac. Sci. Technol. B **17**, 3177–3181 (1999).
[17]S. An, E. Baek, J.-A. Kim, K.-S. Lee, and C.-Y. You, "Improved spin–orbit torque induced magnetization switching efficiency by helium ion irradiation," Sci. Rep. **12**, 3465 (2022).
[18]H. T. Nembach, E. Jué, K. Poetzger, J. Fassbender, T. J. Silva, and J. M. Shaw, "Tuning of the Dzyaloshinskii-Moriya interaction by He^+ ion irradiation," J. Appl. Phys. **131**, 143901 (2022).
[19]L.-M. Kern, B. Pfau, V. Deinhart, M. Schneider, C. Klose, K. Gerlinger, S. Wittrock, D. Engel, I. Will, C. M. Günther *et al.*, "Deterministic generation and guided motion of magnetic skyrmions by focused He^+-ion irradiation," Nano Lett. **22**, 4028 (2022).
[20]M. Fattouhi, F. García-Sánchez, R. Yanes, V. Raposo, E. Martínez, and L. Lopez-Diaz, "Electric field control of the skyrmion Hall effect in piezoelectric-magnetic devices," Phys. Rev. Appl. **16**, 044035 (2021).
[21]T. Devolder, S. Pizzini, J. Vogel, H. Bernas, C. Chappert, V. Mathet, and M. Borowski, "X-ray absorption analysis of sputter-grown Co/Pt stackings before and after helium irradiation," Eur. Phys. J. B **22**, 193–201 (2001).
[22]J. F. Ziegler, M. D. Ziegler, and J. P. Biersack, "SRIM – the stopping and range of ions in matter (2010)," Nucl. Instrum. Methods Phys. Res., Sect. B **268**, 1818–1823 (2010).
[23]A. Benninghoven, F. Rudenauer, and H. W. Werner, *Secondary Ion Mass Spectrometry: Basic Concepts, Instrumental Aspects, Applications and Trends* (Wiley-Interscience, 1987).
[24]R. N. Sodhi, "Time-of-flight secondary ion mass spectrometry (ToF-SIMS):–Versatility in chemical and imaging surface analysis," Analyst **129**, 483–487 (2004).
[25]J. C. Vickerman and D. Briggs, *ToF-SIMS: Materials Analysis by Mass Spectrometry* (IM Publications, 2013).
[26]A. Lamperti, E. Cianci, O. Salicio, L. Lamagna, S. Spiga, and M. Fanciulli, "Thermal stability of high-κ oxides on SiO_2/Si or $Si_xN_y/SiO_2/Si$ for charge-trapping nonvolatile memories," Surf. Interface Anal. **45**, 390–393 (2013).
[27]R. L. Conte, E. Martinez, A. Hrabec, A. Lamperti, T. Schulz, L. Nasi, L. Lazzarini, R. Mantovan, F. Maccherozzi, S. Dhesi *et al.*, "Role of B diffusion in the interfacial Dzyaloshinskii-Moriya interaction in $Ta/Co_{20}Fe_{60}B_{20}/MgO$ nanowires," Phys. Rev. B **91**, 014433 (2015).
[28]S. Srivastava, R. Kumar, A. Gupta, R. Patel, A. Majumdar, and D. Avasthi, "Swift heavy ion induced mixing in Fe/Ni multilayer," Nucl. Instrum. Methods Phys. Res., Sect. B **243**, 304–312 (2006).
[29]G. Masciocchi, M. Fattouhi, A. Kehlberger, L. Lopez-Diaz, M.-A. Syskaki, and M. Kläui, "Strain-controlled domain wall injection into nanowires for sensor applications," J. Appl. Phys. **130**, 183903 (2021).
[30]A. Bur, T. Wu, J. Hockel, C.-J. Hsu, H. K. Kim, T.-K. Chung, K. Wong, K. L. Wang, and G. P. Carman, "Strain-induced magnetization change in patterned ferromagnetic nickel nanostructures," J. Appl. Phys. **109**, 123903 (2011).
[31]S. Finizio, M. Foerster, M. Buzzi, B. Krüger, M. Jourdan, C. A. Vaz, J. Hockel, T. Miyawaki, A. Tkach, S. Valencia *et al.*, "Magnetic anisotropy engineering in thin film Ni nanostructures by magnetoelastic coupling," Phys. Rev. Appl. **1**, 021001 (2014).
[32]N. Martin, J. McCord, A. Gerber, T. Strache, T. Gemming, I. Mönch, N. Farag, R. Schäfer, J. Fassbender, E. Quandt *et al.*, "Local stress engineering of magnetic anisotropy in soft magnetic thin films," Appl. Phys. Lett. **94**, 062506 (2009).
[33]G. Choe and B. Megdal, "High precision magnetostriction measurement employing the BH looper bending method," IEEE Trans. Magn. **35**, 3959–3961 (1999).
[34]A. Raghunathan, J. E. Snyder, and D. Jiles, "Comparison of alternative techniques for characterizing magnetostriction and inverse magnetostriction in magnetic thin films," IEEE Trans. Magn. **45**, 3269–3273 (2009).
[35]C. Hill, W. Hendren, R. Bowman, P. McGeehin, M. Gubbins, and V. Venugopal, "Whole wafer magnetostriction metrology for magnetic films and multilayers," Meas. Sci. Technol. **24**, 045601 (2013).
[36]R. M. Bozorth, *Ferromagnetism* (Wiley-IEEE Press, 1993).
[37]B. D. Cullity and C. D. Graham, *Introduction to Magnetic Materials* (John Wiley & Sons, 2011), Chap. 8, pp. 243–257.
[38]M. Hollingworth, M. Gibbs, and S. Murdoch, "Magnetostriction and surface roughness of ultrathin NiFe films deposited on SiO_2," J. Appl. Phys. **94**, 7235–7239 (2003).
[39]C. Favieres, J. Vergara, and V. Madurga, "Interface effects on magnetostriction in pulsed laser deposited Co/Fe/Co cylindrical soft magnetic multilayers," J. Phys. D: Appl. Phys. **40**, 4101 (2007).
[40]S. Jen, T. Wu, C. Lin, and K. Chang, "Anisotropic magnetoresistance and magnetostriction of [$Fe_{15}Ni_{85}/Fe_{25}Ni_{75}$] and [$Co_{35}Ni_{65}/Fe_{25}Ni_{75}$] multilayers," Solid State Commun. **132**, 259–262 (2004).

Optimization of Permalloy Properties for Magnetic Field Sensors Using He^+ Irradiation

G. Masciocchi,[1,2,*] J.W. van der Jagt,[3,4] M.-A. Syskaki,[1,5] J. Langer,[5] G. Jakob,[1] J. McCord,[6,7] B. Borie,[3] A. Kehlberger,[2] D. Ravelosona,[3,8] and M. Kläui[1,†]

[1] *Institute of Physics, Johannes Gutenberg University Mainz, Staudingerweg 7, 55128 Mainz, Germany*
[2] *Sensitec GmbH, Walter-Hallstein-Straße 24, 55130 Mainz, Germany*
[3] *Spin-Ion Technologies, 10 boulevard Thomas Gobert, 91120 Palaiseau, France*
[4] *Université Paris-Saclay, 3 rue Juliot Curie, 91190 Gif-sur-Yvette, France*
[5] *Singulus Technologies AG, Hanauer Landstraße 107, 63796 Kahl am Main, Germany*
[6] *Faculty of Engineering, Institute for Material Science, Synthesis and Real Structure, Kiel University, Kaiserstraße 2, 24143 Kiel, Germany*
[7] *Kiel Nano, Surface and Interface Science (KiNSIS), Kiel University, Christian-Albrechts-Platz 4, 24118 Kiel, Germany*
[8] *C2N, CNRS, Université Paris-Saclay, 10 boulevard Thomas Gobert, 91120 Palaiseau, France*

(Received 1 March 2023; revised 5 May 2023; accepted 8 June 2023; published 5 July 2023)

Permalloy, despite being a widely used soft magnetic material, still requires optimization in terms of magnetic softness and magnetostriction for its use in magnetoresistive-sensor applications. Conventional annealing methods are often insufficient to locally achieve the desired properties for a narrow parameter range. In this study, we report a significant improvement in the magnetic softness and magnetostriction in a 30-nm permalloy film after He^+ irradiation. The irradiation treatment reduces the induced anisotropy by a factor of 10 and the hard-axis coercivity by a factor of 5 compared with the values in the as-deposited state. In addition, the effective magnetostriction of the film is significantly reduced by a factor ten (below 1×10^{-7}) after irradiation. All the above-mentioned effects can be attributed to the isotropic crystallite growth of the $Ni_{81}Fe_{19}$ alloy and to the intermixing at the magnetic layer interfaces under light-ion irradiation. We support our findings with X-ray-diffraction analysis of the textured $Ni_{81}Fe_{19}$ alloy. Importantly, the sizable magnetoresistance is preserved after the irradiation. Our results show that compared with traditional annealing methods, the use of He^+ irradiation leads to significant improvements in the magnetic softness and reduces strain cross-sensitivity in permalloy films required for 3D positioning and compass applications. These improvements, in combination with the local nature of the irradiation process, make our findings valuable for the optimization of monolithic integrated sensors, where classic annealing methods cannot be applied due to complex interplay within the components in the device.

DOI: 10.1103/PhysRevApplied.20.014001

I. INTRODUCTION

Permalloy, a typical soft magnetic $Ni_{81}Fe_{19}$ alloy, is used as an active sensor layer in several magnetoresistive-sensor applications [1]. To have a small magnetostriction and low coercivity, most of these devices are designed around the alloy composition of $Ni_{81}Fe_{19}$, which also possesses significant anisotropic magnetoresistance (AMR). Optimization of permalloy for AMR sensors has been studied for a long time [2–4] and includes different aspects: primarily, improvement of magnetic softness and low magnetostriction. To achieve that, negligible crystalline anisotropy is firstly required. The single thin-film elements typically feature a stripe-shaped geometry to induce a strong shape anisotropy, providing the sensor with a well-defined orientation of sensitivity. Furthermore, this design of the sensitive elements ensures a fixed configuration of the magnetic domains, thus enabling a very high signal-to-noise ratio. Additional anisotropies of other sources, if not oriented in the same direction as the shape anisotropy, would hinder this directional sensitivity [5]. Moreover, to achieve low hysteresis, the coercivity in the hard-axis magnetization direction must be very low and the specific AMR must be as high as possible [6] to maximize sensitivity. Finally, to avoid parasitic anisotropies, low magnetostriction (source of magnetoelastic anisotropy) is required. In this case, strain in the

*gmascioc@uni-mainz.de
†klaeui@uni-mainz.de

material has a small or negligible impact on the magnetic properties. The low magnetoelastic anisotropy is particularly important for sensors on flexible substrates [1,7–10], which have attracted great interest in recent years in wearable electronics and biomedical applications. To obtain this particular material property, growth optimization [11] and annealing [12] are viable options. However, none of these techniques allows a local treatment of the film properties.

Ion irradiation is an excellent tool to tune locally the magnetic and structural properties of thin films through ordering [13–16] and interface intermixing [17–20]. In permalloy films, ion irradiation has been shown to change the magnetic anisotropy [21–23] and the magnetoresistive response in the presence of exchange bias [4,24]. However, most of these studies used ion implantation [25–27], high ion energies [28,29], or heavy ions [30], which can result in significant damage to the sample. This can be avoided by use of lighter ions—such as He^+—with energies in the range of 10–30 keV [17,31]. In this way, collision cascades are absent and the structural modifications are confined to the vicinity of the ion path in a metal. Furthermore, the effect of irradiation on the magnetoelastic properties of single permalloy films and a direct comparison between field-free ion irradiation and annealing have not yet been reported [32].

In this work, we propose and explore the use of He^+ irradiation on a sputtered layer of $Ni_{81}Fe_{19}$ (30 nm) as material preparation technique for magnetic field sensors and we compare it with standard field-free annealing. Using Kerr microscopy and vibrating-sample magnetometry, we show that 20-keV He^+ ions significantly reduce the coercivity and the induced magnetic anisotropy of our magnetic material. The result is a soft magnetic film with in-plane magnetic anisotropy of less than 10 J/m^3 and a coercive field of approximately 0.05 mT, which is a further improvement over the values that can be obtained by the field-free annealing process by a factor of 5 and 10, respectively. The anisotropy measurements are supported by a detailed comparison using the remanent domain pattern. Additionally, we show that the polycrystalline magnetostriction can be progressively reduced by a factor of 10 for irradiation doses of 5×10^{16} cm^{-2}. This reduction in magnetoelastic coupling is attributed to crystallization and changes to the interface magnetostriction caused by intermixing at the magnetic layer boundaries. We support our findings with structural characterization performed using X-ray diffraction (XRD). The results show an overall improvement in the crystallization after irradiation and annealing. We attribute the reduction in magnetic anisotropy to the absence of a preferential direction of atomic ordering and to stress relaxation during irradiation. As postgrowth He^+ irradiation improves magnetic softness and minimizes strain cross-sensitivity of permalloy, AMR magnetic sensors with high sensitivity and low hysteresis can be envisioned even for integrated devices.

II. EXPERIMENTAL METHODS

The samples are prepared by dc magnetron sputtering using a Singulus Rotaris system on 1.5-μm-thick, thermally oxidized SiO_x on top of a 625-μm-thick Si substrate. A layer of $Ni_{81}Fe_{19}$ (30 nm)—typical thickness used for various sensor applications—is sputtered at room temperature in the presence of a rotating magnetic field of 5 mT on a Ni-Fe-Cr (5 nm) seed layer and capped with 4 nm of Ta as shown in Fig. 1(b). The following sputtering conditions are used for the magnetic layer growth: base pressure 5×10^{-8} mbar, sputtering power 1200 W, and Ar^+ flow 90 sccm. The seed layer is used to promote a $Ni_{81}Fe_{19}(111)$ texture during growth and it is known to improve magnetoresistance [25,33]. After deposition, optical lithography and ion etching are used to pattern arrays of disks (diameter of 80 μm and spacing of 3 μm) on the samples to probe the local film properties. Multiple copies of the samples are irradiated at an energy of 20 keV with different fluences of He^+ ions from 5×10^{13} to 5×10^{16} cm^{-2}. Under these irradiation conditions, most of the ions reach the substrate (roughly 94% from Monte Carlo TRIM [34,35] simulations), resulting in homogeneous irradiation of the entire layer stack. To process thicker permalloy layers (100 nm), a higher acceleration energy of the ions would be required to obtain comparable irradiation profiles. The results of the TRIM simulations for this case can be found in Sec. S2 in Supplemental Material [36].

To compare the effect of ion irradiation with that of thermal annealing, the same magnetic material is consecutively annealed for 3 h at 200, 265, and 300 °C at a pressure of 10^{-7} mbar. To avoid a magnetization-induced preferential direction of ordering [26,37], external magnetic fields are minimized during the irradiation and annealing steps. The magnetic properties of the thin films are measured by Kerr microscopy and vibrating-sample magnetometry. The magnetic properties of the films are summarized in Table I. Because of the negligible implantation [31], the value of Young's modulus is assumed to be unaffected by our irradiation and annealing step. Electrical measurement of AMR is performed with four contacts in line in the presence of a rotating magnetic field of 10 mT.

To apply strain to our devices, the substrate is bent mechanically with a three-point bending method. As reported in our previous work [39], a tensile and uniaxial strain is generated [40]. Moreover, the strain is uniform in the central area of the sample and thus in the measured region. As the thin films are in total 40 nm thick, we assume that the strain is entirely transferred from the substrate and that shear strain is negligible. Structural modifications caused by ion irradiation and annealing are probed by XRD with use of a Bruker D8 Discover system.

TABLE I. Parameter values of the magnetic materials (thickness 30 nm) after deposition, annealing, and He^+ irradiation. The values without reference are quantified experimentally. Here M_s is the saturation magnetization, K_u is the uniaxial anisotropy constant, H_c is the coercive field, λ_s is the saturation magnetostriction, and Y is Young's modulus. The same value for Y is considered in all cases.

$Ni_{81}Fe_{19}$	M_s (T)	K_u (J/m^3)	H_c (mT)	$\lambda_s \times 10^{-6}$	Y (GPa)
As deposited	0.95(1)	78(5)	0.20(5)	−0.7(1)	200 [38]
Annealing at 265 °C	0.95(1)	70(5)	0.15(5)	+0.04(9)	200 [38]
He^+ 5×10^{16} cm^{-2}	0.91(1)	8(7)	0.05(5)	+0.01(9)	200 [38]

Angular $2\Theta/\Theta$ scans and rocking-curve measurements are performed on 1×1 cm^2 samples.

III. RESULTS AND DISCUSSION

To compare the structural modifications induced by different material treatments on a $Ni_{81}Fe_{19}$ alloy, XRD measurements on the $Ni_{81}Fe_{19}$ (30 nm) film as deposited and after irradiation and annealing are performed and are reported in Fig. 1. Figure 1(a) shows $2\Theta/\Theta$ angular scans of the permalloy film. A well-defined crystalline texture of $Ni_{81}Fe_{19}$(111) (and its second-order peak) is present for the material in the as-deposited state and persists after irradiation and annealing in all the fluence and temperature ranges explored. The full width at half maximum (FWHM) of the (111) peak can be estimated, and the quantitative values are reported in Sec. S1 in Supplemental Material [36] as a function of the irradiation fluence and the temperature during annealing. In both cases, the FWHM of the (111) peak decreases by about 15% with increasing ion fluence and annealing temperature with respect to the as-deposited case. The crystallite size (or the size of a coherently diffracting domain in the material along the sample thickness) is a fundamental property that can be extracted from the XRD profile [41]. According to the Scherrer equation [42],

$$D = \frac{K\lambda}{\beta \cos\theta}, \tag{1}$$

the size of crystallites is inversely proportional to the FWHM of a diffraction peak. Here $K = 0.9$ is a dimensionless shape factor, D is the crystallite size, $\lambda = 1.5406$ Å is the wavelength of the Cu $K\alpha$ radiation, θ is the diffraction angle, and β is the line broadening at the FWHM of the XRD peak in radians, after subtraction of the instrumental line broadening. As reported in Fig. 1(c), both annealing at $T > 265$ °C and ion irradiation with a fluence greater than 1×10^{16} cm^{-2} increase the size of crystallites in our films. The size of the diffracting domains estimated with use of Eq. (1) is 22(1) nm for the as-deposited case and more than 24(1) nm after the two material treatments. Additionally,

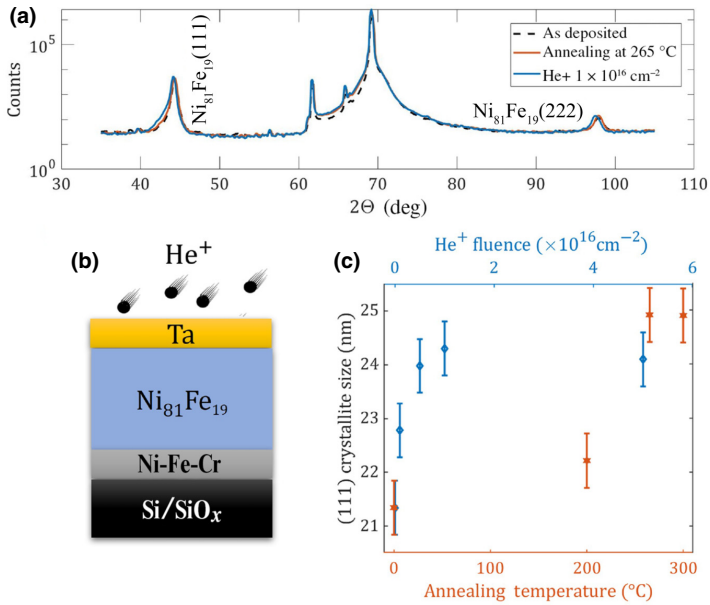

FIG. 1. (a) $2\Theta/\Theta$ XRD angular scan of the $Ni_{81}Fe_{19}$ samples for the sample in the as-deposited state, after annealing and after irradiation. (b) The Ni-Fe-Cr(5 nm)/$Ni_{81}Fe_{19}$(30 nm)/Ta(4 nm) stack. (c) Size of the (111) crystallites of the $Ni_{81}Fe_{19}$ film as a function of He^+ fluence and as a function of annealing temperature. These values are obtained with use of the FWHM of the $Ni_{81}Fe_{19}$(111) peak and Eq. (1).

rocking-curve measurements [43] of the $Ni_{81}Fe_{19}(111)$ peak are performed, and more information can be found in Sec. S1 in Supplemental Material [36]. For both the irradiated samples and the annealed samples, a decrease in the FWHM of the rocking curve is observed, indicating improvement in the film crystalline phase [44]. As Fig. 1(c) shows, the size of the crystallites does not increase further for annealing temperatures above 265 °C and irradiation fluences greater than 1×10^{16} cm^{-2}, in agreement with previous studies [45].

The major effect of room-temperature irradiation has been shown to be improved material uniformity [46] and interface intermixing [17]. In the same way, thermal annealing is widely used to induce crystallization [47] and promote atomic diffusion [48]. Similar effects have been reported in the literature for amorphous alloys, where annealing [45] and He^+ irradiation [15,16] providing high short-range atomic mobility enable a mechanism for growth of the ordered phase at the expense of its disordered or less-ordered counterpart.

The magnetic properties of the thin films are measured by Kerr microscopy and are reported in Fig. 2. Figures 2(a)–2(c) show the hysteresis curves for the Ni-Fe-Cr(5 nm)/$Ni_{81}Fe_{19}$(30 nm)/Ta(4 nm) sample for two perpendicular in-plane directions of the applied magnetic field: for the as-deposited state [Fig. 2(a)], after annealing [Fig. 2(b)], and after irradiation [Fig. 2(c)]. The curves refer to the magnetic contrast of the structured film into 80-μm-diameter disks.

The magnetic response of the permalloy film in the as-deposited state can be seen in Fig. 2(a). As the magnetization curves at $\Phi = 0^\circ$ and $\Phi = 90^\circ$ are different, a weak uniaxial magnetic anisotropy K_u is present in the as-deposited $Ni_{81}Fe_{19}$ and might be associated with internal stresses during the material growth or asymmetries in the deposition system [49]. $K_u = 80(7)$ J/m^3 is obtained from the area enclosed by easy-axis and hard-axis loops of the as-deposited state. The direction of the magnetic-easy-axis anisotropy can be seen in the orientation of the magnetic domains for the remanent state [inset in Fig. 2(a)]. The field is applied along $\Phi = 0^\circ$ and then reduced to zero. A vector image of the in-plane magnetization is obtained by the sum of the horizontal and vertical components of the magnetic contrast. In this case, the domains align along the easy-axis direction. The measurement is repeated for the same film after annealing and is reported in Fig. 2(b). After the annealing, the in-plane hysteresis loops still show the presence of a uniaxial magnetic anisotropy. This is confirmed by the remanent magnetic state [inset in Fig. 2(b)] as the magnetic domains again orient themselves in the easy-axis direction $\Phi \simeq 90^\circ$. Additional measurements for films annealed at 200 and 300 °C are reported in Sec. S4 in Supplemental Material [36]. Interestingly, the magnetic response of the irradiated permalloy reported in Fig. 2(c) is significantly different with respect to the as-deposited and annealed cases. The change of slope for low fields in the hysteresis in Fig. 2(c) is caused by the formation of a magnetic vortex [shown in the inset in Fig. 2(c)], accompanied by an abrupt decrease in magnetization when the field is decreased from saturation [50]. Additionally, the hysteresis loops now show a negligible angular dependence on Φ. Both the magnetic anisotropy and the hard-axis coercivity H_c are now significantly reduced. The reduction of the anisotropy in the permalloy after irradiation allows the formation of a vortex-type magnetization distribution at remanence, which is energetically favorable for disks with weak crystalline and induced anisotropy [inset in Fig. 2(c)] and thus dominated by shape anisotropy. The hard-axis coercivity H_c is also reduced by irradiation, as the linear motion of the vortex core for low fields in vortex structures minimizes the hysteresis [51].

Figure 2(d) shows the angular plot of the normalized remanent magnetization for the three samples considered. The as-deposited case and the annealed case (in blue and green, respectively) show a signature of uniaxial magnetic anisotropy with easy-axis and sizable remanent magnetization at $\Phi \simeq 90^\circ$. The irradiated sample, instead, shows reduced remanent magnetization for all angles. The low remanent magnetization is typical of the vortex state in the inset in Fig. 2(c). To further understand the improvement in the magnetic softness of our permalloy after irradiation, we gradually increase the He^+ fluence while keeping the ion energy constant. The measurements of H_c and K_u as a function of the fluence of He^+ ions during irradiation are reported in Fig. 2(e). The values for the film as deposited and after annealing are given for comparison as dashed lines. For low fluences, no sizable effects are noted. At fluences greater than 5×10^{13} cm^{-2}, the coercivity and the anisotropy are progressively reduced as the He^+ fluence is increased. For the maximum fluence of 5×10^{16} cm^{-2}, H_c is 5 times lower than for the as-deposited state, while the induced anisotropy is decreased by a factor of 10. We do not observe a similar substantial reduction of these magnetic parameters after the annealing.

A possible explanation for this dissimilarity is the different mechanism of ordering promoted by irradiation and field-free annealing. Improved atomic ordering in permalloy after annealing and irradiation with different ions [30,52] has been reported in the literature. Some of these studies on polycrystalline films [53,54] show that crystalline grain growth is more homogeneous for irradiation than for thermal annealing in the temperature range from 200 to 300 °C. This difference originates from the distinct mechanism with which chemical ordering of the alloy is changed during the two processes [55]. As we see from these studies, radiation-enhanced mobility is more isotropic in the absence of an applied magnetic field when compared with heat-induced mobility [22,55]. Accordingly, a greater reduction in the magnetic anisotropy for the irradiated samples can be expected.

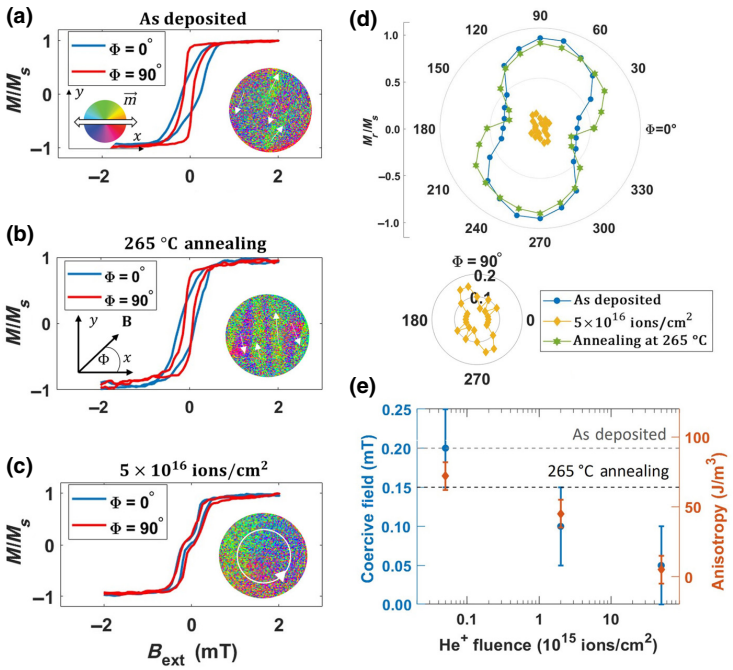

FIG. 2. (a)–(c) In-plane hysteresis loops of Ni-Fe-Cr(5 nm)/$Ni_{81}Fe_{19}$(30 nm)/Ta(4 nm) after sputtering, after thermal annealing, and after He^+ irradiation, respectively. In the insets, the corresponding remanent magnetic state ($B_{ext} = 0$ mT) for 80-μm-diameter disks is shown. The color code corresponds to the in-plane magnetization orientation as indicated by the white arrows. The field is applied along $\Phi = 0°$. (d) Angular plot of the normalized remanent magnetization M_r/M_s as a function of the in-plane magnetic field direction Φ for as-deposited, irradiated, and annealed samples. The measurements after irradiation are highlighted in the inset for clarity. (e) Coercive field (blue) and uniaxial magnetic anisotropy (orange) measured along the field direction $\Phi = 0°$ on a permalloy sample irradiated with different fluences of He^+ ions. For comparison, the values after annealing and in the as-deposited state are reported with dashed lines.

A first indication for the observed reduction in coercivity in our irradiated samples is the formation of a magnetic vortex in disk-patterned permalloy [50] [inset in Fig. 2(c)]. A comparison between ion irradiation and thermal annealing analyzing the microscopic pinning parameters for domain-wall motion was conducted recently [46]. In this work, the annealed sample shows strong but widely distributed pinning sites. In contrast to this, the irradiated sample exhibits weaker defects with a higher density. A further possible explanation for the observed reduction in coercivity in our irradiated samples, is therefore an overall smoother domain-wall energy landscape after irradiation, which allows domain formation and switching of the magnetization at lower magnetic fields. In addition, the release of internal stresses in the film, which has been reported during irradiation [56,57], can also be responsible for improvements in the soft magnetic properties of our permalloy [49].

To evaluate the effect of ion irradiation and annealing on the magnetoelastic coupling of a thin magnetic $Ni_{81}Fe_{19}$ alloy, the strain-dependent magnetic properties are investigated. Uniaxial in-plane strain is applied to a full film of Ni-Fe-Cr(5 nm)/$Ni_{81}Fe_{19}$(30 nm)/Ta(4 nm) by the three-point bending method as previously reported [39]. Since the magnetization is coupled to the external strain via the expression of the anisotropy energy, the magnetic anisotropy before and after the application of strain is measured by Kerr microscopy. A strain of $\epsilon_{xx} = 0.06\%$ (tensile) is applied along the in-plane direction $\Phi = 0°$. The expression for the magnetoelastic anisotropy depends on the saturation magnetostriction λ_s of the material according to [58]

$$K_{ME} = \frac{3}{2}\lambda_s Y \epsilon, \tag{2}$$

where Y is Young's modulus and ϵ is the uniaxial tensile strain. Using Eq. (2) and the values of Young's modulus in Table I, we calculate the effective magnetostriction of the film for different He^+ fluences. The calculated values are reported in Fig. 3(a). In the as-deposited state, as well as for He^+ fluences on the order of 10^{13} cm^{-2}, $\lambda_s = -7(2) \times 10^{-7}$ is negative. In this case, a tensile strain increases the anisotropy field in the direction $\Phi = 0°$. For greater fluences of ions during irradiation, the magnetostriction is progressively reduced and reaches values close to zero for a fluence of 5×10^{16} cm^{-2}. In this case, the magnetoelastic anisotropy is negligible and the material is insensitive to the applied strain. For this reason, the magnetization curves before and after the application of uniaxial strain $\epsilon_{xx} = 0.06\%$ are almost unchanged. The saturation magnetostriction of the magnetic layer after annealing is measured and is reported in Fig. 3(a) for comparison. After the annealing, $\lambda_s \simeq 0$ is reported.

An additional confirmation of the magnetic behavior of the stack under strain is obtained by our imaging domain

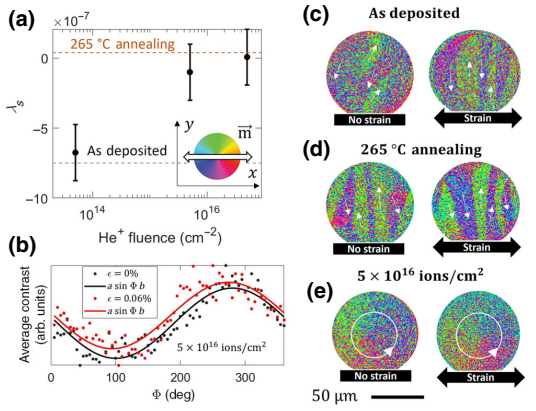

FIG. 3. (a) Saturation magnetostriction λ_s as a function of He^+ fluence during irradiation. The values for the as-deposited sample and the sample after annealing are reported for comparison with dashed lines. (b) Average contrast for 80-μm-diameter disks as a function of the in-plane angle Φ for the irradiated sample in the remanent state (magnetic vortex state) before and after the application of strain. (c)–(e) Remanent magnetic state for 80-μm-diameter disks before (left) and during (right) application of uniaxial strain of 0.06% for as-deposited, annealed, and irradiated permalloy, respectively.

formation using the magneto-optical Kerr effect (MOKE). The MOKE images shown in Figs. 3(c)–3(e) show how the magnetoelastic anisotropy alters the preferential direction of magnetic domains before (left) and after (right) the application of strain. We first consider the as-deposited state [Fig. 3(c)]. Before the application of strain, the magnetization aligns with the deposition-induced anisotropy easy axis. After the application of strain, the negative magnetostriction of the as-deposited sample orients the magnetic domains along the y direction, perpendicular to the uniaxial strain ϵ_{xx}. Figure 3(d) shows, instead, the domain pattern for a sample annealed at 265 °C. In this case the remanent magnetic state is almost not altered by the applied strain. This is in agreement with the extremely low magnetostriction measured, which results in negligible magnetoelastic anistropy $K_{\mathrm{ME}} << K_u$. The remanent state for the sample irradiated with a He^+ fluence of 5×10^{16} cm^{-2} [Fig. 3(e)] exhibits instead a magnetic vortex state that is not altered after the application of $\epsilon_{xx} = 0.06\%$. The initial vortex state, unchanged under the application of strain, highlights that the contributions of induced and magnetoelastic anisotropy have been reduced to a point where only the shape anisotropy determines the remanent domain pattern.

To compare more quantitatively the MOKE images and the vortex state of the irradiated sample, the average radial magnetization is calculated from the longitudinal component of the vector image for different in-plane Φ directions [59]. The average contrast is calculated for a single 80-μm-diameter disk for the images in Fig. 3(e) and is reported in Fig. 3(b). For the unstrained state seen on the left in Fig. 3(e), the disk's magnetization is a circularly symmetric vortex, and the average contrast varies periodically with the angular position on the disk. The values well follow the expression $a \sin \Phi b$ [black line in Fig. 3(b)]. After the application of strain, as a consequence of the extremely small magnetostriction, the average contrast [red line in Fig. 3(b)] still follows the periodic behavior $a \sin \Phi b$.

A possible explanation for the reported reduction in saturation magnetostriction after ion irradiation and annealing is the increase in size–probed along the vertical direction—of the crystallites in the Ni-Fe-Cr(5 nm)/$Ni_{81}Fe_{19}$(30 nm)/Ta(4 nm) sample, already highlighted in Fig. 1(c). The magnetostriction of isotropic oriented cubic crystallites can be written as the combination of the saturation-magnetostriction constants λ_{100} and λ_{111} in the (100) and (111) directions, respectively [60]:

$$\lambda_s = \frac{2\lambda_{100} + 3\lambda_{111}}{5}. \tag{3}$$

In permalloy, the two components of the magnetostriction change significantly over the relative Ni and Fe composition range, altering the effective magnetostriction, λ_s. The composition used in this work, $Ni_{81}Fe_{19}$, is predicted to have λ_s close to zero [61]. In our XRD measurement, a 15% reduction of the FWHM of the (111) peak is observed after irradiation and annealing. This crystallization measured along the film thickness can alter the relative contribution of λ_{100} and λ_{111} in the magnetic layer. Following Eq. (3), the effective magnetostriction of the film is changed. As shown in Fig. 3(a), the magnetostriction is progressively reduced for higher fluences and annealing temperatures as the size of the crystallites caused by irradiation and annealing increases. In addition, increased intermixing at the magnetic layer boundaries could alter the interface magnetostriction [62] (inversely proportional to the film thickness [63,64]), thus playing a role in the effective magnetostriction of the film.

Previous studies reported strong changes to the magnetoresistance after irradiation, in particular with heavy ions [32]. To validate the applicability of our irradiated permalloy layer for sensing applications, transport measurements are conducted. The AMR measurements are shown in Sec. S3 in Supplemental Material [36] for a full film as deposited and after irradiation with 5×10^{16} ions/cm^2. The electrical characterization confirms that the Ni-Fe-Cr(5 nm)/$Ni_{81}Fe_{19}$(30 nm)/Ta(4 nm) sample has sizable AMR, $\Delta R/R = 1.1(1)\%$. As the AMR does not change after irradiation with He^+ ions, the proposed material treatment is suitable for improving magnetic properties of magnetic material for magnetic sensing applications.

IV. CONCLUSIONS

In conclusion, we investigate the effects of He^+ irradiation and thermal annealing on the magnetic properties of Ni-Fe-Cr(5 nm)/$Ni_{81}Fe_{19}$(30 nm)/Ta(4 nm). Our XRD analysis suggests that both irradiation and annealing promote crystalline growth of the textured $Ni_{81}Fe_{19}$ alloy. While the irradiation treatment strongly reduces the hard-axis coercivity to 0.05 mT and the deposition-induced anisotropy by a factor of 10, the field-free annealing does not significantly improve the magnetic softness. We mainly attribute this to stress relaxation in the film after irradiation and to the different mechanism for atomic ordering, which is completely isotropic in the case of irradiation only. In addition, the effective magnetostriction of the film is reduced by a factor of 10 after irradiation and annealing as confirmed by anisotropy measurements in the presence of in-plane strain. Importantly, we show that the sizable magnetoresistance is preserved after the irradiation. As a result, postgrowth He^+ irradiation is an excellent tool to improve magnetic softness and minimize strain cross-sensitivity of permalloy. In contrast to thermal annealing, ion irradiation offers the advantage of performing a local material treatment [21,45,65] to adjust the anisotropy and write magnetic domain patterns directly into thin-film structured devices. As a consequence, we can locally tune the properties of a magnetic material to make it suitable, for instance, for high-sensitivity and low-hysteresis integrated AMR sensors that are insensitive to strain.

ACKNOWLEDGMENTS

This work has received funding from the European Union's Horizon 2020 research and innovation program under Marie Skłodowska-Curie Grant Agreement No. 860060 ["Magnetism and the Effect of Electric Field" (MagnEFi)], the Deutsche Forschungsgemeinschaft (DFG; TRR 173, 268565370, projects A01 and B02), the DFG-funded Collaborative Research Center 1261 (project A1), and the Austrian Research Promotion Agency (FFG). The authors acknowledge support by the chip production facilities of Sensitec GmbH (Mainz, Germany), where part of this work was performed, and the Max Planck Graduate Center with Johannes Gutenberg University Mainz.

[1] M. A. Khan, J. Sun, B. Li, A. Przybysz, and J. Kosel, Magnetic sensors-a review and recent technologies, Eng. Res. Express **3**, 022005 (2021).

[2] W. Kwiatkowski and S. Tumanski, The permalloy magnetoresistive sensors-properties and applications, J. Phys. E: Sci. Instrum. **19**, 502 (1986).

[3] J. Groenland, C. Eijkel, J. Fluitman, and R. de Ridder, Permalloy thin-film magnetic sensors, Sens. Actuators A: Phys. **30**, 89 (1992).

[4] J. Trützschler, K. Sentosun, M. Langer, I. Mönch, R. Mattheis, J. Fassbender, and J. McCord, Optimization of magneto-resistive response of ion-irradiated exchange biased films through zigzag arrangement of magnetization, J. Appl. Phys. **115**, 103901 (2014).

[5] L. Jogschies, D. Klaas, R. Kruppe, J. Rittinger, P. Taptimthong, A. Wienecke, L. Rissing, and M. C. Wurz, Recent developments of magnetoresistive sensors for industrial applications, Sensors **15**, 28665 (2015).

[6] K.-M. Lenssen, D. Adelerhof, H. Gassen, A. Kuiper, G. Somers, and J. Van Zon, Robust giant magnetoresistance sensors, Sens. Actuators A: Phys. **85**, 1 (2000).

[7] G. S. Cañón Bermúdez and D. Makarov, Magnetosensitive E-Skins for interactive devices, Adv. Funct. Mater. **31**, 2007788 (2021).

[8] E. S. Oliveros Mata, G. S. Cañón Bermúdez, M. Ha, T. Kosub, Y. Zabila, J. Fassbender, and D. Makarov, Printable anisotropic magnetoresistance sensors for highly compliant electronics, Appl. Phys. A **127**, 1 (2021).

[9] M. Melzer, D. Makarov, and O. Schmidt, A review on stretchable magnetic field sensorics, J. Phys. D: Appl. Phys. **53**, 083002 (2019).

[10] S. Amara, G. A. T. Sevilla, M. Hawsawi, Y. Mashraei, H. Mohammed, M. E. Cruz, Y. P. Ivanov, S. Jaiswal, G. Jakob, and M. Kläui, *et al.*, High-performance flexible magnetic tunnel junctions for smart miniaturized instruments, Adv. Eng. Mater. **20**, 1800471 (2018).

[11] G. Wang, C. Dong, W. Wang, Z. Wang, G. Chai, C. Jiang, and D. Xue, Observation of rotatable stripe domain in permalloy films with oblique sputtering, J. Appl. Phys. **112**, 093907 (2012).

[12] T. Iwata and F. Hagedorn, Annealing behavior of induced anisotropy and related magnetic properties in permalloy films, J. Appl. Phys. **40**, 2258 (1969).

[13] X. Jiang, X. Fan, J. Huang, C. Zhang, and D. Xue, Improving the quality of AMR of permalloy films by N^{2+} ion irradiation, Nucl. Instrum. Methods Phys, Res. Sect. B: Beam Interact. Mater. At. **430**, 54 (2018).

[14] M. Jaafar, R. Sanz, J. McCord, J. Jensen, R. Schäfer, M. Vázquez, and A. Asenjo, Pattern-induced magnetic anisotropy in FePt thin films by ion irradiation, Phys. Rev. B **83**, 094422 (2011).

[15] T. Devolder, I. Barisic, S. Eimer, K. Garcia, J.-P. Adam, B. Ockert, and D. Ravelosona, Irradiation-induced tailoring of the magnetism of CoFeB/MgO ultrathin films, J. Appl. Phys. **113**, 203912 (2013).

[16] D. Ravelosona, C. Chappert, V. Mathet, and H. Bernas, Chemical order induced by ion irradiation in FePt (001) films, Appl. Phys. Lett. **76**, 236 (2000).

[17] G. Masciocchi, J. W. van der Jagt, M.-A. Syskaki, A. Lamperti, N. Wolff, A. Lotnyk, J. Langer, L. Kienle, G. Jakob, B. Borie, A. Kehlberger, D. Ravelosona, and M. Kläui, Control of magnetoelastic coupling in Ni/Fe multilayers using He^+ ion irradiation, Appl. Phys. Lett. **121**, 182401 (2022).

[18] M. C. H. de Jong, M. J. Meijer, J. Lucassen, J. van Liempt, H. J. M. Swagten, B. Koopmans, and R. Lavrijsen, Local control of magnetic interface effects in chiral Ir— Co— Pt multilayers using Ga^+ ion irradiation, Phys. Rev. B **105**, 064429 (2022).

[19] X. Zhao, B. Zhang, N. Vernier, X. Zhang, M. Sall, T. Xing, L. H. Diez, C. Hepburn, L. Wang, and G. Durin, *et al.*, Enhancing domain wall velocity through interface intermixing in W-CoFeB-MgO films with perpendicular anisotropy, Appl. Phys. Lett. **115**, 122404 (2019).

[20] L. H. Diez, M. Voto, A. Casiraghi, M. Belmeguenai, Y. Roussigné, G. Durin, A. Lamperti, R. Mantovan, V. Sluka, and V. Jeudy, *et al.*, Enhancement of the Dzyaloshinskii-Moriya interaction and domain wall velocity through interface intermixing in Ta/CoFeB/MgO, Phys. Rev. B **99**, 054431 (2019).

[21] S. Woods, S. Ingvarsson, J. Kirtley, H. Hamann, and R. Koch, Local magnetic anisotropy control in NiFe thin films via ion irradiation, Appl. Phys. Lett. **81**, 1267 (2002).

[22] A. Schindler, R. Kernohan, and J. Weertman, Effect of irradiation on magnetic properties of Fe-Ni alloys, J. Appl. Phys. **35**, 2640 (1964).

[23] A. Mougin, T. Mewes, M. Jung, D. Engel, A. Ehresmann, H. Schmoranzer, J. Fassbender, and B. Hillebrands, Local manipulation and reversal of the exchange bias field by ion irradiation in FeNi/FeMn double layers, Phys. Rev. B **63**, 060409(R) (2001).

[24] J. Trützschler, K. Sentosun, B. Mozooni, R. Mattheis, and J. McCord, Magnetic domain wall gratings for magnetization reversal tuning and confined dynamic mode localization, Sci. Rep. **6**, 30761 (2016).

[25] J. Fassbender, J. von Borany, A. Mücklich, K. Potzger, W. Möller, J. McCord, L. Schultz, and R. Mattheis, Structural and magnetic modifications of Cr-implanted permalloy, Phys. Rev. B **73**, 184410 (2006).

[26] J. Fassbender and J. McCord, Control of saturation magnetization, anisotropy, and damping due to Ni implantation in thin NiFe layers, Appl. Phys. Lett. **88**, 252501 (2006).

[27] J. Fassbender, A. Mücklich, K. Potzger, and W. Möller, Mixing and subsequent amorphization of ultrathin NiFe/Ta bilayers by 30 keV Ni implantation, Nucl. Instrum. Methods Phys. Res. Sect. B: Beam Interact. Mater. At. **248**, 343 (2006).

[28] G. C. Bailey, A. I. Schindler, and P. H. Meijer, Ferromagnetic resonance of ^{3}He-irradiated thin metal films, J. Appl. Phys. **38**, 4004 (1967).

[29] G. Bailey, Dependence of spin-wave resonance in thin films on irradiation, Phys. Lett. A **30**, 58 (1969).

[30] R. Gupta, K. Lieb, Y. Luo, G. Müller, P. Schaaf, and K. Zhang, Argon and krypton ion-induced changes in permalloy thin films, Eur. Phys. J. B **63**, 501 (2008).

[31] J. Fassbender, D. Ravelosona, and Y. Samson, Tailoring magnetism by light-ion irradiation, J. Phys. D: Appl. Phys. **37**, R179 (2004).

[32] J. Baglin, M. Tabacniks, R. Fontana, A. Kellock, and T. Bardin, in *Materials Science Forum*, Vol. 248 (Trans Tech Publ, 1997), p. 87.

[33] W. Lee, M. Toney, and D. Mauri, High magnetoresistance in sputtered Permalloy thin films through growth on seed layers of $(Ni_{0.81}Fe_{0.19})_{1-x}/Cr_x$, IEEE Trans. Magn. **36**, 381 (2000).

[34] J. F. Ziegler, M. D. Ziegler, and J. P. Biersack, SRIM – the stopping and range of ions in matter (2010), Nucl. Instrum. Methods Phys. Res. Sect. B: Beam Interact. Mater. At. **268**, 1818 (2010).

[35] J. Vukanić and P. Sigmund, Total backscattering of keV light ions from solid targets in single-collision approximation, Appl. Phys. **11**, 265 (1976).

[36] See Supplemental Material at http://link.aps.org/supplemental/10.1103/PhysRevApplied.20.014001 for the X-ray-diffraction rocking-curve measurements, the TRIM simulations, AMR measurements, and magnetic hysteresis loops after annealing at different temperatures.

[37] C. Okay, P. Aksu, C. Deger, and F. Yildiz, Tailoring the magnetic anisotropy of cobalt-gold thin films, Turk. J. Phys. **42**, 335 (2018).

[38] E. Klokholm and J. Aboaf, The saturation magnetostriction of permalloy films, J. Appl. Phys. **52**, 2474 (1981).

[39] G. Masciocchi, M. Fattouhi, A. Kehlberger, L. Lopez-Diaz, M.-A. Syskaki, and M. Kläui, Strain-controlled domain wall injection into nanowires for sensor applications, J. Appl. Phys. **130**, 183903 (2021).

[40] A. Raghunathan, J. E. Snyder, and D. Jiles, Comparison of alternative techniques for characterizing magnetostriction and inverse magnetostriction in magnetic thin films, IEEE Trans. Magn. **45**, 3269 (2009).

[41] M. Ahmadipour, M. J. Abu, M. F. Ab Rahman, M. F. Ain, and Z. A. Ahmad, Assessment of crystallite size and strain of $CaCu_3Ti_4O_{12}$ prepared via conventional solid-state reaction, Micro Nano Lett. **11**, 147 (2016).

[42] A. K. Zak, W. A. Majid, M. E. Abrishami, and R. Yousefi, X-ray analysis of ZnO nanoparticles by Williamson-Hall and size-strain plot methods, Solid State Sci. **13**, 251 (2011).

[43] V. Speriosu and T. Vreeland Jr, X-ray rocking curve analysis of superlattices, J. Appl. Phys. **56**, 1591 (1984).

[44] S. Park, D. Norton, and V. Selvamanickam, Ion-beam texturing of uniaxially textured Ni films, Appl. Phys. Lett. **87**, 031907 (2005).

[45] J. McCord, T. Gemming, L. Schultz, J. Fassbender, M. O. Liedke, M. Frommberger, and E. Quandt, Magnetic anisotropy and domain patterning of amorphous films by He-ion irradiation, Appl. Phys. Lett. **86**, 162502 (2005).

[46] J. W. van der Jagt, V. Jeudy, A. Thiaville, M. Sall, N. Vernier, L. Herrera Diez, M. Belmeguenai, Y. Roussigné, S. M. Chérif, and M. Fattouhi, *et al.*, Revealing nanoscale disorder in W/Co-Fe-B/MgO ultrathin films using domain-wall motion, Phys. Rev. Appl. **18**, 054072 (2022).

[47] W. Wang, J. Jordan-Sweet, G. Miao, C. Ni, A. Rumaiz, L. Shah, X. Fan, P. Parsons, R. Stearrett, and E. Nowak, *et al.*, In-situ characterization of rapid crystallization of amorphous CoFeB electrodes in CoFeB/MgO/CoFeB junctions during thermal annealing, Appl. Phys. Lett. **95**, 242501 (2009).

[48] F. Schulz, R. Lawitzki, H. Głowiński, F. Lisiecki, N. Träger, P. Kuświk, E. Goering, G. Schütz, and J. Gräfe, Increase of Gilbert damping in permalloy thin films due to heat-induced structural changes, J. Appl. Phys. **129**, 153903 (2021).

[49] P. Zou, W. Yu, and J. A. Bain, Influence of stress and texture on soft magnetic properties of thin films, IEEE Trans. Magn. **38**, 3501 (2002).

[50] K. Y. Guslienko, V. Novosad, Y. Otani, H. Shima, and K. Fukamichi, Field evolution of magnetic vortex state in ferromagnetic disks, Appl. Phys. Lett. **78**, 3848 (2001).
[51] T. Wurft, W. Raberg, K. Prügl, A. Satz, G. Reiss, and H. Brückl, Evolution of magnetic vortex formation in micron-sized disks, Appl. Phys. Lett. **115**, 132407 (2019).
[52] R. Gupta, K.-H. Han, K. Lieb, G. Müller, P. Schaaf, and K. Zhang, Influence of ion implantation on the magnetic properties of thin FeCo films, J. Appl. Phys. **97**, 073911 (2005).
[53] L. Jian, J. Liu, and J. Mayer, Ar^+ ion irradiation induced grain growth in Au and Pt thin films, Nucl. Instrum. Methods Phys. Res. Sect. B: Beam Interact. Mater. At. **36**, 306 (1989).
[54] J. C. Liu, M. Nastasi, and J. Mayer, Ion irradiation induced grain growth in Pd polycrystalline thin films, J. Appl. Phys. **62**, 423 (1987).
[55] J. C. Liu and J. Mayer, Ion irradiation induced grain growth in Ni polycrystalline thin films, Nucl. Instrum. Methods Phys. Res. Sect. B: Beam Interact. Mater. At. **19**, 538 (1987).
[56] T. Devolder, Light ion irradiation of Co/Pt systems: Structural origin of the decrease in magnetic anisotropy, Phys. Rev. B **62**, 5794 (2000).
[57] A. Maziewski, P. Mazalski, Z. Kurant, M. O. Liedke, J. McCord, J. Fassbender, J. Ferré, A. Mougin, A. Wawro, L. T. Baczewski, A. Rogalev, F. Wilhelm, and T. Gemming, Tailoring of magnetism in Pt/Co/Pt ultrathin films by ion irradiation, Phys. Rev. B **85**, 054427 (2012).
[58] S. Finizio, M. Foerster, M. Buzzi, B. Krüger, M. Jourdan, C. A. F. Vaz, J. Hockel, T. Miyawaki, A. Tkach, S. Valencia, F. Kronast, G. P. Carman, F. Nolting, and M. Kläui, Magnetic Anisotropy Engineering in Thin Film Ni Nanostructures by Magnetoelastic Coupling, Phys. Rev. Appl. **1**, 021001(R) (2014).
[59] I. Gilbert, A. C. Chavez, D. T. Pierce, J. Unguris, W.-Y. Sun, C.-Y. Liang, and G. P. Carman, Magnetic microscopy and simulation of strain-mediated control of magnetization in PMN-PT/Ni nanostructures, Appl. Phys. Lett. **109**, 162404 (2016).
[60] R. M. Bozorth, *Ferromagnetism, p. 263* (1993).
[61] J. W. Judy, Magnetic microactuators with polysilicon flexures, Masters Report (1994).
[62] E. Singleton and K. Duxstad, Interfacial contributions to magnetostriction of ferromagnetic layers for magnetoresistive sensors, MRS Online Proc. Library **721**, 1 (2002).
[63] G. Choe, Giant interface magnetostriction and temperature dependence in NiFe films encapsulated with Ta and AlOx layers, IEEE Trans. Magn. **35**, 3838 (1999).
[64] O. Song, C. Ballentine, and R. O'Handley, Giant surface magnetostriction in polycrystalline Ni and NiFe films, Appl. Phys. Lett. **64**, 2593 (1994).
[65] J. Fassbender and J. McCord, Magnetic patterning by means of ion irradiation and implantation, J. Magn. Magn. Mater. **320**, 579 (2008).

Journal of Applied Physics ARTICLE pubs.aip.org/aip/jap

Strain effects on magnetic compensation and spin reorientation transition of Co/Gd synthetic ferrimagnets

Cite as: J. Appl. Phys. **134**, 013904 (2023); doi: 10.1063/5.0152180
Submitted: 28 March 2023 · Accepted: 19 June 2023 ·
Published Online: 7 July 2023

Giovanni Masciocchi,[1,2] Thomas J. Kools,[3] Pingzhi Li,[3] Adrien A. D. Petrillo,[3] Bert Koopmans,[3] Reinoud Lavrijsen,[3] Andreas Kehlberger,[2] and Mathias Kläui[1,a)]

AFFILIATIONS

[1]Institute of Physics, Johannes Gutenberg University Mainz, Staudingerweg 7, 55128 Mainz, Germany
[2]Sensitec GmbH, Walter-Hallstein-Straße 24, 55130 Mainz, Germany
[3]Department of Applied Physics, Eindhoven University of Technology, P.O. Box 513, 5600 MB Eindhoven, The Netherlands

[a)]**Author to whom correspondence should be addressed:** klaeui@uni-mainz.de

ABSTRACT

Synthetic ferrimagnets are an attractive material class for spintronics as they provide access to all-optical switching of magnetization and, at the same time, allow for ultrafast domain wall motion at angular momentum compensation. In this work, we systematically study the effects of strain on the perpendicular magnetic anisotropy and magnetization compensation of Co/Gd and Co/Gd/Co/Gd synthetic ferrimagnets. First, the spin reorientation transition of a bilayer system is investigated in wedge type samples, where we report an increase in the perpendicular magnetic anisotropy in the presence of in-plane strain. Using a model for magnetostatics and spin reorientation transition in this type of system, we confirm that the observed changes in anisotropy field are mainly due to the Co magnetoelastic anisotropy. Second, the magnetization compensation of a quadlayer is studied. We find that magnetization compensation of this synthetic ferrimagnetic system is not altered by external strain. This confirms the resilience of this material system against strain that may be induced during the integration process, making Co/Gd ferrimagnets suitable candidates for spintronics applications.

I. INTRODUCTION

Recent advances in spintronics have opened new possibilities for electronic applications beyond the CMOS standard. New concepts of high density and ultrafast non-volatile data storage have been proposed in magnetic memories.[1,2] Throughout the years, magnetic memories have evolved[3,4] exploiting different geometries[5] and new material platforms such as ferrimagnets[6] have been used to improve storage density,[7] reading and writing speed[8] and energy efficiency.[9,10] At the same time, single-pulse optical switching (AOS) of magnetization has reduced the switching speed of the magnetization below ps timescale.[11–14] This bears promise for a new generation of ultrafast data buffering in a single chip that integrates photonics with spintronics.[15–19]

Ferrimagnets are a class of magnets with unbalanced antiparallel-aligned sublattice moments. The compensation of the two inequivalent sublattices combines the advantages of both antiferromagnets (antiparallel alignment of magnetic moments) and ferromagnets (finite Zeeman coupling and spin polarization).[16,20] Moreover, the drastic contrast between the two sublattices in non-adiabatic dynamics could potentially accommodate AOS by a femtosecond laser pulse.[12,16] Single-pulse AOS is typically observed in rare earth–transition metal (RE–TM) ferrimagnetic alloys like GdFeCo[20] or in multilayer synthetic ferrimagnet, such as Co/Gd and $[Co/Tb]_n$.[21,22] In particular, the one based on multilayer of Co/Gd is a good candidate for integrated opto-spintronics devices as it shows AOS— without the constrains on the composition as imposed by the alloy system[23,24]—and at the same time exhibits magnetic and angular momentum compensation, allowing ultrafast domain wall motion.[25,26] For instance, the integration of Co/Gd synthetic ferrimagnets in an optically switchable magnetic tunnel junction has been recently reported.[27]

When it comes to technological implementation, strain-induced effects must be considered, which could be incurred from processing

steps such as packaging and layer deposition.[28] Intrinsic stress and strain could affect the magnetic anisotropy via changes to the spin–orbit coupling (SOC)[29] or to the magnetization compensation of ferrimagnets especially in RE–TM alloys[30,31] where compensation temperature has been reported to be affected by strain.[32,33] Strain is omnipresent in applications,[34–36] it is, therefore, of interest to explore strain-dependent effects also in synthetic ferrimagnets. In this work, we present a systematic study of the effects of strain on Co/Gd synthetic ferrimagnets. By the application of external strain, using substrate bending, we investigate the impact of strain on the perpendicular magnetic anisotropy (PMA) and the magnetization compensation of [Co/Gd] and $[Co/Gd]_2$ multilayers, respectively. Using wedge samples in a bilayer system of Co/Gd measured by the polar magneto-optic Kerr effect (pMOKE), we confirm that the PMA is increased by in-plane tensile strain and a negative magnetostriction is reported. By including the contribution of the strain-anisotropy for this system in a model for the magnetostatics, we show that the effects of strain on the magnetization are mainly due to the modification of the spin–orbit coupling within the magnetic layer and at the Pt/Co interface that increases the magnetic anisotropy via magnetoelastic coupling. Additionally, we find that the magnetization compensation point is not affected significantly by strain as the magnetoelastic coupling affects the anisotropy rather than the magnetization of the two sublattices. Our study explores the mechanisms that underlie the influence of strain on the magnetic anisotropy of Co/Gd ferrimagnets and contributes to a better understanding of the magnetoelastic effects of ferrimagnetic multilayers. These results could be employed for the optimization and development of spintronics devices, as well as for potential applications in fields such as magnetic memory and sensing.

II. METHODS AND SAMPLE FABRICATION

The samples were grown on a 1.5 μm thick, thermally oxidized SiOx on top of a 625 μm thick Si substrate by DC magnetron sputtering in a chamber with a typical base pressure of 5×10^{-9} mBar. To obtain a variable thickness (wedge) along the sample surface, a shutter in the close proximity of the sample is gradually closed during deposition. This allows us to study the compensation and spin reorientation transition (SRT) within a single sample. Two types of samples are realized. First, a bilayer of Ta(4 nm)/Pt(4)/Co(0-2)/Gd(t_{Gd})/TaN(4) with a constant Gd layer on top of a Co wedge is considered to study the SRT. In addition, a quadlayer of Ta(4)/Pt(4)/Co(0.6)/Gd(0-2)/Co(0.6)/Gd(1.5)/TaN(4), this time with a Gd wedge, is grown to study the magnetization compensation.

The magnetic properties of these wedge samples were investigated by pMOKE with a 658 nm laser. In this configuration, we mostly probe the out-of-plane (OOP) component of the Co magnetization[37] as we measure positive remanence in Co dominated samples and negative remanence for Gd dominated samples. According to Fig. 1(a), the surface of the sample is scanned along the y-direction using a focused laser spot with a spot-size of $\simeq$250 μm diameter. Accordingly, the local magnetic properties and hysteresis loops can be measured as a function of layer thickness, with a negligible thickness gradient $<$0.025 nm within the used laser spot. All the measurements are performed at room temperature. To apply in-plane tensile strain to our multilayer, the substrate

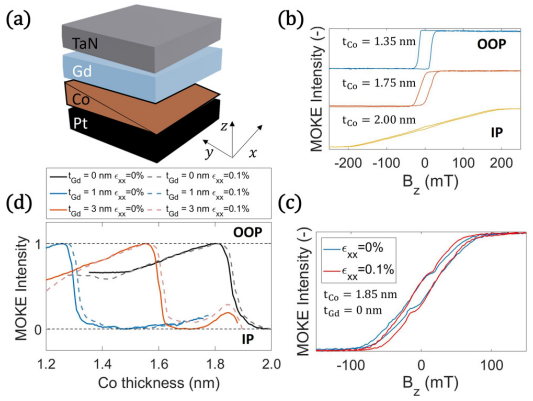

FIG. 1. (a) Sample sketch of the Co/Gd synthetic ferrimagnet used for the spin reorientation transition studies. The red arrow indicates the direction of the applied tensile strain. (b) Hysteresis loops of a Pt/Co/TaN stack for different Co thicknesses, the magnetic field was in the OOP direction, along z. (c) OOP hysteresis loops of Pt/Co(1.85 nm)/TaN before (blue) and after (red) application of 0.1% in-plane strain. (d) MOKE intensity scan at remanence (no applied magnetic field) of Pt/Co/Gd/TaN films along the Co wedge before (solid lines) and during (dashed lines) the application of in-plane strain. Three different thicknesses of the Gd layer t_{Gd} = 0, 1, and 3 nm have been considered and are reported, in order, in black, blue, and orange.

is mechanically bent using a three-point method.[38] A square sample of 1 × 1 cm is vertically constrained on two sides and pushed uniformly from below by a cylinder that has off-centered rotation axis. The device generates a tensile strain in the plane of the sample when the cylinder is rotated. As previously reported, the tensile strain is uniaxial along x and uniform in the measured area of the sample. The in-plane strain magnitude is 0.1% and has been measured with a strain gauge (RS PRO). More details about the strain generating device can be found in Sec. S1 in the supplementary material.

III. RESULTS AND DISCUSSION

A. Spin reorientation transition in the Co/Gd bilayer

The use of magnetic materials for high density data storage requires magnetic systems that are OOP magnetized.[39,40] In thin films, an OOP magnetic easy axis can be obtained by magnetocrystalline anisotropy induced at the interface with heavy metal.[41,42] In addition to that, strain has been shown to affect the magnetic easy axis direction in systems with PMA.[43] To understand the effect of external strain on Co/Gd systems with PMA, we investigate bilayer samples consisting of Ta(4 nm)/Pt(4)/ Co(0–2)/Gd(t_{Gd})/TaN(4). Specifically, the Co thickness is varied between 0 and 2 nm over a few mm along the y direction, whereas t_{Gd} is constant [as in Fig. 1(a)]. In this system, the balance between the interfacial anisotropy energy (magnetocrystalline anisotropy energy at the Pt/Co interface) and demagnetization energy determines the effective

magnetic anisotropy. In such a system, the demagnetization energy increases with the thickness of the Co magnetic layer, and consequently, the magnetization will go from out-of-plane (OOP) to in-plane (IP). To probe the magnetization of our wedge sample, we record hysteresis loops from the pMOKE signal. We repeat the measurement moving the laser spot along the wedge in the y-direction. First, a sample where t_{Gd}=0 is considered. This measurement can be seen in Figs. 1(b) and 1(c). Figure 1(b) reports the magnetic response of the Ta(4 nm)/Pt(4)/Co(0–2)/TaN(4) sample to an OOP magnetic film for different t_{Co}. The effective anisotropy K_{eff} was estimated[41] recording hysteresis loops with magnetic field applied OOP and IP, and the corresponding anisotropy energy per unit area is $K_s = 1.7\ \mathrm{mJ/m^2}$. For $t_{Co} = 1.35$ nm, the square-shaped loop indicates PMA with $K_{eff} = 1.5(2)\times10^5\ \mathrm{J/m^3}$. A value of $M_{Co} = 1.3$ MA/m was used in the calculation. As the thickness of Co is increased (moving the laser spot along the wedge direction—y), the remanence and squareness of the hysteresis loop decreases together with the PMA of the system. For $t_{Co} = 2.00$ nm, the sample is IP magnetized and $K_{eff} = -0.8(2) \times 10^5\ \mathrm{J/m^3}$ is negative. The OOP to IP transition occurs at $t_{Co} = 1.85(2)$ nm in this system.

To investigate the effects of externally applied in-plane strain, we repeat the measurement while the sample is mechanically bent. The magnetization is coupled to the external strain and can be described by the expression for the anisotropy energy,[38]

$$K_{ME} = -\frac{3}{2}\lambda_s Y \varepsilon, \tag{1}$$

where λ_s is the saturation magnetostriction, Y is Young's modulus, and ε is the strain. If the strain in the film is non-zero, the magnetoelastic coupling of Co contributes in principle to the effective anisotropy. Accordingly, the total anisotropy K_{eff} of the magnetic stack is expected to change in the presence of external strain. Figure 1(c) shows the OOP hysteresis loops of Ta(4 nm)/Pt(4)/Co(1.85)/TaN(4) sample before (blue) and after (red) the application of $\varepsilon_{xx} = 0.1\%$. We observe that the magnetization curves are changed in the presence of in-plane strain. The area enclosed between the two curves below saturation can be calculated and is used to determine the magnetoelastic anisotropy K_{ME}.[44] In this system, the strain-induced magnetoelastic anisotropy $K_{ME} = 0.02\ \mathrm{mJ/m^2}$ is positive, as we expect from a material with negative magnetostriction like Co.[43,45] More details about the calculations of magnetoelastic anisotropy can be found in Sec. S1 in the supplementary material. Accordingly, the PMA is increased by the applied strain, i.e., the system is expected to be OOP magnetized for thicker Co if compared to samples without strain.

After this preliminary study on Pt/Co systems, we focused our attention on the magnetostriction of Co/Gd multilayers. In Co–Gd alloys, the magnetostriction has been reported to be strongly dependent on the composition[29,46] due to the structural modification occurring with different atomic contents. In contrast to this case, the effects of magnetostriction of a multilayer are expected to be dependent on the magnetoelastic coupling of the individual layers.[47]

To study the magnetostriction of a Co/Gd multilayer, a constant layer of Gd on top of the Co wedge is added. To perform thickness-dependent studies, a thickness $t_{Gd} = 1$ and 3 nm is considered. In the bilayer system, the magnetization in the Gd layers is mainly induced at the interface with the Co layer and couples antiparallel the Co magnetization.[21] Accordingly, the thickness t_{Co} required to reach the SRT is expected to change with increasing t_{Gd}.[48] To compare the SRT of Ta(4 nm)/Pt(4)/Co(0–2)/Gd (t_{Gd})/TaN(4) samples with different t_{Gd}, we performed remanent intensity scan along our Co wedge, in addition to hysteresis loop measurements. After the sample is saturated with an OOP magnetic field of 1 T, we determine the thickness-dependent remanence from the pMOKE signal without external magnetic field. The remanent intensity scans are reported in Fig. 1(d). As the pMOKE signal is mainly sensitive to the OOP component of Co magnetization, the normalized remanent intensity will drop to zero at the SRT when the magnetization rotates IP. The SRT can be observed in Fig. 1(d) in samples with different thicknesses of Gd before and after the application of strain. As previously reported,[48] the critical thickness $t_{Co} = t_c$, at which SRT occurs, changes significantly in the presence of a Gd layer. For all the considered samples, the in-plane strain shifts the OOP to IP transition toward larger Co thickness. This suggests that the effective magnetostriction of the Co/Gd bilayer is negative and its value $\lambda_s = -10(5) \times 10^{-6}$ is not significantly altered by the presence of the Gd layer.

To obtain a quantitative understanding of the shape of the spin reorientation boundary, we employ an analytical model[48] describing the magnetostatic free energy of the anisotropy, which is zero at the SRT boundary. The first constituent energies of the model are the demagnetization energies of the Co layer,

$$E_{d,Co} = \frac{1}{2}\mu_0 \int_0^y M_{Co}^2\, dq = \frac{1}{2}\mu_0 M_{Co}^2 y, \tag{2}$$

and of the Gd layer,

$$E_{d,Gd} = \frac{1}{2}\mu_0 \int_0^x M_{Gd}^2 \exp(-2q/\lambda_{Gd})\, dq = \frac{1}{4}\mu_0 M_{Gd}^2 \lambda_{Gd}\left(1 - \exp\left(\frac{-2x}{\lambda_{Gd}}\right)\right), \tag{3}$$

where λ_{Gd} is the characteristic decay length of the Gd magnetization, which is induced at the Co/Gd interface, M_{Co} is the magnetization of the Co layer, M_{Gd} is the effective Gd magnetization at the interface between Co and Gd, and x and y are, respectively, the Gd and Co thicknesses in the diagram of Fig. 2(a). The plot axes in Fig. 2(a) have been inverted for a better comparison with the other figures. The magnetocrystalline anisotropy is included with the term

$$E_K = K_s - \Delta K\left(1 - \exp\left(\frac{-2x}{\lambda_K}\right)\right), \tag{4}$$

and it is also considered to decay with a characteristic decay length λ_K and magnitude ΔK. The second term in Eq. (4) phenomenologically addressed the experimentally observed decay in the effective anisotropy, which may be caused by sputter induced disorder of the Co.[49] Using a numerical fit to the experimentally determined SRT, the parameters λ_K, λ_{Gd}, and ΔK for our Co/Gd bilayer are determined. All the other parameters were either experimentally measured or taken from the literature and are reported in Table S I , Sec. S2 in

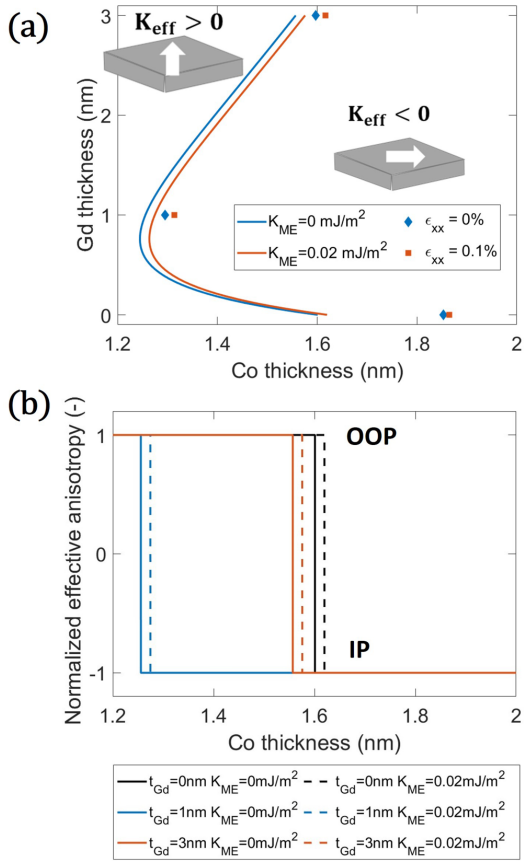

FIG. 2. (a) 2D phase diagram of the SRT of the a Ta(4 nm)/Pt(4)/Co(t_{Co})/Gd(t_{Gd})/TaN(4) stack as a function of t_{Gd} (x) and t_{Co} (y). The axes have been inverted for a better comparison with other figures. Blue diamonds and red squares correspond to the experimental data, reported without and with strain applied, respectively. The solid lines indicate the calculated values using the model for the magnetostatics and Eq. (6). A magnetoelastic anisotropy $K_{ME} = 0$ and 0.02 mJ/m^2 is considered, respectively, for the blue and orange curve. (b) Spin reorientation transition of a Ta(4)/Pt(4)/Co(t_{Co})/Gd(t_{Gd})/TaN(4) sample calculated for values of $t_{Gd} = 0$, 1, and 3 nm and plotted as a function of t_{Co}. The SRT is represented here by a step function. Solid and dashed lines consider $K_{ME} = 0$ and 0.02 mJ/m^2, respectively.

the supplementary material. In addition to the anisotropy term, an additional energy term E_{mix} is included in the model. E_{mix} takes into account the mixing at the magnetic layer interfaces where the local net magnetization is zero. More details about the expression for this term and the determination of the fitting parameters can be found in the supplementary material and in the work of Kools *et al.*[48] In this model, the expression of the total free energy density per unit area is, considering all the terms mentioned so far,

$$E_{tot} = -E_K - E_{mix} + E_{d,Co} + E_{d,Gd}. \quad (5)$$

The magnetocrystalline anisotropy energy per unit area K_s due to the Pt/Co interface is assumed constant.

Equation (5), describing the total energy of a Ta(4 nm)/Pt(4)/Co(t_{Co})/Gd(t_{Gd})/TaN(4) sample, can be solved for y (t_{Co}) by imposing $E_{tot} = 0$ (spin reorientation transition). The solution for the SRT obtained with the model described above is reported in Fig. 2(a) with a blue solid line in a phase diagram, where t_{Gd} (x) and t_{Co} (y) are continuously varied from 0 to 3 and from 0 to 2 nm, respectively. Together with the calculations, the SRT measured experimentally without externally applied strain is reported with blue diamonds in Fig. 2(a). The experimental data follow well the general trend of the calculations. Discrepancies between model and experimental values for $t_{Gd} = 0$ might be due to additional mixing between the layers.

To include the effects of strain, a magnetoelastic anisotropy K_{ME} is added to Eq. (5) that becomes

$$E_{tot} = -E_K - E_{mix} - K_{ME} + E_{d,Co} + E_{d,Gd}. \quad (6)$$

In our case, $K_{ME} = 0.02$ mJ/m^2 corresponds to the value of magnetoelastic anisotropy induced with 0.1% externally applied in-plane strain in our experiments. As showed in Fig. 1(d), we do not observe significant changes to K_{ME} with increasing t_{Gd}. Again considering the SRT boundary to be at $E_{tot} = 0$, the solution of Eq. (6) (that includes the magnetoelastic term) is reported in Fig. 2(a) with an orange solid line. As expected from a material with negative magnetostriction, K_{ME} sums to K_s and the PMA is enhanced by in-plane strain. The SRT calculated including K_{ME} to Eq. (6) is consequently shifted to larger values of t_{Co}. This trend is in agreement with the experimentally determined SRT when and external strain $\varepsilon_{xx} = 0.1\%$ is applied [orange squares in Fig. 2(a)].

Another way to visualize the SRT is solving Eq. (6) for fixed values of t_{Gd} and obtaining the critical thickness of t_{Co} such that $E_{tot} = 0$. Then, the SRT can be represented as a step function in the diagram of Fig. 2(b), analog to the MOKE remanence scan shown in Fig. 1(d). The values of Gd thicknesses considered are $t_{Gd} = 0$, 1, and 3 nm and are plotted in Fig. 2(b) with solid lines in black, blue, and orange, in order. Solid lines consider $K_{ME} = 0$ mJ/m^2. Dashed lines consider instead $K_{ME} = 0.02$ mJ/m^2 in Fig. 2(b). The information contained here can be correlated to the experimental remanent intensity scan in Fig. 1(d). Comparing Fig. 2(b) with Fig. 1(d), a similar behavior can be observed. First we note that the model predicts the SRT to shift when the thickness of the Gd layer is $t_{Gd} > 0$. Second, we observe a similar shift of the SRT point in Figs. 1(d) and 2(b) due to the effect of magnetoelastic anisotropy and of the external strain, respectively. As we expect from a material with negative magnetostriction, K_s adds to K_{ME}; therefore, the PMA is increased and the Co/Gd bilayer stays OOP magnetized for thicker Co (corresponding to larger $E_{d,Co}$). We confirm that the major effect of strain on the Ta(4 nm)/Pt(4)/ Co(0-2)/Gd(t_{Gd})/TaN(4) sample is the alteration of the PMA. Moreover, the estimated effective magnetostriction of the stack—$\lambda_s = -10(5) \times 10^{-6}$—is not significantly

altered by the presence of the Gd layer in the thickness range considered.

In this section, we examined the impact of in-plane strain on the effective PMA of a Co/Gd ferrimagnetic bilayer. Our results suggest negative magnetostriction of the stack for the investigated thickness values. We employ a recent model for the magnetostatics of these type of systems, where we include the effects of strain purely as magnetoelastic anisotropy. Our experimental findings are in good agreement with the predictions made by this model, providing deeper understanding of the response of this material platform to external strain.

B. Magnetization compensation in quadlayer systems

In ferrimagnets, magnetization compensation can be achieved. This occurs when the net magnetization $\vec{M}_{tot} = \vec{M}_{Gd} + \vec{M}_{Co}$ vanishes because the magnetization, coming from the two sublattices, is equal in magnitude and opposite in sign.

In recent studies, changes to the saturation magnetization in the presence of strain were reported in epitaxial films[31] and rare earth free ferrimagnets.[30] To study the effects of strain on magnetization compensation of synthetic ferrimagnets, we consider a quadlayer sample[48] consisting of Ta(4 nm)/Pt(4)/Co(0.6)/Gd(0–2)/Co(0.6)/Gd(1.5)/TaN(4) as schematically drawn in Fig. 3(a). In this case, the thickness of the bottom Gd layer is varied between 0 and 2 nm over a few mm, whereas all the other layers have constant thickness. The reason for this choice is that compared to the Co/Gd bilayer, the magnetic volume of the Co is doubled while the number of Co/Gd interfaces where magnetization is induced in the Gd through direct exchange with the Co is tripled. In this way, magnetization compensation can be more readily achieved.

The growing thickness of Gd increases the contribution of $\vec{M}_{Gd}$ to $\vec{M}_{tot}$. For this reason, some areas of the wedge sample will be Co dominated (for $t_{Gd} < t_{comp}$) and other will be Gd dominated (for $t_{Gd} > t_{comp}$) with $\vec{M}_{tot} = 0$ at $t_{Gd} = t_{comp}$. Here, t_{comp} is the thickness where magnetization compensation is obtained. At magnetization compensation, two effects are expected: a divergence of the coercivity and a sign change in the remanent pMOKE signal (Kerr rotation, normalized to its value in absence of Gd). The measurements for coercivity and intensity are reported in Figs. 3(b) and 3(c), respectively. The coercivity data were extracted from hysteresis loops measured across the wedge direction (along y). The reason for the sign change in the pMOKE signal is the alignment of the Gd magnetization along the field direction in the Gd dominated regime. We report magnetization compensation in this quadlayer for $t_{Gd} = 1.25$ nm.

In a similar fashion to what we have done investigating the PMA in the bilayer system, we repeat the experiment in the presence of $\varepsilon_{xx} = 0.1\%$ in-plane strain. The results are reported in orange in Figs. 3(b) and 3(c). Remarkably, the compensation point of the Co/Gd quadlayer is unchanged by the application of this externally applied strain.

Figures 3(d) and 3(e) contain OOP hysteresis loops of Ta(4 nm)/Pt(4)/Co(0.6)/Gd(t_{Gd})/Co(0.6)/Gd(1.5)/TaN(4) samples for $t_{Gd} = 1.15$ nm and $t_{Gd} = 1.35$ nm, respectively, and further show the effects of magnetization compensation. The sample is in this case OOP magnetized. As the thickness of Gd is increased, the magnetization of the sample goes from Co dominated [Fig. 3(d)] to Gd dominated [Fig. 3(e)]. The inversion of hysteresis loops happens because for $t_{Gd} > 1.25$ nm the Co magnetization aligns antiparallel to the field, leading to the change in sign of the pMOKE signal. When the measurement is repeated in the presence of $\varepsilon_{xx} = 0.1\%$ strain (orange line), no significant changes to the remanent intensity or coercivity are reported, if compared to the unstrained case (blue line). This suggests that magnetization compensation can be achieved in these multilayer systems in the presence

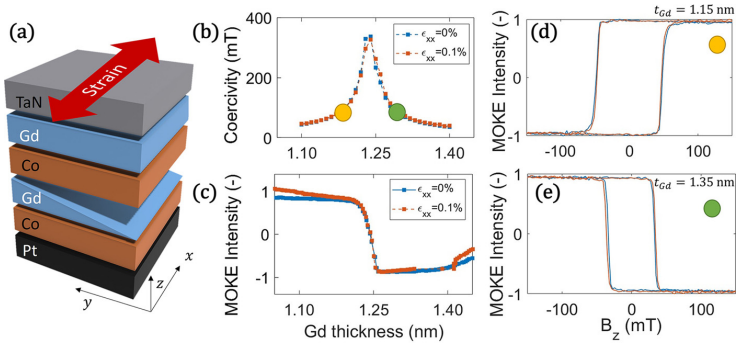

FIG. 3. (a) Layer stack consisting of a Co/Gd quadlayer used to obtain magnetization compensation. In this case, the bottom Gd layer is varied along the sample surface while all the other layers thickness is kept constant. (b) Coercivity and (c) remanent pMOKE intensity scan as a function of t_{Gd}. Measurements before (blue) and after (orange) application of in-plane strain are reported. (d) Hysteresis loops in the Co dominated and (e) Gd dominated state. Both curves with (orange) and without (blue) in-plane strain applied are shown. The magnetic field was applied in the OOP direction, along z.

of external strain and, most importantly, that the magnetization compensation point is unaffected, in contrast with what has been recently observed in ferrimagnetic alloys.[32,33]

In the related work of Wang and co-workers,[33] strain is observed to induce changes to the compensation temperature of GdFeCo ferrimagnetic alloys and those changes in compensation are attributed to lattice constant variation with strain. As explained by first principle calculations, this lattice strain alters the exchange coupling strength in GdFeCo and the moment of the Gd accordingly. This is expected to be different in the case of synthetic ferrimagnets, where the ferromagnetic coupling within each layer will not be strongly affected by the in-plane strain.

Synthetic ferrimagnets have the two sublattices confined in separate layers and the Gd magnetization is induced at the Co/Gd interface where the exchange energy is maximum.[21,23] In other words, this means that the composition gradient (where the magnetization is mostly induced) is primarily in the z-direction. Accordingly, in synthetic ferrimagnets, magnetization compensation is due to the balance in Co magnetization and the Gd magnetization[25,48] in the individual layers and the total magnetic moment per unit area $\vec{M}_{tot}$ is obtained by integrating the magnetization of the Co and Gd sublattices over the respective layer thicknesses.

In multilayer samples with PMA, the dominant effect of in-plane strain in the order of 0.1% is the alteration of the spin–orbit coupling within one layer.[50] This alters the magnetocrystalline anisotropy energy of the system[51] rather than the magnetic moment of Co and Gd within one layer. Accordingly, in a ferrimagnetic multilayer, in-plane strain is not expected to affect the induced magnetic moment from the Co onto the Gd, thus not altering magnetization compensation. This is consistent with our observations of a strain-independent magnetization compensation in a synthetic ferrimagnet for the magnitudes of strain considered.

IV. CONCLUSIONS

This work reveals the effect that external strain has on PMA and magnetization compensation of Co/Gd systems at room temperature. Growing wedge samples, where the thickness of one of the magnetic layers was varied, has allowed us to determine thickness dependent transition in the magnetostatics of this multilayer system. Deliberate in-plane strain was applied to the sample. In a bilayer Pt/Co/Gd system, we experimentally show that a sizable magnetoelastic coupling changes the SRT in the presence of strain. The contribution of the strain-anisotropy for this system has been included in a model for the magnetostatics, describing the experimental observations well if an effective negative magnetostriction is considered. In a Pt/Co/Gd/Co/Gd quadlayer, we obtain magnetization compensation of the two sublattices by varying the thickness of the bottom Gd layer. Here, we find that the application of 0.1% in-plane strain does not affect the magnetization compensation. The induced magnetic moment from the Co onto the Gd, being an interface effect in a multilayer system, is not altered by such mechanical deformation. To conclude, this work provides a broad understanding of the magnetoelastic properties of these multilayer systems. As PMA and magnetic compensation are maintained in the presence of externally applied strain, this material system is a good candidate for technological implementation of ferrimagnets.

SUPPLEMENTARY MATERIAL

See the supplementary material for the magnetostatics model for the spin reorientation transition and for more details about the setup used for application of strain.

ACKNOWLEDGMENTS

This project has received funding from the European Union's Horizon 2020 Research and Innovation Program under the Marie Skłodowska-Curie Grant Agreement No. 860060 "Magnetism and the effect of Electric Field" (MagnEFi), the Deutsche Forschungsgemeinschaft (DFG, German Research Foundation)—TRR 173 —268565370 (Projects A01 and B02) and the Austrian Research Promotion Agency (FFG). The authors acknowledge support by the Max-Planck Graduate Centre with Johannes Gutenberg University.

AUTHOR DECLARATIONS

Conflict of Interest

The authors have no conflicts to disclose.

Author Contributions

Giovanni Masciocchi: Conceptualization (equal); Data curation (equal); Formal analysis (equal); Investigation (equal); Writing – original draft (equal); Writing – review & editing (equal). **Thomas J. Kools:** Conceptualization (supporting); Data curation (equal); Formal analysis (equal); Investigation (lead); Writing – original draft (lead); Writing – review & editing (equal). **Pingzhi Li:** Conceptualization (equal); Data curation (equal); Formal analysis (supporting); Writing – review & editing (equal). **Adrien A. D. Petrillo:** Conceptualization (equal); Data curation (equal); Formal analysis (supporting); Investigation (supporting); Writing – review & editing (supporting). **Bert Koopmans:** Investigation (supporting); Writing – review & editing (equal). **Reinoud Lavrijsen:** Conceptualization (equal); Writing – review & editing (equal). **Andreas Kehlberger:** Conceptualization (equal); Formal analysis (supporting); Writing – review & editing (equal). **Mathias Kläui:** Conceptualization (equal); Formal analysis (equal); Writing – review & editing (equal).

DATA AVAILABILITY

The data that support the findings of this study are available from the corresponding author upon reasonable request.

REFERENCES

[1]T. Endoh, H. Honjo, K. Nishioka, and S. Ikeda, "Recent progresses in STT-MRAM and SOT-MRAM for next generation MRAM," in *2020 IEEE Symposium on VLSI Technology* (IEEE, 2020), pp. 1–2.
[2]S. S. Parkin, M. Hayashi, and L. Thomas, "Magnetic domain-wall racetrack memory," Science **320**, 190–194 (2008).
[3]S. Tehrani, "Status and outlook of MRAM memory technology," in *2006 International Electron Devices Meeting* (IEEE, 2006), pp. 1–4.
[4]K. Garello, F. Yasin, and G. S. Kar, "Spin-orbit torque MRAM for ultrafast embedded memories: From fundamentals to large scale technology integration," in *2019 IEEE 11th International Memory Workshop (IMW)* (IEEE, 2019), pp. 1–4.

[5]K. Gu, Y. Guan, B. K. Hazra, H. Deniz, A. Migliorini, W. Zhang, and S. S. Parkin, "Three-dimensional racetrack memory devices designed from free-standing magnetic heterostructures," Nat. Nanotechnol. **17**, 1065–1071 (2022).
[6]S.-H. Yang, K.-S. Ryu, and S. Parkin, "Domain-wall velocities of up to 750 ms^{-1} driven by exchange-coupling torque in synthetic antiferromagnets," Nat. Nanotechnol. **10**, 221–226 (2015).
[7]R. Tomasello, V. Puliafito, E. Martinez, A. Manchon, M. Ricci, M. Carpentieri, and G. Finocchio, "Performance of synthetic antiferromagnetic racetrack memory: Domain wall versus skyrmion," J. Phys. D: Appl. Phys. **50**, 325302 (2017).
[8]S.-H. Yang, C. Garg, T. Phung, C. Rettner, and B. Hughes, "Spin-orbit torque driven one-bit magnetic racetrack devices-memory and neuromorphic applications," in *2019 International Symposium on VLSI Technology, Systems and Application (VLSI-TSA)* (IEEE, 2019), pp. 1–2.
[9]Q. Shao, Z. Wang, and J. J. Yang, "Efficient AI with MRAM," Nat. Electron. **5**, 67–68 (2022).
[10]S. Parkin and S.-H. Yang, "Memory on the racetrack," Nat. Nanotechnol. **10**, 195–198 (2015).
[11]I. Radu, K. Vahaplar, C. Stamm, T. Kachel, N. Pontius, H. Dürr, T. Ostler, J. Barker, R. Evans, R. Chantrell *et al.*, "Transient ferromagnetic-like state mediating ultrafast reversal of antiferromagnetically coupled spins," Nature **472**, 205–208 (2011).
[12]T. Ostler, J. Barker, R. Evans, R. Chantrell, U. Atxitia, O. Chubykalo-Fesenko, S. El Moussaoui, L. Le Guyader, E. Mengotti, L. Heyderman *et al.*, "Ultrafast heating as a sufficient stimulus for magnetization reversal in a ferrimagnet," Nat. Commun. **3**, 666 (2012).
[13]A. V. Kimel and M. Li, "Writing magnetic memory with ultrashort light pulses," Nat. Rev. Mater. **4**, 189–200 (2019).
[14]P. Zhang, T.-F. Chung, Q. Li, S. Wang, Q. Wang, W. L. Huey, S. Yang, J. E. Goldberger, J. Yao, and X. Zhang, "All-optical switching of magnetization in atomically thin CrI_3," Nat. Mater. **21**, 1373–1378 (2022).
[15]E. K. Sobolewska, J. Pelloux-Prayer, H. Becker, G. Li, C. S. Davies, C. Krückel, L. A. Félix, A. Olivier, R. C. Sousa, I.-L. Prejbeanu *et al.*, "Integration platform for optical switching of magnetic elements," Proc. SPIE **11461**, 114612B (2020).
[16]S. K. Kim, G. S. Beach, K.-J. Lee, T. Ono, T. Rasing, and H. Yang, "Ferrimagnetic spintronics," Nat. Mater. **21**, 24–34 (2022).
[17]L. Avilés-Félix, L. Álvaro-Gómez, G. Li, C. Davies, A. Olivier, M. Rubio-Roy, S. Auffret, A. Kirilyuk, A. Kimel, T. Rasing *et al.*, "Integration of Tb/Co multilayers within optically switchable perpendicular magnetic tunnel junctions," AIP Adv. **9**, 125328 (2019).
[18]M. L. Lalieu, R. Lavrijsen, and B. Koopmans, "Integrating all-optical switching with spintronics," Nat. Commun. **10**, 110 (2019).
[19]H. Becker, C. J. Krückel, D. Van Thourhout, and M. J. Heck, "Out-of-plane focusing grating couplers for silicon photonics integration with optical MRAM technology," IEEE J. Sel. Top. Quantum Electron. **26**, 8300408 (2019).
[20]K.-J. Kim, S. K. Kim, Y. Hirata, S.-H. Oh, T. Tono, D.-H. Kim, T. Okuno, W. S. Ham, S. Kim, G. Go *et al.*, "Fast domain wall motion in the vicinity of the angular momentum compensation temperature of ferrimagnets," Nat. Mater. **16**, 1187–1192 (2017).
[21]M. Lalieu, M. Peeters, S. Haenen, R. Lavrijsen, and B. Koopmans, "Deterministic all-optical switching of synthetic ferrimagnets using single femtosecond laser pulses," Phys. Rev. B **96**, 220411 (2017).
[22]L. Avilés-Félix, A. Olivier, G. Li, C. S. Davies, L. Álvaro-Gómez, M. Rubio-Roy, S. Auffret, A. Kirilyuk, A. Kimel, T. Rasing *et al.*, "Single-shot all-optical switching of magnetization in Tb/Co multilayer-based electrodes," Sci. Rep. **10**, 5211 (2020).
[23]M. Beens, M. L. Lalieu, A. J. Deenen, R. A. Duine, and B. Koopmans, "Comparing all-optical switching in synthetic-ferrimagnetic multilayers and alloys," Phys. Rev. B **100**, 220409 (2019).
[24]Y. Xu, M. Deb, G. Malinowski, M. Hehn, W. Zhao, and S. Mangin, "Ultrafast magnetization manipulation using single femtosecond light and hot-electron pulses," Adv. Mater. **29**, 1703474 (2017).
[25]T. H. Pham, J. Vogel, J. Sampaio, M. Vaňatka, J.-C. Rojas-Sánchez, M. Bonfim, D. Chaves, F. Choueikani, P. Ohresser, E. Otero *et al.*, "Very large domain wall velocities in Pt/Co/GdOx and Pt/Co/Gd trilayers with Dzyaloshinskii-Moriya interaction," Europhys. Lett. **113**, 67001 (2016).
[26]P. Li, T. J. Kools, B. Koopmans, and R. Lavrijsen, "Ultrafast racetrack based on compensated Co/Gd-based synthetic ferrimagnet with all-optical switching," Adv. Electron. Mater. **9**, 2200613 (2023).
[27]L. Wang, H. Cheng, P. Li, Y. L. van Hees, Y. Liu, K. Cao, R. Lavrijsen, X. Lin, B. Koopmans, and W. Zhao, "Picosecond optospintronic tunnel junctions," Proc. Natl. Acad. Sci. U.S.A. **119**, e2204732119 (2022).
[28]H. Windischmann, "Intrinsic stress in sputter-deposited thin films," Crit. Rev. Solid State Mater. Sci. **17**, 547–596 (1992).
[29]K. Twarowski and H. Lachowicz, "Magnetostriction and anisotropy of amorphous Gd-Co RF sputtered thin films," J. Appl. Phys. **50**, 7722–7724 (1979).
[30]Z. Chen, X. Shi, X. Liu, X. Chen, Z. Zhang, and W. Mi, "Modulating saturation magnetization and topological Hall resistivity of flexible ferrimagnetic Mn_4N films by bending strains," J. Appl. Phys. **132**, 233906 (2022).
[31]M. Zheng, P. Guan, and H. Fan, "Mechanically enhanced magnetism in flexible semitransparent $CuFe_2O_4$/mica epitaxial heterostructures," Appl. Surf. Sci. **584**, 152586 (2022).
[32]S. Ota, P. Van Thach, H. Awano, A. Ando, K. Toyoki, Y. Kotani, T. Nakamura, T. Koyama, and D. Chiba, "Strain-induced modulation of temperature characteristics in ferrimagnetic Tb-Fe films," Sci. Rep. **11**, 6237 (2021).
[33]J. Wang, M. Li, C. Li, R. Tang, M. Si, G. Chai, J. Yao, C. Jia, and C. Jiang, "Piezostrain-controlled magnetization compensation temperature in ferrimagnetic GdFeCo alloy films," Phys. Rev. B **107**, 184424 (2023).
[34]A. Tavassolizadeh, K. Rott, T. Meier, E. Quandt, H. Hölscher, G. Reiss, and D. Meyners, "Tunnel magnetoresistance sensors with magnetostrictive electrodes: Strain sensors," Sensors **16**, 1902 (2016).
[35]A. M. Sahadevan, R. K. Tiwari, G. Kalon, C. S. Bhatia, M. Saeys, and H. Yang, "Biaxial strain effect of spin dependent tunneling in MgO magnetic tunnel junctions," Appl. Phys. Lett. **101**, 042407 (2012).
[36]Q. Wang, J. Domann, G. Yu, A. Barra, K. L. Wang, and G. P. Carman, "Strain-mediated spin-orbit-torque switching for magnetic memory," Phys. Rev. Appl. **10**, 034052 (2018).
[37]J. Erskine and E. Stern, "Magneto-optic Kerr effects in gadolinium," Phys. Rev. B **8**, 1239 (1973).
[38]G. Masciocchi, M. Fattouhi, A. Kehlberger, L. Lopez-Diaz, M.-A. Syskaki, and M. Kläui, "Strain-controlled domain wall injection into nanowires for sensor applications," J. Appl. Phys. **130**, 183903 (2021).
[39]C. Chappert, A. Fert, and F. N. Van Dau, "The emergence of spin electronics in data storage," Nat. Mater. **6**, 813–823 (2007).
[40]B. Tudu and A. Tiwari, "Recent developments in perpendicular magnetic anisotropy thin films for data storage applications," Vacuum **146**, 329–341 (2017).
[41]M. Johnson, P. Bloemen, F. Den Broeder, and J. De Vries, "Magnetic anisotropy in metallic multilayers," Rep. Prog. Phys. **59**, 1409 (1996).
[42]F. Den Broeder, W. Hoving, and P. Bloemen, "Magnetic anisotropy of multilayers," J. Magn. Magn. Mater. **93**, 562–570 (1991).
[43]K. Kyuno, J.-G. Ha, R. Yamamoto, and S. Asano, "Theoretical study on the strain dependence of the magnetic anisotropy of X/Co (X= Pt, Cu, Ag, and Au) metallic multilayers," J. Appl. Phys. **79**, 7084–7089 (1996).
[44]R. O'Handley, O.-S. Song, and C. Ballentine, "Determining thin-film magnetoelastic constants," J. Appl. Phys. **74**, 6302–6307 (1993).
[45]S. Hashimoto, Y. Ochiai, and K. Aso, "Perpendicular magnetic anisotropy and magnetostriction of sputtered Co/Pd and Co/Pt multilayered films," J. Appl. Phys. **66**, 4909–4916 (1989).
[46]K. Twarowski, H. Lachowicz, M. Gutowski, and H. Szymczak, "On the origin of the perpendicular anisotropy and magnetostriction in amorphous RF sputtered Gd–Co films," Phys. Status Solidi A **63**, 103–108 (1981).
[47]G. Masciocchi, J. W. van der Jagt, M.-A. Syskaki, A. Lamperti, N. Wolff, A. Lotnyk, J. Langer, L. Kienle, G. Jakob, B. Borie *et al.*, "Control of magnetoelastic coupling in Ni/Fe multilayers using He^+ ion irradiation," Appl. Phys. Lett. **121**, 182401 (2022).

[48]T. J. Kools, M. C. van Gurp, B. Koopmans, and R. Lavrijsen, "Magnetostatics of room temperature compensated Co/Gd/Co/Gd-based synthetic ferrimagnets," Appl. Phys. Lett. **121**, 242405 (2022).
[49]G. Bertero, T. Hufnagel, B. Clemens, and R. Sinclair, "TEM analysis of Co-Gd and Co-Gd multilayer structures," J. Mater. Res. **8**, 771–774 (1993).
[50]B. Zhang, K. M. Krishnan, C. Lee, and R. Farrow, "Magnetic anisotropy and lattice strain in Co/Pt multilayers," J. Appl. Phys. **73**, 6198–6200 (1993).
[51]D. B. Gopman, C. L. Dennis, P. Chen, Y. L. Iunin, P. Finkel, M. Staruch, and R. D. Shull, "Strain-assisted magnetization reversal in Co/Ni multilayers with perpendicular magnetic anisotropy," Sci. Rep. **6**, 27774 (2016).

Applied Physics Letters ARTICLE pubs.aip.org/aip/apl

Generation of imprinted strain gradients for spintronics

Cite as: Appl. Phys. Lett. **123**, 022404 (2023); doi: 10.1063/5.0157687
Submitted: 10 May 2023 · Accepted: 20 June 2023 ·
Published Online: 11 July 2023

G. Masciocchi,[1,2] M. Fattouhi,[3] E. Spetzler,[4] M.-A. Syskaki,[1,5] R. Lehndorff,[6] E. Martinez,[3] J. McCord,[4,7] L. Lopez-Diaz,[3] A. Kehlberger,[2] and M. Kläui[1,a)]

AFFILIATIONS

[1]Institute of Physics, Johannes Gutenberg University Mainz, Staudingerweg 7, Mainz 55099, Germany
[2]Sensitec GmbH, Walter-Hallstein-Straße 24, Mainz 55130, Germany
[3]Department of Applied Physics, Universidad de Salamanca, Salamanca E-37008, Spain
[4]Institute for Materials Science, Kiel University, Kaiserstraße 2, Kiel 24143, Germany
[5]Singulus Technologies AG, Hanauer Landstrasse 107, Kahl am Main 63796, Germany
[6]Allegro MicroSystems Germany GmbH, Vangerowstraße 18/1, Heidelberg 69115, Germany
[7]Kiel Nano, Surface and Interface Science (KiNSIS), Kaiserstraße 2, Kiel 24143, Germany

[a)]**Author to whom correspondence should be addressed:** klaeui@uni-mainz.de

ABSTRACT

In this work, we propose and evaluate an inexpensive and CMOS-compatible method to locally apply strain on a Si/SiOx substrate. Due to high growth temperatures and different thermal expansion coefficients, a SiN passivation layer exerts a compressive stress when deposited on a commercial silicon wafer. Removing selected areas of the passivation layer alters the strain on the micrometer range, leading to changes in the local magnetic anisotropy of a magnetic material through magnetoelastic interactions. Using Kerr microscopy, we experimentally demonstrate how the magnetoelastic energy landscape, created by a pair of openings, enables in a magnetic nanowire the creation of pinning sites for in-plane vortex walls that propagate in a magnetic racetrack. We report substantial pinning fields up to 15 mT for device-relevant ferromagnetic materials with positive magnetostriction. We support our experimental results with finite element simulations for the induced strain, micromagnetic simulations, and 1D model calculations using the realistic strain profile to identify the depinning mechanism. All the observations above are due to the magnetoelastic energy contribution in the system, which creates local energy minima for the domain wall at the desired location. By controlling domain walls with strain, we realize the prototype of a true power-on magnetic sensor that can measure discrete magnetic fields or Oersted currents. This utilizes a technology that does not require piezoelectric substrates or high-resolution lithography, thus enabling wafer-level production.

One of the promising "Beyond CMOS" technologies is nanomagnetic and spintronic devices due to their nonvolatile nature, high operating speed, low power consumption, and well explored routes to read and write data.[1] One example is nanomagnetic tracks, where information (stored in domain walls—DWs) is propagated and manipulated by dipolar interaction along soft ferromagnetic nanowires.[2,3] The manipulation of DWs has quite a long history, and a turning point in this research area was the demonstration of a current-controlled magnetic DW shift register[4,5] (racetrack memory). Since then, more work has been done on the development of DW-based memories,[6] logic devices,[7] sensors,[8–11] and neuromorphic computing circuits.[12,13] However, feasibility of the fabrication process and compatibility with existing CMOS devices must be ensured before full technological realization is achieved.

One of the key challenges with these devices is the control of DWs,[14] typically realized using geometric constraints (notches)[15–17] or the local manipulation of the magnetic anisotropy through strain[18,19] using magnetostrictive/piezoelectric systems.[20–23] However, these approaches are not attractive for most sensor manufacturers due to high cost and complexity, respectively, because high-resolution notches and presence of the multiferroic stack would require significant investments in tools for high-resolution lithography and layer deposition. Also, the presence of voltages for piezoelectric actuation via metallic contacts increases design complexity and area usage. It is, moreover, difficult to realize an arbitrary shape of strain and strain gradients down to the micrometer range with piezoelectric substrates because it is technologically nontrivial to confine the electric fields.[24]

An alternative method of transferring strain to a thin film[25,26] is the use of capping layers[27] widely used in the semiconductor and photovoltaic industries because they provide protection from harsh environments.

In this work, we propose and experimentally demonstrate a low-cost and CMOS-compatible method to induce local strain on a Si/SiOx substrate by removing selected regions of the passivation layer. Arbitrary strain magnitudes and strain gradients can be realized by simply choosing the design of the removed part. The magnitude and profile of the strain are determined by combining anisotropy and stress measurements with finite elements simulations. We experimentally demonstrate, using Kerr microscopy, that this local strain allows for domain wall pinning in a racetrack element. This is verified by micromagnetic simulations and 1D model calculations. Finally, to show the technological relevance of this method, we propose and verify a nonvolatile magnetic peak-field sensor based on this technology.

Samples of $Co_{70}Fe_{30}$(30 nm) and $Co_{40}Fe_{40}B_{20}$(30 nm) were prepared by DC magnetron sputtering using a Singulus Rotaris system on a SiOx(1.5 μm)/Si(625 μm) substrate. The ferromagnetic layers were capped with AlOx(10 nm)/HfOx(10) layers to preserve their functionalities during the fabrication process. Using optical lithography and etching, nanowires were fabricated with a variable width—between 800 and 500 nm—and a length of 70 μm. A reservoir at the left end allows for DWs injection at lower fields. After the first lithography step, the wafer was covered with a 1 μm thick SiN layer using plasma-enhanced chemical vapor deposition (PECVD) at a temperature of 250 °C. The residual stress on the wafer is quantified using a standard wafer bow measurement. A second optical lithography step is used in combination with reactive ion etching (RIE) to remove selected areas (up to 20 × 20 μm^2) of the SiN layer (openings) without damaging the magnetic layer, as shown in Figs. 1(a)–1(d), while the wafer surface is still largely covered. The values of magnetostriction of the thin films were measured using a BH-looper with three-point bending stage. The magneto-optic Kerr effect (MOKE) was used to image the magnetization state in the devices.[28,29]

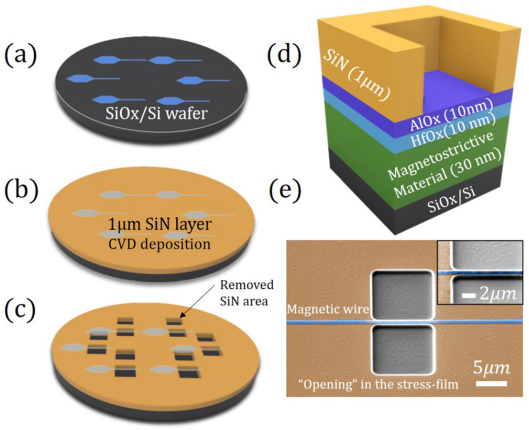

FIG. 1. Racetracks structuring (a), SiN layer deposition (uniform strain generated) (b), and locally relieved strain after RIE (c). (d) Section of the layers used in this work. (e) SEM image of a pair of openings in the SiN in the proximity of a magnetic nanowire.

To understand the origin of the intrinsic stress in our system, one should consider the coefficients of thermal expansion of a film and a substrate, along with the high temperature during deposition. If the thermal expansion coefficients are different, thermal stresses arise when the whole stack cools down to room temperature after deposition.[30] Relaxation of this stress leads to a deformation, i.e., bending, of the wafer [Figs. 1(a) and 1(b)] allowing for the residual stress to be estimated.[31] The measured in-plane (compressive) stress is planar and, in our case, has a magnitude of −495(5) MPa. To create a non-uniform stress on the substrate surface, selected areas of the SiN are completely removed, creating openings in the passivation layer [Fig. 1(c)]. The etching is monitored to stop the process at the AlOx/SiN interface, as shown in Fig. 1(d), so that the integrity of the magnetic layer is preserved. An example of the final device is shown in a scanning electron microscopy image (SEM) in Fig. 1(e) for a pair of square apertures 10 × 10 μm^2 in size. With a suitable lithography mask, arbitrary shapes, sizes, and spacing of the apertures can be realized with sub μm resolution. In the example presented here, the openings are spaced 1 μm apart and the 800 nm wide magnetic track under the SiN layer shows no signs of damage caused by the etching process.

To determine the magnitude of stress relieved, finite-element-method (FEM) simulations were performed using the COMSOL Multiphysics® Structural Mechanics Module.[32] More details about FEM simulations can be found in Section S1 of the supplementary material. To have a well-defined strained region in racetrack type devices, it is convenient to consider a pair of openings—to be realized at each side of a magnetic nanowire. Figures 2(a)–2(d) contain the computed values of the surface strain $\varepsilon_{xx} - \varepsilon_{yy}$ at the interface between SiN/SiOx for two different opening geometries. As shown in Figs. 2(c) and 2(d), the effective surface strain $\varepsilon_{xx} - \varepsilon_{yy}$ is close to zero at a distance greater than 20 μm from the etched areas and becomes non-uniform in their proximity. The geometry of the opening determines the strain profile. This can be seen in Figs. 2(a) and 2(b) where the effective strain is plotted along the dashed line running between the two openings shown in Figs. 2(c) and 2(d), respectively. For a square pair of openings [Fig. 2(a)], the effective uniaxial strain profile $\varepsilon_{xx} - \varepsilon_{yy}$ is mostly flat and confined between them with strain gradient maxima (minima) at the exit (entrance) of the strained area. The strain reaches values of $\varepsilon_{xx} - \varepsilon_{yy} \simeq 0.2\%$. For a diamond shaped pair of openings, the strain is again confined between the openings, but its magnitude increases almost linearly toward the center. This time the strain gradient is mostly constant.

To experimentally confirm the magnitude and sign of this local strain, we measured the magnetization curves of a unpatterned film of AlOx/HfOx/$Co_{70}Fe_{30}$ (30 nm) underneath the patterned SiN. The hysteresis loops were measured with the magnetic field applied along $\Phi = 0°$ at different locations on the sample, selecting a region of interest of 5 × 5 μm^2 size within the field of view of the Kerr microscope. Full angular dependence of the anisotropy is reported in Section S3 of the supplementary material, together with more details about the calculation of the magnetoelastic anisotropy. Since $Co_{70}Fe_{30}$ has considerable magnetostriction ($\lambda_s \simeq 80 \times 10^{-6}$), the strain acting on the film is coupled to the magnetization via the magnetoelastic effect, as expressed in the anisotropy energy,[33]

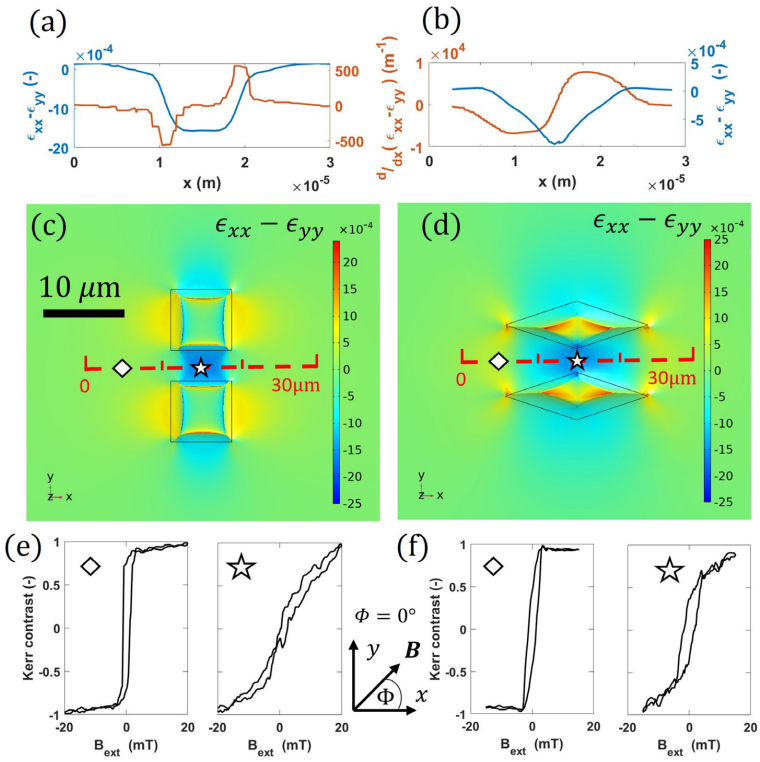

FIG. 2. (a) and (b) Effective strain ($\varepsilon_{xx} - \varepsilon_{yy}$)and strain gradient ($\frac{d}{dx}(\varepsilon_{xx} - \varepsilon_{yy})$) for, respectively, a square and a triangular pair of opening obtained from FEM simulations. The x axis refers to the red dashed line. (c) and (d) Surface strain $\varepsilon_{xx} - \varepsilon_{yy}$ obtained with FEM simulations. (e) and (f) In-plane hysteresis loops obtained with Kerr microscopy on a full film of $Co_{70}Fe_{30}$ (30 nm) for, respectively, a square and a triangular pair of opening. The contrast was measured before the opening (diamond) and between them (star) according to the marker position. The magnetic field was applied along the direction $\Phi = 0°$.

$$K_{ME} = \frac{3}{2}\lambda_s Y(\varepsilon_{xx} - \varepsilon_{yy}), \tag{1}$$

where Y is Young's modulus and λ_s is the saturation magnetostriction. Measuring hysteresis loops, where an in-plane field is applied along two perpendicular directions, can give us a direct measurement of the local anisotropy by subtracting the area enclosed between the two curves below saturation.[19,34] Comparing the anisotropy in the proximity and far away from the openings allows for the estimation of the changes in K_{ME} between the two areas.[35–37]

In Figs. 2(e) and 2(f), hysteresis loops of an unpatterned film, this time of SiN/AlOx/HfOx/$Co_{70}Fe_{30}$(30 nm), are shown. The openings geometry is the one of Figs. 2(c) and 2(d), respectively. Looking at Fig. 2(e), we can compare the magnetization curve before (diamond) and between (star) the square openings. The anisotropy field increases, due to (uniaxial) magnetoelastic anisotropy. As $Co_{70}Fe_{30}$ has a positive magnetostriction, the increase in anisotropy [due to the magnetoelastic contribution $K_{ME} \simeq 8.9(2)$ kJ/m^3] is caused by a negative (compressive) $\varepsilon_{xx} - \varepsilon_{yy}$ strain, in agreement with our FEM simulation. Using Eq. (1) and the values of magnetoelastic anisotropy difference, we can estimate the strain to be $\varepsilon_{xx} - \varepsilon_{yy} \simeq -0.05(1)\%$ for a square opening of this size. The same measurement can be performed for a diamond-shaped pair of openings and is reported in Fig. 2(f). The calculated maximum strain difference for this case is $\varepsilon_{xx} - \varepsilon_{yy} \simeq -0.02(1)\%$. Signal coming from areas outside the 5×5 μm^2 spot can explain an experimental value smaller than FEM predictions.

The strain, created by removing specific areas of the SiN layer, could be used as a mechanism to move, change direction, or stop a DW, a feature often needed in the device implementation.[9,19] Typical ways to do so rely on the modification of the DW energy making it a spatially variable quantity. In analogy with the conventional field-driven case, the magnetoelastic field can be considered as a force that pushes the DW along the direction of decreasing energy, i.e., increasing compressive strain if $\lambda_s > 0$ for the in-plane-strain-gradient case. This force is proportional to the local gradient of the spatially variable quantity,[18,38,39] and its effect is essentially that of an effective (magnetoelastic) field,

$$B_{ME} = -\frac{1}{M_s}\frac{du_{ME}}{dx}, \tag{2}$$

where u_{ME} is the magnetoelastic DW energy per unit area.

For this study, a 500 nm wide magnetic racetrack of $Co_{70}Fe_{30}$(30 nm) is considered together with a pair of square openings in SiN 10×10 μm^2 in size. We use Kerr microscopy in the transverse mode to image the magnetic state of the device, while the in-plane

magnetic field is applied parallel to the wire along x. Figures 3(a)–3(c) show the position of a DW along the magnetic racetrack as a function of the applied magnetic field. When the field is sufficiently large, the DW is injected from the reservoir [Fig. 3(a)] into the magnetic wire. As can be seen in Fig. 3(b), after injection, the wall does not propagate until the end of the magnetic channel, but is pinned in the area between the SiN openings corresponding to the strained area. The corresponding surface strain was shown with a simulation in Figs. 2(a) and 2(c). Only for larger magnetic fields, the wall can continue to propagate to the other end of the magnetic channel, as shown in Fig. 3(c).

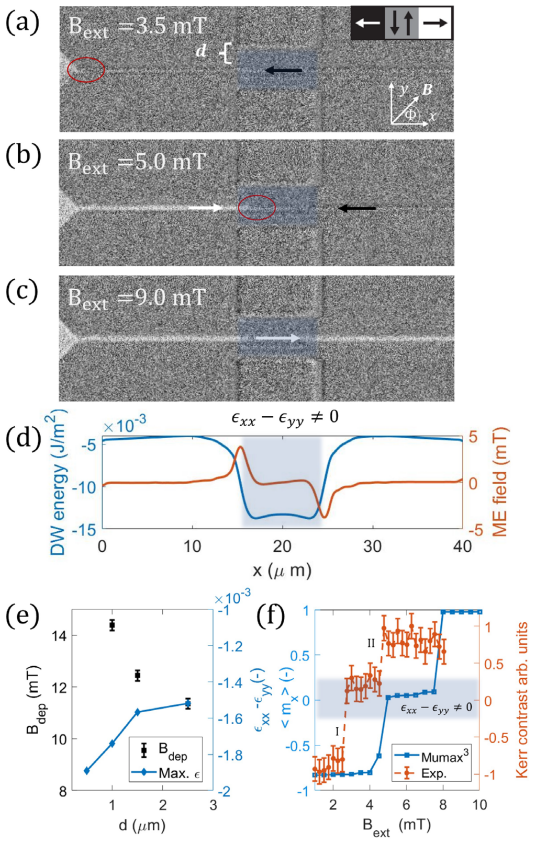

FIG. 3. MOKE images showing a DW (a) injected, (b) pinned in the strained area, and (c) continuing propagation for larger magnetic fields. (d) 1D model calculations of energy profile and the corresponding local magnetoelastic field for a vortex wall in the strain profile shown in Fig. 2(a) as a function of the DW position. (e) Experimental values of depinning field (black squares) and maximum strain $\varepsilon_{xx} - \varepsilon_{yy}$ (blue diamonds) for different distances between a pair of square openings. The values consider a 500 nm wire of $Co_{70}Fe_{30}$ with 30 nm thickness. (f) Micromagnetic simulations magnetization (blue) and experimentally measured Kerr contrast (orange) for a 800 nm wide nanowire as a function of applied field. The averaged wire magnetization along x direction ($\langle m_x \rangle$) is proportional to the DW position.

For a $Ni_{81}Fe_{19}$ sample with nearly no magnetostriction, no DW pinning was found above the DW injection field (2 mT), supporting the idea of a strain-based pinning. We repeated the same measurement for devices with different distance d between racetrack and openings. According to FEM simulations, the absolute value of the (compressive) strain increases as the opening distance d is reduced [blue diamonds in Fig. 3(e)]. As shown in Fig. 3(e), the depinning field (black squares) increases from 11.0(2) to 14.5(2) mT for a distance between the opening and the magnetic racetrack decreasing from 2.5 to 1 μm. A larger depinning field B_{dep} for smaller opening spacing confirms that the magnetoelastic energy is indeed the dominant pinning cause in our system.[20,40]

To support our experimental findings, we performed micromagnetic simulations and 1D model calculations where the strain profile from FEM simulations was used. The results are summarized in Figs. 3(d) and 3(f) and consider nanowires made of 30 nm thick $Co_{40}Fe_{40}B_{20}$. For more details about the micromagnetic simulations and the 1D analytical model, see Section S2 of the supplementary material. Figure 3(d) shows the DW energy per unit area and the corresponding magnetoelastic field as a function of the DW position for a nanowire $w = 500$ nm wide, calculated considering the strain profile shown in Fig. 2(a) and a rigid profile for the DW. Comparing Fig. 3(d) with Fig. 3(b), it is clear that the point where the DW sits is the minimum of DW energy. At the sides of the pinning site, the effective magnetoelastic field—proportional to $\frac{d}{dx}(\varepsilon_{xx} - \varepsilon_{yy})$ according to Eq. (2)—is non-zero and opposite to the applied external field. This equivalent force prevents the DW to move forward unless the external applied field is increased.

For the Mumax[41] micromagnetic simulations, a wire of 800 nm width has been considered. The magnetization has been initialized in the system with a DW on the left side of the strained area, and then a magnetic field has been applied. Multiple dynamic simulations have been performed at different values of external magnetic field, and the results are summarized in Fig. 3(f). As can be seen, the averaged magnetization along the x direction (proportional to the DW position) coincides with the strained area (state I) for external fields $B_{ext} < B_{dep}$. When the applied magnetic field is increased above B_{dep}, the domain wall is free to propagate and reaches the right end of the wire (state II). For comparison, the experimental values for the DW position as a function of B_{ext} are reported in Fig. 3(f) for a 800 nm width $Co_{40}Fe_{40}B_{20}$ wire. The pinning position (where $\varepsilon_{xx} - \varepsilon_{yy} \neq 0$) coincides, and discrepancies between the simulations and experiments for the value of B_{dep} can be due to thermally activated depinning events that are not fully captured by micromagnetic simulations.

The ability to adjust the maximum value of the strain, and thus the value of the depinning field, by changing the aperture design—as shown in Fig. 3(e)—allows for the realization of a nonvolatile magnetic field sensor capable of detecting discrete values of magnetic fields or current peaks from wires or coils in the sensor proximity. Previous work[17] suggested similar concepts; however, the one proposed here does not require sub 100 nm lithography resolution for the notches.

The conceptualization of the peak-field sensor is presented in Fig. 4. The device comprises of a magnetic nanowire for DWs propagation with a number of pinning sites along it. As shown in Figs. 4(a) and 4(b), if the spacing between the SiN openings—acting as pinning sites—decreases, the strain magnitude is increased progressively. According to Fig. 3(e), the depinning field B_{dep} will increase going

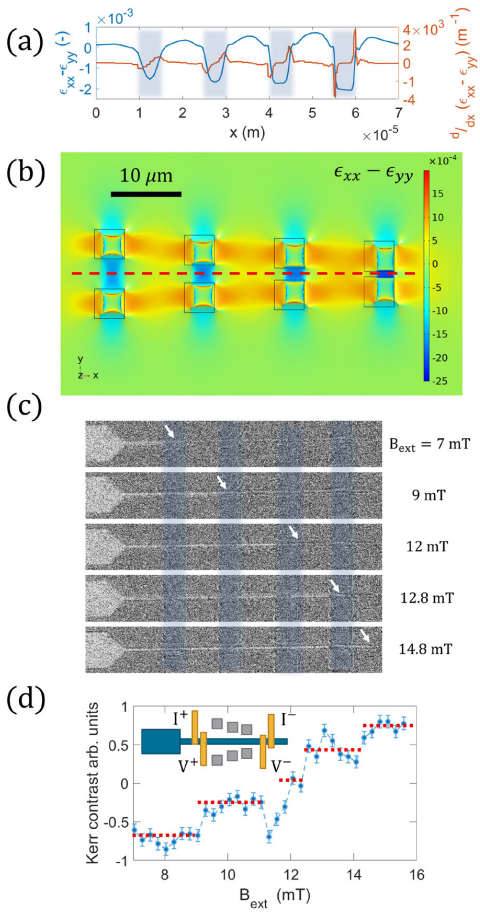

FIG. 4. (a) surface strain and strain gradient along the racetrack path, which is highlighted with a dashed line in (b) calculated with FEM. (c) MOKE images of the DW position (white arrow) in the device for different magnetic field steps. (d) Magnetic contrast along the racetrack obtained with Kerr microscopy averaging five repeated measurements. The sample is made of $Co_{70}Fe_{30}$, and the width of the wire is 500 nm. The inset shows a possible contacts configuration for resistivity measurements of the DW position.

from left to right. The device considered here presents four pair of openings and is therefore able to identify four discrete levels of external magnetic fields.

The proof of concept of the realized device is presented in Figs. 4(c) and 4(d). We consider, in this case, a magnetic wire of 500 nm width and realized with a $Co_{70}Fe_{30}$ magnetic layer. The shape of the openings is 5×5 μm^2, and the distance between the pairs is in the order of 5, 3, 2, and 1 μm, as shown in Fig. 4(b).

The device is initialized with large, negative magnetic field in the x direction creating a uniform magnetic state. After that, the positive magnetic field is gradually increased, while the magnetic state in the wire is monitored using Kerr microscopy. The magnetic contrast in Fig. 4(d) shows how the magnetization has well defined discrete levels as B_{ext} is increased. This occurs because a DW propagating into the nanowire occupies only discrete positions along x, as shown in Fig. 4(c) in the strained area between the openings. The number of detectable magnetic field steps can be increased by realizing more openings along the racetrack. The position of the DW in the magnetic channel (output) will indicate the maximum field (input) that the device has seen after initialization. The magnetic state is measured in Fig. 4(d) with optical methods; however, electrical readout of the DW position is possible using, e.g., giant magnetoresistive effect (GMR)[9] and two electrical contacts at the extremity of the magnetic channel. This sensing solution is particularly suitable for hardly accessible measurement environments and energy efficient devices as electrical power is required only for readout and initialization. As an example, the sensor could measure the maximum magnetic field that a medical implant has experienced.

In summary, in this work, we propose and validate a method for generating a local strain on a rigid substrate that is compatible with standard CMOS technologies. The intrinsic stress that occurs at the substrate/layer interface during SiN deposition can be modified when selected regions of the passivation layer are removed by etching. The strain is only modified near the removed material, as shown by FEM simulations. Using *in situ* measurements of the magnetoelastic anisotropy, we experimentally determine the magnitude of the uniaxial strain up to 0.05(1)%. The magnitude and the gradient of the in-plane strain can be tuned depending on the geometry and position of the openings in the stress-generating layer. We validate the use of the above-mentioned strain gradients for the manipulation of magnetic domain walls in spintronic devices by exploiting magnetoelastic coupling in magnetostrictive materials. Using Kerr microscopy, we experimentally show how the magnetoelastic energy landscape enables the creation of engineered pinning sites, which represent local energy minima for in-plane vortex walls. We report substantial pinning fields of up to 15 mT and support our experimental findings with micromagnetic simulations and 1D model calculations using a realistic strain profile. This provides the opportunity to realize an alternative generation of DW-based devices with technology compatible with wafer-level production, and an example of a discrete magnetic field or current sensor using imprinted strain gradients is demonstrated.

See the supplementary material for details about the material parameters used, the finite-element-method, micromagnetic simulations, and the anisotropy measurements.

This project has received funding from the European Union's Horizon 2020 Research and Innovation Program under the Marie Skłodowska-Curie Grant Agreement No. 860060 "Magnetism and the effect of Electric Field" (MagnEFi), the Deutsche Forschungsgemeinschaft (DFG, German Research Foundation)—TRR 173-268565370 (Project Nos. A01 and B02), the DFG Funded Collaborative Research Center (CRC)1261/project A10, and the Austrian Research Promotion Agency (FFG). The work by L. L. Diaz and E. Martinez was partially supported via Project No.

PID2020117024GB-C41 funded by Ministerio de Ciencia e Innovacion from the Spanish Government and from Consejeria de Educacion of Junta de Castilla y León via Project No. SA114P20. The authors also acknowledge support by the chip production facilities of Sensitec GmbH (Mainz, DE), where a part of this work was carried out, and the Max Planck Graduate Centre with Johannes Gutenberg University.

AUTHOR DECLARATIONS

Conflict of Interest

The authors have no conflicts to disclose.

Author Contributions

Giovanni Masciocchi: Conceptualization (equal); Data curation (equal); Formal analysis (equal); Investigation (equal); Writing – original draft (equal); Writing – review & editing (equal). **Mathias Kläui:** Conceptualization (equal); Funding acquisition (equal); Project administration (equal); Resources (equal); Supervision (equal); Validation (equal); Writing – original draft (equal); Writing – review & editing (equal). **Mouad Fattouhi:** Conceptualization (equal); Data curation (equal); Formal analysis (equal); Investigation (equal); Validation (equal); Writing – original draft (lead); Writing – review & editing (equal). **Elizaveta Spetzler:** Formal analysis (supporting); Investigation (equal); Software (equal); Writing – review & editing (equal). **Maria-Andromachi Syskaki:** Formal analysis (supporting); Investigation (equal); Software (equal); Validation (equal); Writing – review & editing (equal). **Ronald Lehndorff:** Conceptualization (equal); Investigation (equal). **Eduardo Martinez:** Conceptualization (equal); Data curation (equal); Formal analysis (equal); Writing – review & editing (equal). **Jeffrey McCord:** Data curation (equal); Formal analysis (equal); Methodology (equal); Supervision (equal); Writing – review & editing (equal). **Luis Lopez-Diaz:** Conceptualization (equal); Formal analysis (equal); Methodology (equal); Supervision (equal); Writing – review & editing (equal). **Andreas Kehlberger:** Conceptualization (equal); Formal analysis (equal); Supervision (equal); Validation (equal); Writing – original draft (equal); Writing – review & editing (equal).

DATA AVAILABILITY

The data that support the findings of this study are available from the corresponding author upon reasonable request.

REFERENCES

[1]S. Manipatruni, D. E. Nikonov, and I. A. Young, "Beyond CMOS computing with spin and polarization," Nat. Phys. **14**, 338–343 (2018).
[2]T. Ono, H. Miyajima, K. Shigeto, K. Mibu, N. Hosoito, and T. Shinjo, "Propagation of a magnetic domain wall in a submicrometer magnetic wire," Science **284**, 468–470 (1999).
[3]D. Atkinson, D. A. Allwood, G. Xiong, M. D. Cooke, C. C. Faulkner, and R. P. Cowburn, "Magnetic domain-wall dynamics in a submicrometre ferromagnetic structure," Nat. Mater. **2**, 85–87 (2003).
[4]M. Hayashi, L. Thomas, R. Moriya, C. Rettner, and S. S. Parkin, "Current-controlled magnetic domain-wall nanowire shift register," Science **320**, 209–211 (2008).
[5]D. Kumar, T. Jin, R. Sbiaa, M. Kläui, S. Bedanta, S. Fukami, D. Ravelosona, S.-H. Yang, X. Liu, and S. Piramanayagam, "Domain wall memory: Physics, materials, and devices," Phys. Rep. **958**, 1–35 (2022).
[6]J. Franken, H. Swagten, and B. Koopmans, "Shift registers based on magnetic domain wall ratchets with perpendicular anisotropy," Nat. Nanotechnol. **7**, 499–503 (2012).
[7]Z. Luo, A. Hrabec, T. P. Dao, G. Sala, S. Finizio, J. Feng, S. Mayr, J. Raabe, P. Gambardella, and L. J. Heyderman, "Current-driven magnetic domain-wall logic," Nature **579**, 214–218 (2020).
[8]X. Zhang, N. Vernier, Z. Cao, Q. Leng, A. Cao, D. Ravelosona, and W. Zhao, "Magnetoresistive sensors based on the elasticity of domain walls," Nanotechnology **29**, 365502 (2018).
[9]M. Diegel, S. Glathe, R. Mattheis, M. Scherzinger, and E. Halder, "A new four bit magnetic domain wall based multiturn counter," IEEE Trans. Magn. **45**, 3792–3795 (2009).
[10]M. A. Khan, J. Sun, B. Li, A. Przybysz, and J. Kosel, "Magnetic sensors-A review and recent technologies," Eng. Res. Express **3**, 022005 (2021).
[11]B. Borie, J. Wahrhusen, H. Grimm, and M. Kläui, "Geometrically enhanced closed-loop multi-turn sensor devices that enable reliable magnetic domain wall motion," Appl. Phys. Lett. **111**, 242402 (2017).
[12]M. Alamdar, T. Leonard, C. Cui, B. P. Rimal, L. Xue, O. G. Akinola, T. Patrick Xiao, J. S. Friedman, C. H. Bennett, M. J. Marinella *et al.*, "Domain wall-magnetic tunnel junction spin–orbit torque devices and circuits for in-memory computing," Appl. Phys. Lett. **118**, 112401 (2021).
[13]K. Yue, Y. Liu, R. K. Lake, and A. C. Parker, "A brain-plausible neuromorphic on-the-fly learning system implemented with magnetic domain wall analog memristors," Sci. Adv. **5**, eaau8170 (2019).
[14]O. Boulle, G. Malinowski, and M. Kläui, "Current-induced domain wall motion in nanoscale ferromagnetic elements," Mater. Sci. Eng.: R: Rep. **72**, 159–187 (2011).
[15]K. A. Omari, T. J. Broomhall, R. W. Dawidek, D. A. Allwood, R. C. Bradley, J. M. Wood, P. W. Fry, M. C. Rosamond, E. H. Linfield, M.-Y. Im *et al.*, "Toward chirality-encoded domain wall logic," Adv. Funct. Mater. **29**, 1807282 (2019).
[16]D.-S. Shiu, K.-F. Lai, Y.-Y. Liu, Y.-T. Li, Z.-E. Gao, Y.-M. Kao, J.-C. Wu, and L. Horng, "Depinning behavior of the vortex domain wall at the asymmetric triangular notch in permalloy wires," J. Phys. Commun. **5**, 075014 (2021).
[17]M. Al Bahri, B. Borie, T. Jin, R. Sbiaa, M. Kläui, and S. Piramanayagam, "Staggered magnetic nanowire devices for effective domain-wall pinning in racetrack memory," Phys. Rev. Appl. **11**, 024023 (2019).
[18]M. Fattouhi, F. Garcia-Sanchez, R. Yanes, V. Raposo, E. Martinez, and L. Lopez-Diaz, "Absence of Walker breakdown in the dynamics of chiral Neel domain walls driven by in-plane strain gradients," Phys. Rev. Appl. **18**, 044023 (2022).
[19]G. Masciocchi, M. Fattouhi, A. Kehlberger, L. Lopez-Diaz, M.-A. Syskaki, and M. Kläui, "Strain-controlled domain wall injection into nanowires for sensor applications," J. Appl. Phys. **130**, 183903 (2021).
[20]N. Lei, T. Devolder, G. Agnus, P. Aubert, L. Daniel, J.-V. Kim, W. Zhao, T. Trypiniotis, R. P. Cowburn, C. Chappert *et al.*, "Strain-controlled magnetic domain wall propagation in hybrid piezoelectric/ferromagnetic structures," Nat. Commun. **4**, 1378 (2013).
[21]H. Zhou, S. Shi, D. Nian, S. Cui, J. Luo, Y. Qiu, H. Yang, M. Zhu, and G. Yu, "Voltage control of magnetic domain wall injection into strain-mediated multiferroic heterostructures," Nanoscale **12**, 14479–14486 (2020).
[22]J.-M. Hu, T. Yang, K. Momeni, X. Cheng, L. Chen, S. Lei, S. Zhang, S. Trolier-McKinstry, V. Gopalan, G. P. Carman *et al.*, "Fast magnetic domain-wall motion in a ring-shaped nanowire driven by a voltage," Nano Lett. **16**, 2341–2348 (2016).
[23]J. Dean, M. Bryan, T. Schrefl, and D. Allwood, "Stress-based control of magnetic nanowire domain walls in artificial multiferroic systems," J. Appl. Phys. **109**, 023915 (2011).
[24]A. Barra, A. Ross, O. Gomonay, L. Baldrati, A. Chavez, R. Lebrun, J. Schneider, P. Shirazi, Q. Wang, J. Sinova *et al.*, "Effective strain manipulation of the antiferromagnetic state of polycrystalline NiO," Appl. Phys. Lett. **118**, 172408 (2021).
[25]M. Chu, Y. Sun, U. Aghoram, and S. E. Thompson, "Strain: A solution for higher carrier mobility in nanoscale MOSFETs," Annu. Rev. Mater. Res. **39**, 203–229 (2009).
[26]J. L. Doherty, S. G. Noyce, Z. Cheng, H. Abuzaid, and A. D. Franklin, "Capping layers to improve the electrical stress stability of MoS_2 transistors," ACS Appl. Mater. Interfaces **12**, 35698–35706 (2020).

[27]N. Martin, J. McCord, A. Gerber, T. Strache, T. Gemming, I. Mönch, N. Farag, R. Schäfer, J. Fassbender, E. Quandt *et al.*, "Local stress engineering of magnetic anisotropy in soft magnetic thin films," Appl. Phys. Lett. **94**, 062506 (2009).
[28]J. McCord, "Progress in magnetic domain observation by advanced magneto-optical microscopy," J. Phys. D: Appl. Phys. **48**, 333001 (2015).
[29]I. Soldatov and R. Schäfer, "Selective sensitivity in Kerr microscopy," Rev. Sci. Instrum. **88**, 073701 (2017).
[30]M. Ohring, "Mechanical properties of thin films," in *Materials Science of Thin Films: Deposition and Structure,* 2nd ed. (Academic Press, 2002), Chap. 12.
[31]M. R. Marks, Z. Hassan, and K. Y. Cheong, "Characterization methods for ultrathin wafer and die quality: A review," IEEE Trans. Compon., Packaging Manuf. Technol. **4**, 2042–2057 (2014).
[32]COMSOL AB, Stockholm, Sweden, "COMSOL Multiphysics® v. 6.1," 2023.
[33]S. Finizio, M. Foerster, M. Buzzi, B. Krüger, M. Jourdan, C. A. Vaz, J. Hockel, T. Miyawaki, A. Tkach, S. Valencia *et al.*, "Magnetic anisotropy engineering in thin film Ni nanostructures by magnetoelastic coupling," Phys. Rev. Appl. **1**, 021001 (2014).
[34]G. Masciocchi, J. W. van der Jagt, M.-A. Syskaki, A. Lamperti, N. Wolff, A. Lotnyk, J. Langer, L. Kienle, G. Jakob, B. Borie *et al.*, "Control of magnetoelastic coupling in Ni/Fe multilayers using He^+ ion irradiation," Appl. Phys. Lett. **121**, 182401 (2022).
[35]J. McCord, "Irregular domain patterns in structured magnetic thick films," J. Appl. Phys. **95**, 6855–6857 (2004).
[36]N. O. Urs, I. Teliban, A. Piorra, R. Knöchel, E. Quandt, and J. McCord, "Origin of hysteretic magnetoelastic behavior in magnetoelectric 2–2 composites," Appl. Phys. Lett. **105**, 202406 (2014).
[37]K. Thórarinsdóttir, N. Strandqvist, V. Sigurjónsdóttir, E. Thorsteinsson, B. Hjörvarsson, and F. Magnus, "Finding order in disorder: Magnetic coupling distributions and competing anisotropies in an amorphous metal alloy," APL Mater. **10**, 041103 (2022).
[38]D. Wen, Z. Chen, W. Li, M. Qin, D. Chen, Z. Fan, M. Zeng, X. Lu, X. Gao, and J.-M. Liu, "Ultralow-loss domain wall motion driven by a magnetocrystalline anisotropy gradient in an antiferromagnetic nanowire," Phys. Rev. Res. **2**, 013166 (2020).
[39]M. Fattouhi, F. García-Sánchez, R. Yanes, V. Raposo, E. Martínez, and L. Lopez-Diaz, "Electric field control of the skyrmion hall effect in piezoelectric-magnetic devices," Phys. Rev. Appl. **16**, 044035 (2021).
[40]J. Franken, Y. Yin, A. Schellekens, A. van den Brink, H. Swagten, and B. Koopmans, "Voltage-gated pinning in a magnetic domain-wall conduit," Appl. Phys. Lett. **103**, 102411 (2013).
[41]A. Vansteenkiste, J. Leliaert, M. Dvornik, M. Helsen, F. Garcia-Sanchez, and B. van Waeyenberge, "The design and verification of MuMax3," AIP Adv. **4**, 107133 (2014).

Bibliography

[1] Markets and Markets. Magnetic Sensors market - Global forecasts, 2023.

[2] Mohammed Asadullah Khan, Jian Sun, Bodong Li, Alexander Przybysz, and Jürgen Kosel. Magnetic sensors-a review and recent technologies. *Engineering Research Express*, 3(2):022005, 2021.

[3] James Lenz and S Edelstein. Magnetic sensors and their applications. *IEEE Sensors journal*, 6(3):631–649, 2006.

[4] T McGuire and RL Potter. Anisotropic magnetoresistance in ferromagnetic 3d alloys. *IEEE Transactions on Magnetics*, 11(4):1018–1038, 1975.

[5] Ana V Silva, Diana C Leitao, Joao Valadeiro, José Amaral, Paulo P Freitas, and Susana Cardoso. Linearization strategies for high sensitivity magnetoresistive sensors. *The European Physical Journal Applied Physics*, 72(1):10601, 2015.

[6] Grünberg Binasch, Peter Grünberg, F Saurenbach, and W Zinn. Enhanced magnetoresistance in layered magnetic structures with antiferromagnetic interlayer exchange. *Physical review B*, 39(7):4828, 1989.

[7] Mario Norberto Baibich, Jean Marc Broto, Albert Fert, F Nguyen Van Dau, Frédéric Petroff, P Etienne, G Creuzet, A Friederich, and J Chazelas. Giant magnetoresistance of (001) Fe/(001) Cr magnetic superlattices. *Physical review letters*, 61(21):2472, 1988.

[8] N. Smith, A.M. Zeltser, D.L. Yang, and P.V. Koeppe. Very high sensitivity gmr spin-valve magnetometer. *IEEE Transactions on Magnetics*, 33(5):3385–3387, 1997.

[9] Michel Julliere. Tunneling between ferromagnetic films. *Physics letters A*, 54(3):225–226, 1975.

[10] Thomas Scheike, Zhenchao Wen, Hiroaki Sukegawa, and Seiji Mitani. 631% room temperature tunnel magnetoresistance with large oscillation effect in CoFe/MgO/CoFe (001) junctions. *Applied Physics Letters*, 122(11):112404, 2023.

[11] Shaohua Yan, Zitong Zhou, Yaodi Yang, Qunwen Leng, and Weisheng Zhao. Developments and applications of tunneling magnetoresistance sensors. *Tsinghua Science and Technology*, 27(3):443–454, 2021.

[12] Marco Diegel, Sascha Glathe, Roland Mattheis, Manfred Scherzinger, and Ernst Halder. A new four bit magnetic domain wall based multiturn counter. *IEEE Transactions on Magnetics*, 45(10):3792–3795, 2009.

[13] H Corte-León, P Krzysteczko, HW Schumacher, Alessandra Manzin, D Cox, V Antonov, and O Kazakova. Magnetic bead detection using domain wall-based nanosensor. *Journal of Applied Physics*, 117(17):17E313, 2015.

[14] MA Bashir, MT Bryan, DA Allwood, T Schrefl, JS Claydon, G Burnell, and CH Marrows. Remote domain wall chirality measurement via stray field detection. *Journal of Applied Physics*, 110(12):123912, 2011.

[15] Lisa Jogschies, Daniel Klaas, Rahel Kruppe, Johannes Rittinger, Piriya Taptimthong, Anja Wienecke, Lutz Rissing, and Marc Christopher Wurz. Recent developments of magnetoresistive sensors for industrial applications. *Sensors*, 15(11):28665–28689, 2015.

[16] Clifton Dey, Parsa Yari, and Kai Wu. Recent advances in magnetoresistance biosensors: a short review. *Nano Futures*, 2023.

[17] Sebastian Fischer. *Einfluss der Aufbau-und Verbindungstechnik auf die funktionalen Eigenschaften thermomechanisch belasteter Sensoren*. Der Andere Verlag, 2006.

[18] Kailun Yao, Hiroshi Yano, and Noriyuki Iwamuro. Investigations of short-circuit failure in double trench SiC MOSFETs through three-dimensional electro-thermal-mechanical stress analysis. *Microelectronics Reliability*, 122:114163, 2021.

[19] Michael Melzer, Martin Kaltenbrunner, Denys Makarov, Dmitriy Karnaushenko, Daniil Karnaushenko, Tsuyoshi Sekitani, Takao Someya, and Oliver G Schmidt. Imperceptible magnetoelectronics. *Nature communications*, 6(1):6080, 2015.

[20] Chengde Gao, Zihao Zeng, Shuping Peng, and Cijun Shuai. Magnetostrictive alloys: Promising materials for biomedical applications. *Bioactive Materials*, 8:177–195, 2022.

[21] Denys Makarov and Denis D Sheka. *Curvilinear Micromagnetism: From Fundamentals to Applications*, volume 146. Springer Nature, 2022.

[22] Hariharan Nhalil, Daniel Lahav, Moty Schultz, Shai Amrusi, Asaf Grosz, and Lior Klein. Flexible planar Hall effect sensor with sub-200 pT resolution. *Applied Physics Letters*, 123(2):024102, 07 2023.

[23] Pavlo Makushko, Eduardo Sergio Oliveros Mata, Gilbert Santiago Cañón Bermúdez, Mariam Hassan, Sara Laureti, Christian Rinaldi, Federico Fagiani, Gianni Barucca, Nataliia Schmidt, Yevhen Zabila, et al. Flexible magnetoreceptor with tunable intrinsic logic for on-skin touchless human-machine interfaces. *Advanced Functional Materials*, 31(25):2101089, 2021.

[24] Daniil Karnaushenko, Denys Makarov, Max Stöber, Dmitriy D Karnaushenko, Stefan Baunack, and Oliver G Schmidt. High-performance magnetic sensorics for printable and flexible electronics. *Advanced Materials*, 27(5):880–885, 2015.

[25] Selma Amara, Gallo A Torres Sevilla, Mayyada Hawsawi, Yousof Mashraei, Hanan Mohammed, Melvin E Cruz, Yurii P Ivanov, Samridh Jaiswal, Gerhard Jakob, Mathias Kläui, et al. High-performance flexible magnetic tunnel junctions for smart miniaturized instruments. *Advanced Engineering Materials*, 20(10):1800471, 2018.

[26] JH Van Vleck. The classical theory of magnetic susceptibilities. *The Theory of Electric and Magnetic Susceptibilities; Oxford University Press: London, UK*, pages 91–94, 1932.

[27] Stephen Blundell. *Magnetism in condensed matter*. American Association of Physics Teachers, 2003.

[28] Ralph Skomski. *Simple models of magnetism*. Oxford University Press on Demand, 2008.

[29] John MD Coey. *Magnetism and magnetic materials*. Cambridge university press, 2010.

[30] Tôru Moriya. Anisotropic superexchange interaction and weak ferromagnetism. *Physical review*, 120(1):91, 1960.

[31] Igor Dzyaloshinsky. A thermodynamic theory of "weak" ferromagnetism of antiferromagnetics. *Journal of physics and chemistry of solids*, 4(4):241–255, 1958.

[32] Edmund Clifton Stoner. Collective electron ferromagnetism. *Proceedings of the Royal Society of London. Series A. Mathematical and Physical Sciences*, 165(922):372–414, 1938.

[33] Teruya Shinjo. *Nanomagnetism and spintronics*. Elsevier, 2013.

[34] Paul Drude. Zur elektronentheorie der metalle. *Annalen der physik*, 306(3):566–613, 1900.

[35] LALE Landau and Evgeny Lifshitz. On the theory of the dispersion of magnetic permeability in ferromagnetic bodies. In *Perspectives in Theoretical Physics*, pages 51–65. Elsevier, 1992.

[36] Alex Hubert and Rudolf Schäfer. *Magnetic domains: the analysis of magnetic microstructures*. Springer Science & Business Media, 2008.

[37] MT Johnson, R Jungblut, PJ Kelly, and FJA Den Broeder. Perpendicular magnetic anisotropy of multilayers: recent insights. *Journal of magnetism and magnetic materials*, 148(1-2):118–124, 1995.

[38] RA Rytov and NA Usov. A shape visualization of a magnetic anisotropy energy density of single-domain magnetic nanoparticles. *Sci. Vis.*, 12(3):26–37, 2020.

[39] PF Carcia. Perpendicular magnetic anisotropy in Pd/Co and Pt/Co thin-film layered structures. *Journal of applied physics*, 63(10):5066–5073, 1988.

[40] J Wu, J Choi, C Won, YZ Wu, A Scholl, A Doran, Chanyong Hwang, and ZQ Qiu. Stripe-to-bubble transition of magnetic domains at the spin reorientation of (Fe/Ni)/Cu/Ni/Cu (001). *Physical Review B*, 79(1):014429, 2009.

[41] Edmund Clifton Stoner and EP Wohlfarth. A mechanism of magnetic hysteresis in heterogeneous alloys. *Philosophical Transactions of the Royal Society of London. Series A, Mathematical and Physical Sciences*, 240(826):599–642, 1948.

[42] Robert W Balluffi. *Introduction to elasticity theory for crystal defects*. World Scientific Publishing Company, 2016.

[43] Charles Kittel. Physical theory of ferromagnetic domains. *Reviews of modern Physics*, 21(4):541, 1949.

[44] Sōshin Chikazumi and Chad D Graham. *Physics of ferromagnetism*. Number 94. Oxford university press, 1997.

[45] Friederike Junginger, Mathias Kläui, Dirk Backes, Stephen Krzyk, Ulrich Rüdiger, Takeshi Kasama, Rafal E Dunin-Borkowski, J-M Feinberg, Ralph J Harrison, and Laura J Heyderman. Quantitative determination of vortex core dimensions in head-to-head domain walls using off-axis electron holography. *Applied Physics Letters*, 92(11):112502, 2008.

[46] Dieter Suess, Anton Bachleitner-Hofmann, Armin Satz, Herbert Weitensfelder, Christoph Vogler, Florian Bruckner, Claas Abert, Klemens Prügl, Jürgen Zimmer, Christian Huber, et al. Topologically protected vortex structures for low-noise magnetic sensors with high linear range. *Nature Electronics*, 1(6):362–370, 2018.

[47] Naoto Nagaosa and Yoshinori Tokura. Topological properties and dynamics of magnetic skyrmions. *Nature nanotechnology*, 8(12):899–911, 2013.

[48] Jiadong Zang, Vincent Cros, and Axel Hoffmann. *Topology in magnetism*, volume 192. Springer, 2018.

[49] O Boulle, G Malinowski, and Mathias Kläui. Current-induced domain wall motion in nanoscale ferromagnetic elements. *Materials Science and Engineering: R: Reports*, 72(9):159–187, 2011.

[50] June-Seo Kim, Mohamad-Assaad Mawass, André Bisig, Benjamin Krüger, Robert M Reeve, Tomek Schulz, Felix Büttner, Jungbum Yoon, Chun-Yeol You, Markus Weigand, et al. Synchronous precessional motion of multiple domain walls in a ferromagnetic nanowire by perpendicular field pulses. *Nature communications*, 5(1):3429, 2014.

[51] Oleg Tchernyshyov and Gia-Wei Chern. Fractional vortices and composite domain walls in flat nanomagnets. *Physical review letters*, 95(19):197204, 2005.

[52] MT Bryan, S Bance, J Dean, T Schrefl, and DA Allwood. Transverse and vortex domain wall structure in magnetic nanowires with uniaxial in-plane anisotropy. *Journal of Physics: Condensed Matter*, 24(2):024205, 2011.

[53] Aakash Pushp, Timothy Phung, Charles Rettner, Brian P Hughes, See-Hun Yang, Luc Thomas, and Stuart SP Parkin. Domain wall trajectory determined by its fractional topological edge defects. *Nature Physics*, 9(8):505–511, 2013.

[54] D Atkinson, DS Eastwood, and LK Bogart. Controlling domain wall pinning in planar nanowires by selecting domain wall type and its application in a memory concept. *Applied Physics Letters*, 92(2):022510, 2008.

[55] KA Omari and TJ Hayward. Chirality-based vortex domain-wall logic gates. *Physical Review Applied*, 2(4):044001, 2014.

[56] Daniel C Ralph and Mark D Stiles. Spin transfer torques. *Journal of Magnetism and Magnetic Materials*, 320(7):1190–1216, 2008.

[57] Donald G Porter and Michael J Donahue. Velocity of transverse domain wall motion along thin, narrow strips. *Journal of Applied Physics*, 95(11):6729–6731, 2004.

[58] T Suzuki, S Fukami, N Ohshima, K Nagahara, and N Ishiwata. Analysis of current-driven domain wall motion from pinning sites in nanostrips with perpendicular magnetic anisotropy. *Journal of Applied Physics*, 103(11):113913, 2008.

[59] Norman L Schryer and Laurence R Walker. The motion of 180 domain walls in uniform dc magnetic fields. *Journal of Applied Physics*, 45(12):5406–5421, 1974.

[60] HY Yuan and Xiang Rong Wang. Birth, growth and death of an antivortex during the propagation of a transverse domain wall in magnetic nanostrips. *Journal of magnetism and magnetic materials*, 368:70–74, 2014.

[61] Benjamin Borie, Jürgen Wahrhusen, Hubert Grimm, and Mathias Kläui. Geometrically enhanced closed-loop multi-turn sensor devices that enable reliable magnetic domain wall motion. *Applied Physics Letters*, 111(24):242402, 2017.

[62] Benjamin Borie, Michele Voto, Luis Lopez-Diaz, Hubert Grimm, Marco Diegel, Mathias Kläui, and Roland Mattheis. Reliable propagation of magnetic domain walls in cross structures for advanced multiturn sensors. *Physical Review Applied*, 8(4):044004, 2017.

[63] Olga Lozhkina, Robert M Reeve, Robert Frömter, and Mathias Kläui. Control of the walker breakdown by periodical magnetic wire-width modulation. *Journal of Applied Physics*, 131(23):233902, 2022.

[64] Min Xu, Runshui Li, Dexiang Meng, Jinyu Zhang, and Mingming Zhang. Suppression of walker breakdown in nanowires with periodic holes. *Journal of Magnetism and Magnetic Materials*, 532:167988, 2021.

[65] Min Xu, Runshui Li, Jinyu Zhang, and Dexiang Meng. Effect of a local temperature region on the suppression of walker breakdown in a permalloy nanowire. *Solid State Communications*, 329:114259, 2021.

[66] Mouad Fattouhi, Felipe Garcia-Sanchez, Rocio Yanes, Victor Raposo, Eduardo Martinez, and Luis Lopez-Diaz. Absence of walker breakdown in the dynamics of chiral neel domain walls driven by in-plane strain gradients. *Physical Review Applied*, 18(4):044023, 2022.

[67] AP Malozemoff and John C Slonczewski. *Magnetic domain walls in bubble materials: advances in materials and device research*, volume 1. Academic press, 2016.

[68] Eduardo Martinez, Satoru Emori, Noel Perez, Luis Torres, and Geoffrey SD Beach. Current-driven dynamics of Dzyaloshinskii domain walls in the presence of in-plane fields: Full micromagnetic and one-dimensional analysis. *Journal of Applied Physics*, 115(21):213909, 2014.

[69] E Martinez, L Lopez-Diaz, L Torres, C Tristan, and O Alejos. Thermal effects in domain wall motion: Micromagnetic simulations and analytical model. *Physical Review B*, 75(17):174409, 2007.

[70] Eduardo Martinez, Luis Lopez-Diaz, Oscar Alejos, Luis Torres, and Mario Carpentieri. Domain-wall dynamics driven by short pulses along thin ferromagnetic strips: Micromagnetic simulations and analytical description. *Physical Review B*, 79(9):094430, 2009.

[71] CP Kuo, SK Vong, RM Cohen, and GB Stringfellow. Effect of mismatch strain on band gap in iii-v semiconductors. *Journal of Applied Physics*, 57(12):5428–5432, 1985.

[72] H Sato and M Naito. Increase in the superconducting transition temperature by anisotropic strain effect in (001) la1. 85sr0. 15cuo4 thin films on lasralo4 substrates. *Physica C: Superconductivity*, 274(3-4):221–226, 1997.

[73] Simone Finizio, Michael Foerster, M Buzzi, Benjamin Krüger, Martin Jourdan, Carlos AF Vaz, J Hockel, T Miyawaki, Alexander Tkach, S Valencia, et al. Magnetic anisotropy engineering in thin film Ni nanostructures by magnetoelastic coupling. *Physical Review Applied*, 1(2):021001, 2014.

[74] Donald P Seraphim, Peter A Engel, Ronald Lasky, Che-Yu Li, et al. Principles of electronic packaging. 1989.

[75] RFS Hearmon. The elastic constants of anisotropic materials. *Reviews of modern physics*, 18(3):409, 1946.

[76] Milton Ohring. The materials science of thin films. *Appl. Opt*, 31(34):7162, 1992.

[77] Michael Raj Marks, Zainuriah Hassan, and Kuan Yew Cheong. Characterization methods for ultrathin wafer and die quality: A review. *IEEE Transactions on components, packaging and manufacturing technology*, 4(12):2042–2057, 2014.

[78] George Gerald Stoney. The tension of metallic films deposited by electrolysis. *Proceedings of the Royal Society of London. Series A, Containing Papers of a Mathematical and Physical Character*, 82(553):172–175, 1909.

[79] Dwight Viehland, Manfred Wuttig, Jeffrey McCord, and Eckhard Quandt. Magnetoelectric magnetic field sensors. *Mrs Bulletin*, 43(11):834–840, 2018.

[80] Xiangyu Gao, Jikun Yang, Jingen Wu, Xudong Xin, Zhanmiao Li, Xiaoting Yuan, Xinyi Shen, and Shuxiang Dong. Piezoelectric actuators and motors: materials, designs, and applications. *Advanced Materials Technologies*, 5(1):1900716, 2020.

[81] S Fusil, Vincent Garcia, A Barthélémy, and M Bibes. Magnetoelectric devices for spintronics. *Annual Review of Materials Research*, 44:91–116, 2014.

[82] RS Weis and TK Gaylord. Lithium niobate: Summary of physical properties and crystal structure. *Applied Physics A*, 37:191–203, 1985.

[83] RT Smith and FS Welsh. Temperature dependence of the elastic, piezoelectric, and dielectric constants of lithium tantalate and lithium niobate. *Journal of applied physics*, 42(6):2219–2230, 1971.

[84] AW Warner, M Onoe, and GA Coquin. Determination of elastic and piezoelectric constants for crystals in class (3 m). *The journal of the acoustical society of America*, 42(6):1223–1231, 1967.

[85] Tomoaki Yamada, Nobukazu Niizeki, and Hiroo Toyoda. Piezoelectric and elastic properties of lithium niobate single crystals. *Japanese journal of applied physics*, 6(2):151, 1967.

[86] Richard M White and Fred W Voltmer. Direct piezoelectric coupling to surface elastic waves. *Applied physics letters*, 7(12):314–316, 1965.

[87] Yuri V Gulyaev. Review of shear surface acoustic waves in solids. *IEEE transactions on ultrasonics, ferroelectrics, and frequency control*, 45(4):935–938, 1998.

[88] J Dean, MT Bryan, JD Cooper, A Virbule, JE Cunningham, and TJ Hayward. A sound idea: Manipulating domain walls in magnetic nanowires using surface acoustic waves. *Applied Physics Letters*, 107(14):142405, 2015.

[89] Christie RK Marrian and Donald M Tennant. Nanofabrication. *Journal of Vacuum Science & Technology A: Vacuum, Surfaces, and Films*, 21(5):S207–S215, 2003.

[90] Donald M Mattox. *Handbook of physical vapor deposition (PVD) processing*. William Andrew, 2010.

[91] Singulus PVD system. `https://www.singulus.com/sputtering/`. Accessed: 2023-03-06.

[92] Olga Lozhkina, Fabian Kammerbauer, Maria-Andromachi Syskaki, Aravind Puthirath Balan, Pascal Krautscheid, Mehran Vafaee Khanjani, Jan Kubik, Stephen O'Brien, Robert M Reeve, Gerhard Jakob, et al. Tailoring magnetic properties and suppressing anisotropy in permalloy films by deposition in a rotating magnetic field. *Physical Review Applied*, 20(1):014021, 2023.

[93] Giovanni Masciocchi, Mouad Fattouhi, Andreas Kehlberger, Luis Lopez-Diaz, Maria-Andromachi Syskaki, and Mathias Kläui. Strain-controlled domain wall injection into nanowires for sensor applications. *Journal of Applied Physics*, 130(18):183903, 2021.

[94] Michael Wang. *Lithography*. BoD–Books on Demand, 2010.

[95] Daniel Bratton, Da Yang, Junyan Dai, and Christopher K Ober. Recent progress in high resolution lithography. *Polymers for Advanced Technologies*, 17(2):94–103, 2006.

[96] RFW Pease. Electron beam lithography. *Contemporary Physics*, 22(3):265–290, 1981.

[97] Christophe Vieu, F Carcenac, A Pepin, Y Chen, M Mejias, A Lebib, L Manin-Ferlazzo, L Couraud, and H Launois. Electron beam lithography: resolution limits and applications. *Applied surface science*, 164(1-4):111–117, 2000.

[98] T Devolder, I Barisic, S Eimer, K Garcia, J-P Adam, B Ockert, and D Ravelosona. Irradiation-induced tailoring of the magnetism of CoFeB/MgO ultrathin films. *Journal of applied Physics*, 113(20):203912, 2013.

[99] Giovanni Masciocchi, Johannes Wilhelmus van der Jagt, M-A Syskaki, Alessio Lamperti, Niklas Wolff, Andriy Lotnyk, Jürgen Langer, Lorenz Kienle, Gerhard Jakob, Benjamin Borie, et al. Control of magnetoelastic coupling in ni/fe multilayers using he+ ion irradiation. *Applied Physics Letters*, 121(18):182401, 2022.

[100] Jeffrey McCord, Ingolf Mönch, Jürgen Fassbender, Andreas Gerber, and Eckhard Quandt. Local setting of magnetic anisotropy in amorphous films by Co ion implantation. *Journal of Physics D: Applied Physics*, 42(5):055006, 2009.

[101] Young Min Lee, Jun Hayakawa, Shoji Ikeda, Fumihiro Matsukura, and Hideo Ohno. Giant tunnel magnetoresistance and high annealing stability in Co Fe B/ Mg O/ Co Fe B magnetic tunnel junctions with synthetic pinned layer. *Applied Physics Letters*, 89(4):042506, 2006.

[102] Jürgen Fassbender, Daphiné Ravelosona, and Y Samson. Tailoring magnetism by light-ion irradiation. *Journal of Physics D: Applied Physics*, 37(16):R179, 2004.

[103] OD Roshchupkina, T Strache, J McCord, A Mücklich, C Bähtz, and J Grenzer. Structural modifications of thin magnetic Permalloy films induced by ion implantation and thermal annealing: A comparison. *Acta materialia*, 74:278–284, 2014.

[104] Wolfhard Möller. Fundamentals of ion-solid interaction. a compact introduction. Technical report, Helmholtz-Zentrum Dresden-Rossendorf eV, 2017.

[105] Norbert Martin, Jeffrey McCord, Andreas Gerber, Thomas Strache, Thomas Gemming, Ingolf Mönch, Nayel Farag, Rudolf Schäfer, Jürgen Fassbender, Eckhard Quandt, et al. Local stress engineering of magnetic anisotropy in soft magnetic thin films. *Applied Physics Letters*, 94(6):062506, 2009.

[106] GH Kinchin and RS Pease. The displacement of atoms in solids by radiation. *Reports on progress in physics*, 18(1):1, 1955.

[107] Wolfgang Voegeli, Karsten Albe, and Horst Hahn. Simulation of grain growth in nanocrystalline nickel induced by ion irradiation. *Nuclear Instruments and Methods in Physics Research Section B: Beam Interactions with Materials and Atoms*, 202:230–235, 2003.

[108] Robert C O'handley. *Modern magnetic materials: principles and applications*. Wiley, 2000.

[109] Sōshin Chikazumi. Ferromagnetic properties and superlattice formation of iron-nickel alloys (ii). *Journal of the Physical Society of Japan*, 5(5):333–338, 1950.

[110] Sōshin Chikazumi and Tatsurō Oomura. On the origin of magnetic anisotropy induced by magnetic annealing. *Journal of the Physical Society of Japan*, 10(10):842–849, 1955.

[111] MLM Lalieu. Femtomagnetism meets spintronics and magnonics. 2019.

[112] Umesh Tiwari, R Ghosh, and P Sen. Theory of magneto-optic kerr effects. *Physical Review B*, 49(3):2159, 1994.

[113] P Weinberger. John kerr and his effects found in 1877 and 1878. *Philosophical Magazine Letters*, 88(12):897–907, 2008.

[114] IV Soldatov and Rudolf Schäfer. Selective sensitivity in kerr microscopy. *Review of Scientific Instruments*, 88(7):073701, 2017.

[115] Jeffrey McCord. Progress in magnetic domain observation by advanced magneto-optical microscopy. *Journal of Physics D: Applied Physics*, 48(33):333001, 2015.

[116] Jian Wang, Shouxian She, and Sijiong Zhang. An improved helmholtz coil and analysis of its magnetic field homogeneity. *Review of scientific instruments*, 73(5):2175–2179, 2002.

[117] BH looper - SHB instruments. `https://www.shbinstruments.com/mesa`. Accessed: 2023-03-06.

[118] Bertram Eugene Warren. *X-ray Diffraction*. Courier Corporation, 1990.

[119] Mohsen Ahmadipour, Mohamad Johari Abu, Mohd Fariz Ab Rahman, Mohd Fadzil Ain, and Zainal Arifin Ahmad. Assessment of crystallite size and strain of $CaCu_3Ti_4O_{12}$ prepared via conventional solid-state reaction. *Micro & Nano Letters*, 11(3):147–150, 2016.

[120] A Khorsand Zak, WH Abd Majid, Majid Ebrahimizadeh Abrishami, and Ramin Yousefi. X-ray analysis of ZnO nanoparticles by Williamson-Hall and size-strain plot methods. *Solid State Sciences*, 13(1):251–256, 2011.

[121] VS Speriosu and Thad Vreeland Jr. X-ray rocking curve analysis of superlattices. *Journal of applied physics*, 56(6):1591–1600, 1984.

[122] V Holy, J Kubena, I Ohli, K Lischka, W Plotz, et al. X-ray reflection from rough layered systems. *Physical review B*, 47(23):15896, 1993.

[123] Rana NS Sodhi. Time-of-Flight Secondary Ion Mass Spectrometry (ToF-SIMS):—versatility in chemical and imaging surface analysis. *Analyst*, 129(6):483–487, 2004.

[124] Laura Thevenard, Ibrahima Sock Camara, J-Y Prieur, Pauline Rovillain, Aristide Lemaître, Catherine Gourdon, and J-Y Duquesne. Strong reduction of the coercivity by a surface acoustic wave in an out-of-plane magnetized epilayer. *Physical Review B*, 93(14):140405, 2016.

[125] Westin Edrington, Uday Singh, Maya Abo Dominguez, James Rehwaldt Alexander, Rabindra Nepal, and Shireen Adenwalla. Saw assisted domain wall motion in co/pt multilayers. *Applied Physics Letters*, 112(5):052402, 2018.

[126] E De Ranieri, PE Roy, D Fang, EK Vehsthedt, AC Irvine, D Heiss, A Casiraghi, RP Campion, BL Gallagher, T Jungwirth, et al. Piezoelectric control of the mobility of a domain wall driven by adiabatic and non-adiabatic torques. *Nature materials*, 12(9):808–814, 2013.

[127] Jintao Shuai, Mannan Ali, Luis Lopez-Diaz, John E Cunningham, and Thomas A Moore. Local anisotropy control of Pt/Co/Ir thin film with perpendicular magnetic anisotropy by surface acoustic waves. *Applied Physics Letters*, 120(25):252402, 2022.

[128] Arne Vansteenkiste and Ben Van de Wiele. Mumax: A new high-performance micromagnetic simulation tool. *Journal of Magnetism and Magnetic Materials*, 323(21):2585–2591, 2011.

[129] Arne Vansteenkiste, Jonathan Leliaert, Mykola Dvornik, Mathias Helsen, Felipe Garcia-Sanchez, and Bartel Van Waeyenberge. The design and verification of MuMax3. *AIP advances*, 4(10):107133, 2014.

[130] Frederic Vanderveken, Jeroen Mulkers, Jonathan Leliaert, Bartel Van Waeyenberge, Bart Sorée, Odysseas Zografos, Florin Ciubotaru, and Christoph Adelmann. Finite difference magnetoelastic simulator. *Open Research Europe*, 1(35):35, 2021.

[131] Gavin S. Abo, Yang-Ki Hong, Jihoon Park, Jaejin Lee, Woncheol Lee, and Byoung-Chul Choi. Definition of magnetic exchange length. *IEEE Transactions on Magnetics*, 49(8):4937–4939, 2013.

[132] CL Dennis, RP Borges, LD Buda, U Ebels, JF Gregg, M Hehn, E Jouguelet, K Ounadjela, I Petej, IL Prejbeanu, et al. The defining length scales of mesomagnetism: a review. *Journal of Physics: Condensed Matter*, 14(49):R1175, 2002.

[133] Shinya Ota, Akira Ando, and Daichi Chiba. A flexible giant magnetoresistive device for sensing strain direction. *Nature Electronics*, 1(2):124–129, 2018.

[134] H García-Miquel, D Barrera, Rafael Amat, GV Kurlyandskaya, and S Sales. Magnetic actuator based on giant magnetostrictive material Terfenol-D with strain and temperature monitoring using FBG optical sensor. *Measurement*, 80:201–206, 2016.

[135] Yasuhiro Nagai, Masakatsu Senda, and Tomoyuki Toshima. Properties of ion-beam-sputtered Ni/Fe artificial lattice film. *Journal of Applied Physics*, 63(4):1136–1140, 1988.

[136] Masakatsu Senda and Yasuhiro Nagai. Magnetic properties of Fe/Co, Fe/CoFe, and (Fe/Co)/SiO_2 multilayer films. *Journal of Applied Physics*, 65(8):3151–3156, 1989.

[137] S Rengarajan, EJ Yun, WS Kang, and RM Walser. Effect of intermixing on the magnetic properties of $Co_{50}Fe_{50}/Ni_{80}Fe_{20}$ multilayers. *Journal of Applied Physics*, 81(8):4761–4763, 1997.

[138] SU Jen and CC Lin. Magnetostriction and Young's modulus of $[Fe_{15}Ni_{85}/Fe_{25}Ni_{75}]$ multilayers. *Thin Solid Films*, 471(1-2):218–223, 2005.

[139] Mark CH De Jong, Mariëlle J Meijer, Juriaan Lucassen, Jos Van Liempt, Henk JM Swagten, Bert Koopmans, and Reinoud Lavrijsen. Local control of magnetic interface effects in chiral Ir/ Co/ Pt multilayers using Ga^+ ion irradiation. *Physical Review B*, 105(6):064429, 2022.

[140] L Herrera Diez, M Voto, A Casiraghi, M Belmeguenai, Y Roussigné, G Durin, A Lamperti, R Mantovan, V Sluka, V Jeudy, et al. Enhancement of the Dzyaloshinskii-Moriya interaction and domain wall velocity through interface intermixing in Ta/CoFeB/MgO. *Physical Review B*, 99(5):054431, 2019.

[141] Leopold Koch, Fabian Samad, Miriam Lenz, and Olav Hellwig. Manipulating the Energy Balance of Perpendicular-Anisotropy Synthetic Antiferromagnets by He^+-Ion Irradiation. *Physical Review Applied*, 13(2):024029, 2020.

[142] BD Terris, L Folks, D Weller, JEE Baglin, AJ Kellock, H Rothuizen, and P Vettiger. Ion-beam patterning of magnetic films using stencil masks. *Applied Physics Letters*, 75(3):403–405, 1999.

[143] J Juraszek, A Grenier, J Teillet, N Tiercelin, F Petit, J Ben Youssef, and M Toulemonde. Swift ion irradiation of magnetostrictive multilayers. *Nuclear Instruments and Methods in Physics Research Section B: Beam Interactions with Materials and Atoms*, 245(1):157–160, 2006.

[144] William F Cureton, Cameron L Tracy, and Maik Lang. Review of swift heavy ion irradiation effects in CeO_2. *Quantum Beam Science*, 5(2):19, 2021.

[145] W Brückner, S Baunack, M Hecker, J-I Mönch, L Van Loyen, and CM Schneider. Interdiffusion in nife/cu/nife trilayers: Possible failure mechanism for magnetoelectronic devices. *Applied Physics Letters*, 77(3):358–360, 2000.

[146] James F Ziegler, Matthias D Ziegler, and Jochen P Biersack. SRIM-the stopping and range of ions in matter (2010). *Nuclear Instruments and Methods in Physics Research Section B: Beam Interactions with Materials and Atoms*, 268(11-12):1818–1823, 2010.

[147] T Devolder, S Pizzini, J Vogel, H Bernas, C Chappert, V Mathet, and M Borowski. X-ray absorption analysis of sputter-grown Co/Pt stackings before and after helium irradiation. *The European Physical Journal B-Condensed Matter and Complex Systems*, 22(2):193–201, 2001.

[148] Matthew Weyland and David A Muller. Tuning the convergence angle for optimum stem performance. *arXiv preprint arXiv:2008.12870*, 2020.

[149] Steven R Spurgeon, Yingge Du, and Scott A Chambers. Measurement error in atomic-scale scanning transmission electron microscopy—energy-dispersive x-ray spectroscopy (stem-eds) mapping of a model oxide interface. *Microscopy and Microanalysis*, 23(3):513–517, 2017.

[150] Ping Lu, Jaime M Moya, Renliang Yuan, and Jian Min Zuo. Studies of x-ray localization and thickness dependence in atomic-scale elemental mapping by stem energy-dispersive x-ray spectroscopy using single-frame scanning method. *Ultramicroscopy*, 186:23–29, 2018.

[151] Alfred Benninghoven, FG Rudenauer, and Helmut W Werner. Secondary ion mass spectrometry: basic concepts, instrumental aspects, applications and trends. 1987.

[152] John C Vickerman and David Briggs. *ToF-SIMS: materials analysis by mass spectrometry*. IM publications, 2013.

[153] A Lamperti, E Cianci, O Salicio, L Lamagna, S Spiga, and M Fanciulli. Thermal stability of high-κ oxides on SiO_2/Si or $Si_xN_y/SiO_2/Si$ for charge-trapping nonvolatile memories. *Surface and interface analysis*, 45(1):390–393, 2013.

[154] R Lo Conte, E Martinez, A Hrabec, A Lamperti, T Schulz, L Nasi, L Lazzarini, R Mantovan, F Maccherozzi, SS Dhesi, et al. Role of B diffusion in the interfacial Dzyaloshinskii-Moriya interaction in $Ta/Co_{20}Fe_{60}B_{20}/MgO$ nanowires. *Physical Review B*, 91(1):014433, 2015.

[155] SK Srivastava, Ravi Kumar, A Gupta, RS Patel, AK Majumdar, and DK Avasthi. Swift heavy ion induced mixing in Fe/Ni multilayer. *Nuclear Instruments and Methods in Physics Research Section B: Beam Interactions with Materials and Atoms*, 243(2):304–312, 2006.

[156] Bernard Dennis Cullity and Chad D Graham. *Introduction to magnetic materials*. John Wiley & Sons, 2011.

[157] Alexandre Bur, Tao Wu, Joshua Hockel, Chin-Jui Hsu, Hyungsuk KD Kim, Tien-Kan Chung, Kin Wong, Kang L Wang, and Gregory P Carman. Strain-induced magnetization change in patterned ferromagnetic nickel nanostructures. *Journal of Applied Physics*, 109(12):123903, 2011.

[158] Richard M Bozorth. *Ferromagnetism, p. 263*. 1993.

[159] E Klokholm and JA Aboaf. The saturation magnetostriction of permalloy films. *Journal of Applied Physics*, 52(3):2474–2476, 1981.

[160] Jeffrey McCord. Irregular domain patterns in structured magnetic thick films. *Journal of applied physics*, 95(11):6855–6857, 2004.

[161] MP Hollingworth, MRJ Gibbs, and SJ Murdoch. Magnetostriction and surface roughness of ultrathin NiFe films deposited on SiO_2. *Journal of Applied Physics*, 94(11):7235–7239, 2003.

[162] C Favieres, J Vergara, and V Madurga. Interface effects on magnetostriction in pulsed laser deposited Co/Fe/Co cylindrical soft magnetic multilayers. *Journal of Physics D: Applied Physics*, 40(14):4101, 2007.

[163] SU Jen, TC Wu, CC Lin, and KH Chang. Anisotropic magnetoresistance and magnetostriction of $[Fe_{15}Ni_{85}/Fe_{25}Ni_{75}]$ and $[Co_{35}Ni_{65}/Fe_{25}Ni_{75}]$ multilayers. *Solid State Communications*, 132(3-4):259–262, 2004.

[164] Jack William Judy. Magnetic microactuators with polysilicon flexures. *Masters Report*, 1994.

[165] T Devolder, C Chappert, Y Chen, E Cambril, H Launois, HHFH Bernas, J Ferre, and JP Jamet. Patterning of planar magnetic nanostructures by ion irradiation. *Journal of Vacuum Science & Technology B: Microelectronics and Nanometer Structures Processing, Measurement, and Phenomena*, 17(6):3177–3181, 1999.

[166] Suhyeok An, Eunchong Baek, Jin-A Kim, Ki-Seung Lee, and Chun-Yeol You. Improved spin-orbit torque induced magnetization switching efficiency by helium ion irradiation. *Scientific reports*, 12(1):1–10, 2022.

[167] Hans T Nembach, Emilie Jué, Kay Poetzger, Juergen Fassbender, Thomas J Silva, and Justin M Shaw. Tuning of the Dzyaloshinskii-Moriya interaction by He^+ ion irradiation. *Journal of Applied Physics*, 131(14):143901, 2022.

[168] Lisa-Marie Kern, Bastian Pfau, Victor Deinhart, Michael Schneider, Christopher Klose, Kathinka Gerlinger, Steffen Wittrock, Dieter Engel, Ingo Will, Christian M Gunther, et al. Deterministic Generation and Guided Motion of Magnetic Skyrmions by Focused He^+-Ion Irradiation. *Nano Letters*, 2022.

[169] Mouad Fattouhi, Felipe García-Sánchez, Rocío Yanes, Víctor Raposo, Eduardo Martínez, and Luis Lopez-Diaz. Electric Field Control of the Skyrmion Hall Effect in Piezoelectric-Magnetic Devices. *Physical Review Applied*, 16(4):044035, 2021.

[170] Waldemar Kwiatkowski and Slawomir Tumanski. The permalloy magnetoresistive sensors-properties and applications. *Journal of Physics E: Scientific Instruments*, 19(7):502, 1986.

[171] JPJ Groenland, CJM Eijkel, JHJ Fluitman, and RM de Ridder. Permalloy thin-film magnetic sensors. *Sensors and Actuators A: Physical*, 30(1-2):89–100, 1992.

[172] Julia Trützschler, Kadir Sentosun, Manuel Langer, Ingolf Mönch, Roland Mattheis, Jürgen Fassbender, and Jeffrey McCord. Optimization of magneto-resistive response of ion-irradiated exchange biased films through zigzag arrangement of magnetization. *Journal of Applied Physics*, 115(10):103901, 2014.

[173] K-MH Lenssen, DJ Adelerhof, HJ Gassen, AET Kuiper, GHJ Somers, and JBAD Van Zon. Robust giant magnetoresistance sensors. *Sensors and Actuators A: Physical*, 85(1-3):1–8, 2000.

[174] Gilbert Santiago Cañón Bermúdez and Denys Makarov. Magnetosensitive E-Skins for interactive devices. *Advanced Functional Materials*, 31(39):2007788, 2021.

[175] Eduardo Sergio Oliveros Mata, Gilbert Santiago Cañón Bermúdez, Minjeong Ha, Tobias Kosub, Yevhen Zabila, Jürgen Fassbender, and Denys Makarov. Printable anisotropic magnetoresistance sensors for highly compliant electronics. *Applied Physics A*, 127(4):1–6, 2021.

[176] Michael Melzer, D Makarov, and OG Schmidt. A review on stretchable magnetic field sensorics. *Journal of Physics D: Applied Physics*, 53(8):083002, 2019.

[177] Gaoxue Wang, Chunhui Dong, Wenxi Wang, Zhiling Wang, Guozhi Chai, Changjun Jiang, and Desheng Xue. Observation of rotatable stripe domain in permalloy films with oblique sputtering. *Journal of Applied Physics*, 112(9):093907, 2012.

[178] Takao Iwata and FB Hagedorn. Annealing behavior of induced anisotropy and related magnetic properties in permalloy films. *Journal of Applied Physics*, 40(5):2258–2266, 1969.

[179] SI Woods, S Ingvarsson, JR Kirtley, HF Hamann, and RH Koch. Local magnetic anisotropy control in NiFe thin films via ion irradiation. *Applied physics letters*, 81(7):1267–1269, 2002.

[180] AI Schindler, RH Kernohan, and J Weertman. Effect of irradiation on magnetic properties of Fe-Ni alloys. *Journal of Applied Physics*, 35(9):2640–2646, 1964.

[181] A Mougin, T Mewes, M Jung, D Engel, A Ehresmann, H Schmoranzer, J Fassbender, and B Hillebrands. Local manipulation and reversal of the exchange bias field by ion irradiation in FeNi/FeMn double layers. *Physical Review B*, 63(6):060409, 2001.

[182] Julia Trützschler, Kadir Sentosun, Babak Mozooni, Roland Mattheis, and Jeffrey McCord. Magnetic domain wall gratings for magnetization reversal tuning and confined dynamic mode localization. *Scientific reports*, 6(1):30761, 2016.

[183] J Fassbender, J Von Borany, A Mücklich, K Potzger, W Möller, J McCord, L Schultz, and R Mattheis. Structural and magnetic modifications of Cr-implanted permalloy. *Physical Review B*, 73(18):184410, 2006.

[184] J Fassbender and J McCord. Control of saturation magnetization, anisotropy, and damping due to Ni implantation in thin NiFe layers. *Applied Physics Letters*, 88(25):252501, 2006.

[185] J Fassbender, A Mücklich, K Potzger, and W Möller. Mixing and subsequent amorphization of ultrathin NiFe/Ta bilayers by 30 keV Ni implantation. *Nuclear Instruments and Methods in Physics Research Section B: Beam Interactions with Materials and Atoms*, 248(2):343–346, 2006.

[186] R Gupta, KP Lieb, Y Luo, GA Müller, P Schaaf, and K Zhang. Argon and krypton ion-induced changes in permalloy thin films. *The European Physical Journal B*, 63(4):501–506, 2008.

[187] JEE Baglin, MH Tabacniks, R Fontana, AJ Kellock, and TT Bardin. Effects of ion irradiation on ferromagnetic thin films. In *Materials Science Forum*, volume 248, pages 87–94. Trans Tech Publ, 1997.

[188] G. Masciocchi, J.W. van der Jagt, M.-A. Syskaki, J. Langer, G. Jakob, J. McCord, B. Borie, A. Kehlberger, D. Ravelosona, and M. Kläui. Optimization of permalloy properties for magnetic field sensors using he^{+} irradiation. *Phys. Rev. Appl.*, 20:014001, Jul 2023.

[189] J Vukanić and P Sigmund. Total backscattering of keV light ions from solid targets in single-collision approximation. *Applied physics*, 11(3):265–272, 1976.

[190] Cengiz Okay, Perihan Aksu, Caner Deger, and Fikret Yildiz. Tailoring the magnetic anisotropy of cobalt-gold thin films. *Turkish Journal of Physics*, 42(3):335–341, 2018.

[191] SJ Park, DP Norton, and Venkat Selvamanickam. Ion-beam texturing of uniaxially textured Ni films. *Applied Physics Letters*, 87(3):031907, 2005.

[192] Johannes W van der Jagt, Vincent Jeudy, André Thiaville, Mamour Sall, Nicolas Vernier, Liza Herrera Diez, Mohamed Belmeguenai, Yves Roussigné, Salim M Chérif, Mouad Fattouhi, et al. Revealing nanoscale disorder in W/Co-Fe-B/MgO ultrathin films using domain-wall motion. *Physical Review Applied*, 18(5):054072, 2022.

[193] Frank Schulz, Robert Lawitzki, Hubert Głowiński, Filip Lisiecki, Nick Träger, Piotr Kuświk, Eberhard Goering, Gisela Schütz, and Joachim Gräfe. Increase of Gilbert damping in permalloy thin films due to heat-induced structural changes. *Journal of Applied Physics*, 129(15):153903, 2021.

[194] WG Wang, J Jordan-Sweet, GX Miao, C Ni, AK Rumaiz, LR Shah, X Fan, P Parsons, R Stearrett, ER Nowak, et al. In-situ characterization of rapid crystallization of amorphous CoFeB electrodes in CoFeB/MgO/CoFeB junctions during thermal annealing. *Applied Physics Letters*, 95(24):242501, 2009.

[195] Jeffrey McCord, Thomas Gemming, Ludwig Schultz, Jürgen Fassbender, Maciej Oskar Liedke, Michael Frommberger, and Eckhard Quandt. Magnetic anisotropy and domain patterning of amorphous films by He-ion irradiation. *Applied Physics Letters*, 86(16):162502, 2005.

[196] D Ravelosona, C Chappert, V Mathet, and H Bernas. Chemical order induced by ion irradiation in FePt (001) films. *Applied Physics Letters*, 76(2):236–238, 2000.

[197] Pei Zou, Winnie Yu, and James A Bain. Influence of stress and texture on soft magnetic properties of thin films. *IEEE Transactions on Magnetics*, 38(5):3501–3520, 2002.

[198] K Yu Guslienko, Valentyn Novosad, Y Otani, H Shima, and K Fukamichi. Field evolution of magnetic vortex state in ferromagnetic disks. *Applied Physics Letters*, 78(24):3848–3850, 2001.

[199] Tobias Wurft, W Raberg, K Prügl, A Satz, Günter Reiss, and H Brückl. Evolution of magnetic vortex formation in micron-sized disks. *Applied Physics Letters*, 115(13):132407, 2019.

[200] Ratnesh Gupta, K-H Han, KP Lieb, GA Müller, P Schaaf, and K Zhang. Influence of ion implantation on the magnetic properties of thin FeCo films. *Journal of Applied Physics*, 97(7):073911, 2005.

[201] LI Jian, JC Liu, and JW Mayer. Ar^+ ion irradiation induced grain growth in Au and Pt thin films. *Nuclear Instruments and Methods in Physics Research Section B: Beam Interactions with Materials and Atoms*, 36(3):306–311, 1989.

[202] Joyce C Liu, M Nastasi, and JW Mayer. Ion irradiation induced grain growth in Pd polycrystalline thin films. *Journal of Applied Physics*, 62(2):423–428, 1987.

[203] Joyce C Liu and JW Mayer. Ion irradiation induced grain growth in Ni polycrystalline thin films. *Nuclear Instruments and Methods in Physics Research Section B: Beam Interactions with Materials and Atoms*, 19:538–542, 1987.

[204] T Devolder. Light ion irradiation of Co/Pt systems: Structural origin of the decrease in magnetic anisotropy. *Physical Review B*, 62(9):5794, 2000.

[205] A Maziewski, P Mazalski, Z Kurant, MO Liedke, J McCord, J Fassbender, J Ferré, A Mougin, A Wawro, LT Baczewski, et al. Tailoring of magnetism in Pt/Co/Pt ultrathin films by ion irradiation. *Physical Review B*, 85(5):054427, 2012.

[206] Ian Gilbert, Andres C Chavez, Daniel T Pierce, John Unguris, Wei-Yang Sun, Cheng-Yen Liang, and Gregory P Carman. Magnetic microscopy and simulation of strain-mediated control of magnetization in PMN-PT/Ni nanostructures. *Applied Physics Letters*, 109(16):162404, 2016.

[207] EW Singleton and KJ Duxstad. Interfacial contributions to magnetostriction of ferromagnetic layers for magnetoresistive sensors. *MRS Online Proceedings Library*, 721:1–6, 2002.

[208] Geon Choe. Giant interface magnetostriction and temperature dependence in NiFe films encapsulated with Ta and AlOx layers. *IEEE Transactions on Magnetics*, 35(5):3838–3840, 1999.

[209] Ohsung Song, CA Ballentine, and RC O'Handley. Giant surface magnetostriction in polycrystalline Ni and NiFe films. *Applied Physics Letters*, 64(19):2593–2595, 1994.

[210] J Fassbender and J McCord. Magnetic patterning by means of ion irradiation and implantation. *Journal of Magnetism and Magnetic Materials*, 320(3-4):579–596, 2008.

[211] Se Kwon Kim, Geoffrey SD Beach, Kyung-Jin Lee, Teruo Ono, Theo Rasing, and Hyunsoo Yang. Ferrimagnetic spintronics. *Nature Materials*, 21(1):24–34, 2022.

[212] Kab-Jin Kim, Se Kwon Kim, Yuushou Hirata, Se-Hyeok Oh, Takayuki Tono, Duck-Ho Kim, Takaya Okuno, Woo Seung Ham, Sanghoon Kim, Gyoungchoon Go, et al. Fast domain wall motion in the vicinity of the angular momentum compensation temperature of ferrimagnets. *Nature materials*, 16(12):1187–1192, 2017.

[213] TA Ostler, J Barker, RFL Evans, RW Chantrell, U Atxitia, O Chubykalo-Fesenko, S El Moussaoui, LBPJ Le Guyader, E Mengotti, LJ Heyderman, et al. Ultrafast heating as a sufficient stimulus for magnetization reversal in a ferrimagnet. *Nature communications*, 3(1):1–6, 2012.

[214] MLM Lalieu, MJG Peeters, SRR Haenen, R Lavrijsen, and B Koopmans. Deterministic all-optical switching of synthetic ferrimagnets using single femtosecond laser pulses. *Physical review B*, 96(22):220411, 2017.

[215] L Avilés-Félix, Aurélien Olivier, Guanqiao Li, Carl S Davies, Laura Álvaro-Gómez, Miguel Rubio-Roy, Stéphane Auffret, Andrei Kirilyuk, AV Kimel, Th Rasing, et al. Single-shot all-optical switching of magnetization in Tb/Co multilayer-based electrodes. *Scientific reports*, 10(1):1–8, 2020.

[216] Maarten Beens, Mark LM Lalieu, Axel JM Deenen, Rembert A Duine, and Bert Koopmans. Comparing all-optical switching in synthetic-ferrimagnetic multilayers and alloys. *Physical Review B*, 100(22):220409, 2019.

[217] Yong Xu, Marwan Deb, Grégory Malinowski, Michel Hehn, Weisheng Zhao, and Stéphane Mangin. Ultrafast magnetization manipulation using single femtosecond light and hot-electron pulses. *Advanced Materials*, 29(42):1703474, 2017.

[218] Thai Ha Pham, J Vogel, J Sampaio, M Vaňatka, J-C Rojas-Sánchez, M Bonfim, DS Chaves, F Choueikani, P Ohresser, E Otero, et al. Very large domain wall velocities in Pt/Co/GdOx and Pt/Co/Gd trilayers with Dzyaloshinskii-Moriya interaction. *EPL (Europhysics Letters)*, 113(6):67001, 2016.

[219] Pingzhi Li, Thomas J Kools, Bert Koopmans, and Reinoud Lavrijsen. Ultrafast racetrack based on compensated Co/Gd-based synthetic ferrimagnet with All-Optical Switching. *Advanced Electronic Materials*, 9(1):2200613, 2023.

[220] Luding Wang, Houyi Cheng, Pingzhi Li, Youri LW van Hees, Yang Liu, Kaihua Cao, Reinoud Lavrijsen, Xiaoyang Lin, Bert Koopmans, and Weisheng Zhao. Picosecond optospintronic tunnel junctions. *Proceedings of the National Academy of Sciences*, 119(24):e2204732119, 2022.

[221] Tetsuo Endoh, Hiroaki Honjo, Koichi Nishioka, and Shoji Ikeda. Recent progresses in STT-MRAM and SOT-MRAM for next generation MRAM. In *2020 IEEE Symposium on VLSI Technology*, pages 1–2. IEEE, 2020.

[222] Stuart SP Parkin, Masamitsu Hayashi, and Luc Thomas. Magnetic domain-wall racetrack memory. *Science*, 320(5873):190–194, 2008.

[223] See-Hun Yang, Kwang-Su Ryu, and Stuart Parkin. Domain-wall velocities of up to 750 m s- 1 driven by exchange-coupling torque in synthetic antiferromagnets. *Nature nanotechnology*, 10(3):221–226, 2015.

[224] See-Hun Yang, Chirag Garg, Timothy Phung, Charles Rettner, and Brian Hughes. Spin-orbit torque driven one-bit magnetic racetrack devices-memory and neuromorphic applications. In *2019 International Symposium on VLSI Technology, Systems and Application (VLSI-TSA)*, pages 1–2. IEEE, 2019.

[225] Qiming Shao, Zhongrui Wang, and J Joshua Yang. Efficient AI with MRAM. *Nature Electronics*, 5(2):67–68, 2022.

[226] Stuart Parkin and See-Hun Yang. Memory on the racetrack. *Nature nanotechnology*, 10(3):195–198, 2015.

[227] Saied Tehrani. Status and outlook of MRAM memory technology. In *2006 International Electron Devices Meeting*, pages 1–4. IEEE, 2006.

[228] Kevin Garello, Farrukh Yasin, and Gouri Sankar Kar. Spin-orbit torque MRAM for ultrafast embedded memories: From fundamentals to large scale technology integration. In *2019 IEEE 11th International Memory Workshop (IMW)*, pages 1–4. IEEE, 2019.

[229] I Radu, K Vahaplar, C Stamm, T Kachel, N Pontius, HA Dürr, TA Ostler, J Barker, RFL Evans, RW Chantrell, et al. Transient ferromagnetic-like state mediating ultrafast reversal of antiferromagnetically coupled spins. *Nature*, 472(7342):205–208, 2011.

[230] Alexey V Kimel and Mo Li. Writing magnetic memory with ultrashort light pulses. *Nature Reviews Materials*, 4(3):189–200, 2019.

[231] Peiyao Zhang, Ting-Fung Chung, Quanwei Li, Siqi Wang, Qingjun Wang, Warren LB Huey, Sui Yang, Joshua E Goldberger, Jie Yao, and Xiang Zhang. All-optical switching of magnetization in atomically thin CrI3. *Nature materials*, 21(12):1373–1378, 2022.

[232] Elzbieta K Sobolewska, Johan Pelloux-Prayer, Hanna Becker, Guanqiao Li, Carl S Davies, CJ Krückel, L Avilés Félix, Aurélien Olivier, Ricardo C Sousa, Ioan-Lucian Prejbeanu, et al. Integration platform for optical switching of magnetic elements. In *Active Photonic Platforms XII*, volume 11461, pages 54–72. SPIE, 2020.

[233] L Avilés-Félix, L Álvaro-Gómez, G Li, CS Davies, A Olivier, Miguel Rubio-Roy, S Auffret, A Kirilyuk, AV Kimel, Th Rasing, et al. Integration of Tb/Co multilayers within optically switchable perpendicular magnetic tunnel junctions. *Aip Advances*, 9(12):125328, 2019.

[234] Mark LM Lalieu, Reinoud Lavrijsen, and Bert Koopmans. Integrating all-optical switching with spintronics. *Nature communications*, 10(1):110, 2019.

[235] Hanna Becker, Clemens J Krückel, Dries Van Thourhout, and Martijn JR Heck. Out-of-plane focusing grating couplers for silicon photonics integration with optical MRAM technology. *IEEE Journal of Selected Topics in Quantum Electronics*, 26(2):1–8, 2019.

[236] Henry Windischmann. Intrinsic stress in sputter-deposited thin films. *Critical Reviews in Solid State and Material Sciences*, 17(6):547–596, 1992.

[237] Zuolun Chen, Xiaohui Shi, Xiang Liu, Xia Chen, Zeyu Zhang, and Wenbo Mi. Modulating saturation magnetization and topological Hall resistivity of flexible ferrimagnetic Mn4N films by bending strains. *Journal of Applied Physics*, 132(23):233906, 2022.

[238] Ming Zheng, Pengfei Guan, and Heliang Fan. Mechanically enhanced magnetism in flexible semitransparent CuFe2O4/mica epitaxial heterostructures. *Applied Surface Science*, 584:152586, 2022.

[239] Shinya Ota, Pham Van Thach, Hiroyuki Awano, Akira Ando, Kentaro Toyoki, Yoshinori Kotani, Tetsuya Nakamura, Tomohiro Koyama, and Daichi Chiba. Strain-induced modulation of temperature characteristics in ferrimagnetic Tb-Fe films. *Scientific reports*, 11(1):1–7, 2021.

[240] Junshuai Wang, Mingfen Li, Chaozhong Li, Rujun Tang, Mingsu Si, Guozhi Chai, Jinli Yao, Chenglong Jia, and Changjun Jiang. Piezostrain-controlled magnetization compensation temperature in ferrimagnetic GdFeCo alloy films. *Physical Review B*, 107(18):184424, 2023.

[241] Ali Tavassolizadeh, Karsten Rott, Tobias Meier, Eckhard Quandt, Hendrik Hölscher, Günter Reiss, and Dirk Meyners. Tunnel magnetoresistance sensors with magnetostrictive electrodes: Strain sensors. *Sensors*, 16(11):1902, 2016.

[242] Ajeesh M Sahadevan, Ravi K Tiwari, Gopinadhan Kalon, Charanjit S Bhatia, Mark Saeys, and Hyunsoo Yang. Biaxial strain effect of spin dependent tunneling in MgO magnetic tunnel junctions. *Applied Physics Letters*, 101(4):042407, 2012.

[243] Qianchang Wang, John Domann, Guoqiang Yu, Anthony Barra, Kang L Wang, and Gregory P Carman. Strain-mediated spin-orbit-torque switching for magnetic memory. *Physical Review Applied*, 10(3):034052, 2018.

[244] Giovanni Masciocchi, Thomas J. Kools, Pingzhi Li, Adrien A. D. Petrillo, Bert Koopmans, Reinoud Lavrijsen, Andreas Kehlberger, and Mathias Kläui. Strain effects on magnetic compensation and spin reorientation transition of Co/Gd synthetic ferrimagnets. *Journal of Applied Physics*, 134(1):013904, 07 2023.

[245] Claude Chappert, Albert Fert, and Frédéric Nguyen Van Dau. The emergence of spin electronics in data storage. *Nature materials*, 6(11):813–823, 2007.

[246] Bharati Tudu and Ashutosh Tiwari. Recent developments in perpendicular magnetic anisotropy thin films for data storage applications. *Vacuum*, 146:329–341, 2017.

[247] MT Johnson, PJH Bloemen, FJA Den Broeder, and JJ De Vries. Magnetic anisotropy in metallic multilayers. *Reports on Progress in Physics*, 59(11):1409, 1996.

[248] FJA Den Broeder, W Hoving, and PJH Bloemen. Magnetic anisotropy of multilayers. *Journal of magnetism and magnetic materials*, 93:562–570, 1991.

[249] K Kyuno, J-G Ha, R Yamamoto, and S Asano. Theoretical study on the strain dependence of the magnetic anisotropy of X/Co (X= Pt, Cu, Ag, and Au) metallic multilayers. *Journal of applied physics*, 79(9):7084–7089, 1996.

[250] S Hashimoto, Y Ochiai, and K Aso. Perpendicular magnetic anisotropy and magnetostriction of sputtered Co/Pd and Co/Pt multilayered films. *Journal of applied physics*, 66(10):4909–4916, 1989.

[251] K Twarowski and HK Lachowicz. Magnetostriction and anisotropy of amorphous Gd-Co RF sputtered thin films. *Journal of Applied Physics*, 50(B11):7722–7724, 1979.

[252] K Twarowski, HK Lachowicz, M Gutowski, and H Szymczak. On the origin of the perpendicular anisotropy and magnetostriction in amorphous RF sputtered Gd Co films. *physica status solidi (a)*, 63(1):103–108, 1981.

[253] Thomas J Kools, Marnix C van Gurp, Bert Koopmans, and Reinoud Lavrijsen. Magnetostatics of room temperature compensated Co/Gd/Co/Gd-based synthetic ferrimagnets. *Applied Physics Letters*, 121:242405, 2022.

[254] GA Bertero, TC Hufnagel, BM Clemens, and R Sinclair. TEM analysis of Co-Gd and Co-Gd multilayer structures. *Journal of materials research*, 8(4):771–774, 1993.

[255] B Zhang, Kannan M Krishnan, CH Lee, and RFC Farrow. Magnetic anisotropy and lattice strain in Co/Pt multilayers. *Journal of applied physics*, 73(10):6198–6200, 1993.

[256] Daniel B Gopman, Cindi L Dennis, PJ Chen, Yury L Iunin, Peter Finkel, Margo Staruch, and Robert D Shull. Strain-assisted magnetization reversal in Co/Ni multilayers with perpendicular magnetic anisotropy. *Scientific reports*, 6(1):1–8, 2016.

[257] Mathias Kläui. Head-to-head domain walls in magnetic nanostructures. *Journal of Physics: Condensed matter*, 20(31):313001, 2008.

[258] R. Spain. Domain tip propagation logic. *IEEE Transactions on Magnetics*, 2(3):347–351, 1966.

[259] Dan A Allwood, Gang Xiong, CC Faulkner, D Atkinson, D Petit, and RP Cowburn. Magnetic domain-wall logic. *science*, 309(5741):1688–1692, 2005.

[260] P Vavassori, V Metlushko, B Ilic, Marco Gobbi, Marco Donolato, Matteo Cantoni, and Riccardo Bertacco. Domain wall displacement in py square ring for single nanometric magnetic bead detection. *Applied Physics Letters*, 93(20):203502, 2008.

[261] Marco Donolato, Paolo Vavassori, Marco Gobbi, Maria Deryabina, Mikkel F Hansen, Vitali Metlushko, Bojan Ilic, Matteo Cantoni, Daniela Petti, Stefano Brivio, et al. On-chip manipulation of protein-coated magnetic beads via domain-wall conduits. *Advanced materials*, 22(24):2706–2710, 2010.

[262] Elizabeth Rapoport and Geoffrey SD Beach. Dynamics of superparamagnetic microbead transport along magnetic nanotracks by magnetic domain walls. *Applied Physics Letters*, 100(8):082401, 2012.

[263] Marco Diegel, Roland Mattheis, and Ernst Halder. Multiturn counter using movement and storage of 180° magnetic domain walls. *Sensor Letters*, 5(1):118–122, 2007.

[264] R Mattheis, S Glathe, M Diegel, and U Hübner. Concepts and steps for the realization of a new domain wall based giant magnetoresistance nanowire device: From the available 24 multiturn counter to a 212 turn counter. *Journal of Applied Physics*, 111(11):113920, 2012.

[265] B Borie, A Kehlberger, J Wahrhusen, H Grimm, and M Kläui. Geometrical dependence of domain-wall propagation and nucleation fields in magnetic-domain-wall sensors. *Physical Review Applied*, 8(2):024017, 2017.

[266] Felipe Garcia-Sanchez, Attila Kakay, Riccardo Hertel, and Pierre Asselin. Depinning of transverse domain walls from notches in magnetostatically coupled nanostrips. *Applied physics express*, 4(3):033001, 2011.

[267] Duc-Quang Hoang, Xuan-Huu Cao, Hoai-Thuong Nguyen, and Vinh-Ai Dao. Creation and propagation of a single magnetic domain wall in 2D nanotraps with a square injection pad. *Nanotechnology*, 32(9):095703, 2020.

[268] WD Van Driel, JHJ Janssen, GQ Zhang, DG Yang, and LJ Ernst. Packaging induced die stresses-effect of chip anisotropy and time-dependent behavior of a molding compound. *Journal of Electronic Packaging*, 125(4):520–526, 2003.

[269] Na Lei, Thibaut Devolder, Guillaume Agnus, Pascal Aubert, Laurent Daniel, Joo-Von Kim, Weisheng Zhao, Theodossis Trypiniotis, Russell P Cowburn, Claude Chappert, et al. Strain-controlled magnetic domain wall propagation in hybrid piezoelectric/ferromagnetic structures. *Nature communications*, 4(1):1–7, 2013.

[270] RP Cowburn, DA Allwood, Gang Xiong, and MD Cooke. Domain wall injection and propagation in planar permalloy nanowires. *Journal of Applied Physics*, 91(10):6949–6951, 2002.

[271] K Shigeto, T Shinjo, and T Ono. Injection of a magnetic domain wall into a submicron magnetic wire. *Applied Physics Letters*, 75(18):2815–2817, 1999.

[272] Haomiao Zhou, Shengbin Shi, Diqing Nian, Shuting Cui, Jing Luo, Yang Qiu, Han Yang, Mingmin Zhu, and Guoliang Yu. Voltage control of magnetic domain wall injection into strain-mediated multiferroic heterostructures. *Nanoscale*, 12(27):14479–14486, 2020.

[273] Ren-Ci Peng, Jia-Mian Hu, Kasra Momeni, Jian-Jun Wang, Long-Qing Chen, and Ce-Wen Nan. Fast 180° magnetization switching in a strain-mediated multiferroic heterostructure driven by a voltage. *Scientific Reports*, 6(1):1–9, 2016.

[274] Mathias Weiler, Andreas Brandlmaier, Stephan Geprägs, Matthias Althammer, Matthias Opel, Christoph Bihler, Hans Huebl, Martin S Brandt, Rudolf Gross, and Sebastian TB Gönnenwein. Voltage controlled inversion of magnetic anisotropy in a ferromagnetic thin film at room temperature. *New Journal of Physics*, 11(1):013021, 2009.

[275] Yaping Zhang, Xin Fan, Weigang Wang, Xiaoming Kou, Rong Cao, Xing Chen, Chaoying Ni, Liqing Pan, and John Q Xiao. Study and tailoring spin dynamic properties of CoFeB during rapid thermal annealing. *Applied Physics Letters*, 98(4):042506, 2011.

[276] G Venkat Swamy, RK Rakshit, RP Pant, and GA Basheed. Origin of 'in-plane'and 'out-of-plane'magnetic anisotropies in as-deposited and annealed CoFeB ferromagnetic thin films. *Journal of Applied Physics*, 117(17):17A312, 2015.

[277] Angshuman Deka, Bivas Rana, Ryo Anami, Katsuya Miura, Hiromasa Takahashi, YoshiChika Otani, and Yasuhiro Fukuma. Electric-field control of interfacial in-plane magnetic anisotropy in CoFeB/MgO junctions. *Physical Review B*, 101(17):174405, 2020.

[278] B Cui, C Song, YY Wang, WS Yan, F Zeng, and F Pan. Tuning of uniaxial magnetic anisotropy in amorphous CoFeB films. *Journal of Physics: Condensed Matter*, 25(10):106003, 2013.

[279] Arun Raghunathan, John Evan Snyder, and DC Jiles. Comparison of alternative techniques for characterizing magnetostriction and inverse magnetostriction in magnetic thin films. *IEEE Transactions on Magnetics*, 45(9):3269–3273, 2009.

[280] O Thomas, Q Shen, Philippe Schieffer, N Tournerie, and Bruno Lépine. Interplay between anisotropic strain relaxation and uniaxial interface magnetic anisotropy in epitaxial Fe films on (001) GaAs. *Physical Review Letters*, 90(1):017205, 2003.

[281] D McGrouther, S McVitie, JN Chapman, and A Gentils. Controlled domain wall injection into ferromagnetic nanowires from an optimized pad geometry. *Applied Physics Letters*, 91(2):022506, 2007.

[282] Jie Wang. Mechanical control of magnetic order: from phase transition to skyrmions. *Annual Review of Materials Research*, 49:361–388, 2019.

[283] Mi-Young Im, Lars Bocklage, Peter Fischer, and Guido Meier. Direct observation of stochastic domain-wall depinning in magnetic nanowires. *Physical Review Letters*, 102(14):147204, 2009.

[284] LK Bogart, D Atkinson, K O'Shea, D McGrouther, and S McVitie. Dependence of domain wall pinning potential landscapes on domain wall chirality and pinning site geometry in planar nanowires. *Physical Review B*, 79(5):054414, 2009.

[285] Dirk Backes, Christine Schieback, Mathias Kläui, Friederike Junginger, Henri Ehrke, Peter Nielaba, Ulrich Rüdiger, Laura J Heyderman, Cheng-Shi Chen, Takeshi Kasama, et al. Transverse domain walls in nanoconstrictions. *Applied Physics Letters*, 91(11):112502, 2007.

[286] Andreas Brandlmaier, Stephan Geprägs, Mathias Weiler, Andrea Boger, Matthias Opel, Hans Huebl, Christoph Bihler, Martin S Brandt, Bernhard Botters, D Grundler, et al. In situ manipulation of magnetic anisotropy in magnetite thin films. *Physical Review B*, 77(10):104445, 2008.

[287] Robert D McMichael and Michael J Donahue. Head to head domain wall structures in thin magnetic strips. *IEEE Transactions on Magnetics*, 33(5):4167–4169, 1997.

[288] R Yanes, F Garcia-Sanchez, RF Luis, E Martinez, V Raposo, L Torres, and L Lopez-Diaz. Skyrmion motion induced by voltage-controlled in-plane strain gradients. *Applied Physics Letters*, 115(13):132401, 2019.

[289] Safiul Alam Mollick, Ranveer Singh, Mohit Kumar, Satyaranjan Bhattacharyya, and Tapobrata Som. Strong uniaxial magnetic anisotropy in Co films on highly ordered grating-like nanopatterned Ge surfaces. *Nanotechnology*, 29(12):125302, 2018.

[290] Amit Kumar, Sebastian Fähler, Heike Schloerb, Karin Leistner, and Ludwig Schultz. Competition between shape anisotropy and magnetoelastic anisotropy in Ni nanowires electrodeposited within alumina templates. *Physical Review B*, 73(6):064421, 2006.

[291] Sasikanth Manipatruni, Dmitri E Nikonov, and Ian A Young. Beyond CMOS computing with spin and polarization. *Nature Physics*, 14(4):338–343, 2018.

[292] T Ono, H Miyajima, K Shigeto, Ko Mibu, N Hosoito, and T Shinjo. Propagation of a magnetic domain wall in a submicrometer magnetic wire. *Science*, 284(5413):468–470, 1999.

[293] Del Atkinson, Dan A Allwood, Gang Xiong, Michael D Cooke, Colm C Faulkner, and Russell P Cowburn. Magnetic domain-wall dynamics in a submicrometre ferromagnetic structure. *Nature materials*, 2(2):85–87, 2003.

[294] Masamitsu Hayashi, Luc Thomas, Rai Moriya, Charles Rettner, and Stuart SP Parkin. Current-controlled magnetic domain-wall nanowire shift register. *Science*, 320(5873):209–211, 2008.

[295] JH Franken, HJM Swagten, and Bert Koopmans. Shift registers based on magnetic domain wall ratchets with perpendicular anisotropy. *Nature nanotechnology*, 7(8):499–503, 2012.

[296] Zhaochu Luo, Aleš Hrabec, Trong Phuong Dao, Giacomo Sala, Simone Finizio, Junxiao Feng, Sina Mayr, Jörg Raabe, Pietro Gambardella, and Laura J Heyderman. Current-driven magnetic domain-wall logic. *Nature*, 579(7798):214–218, 2020.

[297] Xueying Zhang, Nicolas Vernier, Zhiqiang Cao, Qunwen Leng, Anni Cao, Dafiné Ravelosona, and Weisheng Zhao. Magnetoresistive sensors based on the elasticity of domain walls. *Nanotechnology*, 29(36):365502, 2018.

[298] Mahshid Alamdar, Thomas Leonard, Can Cui, Bishweshwor P Rimal, Lin Xue, Otitoaleke G Akinola, T Patrick Xiao, Joseph S Friedman, Christopher H Bennett, Matthew J Marinella, et al. Domain wall-magnetic tunnel junction spin–orbit torque devices and circuits for in-memory computing. *Applied Physics Letters*, 118(11):112401, 2021.

[299] Kun Yue, Yizhou Liu, Roger K Lake, and Alice C Parker. A brain-plausible neuromorphic on-the-fly learning system implemented with magnetic domain wall analog memristors. *Science advances*, 5(4):eaau8170, 2019.

[300] Albert Fert, Nicolas Reyren, and Vincent Cros. Magnetic skyrmions: advances in physics and potential applications. *Nature Reviews Materials*, 2(7):1–15, 2017.

[301] Khalid A Omari, Thomas J Broomhall, Richard WS Dawidek, Dan A Allwood, Ruth C Bradley, Jonathan M Wood, Paul W Fry, Mark C Rosamond, Edmund H Linfield, Mi-Young Im, et al. Toward chirality-encoded domain wall logic. *Advanced Functional Materials*, 29(10):1807282, 2019.

[302] Deng-Shiang Shiu, Kao-Fan Lai, Yi-Ying Liu, Yuan-Ting Li, Zhi-En Gao, Yee-Mou Kao, Jong-Ching Wu, and Lance Horng. Depinning behavior of the vortex domain wall at the asymmetric triangular notch in permalloy wires. *Journal of Physics Communications*, 5(7):075014, 2021.

[303] M Al Bahri, Benjamin Borie, TL Jin, Rachid Sbiaa, Mathias Kläui, and SN Piramanayagam. Staggered magnetic nanowire devices for effective domain-wall pinning in racetrack memory. *Physical Review Applied*, 11(2):024023, 2019.

[304] A Barra, Andrew Ross, Olena Gomonay, Lorenzo Baldrati, A Chavez, Romain Lebrun, JD Schneider, Paymon Shirazi, Q Wang, Jairo Sinova, et al. Effective strain manipulation of the antiferromagnetic state of polycrystalline nio. *Applied Physics Letters*, 118(17):172408, 2021.

[305] Min Chu, Yongke Sun, Umamaheswari Aghoram, and Scott E Thompson. Strain: A solution for higher carrier mobility in nanoscale MOSFETs. *Annual Review of Materials Research*, 39:203–229, 2009.

[306] James L Doherty, Steven G Noyce, Zhihui Cheng, Hattan Abuzaid, and Aaron D Franklin. Capping layers to improve the electrical stress stability of mos2 transistors. *ACS applied materials & interfaces*, 12(31):35698–35706, 2020.

[307] G. Masciocchi, M. Fattouhi, E. Spetzler, M.-A. Syskaki, R. Lehndorff, E. Martinez, J. McCord, L. Lopez-Diaz, A. Kehlberger, and M. Kläui. Generation of imprinted strain gradients for spintronics. *Applied Physics Letters*, 123(2):022404, 07 2023.

[308] COMSOL AB, Stockholm, Sweden. Comsol multiphysics® v. 6.1, 2023.

[309] KA Thórarinsdóttir, Nanny Strandqvist, VV Sigurjónsdóttir, EB Thorsteinsson, Björgvin Hjörvarsson, and F Magnus. Finding order in disorder: Magnetic coupling distributions and competing anisotropies in an amorphous metal alloy. *APL Materials*, 10(4):041103, 2022.

[310] C Robert. Handley, modern magnetic materials: Principles and applications, 2000.

[311] DL Wen, ZY Chen, WH Li, MH Qin, DY Chen, Z Fan, M Zeng, XB Lu, XS Gao, and J-M Liu. Ultralow-loss domain wall motion driven by a magnetocrystalline anisotropy gradient in an antiferromagnetic nanowire. *Physical Review Research*, 2(1):013166, 2020.

[312] I Polenciuc, AJ Vick, DA Allwood, TJ Hayward, G Vallejo-Fernandez, K O'Grady, and A Hirohata. Domain wall pinning for racetrack memory using exchange bias. *Applied Physics Letters*, 105(16):162406, 2014.

[313] Qianchang Wang, Xu Li, Cheng-Yen Liang, Anthony Barra, John Domann, Chris Lynch, Abdon Sepulveda, and Greg Carman. Strain-mediated 180 switching in CoFeB and Terfenol-D nanodots with perpendicular magnetic anisotropy. *Applied Physics Letters*, 110(10):102903, 2017.

[314] Guoqiang Yu, Zhenxing Wang, Maryam Abolfath-Beygi, Congli He, Xiang Li, Kin L Wong, Paul Nordeen, Hao Wu, Gregory P Carman, Xiufeng Han, et al. Strain-induced modulation of perpendicular magnetic anisotropy in Ta/CoFeB/MgO structures investigated by ferromagnetic resonance. *Applied Physics Letters*, 106(7):072402, 2015.

[315] H Koo, C Krafft, and RD Gomez. Current-controlled bi-stable domain configurations in Ni_{81} Fe_{19} elements: An approach to magnetic memory devices. *Applied physics letters*, 81(5):862–864, 2002.

[316] Damir Vodenicarevic, Nicolas Locatelli, Alice Mizrahi, Joseph S Friedman, Adrien F Vincent, Miguel Romera, Akio Fukushima, Kay Yakushiji, Hitoshi Kubota, Shinji Yuasa, et al. Low-energy truly random number generation with superparamagnetic tunnel junctions for unconventional computing. *Physical Review Applied*, 8(5):054045, 2017.

[317] Bin Yang, Feng Liu, and Max G Lagally. Local strain-mediated chemical potential control of quantum dot self-organization in heteroepitaxy. *Physical review letters*, 92(2):025502, 2004.

[318] Bong Gyu Shin, Gang Hee Han, Seok Joon Yun, Hye Min Oh, Jung Jun Bae, Young Jae Song, Chong-Yun Park, and Young Hee Lee. Indirect bandgap puddles in monolayer MoS_2 by substrate-induced local strain. *Advanced Materials*, 28(42):9378–9384, 2016.

[319] Yee-Chia Yeo. Enhancing CMOS transistor performance using lattice-mismatched materials in source/drain regions. *Semiconductor science and technology*, 22(1):S177, 2006.

[320] CD Wood, JE Cunningham, R O'Rorke, C Wälti, EH Linfield, AG Davies, and SD Evans. Formation and manipulation of two-dimensional arrays of micron-scale particles in microfluidic systems by surface acoustic waves. *Applied Physics Letters*, 94(5):054101, 2009.

[321] Xiaoyun Ding, Peng Li, Sz-Chin Steven Lin, Zackary S Stratton, Nitesh Nama, Feng Guo, Daniel Slotcavage, Xiaole Mao, Jinjie Shi, Francesco Costanzo, et al. Surface acoustic wave microfluidics. *Lab on a Chip*, 13(18):3626–3649, 2013.

[322] Jintao Shuai, Luis Lopez-Diaz, John E Cunningham, and Thomas A Moore. Precise transport of skyrmions by surface acoustic waves. *arXiv preprint arXiv:2305.16006*, 2023.

[323] RD O'Rorke, CD Wood, C Wälti, SD Evans, AG Davies, and JE Cunningham. Acousto-microfluidics: Transporting microbubble and microparticle arrays in acoustic traps using surface acoustic waves. *Journal of Applied Physics*, 111(9):094911, 2012.

[324] Anil Adhikari and Shireen Adenwalla. Surface acoustic waves increase magnetic domain wall velocity. *AIP Advances*, 11(1):015234, 2021.

[325] Jintao Shuai, R Hunt, T Moore, and J Cunningham. Separation of heating and magnetoelastic coupling effects in surface-acoustic-wave-enhanced creep of magnetic domain walls. *Physical Review Applied*, 2023.

[326] Colin Campbell. *Surface Acoustic Wave Devices for Mobile and Wireless Communications, Four-Volume Set*. Academic press, 1998.

[327] A Adhikari, ER Gilroy, TJ Hayward, and S Adenwalla. Surface acoustic wave assisted depinning of magnetic domain walls. *Journal of Physics: Condensed Matter*, 33(31):31LT01, 2021.

[328] G Venkat, DA Allwood, and TJ Hayward. Magnetic domain walls: Types, processes and applications. *arXiv preprint arXiv:2305.17800*, 2023.

[329] K Yu Guslienko, XF Han, DJ Keavney, R Divan, and SD Bader. Magnetic vortex core dynamics in cylindrical ferromagnetic dots. *Physical review letters*, 96(6):067205, 2006.

[330] VS Pribiag, IN Krivorotov, GD Fuchs, PM Braganca, O Ozatay, JC Sankey, DC Ralph, and RA Buhrman. Magnetic vortex oscillator driven by DC spin-polarized current. *Nature physics*, 3(7):498–503, 2007.